



2018

ANNUAL REPORT JAHRESBERICHT

 **Paul-Drude-Institut
für Festkörperelektronik**
Leibniz-Institut im Forschungsverbund Berlin e. V.

Table of Contents

Inhaltsverzeichnis

Preface	
Vorwort	5
Director's Column	
Kolumne des Direktors	9
Scientific Advisory Board	
Wissenschaftlicher Beirat	14
Research Highlights	
Forschungshighlights	17
Core Research Areas	
Forschungsschwerpunkte	41
Brief Reports	
Kurzberichte	67
Departments	
Abteilungen	119
Facts & Figures	
Zahlen & Fakten	143
Contact	
Kontakt	167
Imprint	
Impressum	171



Humboldt-Universität zu Berlin

Hausvogteiplatz 5-7



Paul-Drude-Institut
für Festkörperelektronik



Preface

Vorwort

This annual report of PDI covers the period between the two meetings of our Scientific Advisory Board in October 2017 and October 2018.

As we have done for a number of years now, we take this opportunity to inform not only colleagues from our field, but also to provide the interested public with an insight into our research. The contributions include easy-to-read introductions to our Core Research Areas, they present our departments' expertise and also ponder some aspects of science policy.

A few selected scientific success stories are presented as highlights. These longer contributions are complemented by a selection of shorter reports about projects that have yielded significant progress during the year.

The first two highlight are contributed by the Core Research Area "Nanofabrication", where we work on the fabrication of novel materials in the form of thin films or nanostructures with utmost crystalline perfection. Here, we have pioneered the thin film growth of so-called phase change materials, which consist of germanium telluride (GeTe) and antimony telluride (Sb_2Te_3). While we could show in the past that layered stacks of these materials have superior performance in semiconductor memory devices, we have now investigated the structural properties of such stacks in great detail. Here it is of particular interest that Sb_2Te_3 is a layered material with only very weak forces between the layers, which can thereby not easily be subjected to strain.

Der vor Ihnen liegende Jahresbericht unseres Instituts stellt wissenschaftliche Ergebnisse und Erfolge vor, die wir im Zeitraum zwischen den Treffen unseres wissenschaftlichen Beirats vom Oktober 2017 und Oktober 2018 erarbeitet haben.

Wie wir es seit mittlerweile etlichen Jahren praktizieren, wollen wir mit unserem Jahresbericht nicht nur die Fachkollegen unseres Arbeitsgebietes informieren, sondern auch der wissenschaftlich interessierten Öffentlichkeit einen Eindruck von unserer Arbeit vermitteln. Die Beiträge umfassen daher allgemeinverständliche Einführungen in unsere zentralen Forschungsgebiete (Core Research Areas), sie stellen die Expertise unserer Abteilungen dar und berichten auch aus unserem wissenschaftspolitischen Umfeld.

Einige ausgewählte wissenschaftliche Erfolge präsentieren wir in ausführlicher Form als Highlights. Sie werden ergänzt durch eine Selektion von Kurzbeiträgen.

Die ersten beiden Highlights kommen aus der Core Research Area „Nanofabrication“, in der wir an der Herstellung neuer Materialien in der Form von dünnen Schichten oder Nanostrukturen mit höchster Perfektion arbeiten. Hier haben wir Pionierarbeit bei der Epitaxie von sogenannten Phasenwechselmaterialien geleistet, welche aus Germanium-Tellurid (GeTe) und Antimon-Tellurid (Sb_2Te_3) bestehen. Nachdem wir bislang schon zeigen konnten, dass Schichtstapel aus diesen beiden Materialien sich in besonderer Weise für Halbleiter-Datenspei-

Our studies show that such an opportunity is indeed opened by changing the Sb/Te ratio, providing evidence that the properties of layered materials can be tuned by close control of growth.

The second topic deals with the growth of thin layer stacks of $\text{Fe}_3\text{Si}/\text{Ge}/\text{Fe}_3\text{Si}$, which are a very rare example of the successful epitaxy of a layer system of the type metal/semiconductor/metal. We employ an unusual procedure termed "solid phase epitaxy", in which the stacks are deposited at such low temperature that they remain amorphous at first. In subsequent heating steps we achieve crystalline perfection and abrupt interfaces. Beyond that, we find that our growth scheme leads to the stabilization of crystal structures which do not exist in the form of single thicker layers – another example of creating novel materials by nanostructure epitaxy.

The third highlight builds on many fruits of our work on the growth and physical investigations of GaAs-based nanowire structures on Si. It comes from our Core Research Area "III-V Nanowires for Optoelectronics" where we are aiming at nanoscale light sources that are compatible with Si technology. We can meanwhile control the formation of the two different crystal structures which (again unlike in the growth of bulk material) occur in the growth of nanowires and which have slightly different properties. Together with the incorporation of e.g. InGaAs as an alloy, this allows for quite a variety of radial and axial quantum structures within one nanowire. Using our extensive range of spectroscopic methods and supported by theory and structural investigations, the work of this highlight gives a comprehensive picture of how the electronic structure of nanostructured light emitters can be tuned and controlled.

I would like to take this occasion to thank all members of our institute for their highly creative and committed work, which continuously advances our research. I also

cher eigenen, haben wir jetzt die strukturellen Eigenschaften solcher Stapel in großem Detail untersucht. Es ist dabei von besonderem Interesse, dass Sb_2Te_3 , ein zweidimensionales Material ist, das aufgrund der schwachen Bindungskräfte zwischen den Lagen nur schwer durch Verspannung verändert werden kann. Unsere Studie zeigt, dass eine solche Möglichkeit jedoch durch die Änderung des Sb/Te Verhältnisses geschaffen wird. Dies ist ein Nachweis dafür, dass die Eigenschaften von zweidimensionalen Materialen durch genaue Kontrolle des Wachstums beeinflusst werden können.

Das zweite Thema handelt vom Wachstum dünner Schichtpakete aus $\text{Fe}_3\text{Si}/\text{Ge}/\text{Fe}_3\text{Si}$, die ein sehr seltenes Beispiel von erfolgreichem Wachstum eines Schichtsystems darstellen, das aus Metall/Halbleiter/Metall besteht. Wir verwenden hier ein ungewöhnliches Verfahren in dem die Schichtstapel bei so niedriger Temperatur abgeschieden werden, dass die Materialien zuerst amorph bleiben. In darauf folgenden Temperaturbehandlungen erhalten wir dann sowohl kristalline Perfektion als auch abrupte Grenzflächen. Darüber hinaus konnten wir nachweisen, dass unser Wachstumsverfahren die Stabilisierung von Kristallstrukturen ermöglicht die in dicken, einzelnen Schichten nicht existieren – ein weiteres Beispiel dafür wie neuartige Materialien durch die Epitaxie von Nanostrukturen erzeugt werden können.

Das dritte Highlight basiert auf vielen Ergebnissen unserer bisherigen Arbeit zum Wachstum und zu den physikalischen Eigenschaften von Galliumarsenid-basierten Nanodraht-Strukturen auf Silizium. Es kommt aus unserer Core Research Area „III-V Nanodrähte für die Optoelektronik“ in der wir unter anderem an nanoskaligen Lichtquellen arbeiten, die mit der Si-Technologie kompatibel sind. Mittlerweile können wir die Ausbildung der zwei unterschiedlichen Kristallstrukturen kontrollieren die sich (wiederum anders als im Wachstum von dicken Schichten) beim Wachstum von Nanodrähten.

thank the numerous colleagues who have helped keeping our annual report interesting and attractive.

Furthermore, I would like to thank all our partners from academic and industrial research for numerous fruitful collaborations. As always, I express my special gratitude to the members of our Scientific Advisory Board and to our funding agencies for their continuous support.

Looking forward to further fruitful collaborations, I wish you enjoyable and inspiring reading.

ten ausbilden können, und die etwas unterschiedliche Eigenschaften zeigen. Zusammen mit dem Einbau von Indium lässt sich hiermit eine große Breite von radialen und axialen Quantenstrukturen in einem einzigen Nanodraht erzeugen. Durch Nutzung unserer umfangreichen spektroskopischen Methoden und unterstützt durch Theorie und strukturelle Untersuchungen gibt diese Arbeit ein umfangreiches Bild, wie die elektronischen Eigenschaften von nanostrukturierten Lichtemittern abgestimmt und kontrolliert werden können.

Ich möchte an dieser Stelle allen Mitarbeiterinnen und Mitarbeitern des Instituts meinen ungeteilten Dank dafür aussprechen, dass sie durch ihre kreative und engagierte Arbeit unsere Forschungen beständig vorantreiben. Auch danke ich den zahlreichen Mitarbeiterinnen und Mitarbeitern, die unseren Jahresbericht aktuell und attraktiv gestaltet haben.

Letztlich möchte ich diesen Jahresbericht wiederum nutzen, um allen wissenschaftlichen Kooperationspartnern in unserem akademischen und industriellen Umfeld für die zahlreichen fruchtbaren Zusammenarbeiten zu danken. Herzlich bedanken möchte ich mich ebenso bei den Mitgliedern unseres wissenschaftlichen Beirats für die engagiert kritische Begleitung unserer Arbeit, sowie bei unseren Fördergebern beim Bund und beim Land Berlin.

Ich wünsche Ihnen viel Freude bei der Lektüre und freue mich auf weitere fruchtbare Zusammenarbeit.



Henning Riechert



Leibniz
Forschungsverbund
Berlin e.V.

Leibniz
Forschungsverbund

meter?

metric system
fraction of
inch of a



METER

METER

10⁻¹⁰

insects

toddler

te

microscope

width of strand of
spider web silk
3 – 8 µm

LENGTH OF LIGHT



Paul-Drude-Institut
für Festkörperelektronik
DEVICE INSPIRING RESEARCH



Leibniz
Forschungsverbund
Berlin e.V.

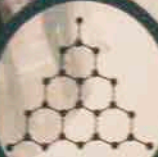
Leibniz
Forschungsverbund

What is a crystal?

Solid material whose atoms are arranged in an ordered microscopic structure forming a crystal

Did you know?

atoms of crystals can be seen under an electron microscope



How to present PDI to the public?

Wie soll sich das PDI in der Öffentlichkeit präsentieren?

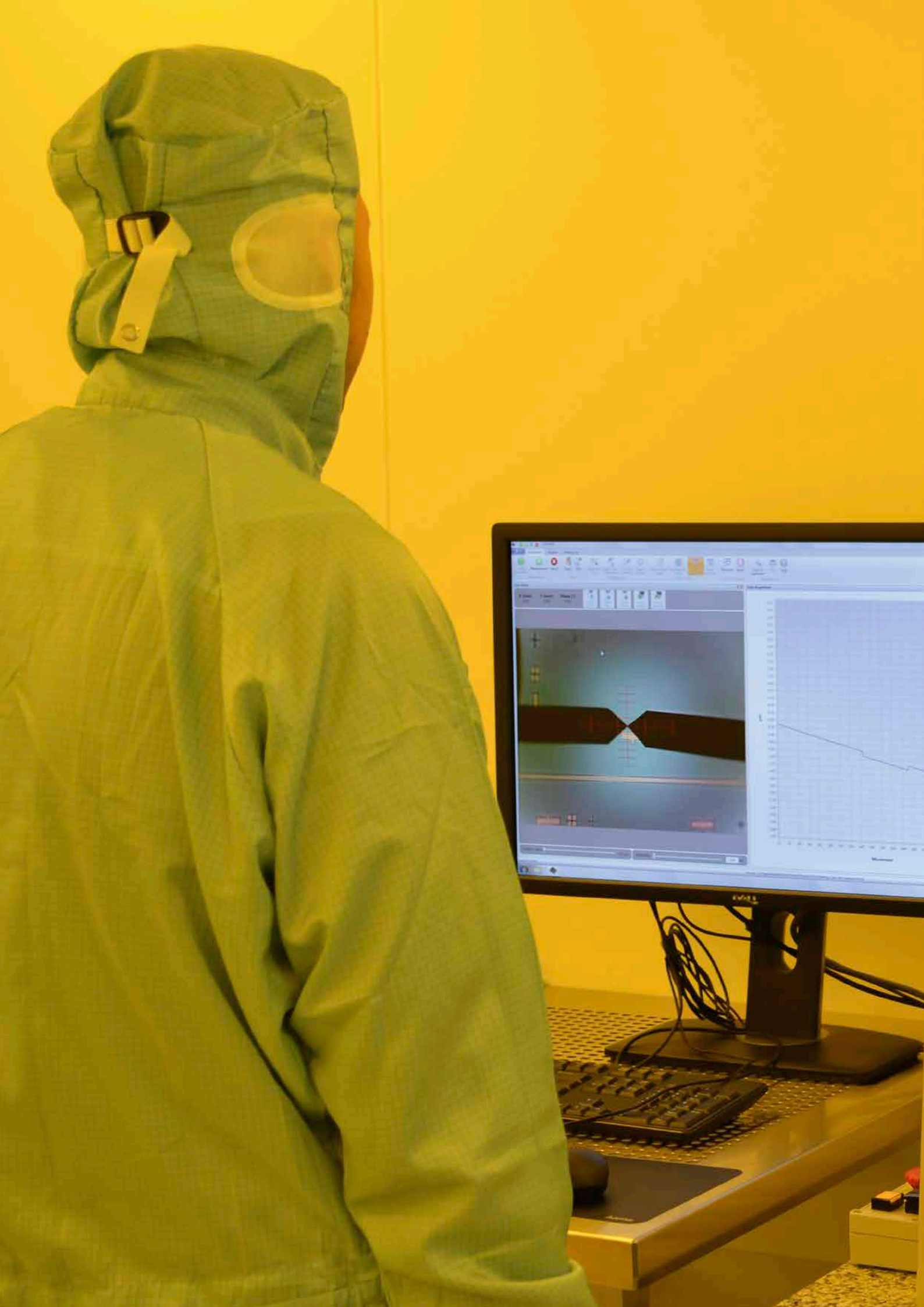
PDI plays a somewhat special role when it comes to presenting its scientific research to the public. On the one hand, there is the advantage of our location in the heart of the city, among the multitude of cultural attractions and in the center of social and political life. On the other hand, our location makes it harder to join larger public activities with our many colleagues, for instance in Adlershof. Therefore we should envisage to act locally and independently.

Our goal is knowledge transfer in a broad sense: we want to convey what we are doing at the institute, and also why we are doing the research we do and in which way scientific work and scientific thinking are important to society. There are two steps in accomplishing knowledge transfer: the first is "public relations", aiming at creating contacts to the public in order to open a dialogue. Therefore, PR functions as a door opener, but it is never a goal in itself. Based on this first step, knowledge transfer should enrich target groups, such as politics, industry, the general public as well as multipliers such as teachers, journalists etc. We have so far followed these activities entirely on our own accord. In the meantime, however, knowledge transfer has become a mandatory demand by our funding agencies. The Leibniz Association, for instance, has committed itself in the "Pact for Research and Innovation" to put primary importance to the transfer and utilization of ideas, research results and knowledge through an intensive exchange with industry, society and politics" – PDI is obviously well positioned.

We have taken part in the Long Night of Science numerous times, often with large numbers of visitors. Quite a number of

Das PDI spielt eine etwas besondere Rolle wenn es darum geht, seine Forschung für die allgemeine Öffentlichkeit zu präsentieren. Zum einen genießen wir die herausgehobene Lage in Mitte, die uns besondere Sichtbarkeit zwischen Museen, Musikhäusern und inmitten von Ministerien und Botschaften bietet. Zum anderen ist es für uns nicht so einfach, uns größeren Aktivitäten, zum Beispiel mit Adlershofer Fachkollegen anzuschließen. Wir sollten also lokal und durchaus eigenständig agieren.

Unser Ziel ist der Wissenstransfer im breiten Sinn: es soll vermittelt werden, was wir am Institut tun, aber auch wieso wir forschen, warum wissenschaftliches Arbeiten und wissenschaftliches Denken für unsere Gesellschaft wichtig ist. Der Prozess hierfür ist immer zweistufig: es gibt zum einen die Öffentlichkeitsarbeit. Hierfür passt der englische Begriff Public Relations sehr gut: es wird eine gute Beziehung mit der Öffentlichkeit aufgebaut, um dann über Inhalte reden zu können. PR ist also der Türöffner, und Öffentlichkeitsarbeit ist damit nie-mals Selbstzweck. Darauf baut der Wissenstransfer auf, der zu einer Bereiche rung der Zielgruppen (Politik, Industrie, die breite Öffentlichkeit aber auch Multiplikatoren wie Lehrer, Journalisten...) führen soll. Diese Aktivitäten haben wir immer aus eigener Überzeugung verfolgt. Mittlerweile allerdings wird Wissenstransfer verstärkt von unseren Geldgebern eingefordert. So hat sich die Leibniz-Gemeinschaft im Rahmen des bis 2030 laufenden Paktes für For schung und Innovation dazu verpflichtet, „dem Transfer und der Nutzbarmachung von Ideen, Forschungsergebnissen und Wissen durch intensiven Austausch mit Wirtschaft, Gesellschaft und Politik einen zen-



PDI employees were actively involved, often bringing their families to the event as well. Through organizational changes of the Long Night of Science, it became more difficult for us to keep drawing a sizeable audience to PDI. Although each time there were numerous truly interested and fascinated visitors, we had to realize that the initial effort was not appropriate anymore.

All the more rewarding it is to see which other formats we have opened up to present ourselves. Among those, the Berlin Science Week has played a central role during the last years. "Mind the Lab", an activity during which we have presented informative stands in several subway stations during rush hours has certainly been a highlight. Its goal was to reach those parts of the population, who would never go to any scientific event voluntarily or quickly zap on when scientific features appear on TV. These activities have been possible thanks to the enthusiasm of younger scientists of our institute, in particular by our PhD students. They gave great visibility to PDI - the format of "Mind the Lab" featured prominently during the press conference of our Governing Mayor and the Berlin Science Week still uses it for advertising.

PDI will certainly participate in the Long Night of Science again, and our presentation in the central offices of the Leibniz Association showed new options and found a very large audience. Still, there is the question how our activities on outreach should continue and how various groups of PDI staff members can participate. The question is not if, but rather how and with how much effort PDI should participate and I have the impression that this question is much discussed among PDI members.

I find it essential that every one of us can contribute with the enthusiasm for their work in their own way. It is certainly not everyone's cup of tea to presents their science in the rush of a subway station and far away from their own experimental setup.

tralen Stellenwert" einzuräumen - das PDI ist also gut positioniert.

Etliche Male haben wir zum Teil mit großem Zustrom erfolgreich an der Langen Nacht der Wissenschaft (LNdW) teilgenommen, wobei sich jeweils ein großer Teil der PDI Mitarbeiter aktiv engagiert und oft auch Familien mitgebracht hat. Durch Veränderungen in der Organisation der Langen Nacht wurde dieses Format für uns schwieriger. Obwohl jedes Mal etliche wirklich interessierte Besucher sich für unsere Arbeit begeistert haben, mussten wir doch feststellen, dass der anfängliche Aufwand nicht mehr angemessen war.

Umso schöner ist es zu sehen, welche anderen Formate wir auftun konnten, um uns der Öffentlichkeit zu präsentieren. Hierbei steht die Berliner Science Week in den letzten Jahren im Mittelpunkt. Ein Höhepunkt dabei war sicherlich die Aktivität „Mind the Lab“, in der wir uns gerade auch in den Zeiten des Berufsverkehrs in U-Bahn Stationen präsentiert haben. Hier ist das Ziel, Bevölkerungsgruppen zu erreichen, die von sich aus nicht zu einem Tag der Offenen Tür kommen würden oder die im Fernsehen bei Wissenschaftssendungen schnell weiterschalten. Bei diesen Aktionen haben sich vor Allem die jüngeren Wissenschaftlerinnen und Wissenschaftler des Instituts, insbesondere die Doktorandinnen und Doktoranden begeistert beteiligt. Und die Sichtbarkeit des PDI war enorm – dieses außergewöhnliche Format war zentral bei der Pressekonferenz des Bürgermeisters vertreten und die Science-Week wirbt noch heute damit.

Das PDI wird sicherlich immer wieder an der LNdW teilnehmen – die diesjährige Präsentation in der Leibniz-Zentrale zeigte interessante neue Möglichkeiten und fand großen Zuspruch. Darüber hinaus stellt sich jedoch die Frage, wie es mit der Öffentlichkeitsarbeit weitergehen soll, auch wie die unterschiedlichen Kreise der PDI Mitarbeiter eingebunden werden können. Dabei ist

REACTION CHAMBER CONTROLLER

EUROTHERM

GAS FLOW

ETCH FLOW

INLET

But there could be different and new ways to contribute – one of them an involvement in upgrading of our ScienceFacade, be it with novel contents or with new interactive methodologies which would allow to find out how users go along with our knowledge offer. Some might be interested in supporting an initiative in which we have started to take our knowledge transfer to another level. We have combined rather didactic formats with debates, such as during our Quantum Physics Exposition in cooperation with the Canadian Embassy in 2017. This helped to attract a new group of participants with a big appetite for science.

Within these various formats, many of our staff members might find interest in contributing to outreach. In my opinion, it is decisive that many of us have ways to present not only scientific information but also the joy in their specific scientific work and in science as such. This is what I would like to advocate for.

es keine Frage ob, sondern eher wie und mit wie viel Aufwand das Institut sich hier engagieren soll und ich habe den Eindruck dass dies auch unter den Mitarbeitern zurzeit diskutiert wird.

Dabei scheint es mir entscheidend zu sein, dass alle auf ihre Weise die Begeisterung für ihre Arbeit einbringen und weitergeben können. Es ist sicherlich nicht jedermann's Sache, in einem trubeligen U-Bahnhof zu stehen und fernab vom eigenen Experiment seine Arbeit zu präsentieren. Aber Möglichkeiten gibt es viele. Zum Beispiel bei einer Weiterentwicklung unserer ScienceFassade, entweder in ihren Inhalten oder bei einer interaktiven Gestaltung mittels neuer Methodiken, um dadurch zu erfahren, wie Nutzer mit unserem Wissensangeboten umgehen. Oder in einer Initiative, in der wir damit begonnen haben, unseren Wissenstransfer auf eine neue Ebene zu heben. So haben wir eher didaktische Formate mit Debatten kombiniert (wie zum Beispiel 2017 unsere Quantenausstellung in Kooperation mit der kanadischen Botschaft), womit wir einen neuen Teilnehmerkreis von engagierten und interessierten Personen anziehen konnten.

Im Rahmen aller dieser Formate sollte sich ein größerer und diverser Kreis unserer Mitarbeiter beteiligen können. Entscheidend finde ich dabei, dass viele von uns neben der wissenschaftlichen Information auch die Freude an ihrer wissenschaftlichen Arbeit und an Wissenschaft per se vermitteln können. Hierfür möchte ich an dieser Stelle nachdrücklich werben.

Prof. Dr. Manfred Bayer

Fakultät Physik, Experimentelle Physik 2, TU Dortmund
44221 Dortmund, Deutschland

Dr. Martin Behringer

OSRAM Opto Semiconductors GmbH, OS CTO TLED R
Leibnizstr. 4, 93055 Regensburg, Deutschland

Prof. Oscar Dubon

UC Berkeley, 210 Hearst Memorial Mining Building #1760
Berkeley, CA 94720, USA

Prof. Nicolas Grandjean

Ecole Polytechnique Federale de Lausanne
EPFL SB IPHYS LASPE, PH D3 325 (Bâtiment PH), Station 3
CH-1015 Lausanne, Switzerland

Dr. Michelle Johannes

Center for Computational Materials Science,
Naval Research Laboratory
Washington DC 20375, U.S.A.

Prof. Dr. Jochen Mannhart

Max Planck Institute for Solid State Research
Heisenbergstrasse 1, 70569 Stuttgart, Deutschland

Dr. Heike Riel

IBM Research – Zurich
Säumerstr. 4, CH-8803 Rüschlikon, Schweiz

Prof. Dr. James S. Speck

Materials Department, University of California
Santa Barbara, CA 93106-5050, U.S.A.

Prof. Werner Wegscheider

Advanced Semiconductor Quantum Materials
Laboratory for Solid State Physics, ETH Zürich
Otto-Stern-Weg 1, CH-8093 Zürich, Schweiz

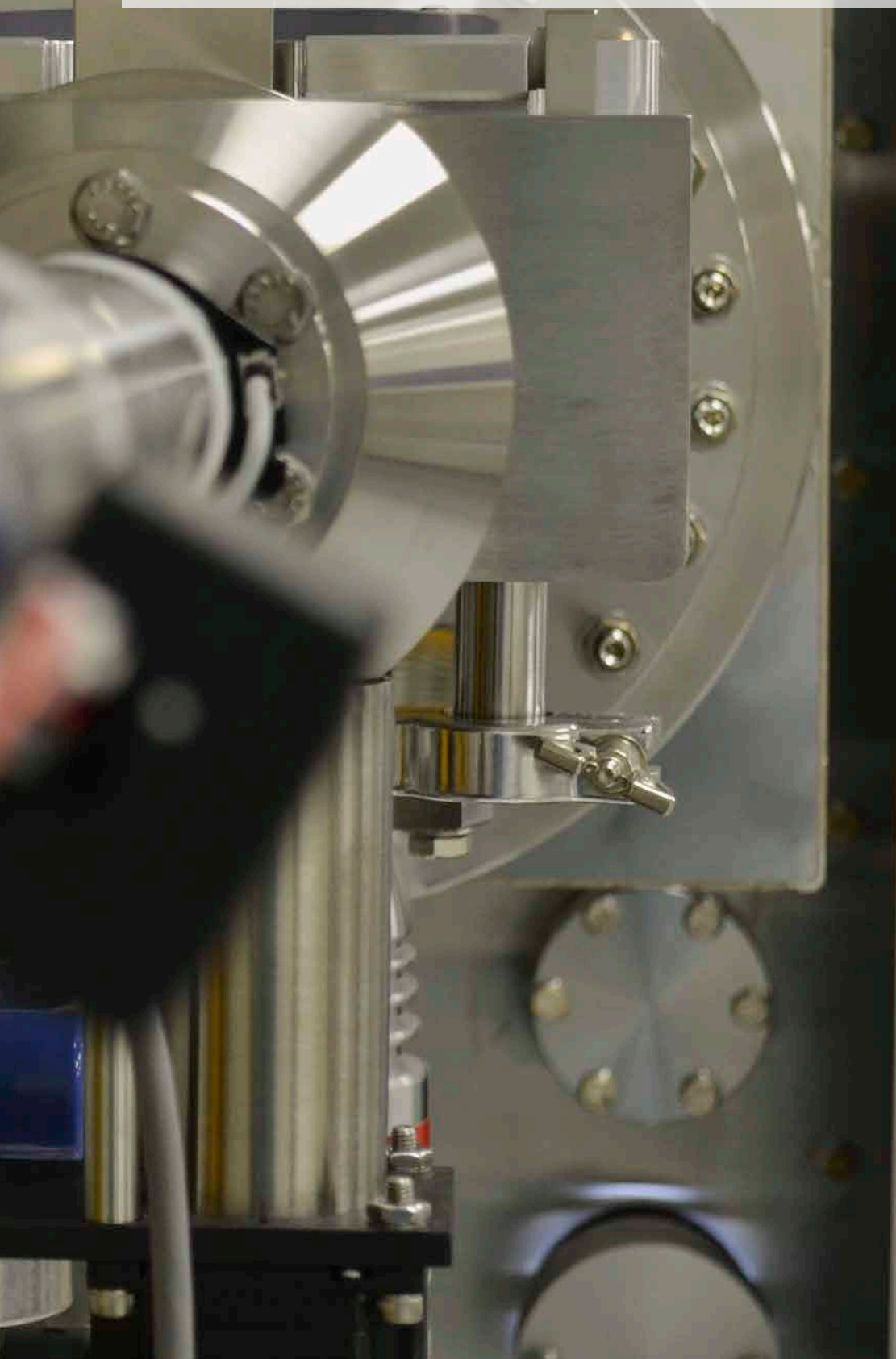
Prof. Dr. Matthias Wuttig

RWTH Aachen, Physikalisches Institut
52056 Aachen, Deutschland

Dr. Hiroshi Yamaguchi

NTT Basic Research Laboratories
Nippon Telegraph and Telephone Corporation
3-1, Morinosato Wakamiya, Atsugi-shi
Kanagawa 243-0198, Japan

Scientific Advisory Board Wissenschaftlicher Beirat





Research Highlights

Forschungshighlights

Zusammenspiel von strukturellen und thermoelektrischen Eigenschaften in epitaktischen $Sb_{2+x}Te_3$ -Legierungen	18
Interplay between structural and thermoelectric properties in epitaxial $Sb_{2+x}Te_3$ alloys	19
Eine geordnete $FeGe_2$ -Struktur stabilisiert durch Festphasenepitaxie	26
Ordered structure of $FeGe_2$ formed during solid-phase epitaxy	27
Radiale (In,Ga)As/GaAs Quantengräben in Zinkblende- verglichen mit Wurtzit-Nanodraht-Segmenten	32
(In,Ga)As/GaAs core-shell quantum wells in zincblende versus wurtzite nanowire segments	33

Zusammenspiel von strukturellen und thermoelektrischen Eigenschaften in epitaktischen $Sb_{2+x}Te_3$ -Legierungen

Antimontellurid ist ein Chalkogenid mit Schichtstruktur, das wegen seiner topologischen Oberflächenzustände wissenschaftlich untersucht und als ein Bestandteil in Phasenwechselmaterial-Speichern und thermoelektrischen Übergitter-Strukturen verwendet wird. Es besteht aus atomaren Te-Sb-Te-Sb-Te-Lagen, den sogenannten „Quintupel-Schichten“ (QS). Zwischen Te-Lagen benachbarter QS liegen dabei nur schwache van-der-Waals-Bindungen (vdW) vor. In der Vergangenheit konnten wir die vdW-Epitaxie von Sb_2Te_3 sowohl auf Si(111) als auch auf Graphen zeigen. Jüngst entdeckten wir nun eine klare Abweichung von solchem Verhalten in Sb_2Te_3 /GeTe-Übergittern. Wir fanden eine teilweise Kopplung zwischen Sb_2Te_3 - und GeTe-Schichten, was es nun ermöglicht, in eigentlich schwach gekoppelten Systemen Verzerrung gezielt zur Modifikation von funktionellen Eigenschaften zu nutzen (*strain engineering*).

Mit Röntgendiffraktometrie (XRD), Röntgenreflektometrie und Raman-Spektroskopie untersuchten wir, wie das Wachstum von epitaktischen $Sb_{2+x}Te_3$ -Legierungen präzise kontrolliert werden kann. Die strukturellen Eigenschaften des mittels Molekularstrahlepitaxie (MBE) gezüchteten Materials ermittelten wir aus XRD-Simulationen. Dabei gelang es uns insbesondere, die Ausbildung sowohl von Sb-Sb- als auch von Sb-Sb-Sb-Sb-Schichten nachzuweisen. Die Ergebnisse dieser Studie geben uns die Möglichkeit, den Bindungscharakter in geschichteten Chalkogeniden zu beeinflussen, und ebnen den Weg zu neuen Strukturen aus Phasenwechselmaterial-Übergittern mit eingestellten Verzerrungen. Unsere Untersuchungen zeigten ferner die starke Verknüpfung zwischen strukturellen und thermoelektrischen Eigenschaften.



Sb_4Te_3 2/2



Interplay between structural and thermoelectric properties in epitaxial $Sb_{2+x}Te_3$ alloys

S. Cecchi, D. Kriegner^{1,2}, F. Arciprete³, E. Zallo, V. Holy^{1,4}, R. Calarco

Antimony telluride (Sb_2Te_3) is a layered chalcogenide material which has been investigated for its topological surface states and used as building block in phase change memory (PCM) and thermoelectric superlattice (SL) structures. It is formed by a stacking of quintuple layer (QL) blocks, in which the Te-Te layers are bonded by weak van der Waals (vdW) forces [see Fig. 1(a)]. In the past, we demonstrated the vdW epitaxy of Sb_2Te_3 on both Si(111) and graphene. Recently, we unveiled a striking devia-

tion from such a behavior in $Sb_2Te_3/GeTe$ SLs [R. Wang *et al.*, *Adv. Funct. Mater.* **28**, 1705901 (2018)]. We found a partial coupling between the constituting layers, which allows strain engineering in weakly coupled systems. Within the homologous series $(Sb_2Te_3)_m(Sb_2)_n$, there exist several ordered antimony telluride phases which could be also implemented in PCM SL structures.

Following our previous results, we aim at demonstrating the possibility to tailor the

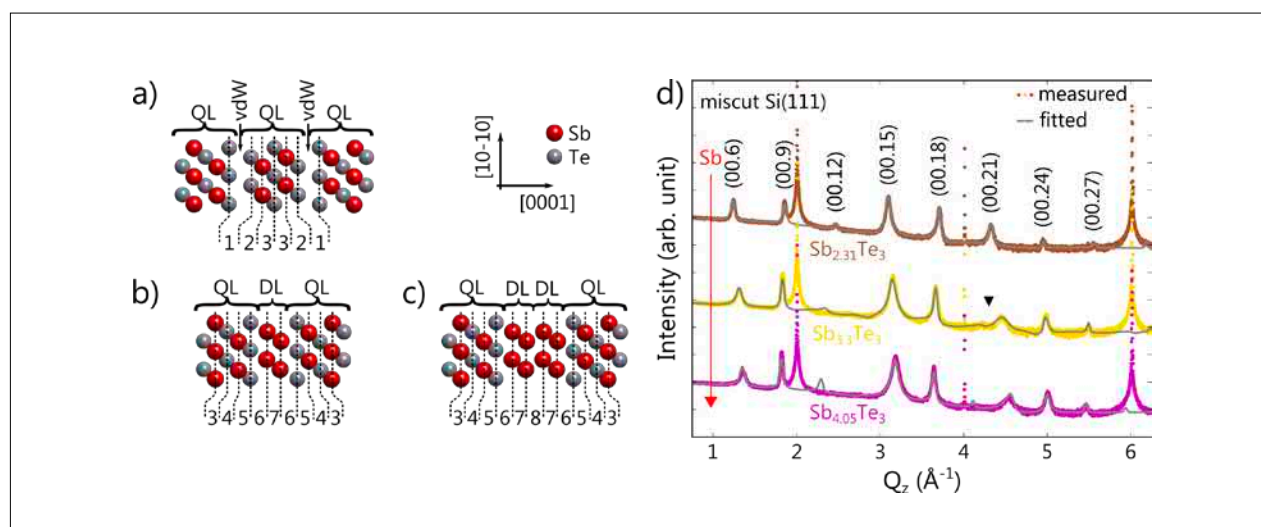


Fig. 1. (a-c) Sketch of the atomic structure of building blocks of $Sb_{2+x}Te_3$. Panel (a) shows the atomic arrangement in a stack of multiple quintuple layers (QLs) as they appear in the Sb_2Te_3 phase. (b) and (c) show the inclusion of 1 and 2 Sb-Sb double layers (DLs) between QLs, respectively. In all panels the numbers of 1–8 correspond to the atomic spacings d_{1-8} used in the simulations. (d) XRD radial scans of $Sb_{2+x}Te_3$ samples grown on miscut Si(111). The curves are plotted in logarithmic scale and vertically shifted for clarity. The fitted curves (solid gray) are superposed to the measurements. The alloy compositions, as calculated from the fits, are also shown. The sharp peaks at $\approx 2, 4$ and 6 \AA^{-1} correspond to the (111), (222), and (333) Bragg reflections of the Si substrate, respectively. Sb_2Te_3 symmetric Bragg reflections are labeled. The red arrows indicate the increase of Sb in the series.

¹ Department of Condensed Matter Physics, Faculty of Mathematics and Physics, Charles University, Praha, Czech Republic.

² Max-Planck-Institute for Chemical Physics of Solids, Dresden, Germany

³ Dipartimento di Fisica, Università di Roma "Tor Vergata", Rome, Italy.

⁴ CEITEC at Masaryk University, Brno, Czech Republic.

coupling in chalcogenide SLs by accurately providing the excess of Sb in $Sb_{2+x}Te_3$ alloys. Considering Sb_4Te_3 , two different stacking structures are proposed in literature, both belonging to the $R-3m$ space group. The 1/1 structure is formed by a stacking of a QL and a single Sb_2 layer [see Fig. 1(b)], while the 2/2 structure features a repetition of 2 QLs and 2 Sb bilayers (Sb_4) [see Fig. 1(c)]. The bonding nature between the two structures is markedly different, since vdW gaps are only present in the latter structure, having contiguous QLs.

$Sb_{2+x}Te_3$ films were fabricated by molecular beam epitaxy (MBE) on passivated surfaces $Si(111)$ - $(\sqrt{3} \times \sqrt{3})R30^\circ$ -Sb. $Si(111)$ substrates with a miscut of 1° were used. These exhibit also a high-resistivity ($> 5000 \Omega cm$), allowing to avoid the contribution of the substrate while measuring lateral electrical transport properties. Starting from stoichiometric Sb_2Te_3 , the composition of $Sb_{2+x}Te_3$ was controlled by increasing the Sb/Te atomic flux ratio, providing the intended Sb excess by increasing the Sb flux while keeping the Te one fixed. All other growth parameters were unchanged. Three samples were prepared with composition close to Sb_2Te_3 , $SbTe$, and Sb_4Te_3 .

To characterize the structural properties of the grown material, we performed X-ray diffraction (XRD), X-ray reflectivity (XRR), and Raman spectroscopy measurements. The diffractometer used for the XRD and XRR characterization is a PANalytical X'Pert PRO MRD system with a Ge(220) hybrid monochromator, employing a $CuK\alpha_1$ ($\lambda = 1.540598 \text{ \AA}$) X-ray radiation. The Raman spectra were acquired in backscattering $z(y,xy)-z$ geometry, the sample was excited with the 632.8 nm line of a He-Ne laser, and the scattered light was analyzed using a spectrometer equipped with a liquid N_2 -cooled charge-coupled device (CCD) detector. The emission was focused by a microscope objective with 0.9 numerical aperture and the same objective was used for the collection of the signal. The spatial

resolution achieved is 0.7 cm^{-1} and a notch filter suppressed the stray light.

The XRD radial scans of the three samples are shown in Fig. 1(d) (dotted curves). Sb_2Te_3 is characterized by a highly periodic layered structure, giving rise to a series of satellite (003*l*) peaks along the symmetric rod. The first sample in our series clearly shows the typical features of Sb_2Te_3 (brown). For the other two samples, instead, the curves are substantially different, testifying the strong evolution of the structural properties of the material as a function of the $Sb_{2+x}Te_3$ composition. This is in analogy to the $Bi_{2+x}Te_3$ system [H. Steiner *et al.*, *J. Appl. Crystallogr.* **47**, 1889 (2014)]. The increased *c* lattice parameter results in a smaller Q_z separation between the peaks. Moreover, a double peak feature (black triangle) is present in the curve of the second sample (yellow), confirming the presence of $(Sb_2Te_3)_m(Sb_2)_n$ superstructures in the films. The fact that only few satellite peaks appear in the curve underlines the formation of an irregular stacking of Sb_2Te_3 and Sb_2 blocks. The formation of non-continuous Sb_2 slabs as well as of thicker Sb_{2n} blocks can also explain such loss of order. This is also in agreement with the case of epitaxial $Bi_{2+x}Te_3$ films. For the third sample (magenta), a distinct peak at 4.53 \AA^{-1} appears, indicating a reduction of the structural disorder towards Sb_4Te_3 composition.

We used the evolution of the XRD curves of $Sb_{2+x}Te_3$ films as a function of the composition to calculate composition and structural quality of the alloys. The simulations of the diffraction signal of the $Sb_{2+x}Te_3$ thin films that we developed are based on the kinematical theory description of random chains of QL and Sb_2 or Sb_4 sequences. The diffraction intensity is thereby calculated in complete analogy to equations (15) and (16) in the work of Steiner *et al.*. The description of the different building blocks thereby considers the following spacing of atomic planes: 1) distance of the Te-Te layers in a van der Waals (vdW) gap between

two QLs (d_1); 2) distance of the Te-Sb layers adjacent to a vdW gap in a QL (d_2); 3) distance of the middle Sb-Te layers in a QL surrounded by other QLs (d_3); 4) distance of the second Sb-Te layers in a QL adjacent to the Sb-Sb double layer (DL) (d_4); 5) distance of the Sb-Te layers in a QL adjacent to the Sb-Sb DL (d_5); 6) distance of the last Te layer in a QL from the first Sb layer in a DL (d_6); 7) distance between the layers in a Sb-Sb DL (d_7); 8) distance between two Sb-Sb DLs (d_8). Three scenarios visualizing the atomic spacing are given in Fig. 1(a–c).

To describe our sample structure, we assume that there is a number of QLs ≥ 1 between two Sb building blocks. In the model, the number of QLs is assumed to follow a Gamma distribution. The Sb building block can either be a Sb-Sb DL or also a stack of two such DLs, i.e. 4 Sb layers. Using the atomic plane distances d_1 to d_8 , the statistical approach described in this paragraph, as well as scaling parameters for primary beam intensity and background we fit the model curves to our experimental data.

The fitted curves are plotted in Fig. 1(d) (solid gray lines) along with the experimental ones. The alloy compositions of the samples, calculated directly from the fits, are also reported here. The accuracy of the simulation can be immediately evaluated in the case of the sample with composition close to Sb_2Te_3 . Apart from small deviations in the intensity profile, all the features are well reproduced. Interestingly, the model allows us to detect even a small deviation of the composition from stoichiometric Sb_2Te_3 (in the present case $x = 0.31$). For the following

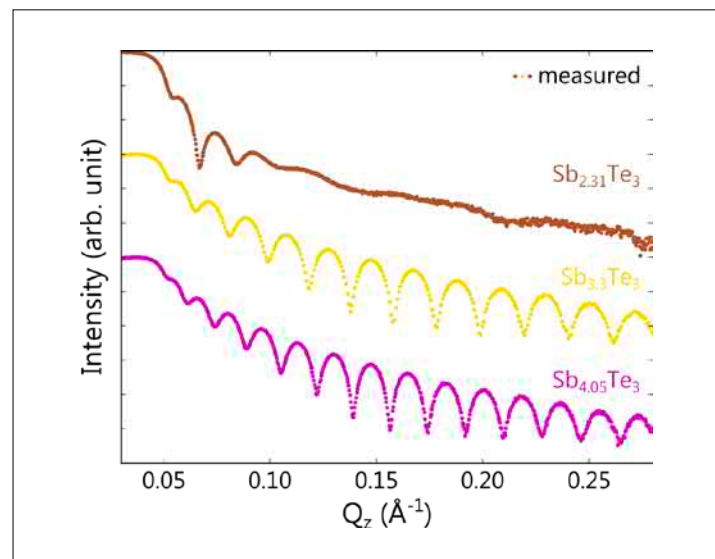


Fig. 2. XRR measurements of $\text{Sb}_{2+x}\text{Te}_3$ samples grown on miscut Si(111). $\text{Sb}_{2.31}\text{Te}_3$, $\text{Sb}_{3.3}\text{Te}_3$ and $\text{Sb}_{4.05}\text{Te}_3$ curves are plotted in brown, yellow and magenta, respectively. The curves are vertically shifted for clarity.

two samples in the series, the fits are also rather good. The small discrepancies between experimental and fitted curves may be attributed to the presence of thicker Sb_{2n} blocks in the films, which are not taken into account by our model. The calculated excess of Sb is $x = 1.3$ (yellow) and $x = 2.05$ (magenta), respectively. We point out that poor results are obtained when only Sb_2 or Sb_4 slabs are used in the simulation. This means that our samples feature random stacking of QLs, Sb_2 , and Sb_4 layers.

We also performed XRR of the three samples (Fig. 2). The film thickness and the root-mean-square (rms) surface roughness, obtained by fitting the reflectivity curves, are

Sample	Thickness (nm)	Growth rate (nm/min)	rms roughness (nm)
$\text{Sb}_{2.31}\text{Te}_3$	25.1	0.28	2.6
$\text{Sb}_{3.3}\text{Te}_3$	29.1	0.32	0.8
$\text{Sb}_{4.05}\text{Te}_3$	33.5	0.37	0.9

Tab. 1. Film thickness, growth rate, and rms surface roughness of $\text{Sb}_{2+x}\text{Te}_3$ samples. The average alloy composition as calculated from the X-ray diffraction fits is reported. Statistical errors for the estimated film thickness and rms roughness are below 0.3 nm.

reported in Table 1. The surface of epitaxial Sb_2Te_3 films on Si(111) is relatively rough, a consequence of the nucleation of Sb_2Te_3 domains which then coalesce forming a continuous film with smooth terraces and quintuple layer (QL) thick steps. Interestingly, the excess of Sb promotes a smoothening of the film surface. Pronounced thickness oscillations in XRR scans are observed for $\text{Sb}_{2+x}\text{Te}_3$ samples with $x > 1$ (see yellow and magenta curves). This effect may be directly related to the presence of Sb_{2n} blocks, which effectively diversifies the characteristic surface step structures, as reported for epitaxial $\text{Bi}_{2+x}\text{Te}_3$ films. Also, considering that Sb is a well known surfactant, it could alter the nucleation of $\text{Sb}_{2+x}\text{Te}_3$ from the very beginning. However, a conclusive understanding of this aspect requires dedicated experiments, which are not the focus of the present study. The roughness slightly increases for the samples with highest Sb content (magenta curve), possibly related to a tradeoff between the beneficial excess of Sb and the growth conditions (namely flux ratio and growth rate).

In the past, we have successfully used Raman spectroscopy to analyze the structure of GeSbTe and $\text{Sb}_2\text{Te}_3/\text{GeTe}$ SLs. Now, we apply the technique to the present case. The Raman spectra of the $\text{Sb}_{2+x}\text{Te}_3$ samples grown on miscut Si(111) are shown in Fig. 3(a). Remarkably, also in this case the changes between the spectra as a function of film composition are pronounced. The spectrum of $\text{Sb}_{2.31}\text{Te}_3$ is very similar to that of Sb_2Te_3 , despite the slight excess of Sb in the film. Increasing the Sb content, we find that the modes of Sb_2Te_3 red shift. This is consistent with the larger lattice parameter of Sb-rich alloys. The Raman shift of the $A_{1g}^{(1)}$ and $E_g^{(2)}$ modes is plotted as a function of the excess of Sb in the films in Fig. 3(b) in black and blue, respectively. The red shift for the $A_{1g}^{(2)}$ mode (not shown) is within 1%, highlighting the weaker link between this mode and the film composition. The intensity of this mode is also not affected by the excess of Sb. In contrast, the $A_{1g}^{(1)}$ and $E_g^{(2)}$ modes, particularly the first one, are much weaker for $\text{Sb}_{3.3}\text{Te}_3$ and $\text{Sb}_{4.05}\text{Te}_3$, which gives evidence that these vibrations are strongly

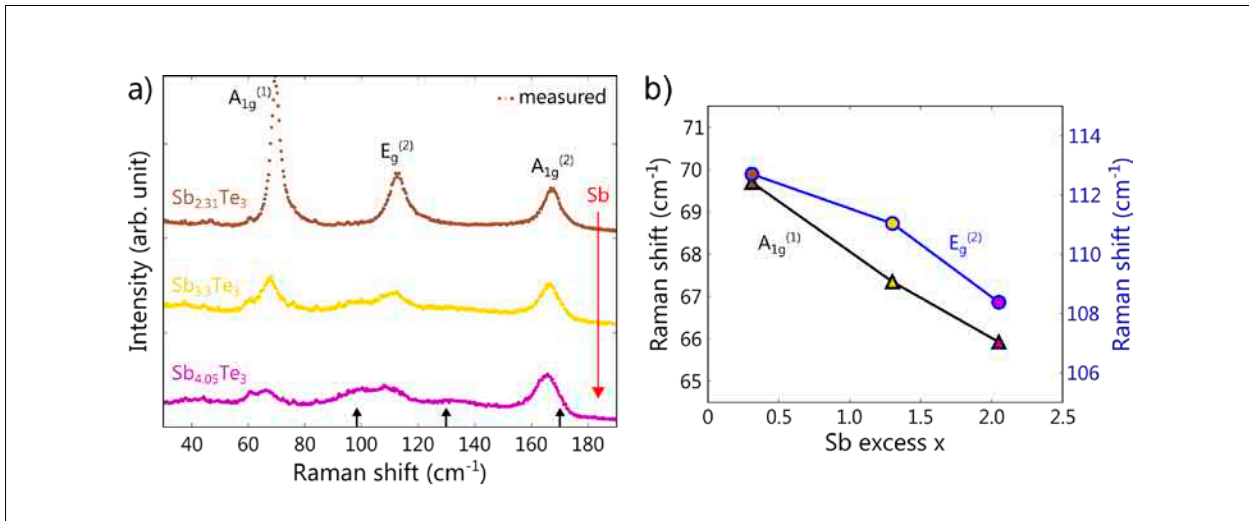


Fig. 3. (a) Raman spectra of $\text{Sb}_{2+x}\text{Te}_3$ samples grown on miscut Si(111). $\text{Sb}_{2.31}\text{Te}_3$, $\text{Sb}_{3.3}\text{Te}_3$, and $\text{Sb}_{4.05}\text{Te}_3$ curves are plotted in brown, yellow and magenta, respectively. The curves are vertically shifted for clarity. The black arrows indicate the features appearing in $\text{Sb}_{2+x}\text{Te}_3$ samples. The red arrows indicate the increase of Sb in the series. (b) Raman shift of the $A_{1g}^{(1)}$ (black) and $E_g^{(2)}$ (blue) modes as a function of the excess of Sb in the films.

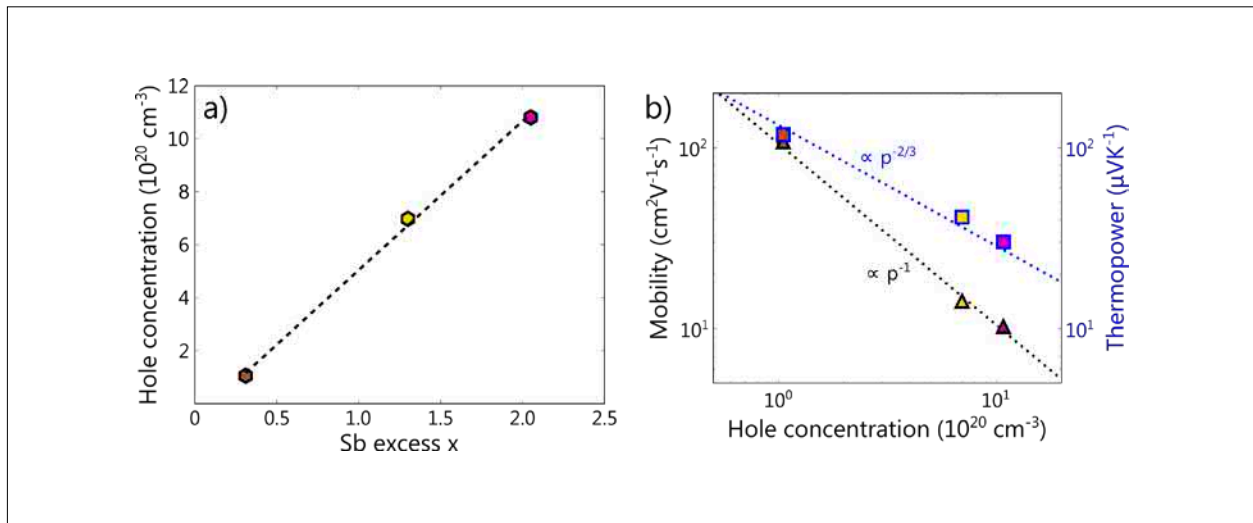


Fig. 4. (a) Room temperature (RT) hole concentration (hexagons) as a function of the Sb excess, calculated from the XRD fits, of the $\text{Sb}_{2+x}\text{Te}_3$ films grown on miscut Si. The linear fit (dashed black line) is a guide to the eyes. (b) RT carrier mobility (triangles with black border) and thermopower (squares with blue borders) as a function of the hole concentration of the $\text{Sb}_{2+x}\text{Te}_3$ films grown on miscut Si. The black and blue dotted lines indicate proportionality to p^{-1} and $p^{-2/3}$, respectively. Both curves are guides to the eyes.

related to the layered structure of Sb_2Te_3 . Notably, new modes not present in the spectrum of Sb_2Te_3 appear in the spectra of $\text{Sb}_{3.3}\text{Te}_3$ and $\text{Sb}_{4.05}\text{Te}_3$ [black arrows in Fig. 3(a)]. While the peak at $\approx 98 \text{ cm}^{-1}$ and the broad one at $\approx 130 \text{ cm}^{-1}$ are present in both spectra, the shoulder at $\approx 170 \text{ cm}^{-1}$ is only visible in the last sample spectrum.

Density functional perturbation theory calculations have been developed in collaboration (not shown here), allowing us to interpret the present findings. In particular, it was possible to distinguish the contributions of the 1/1 and 2/2 structures of Sb_4Te_3 , confirming the presence of both in the samples.

Lateral electrical transport properties of $\text{Sb}_{2+x}\text{Te}_3$ samples were studied by Hall measurements at 300 K. A four-contact van der Pauw configuration was realized by wire bonding the samples to the chip carriers using In droplets and Au wires. The measurements were performed applying currents and magnetic fields of 0.5 mA and 0.5 T,

respectively. The relative errors of the measurements are $< 10^{-4}$ and $< 10^{-2}$ for the sheet resistance and the Hall resistance, respectively. The measurements of the Seebeck coefficient were also performed as follows. A Peltier cooling element was used to apply the temperature gradient ($\approx 3 \text{ }^\circ\text{C}$ in 7 steps). Ag conductive paste in between the Peltier element and the sample improved the thermal contact conductance. The voltage difference was measured in a two-contact configuration.

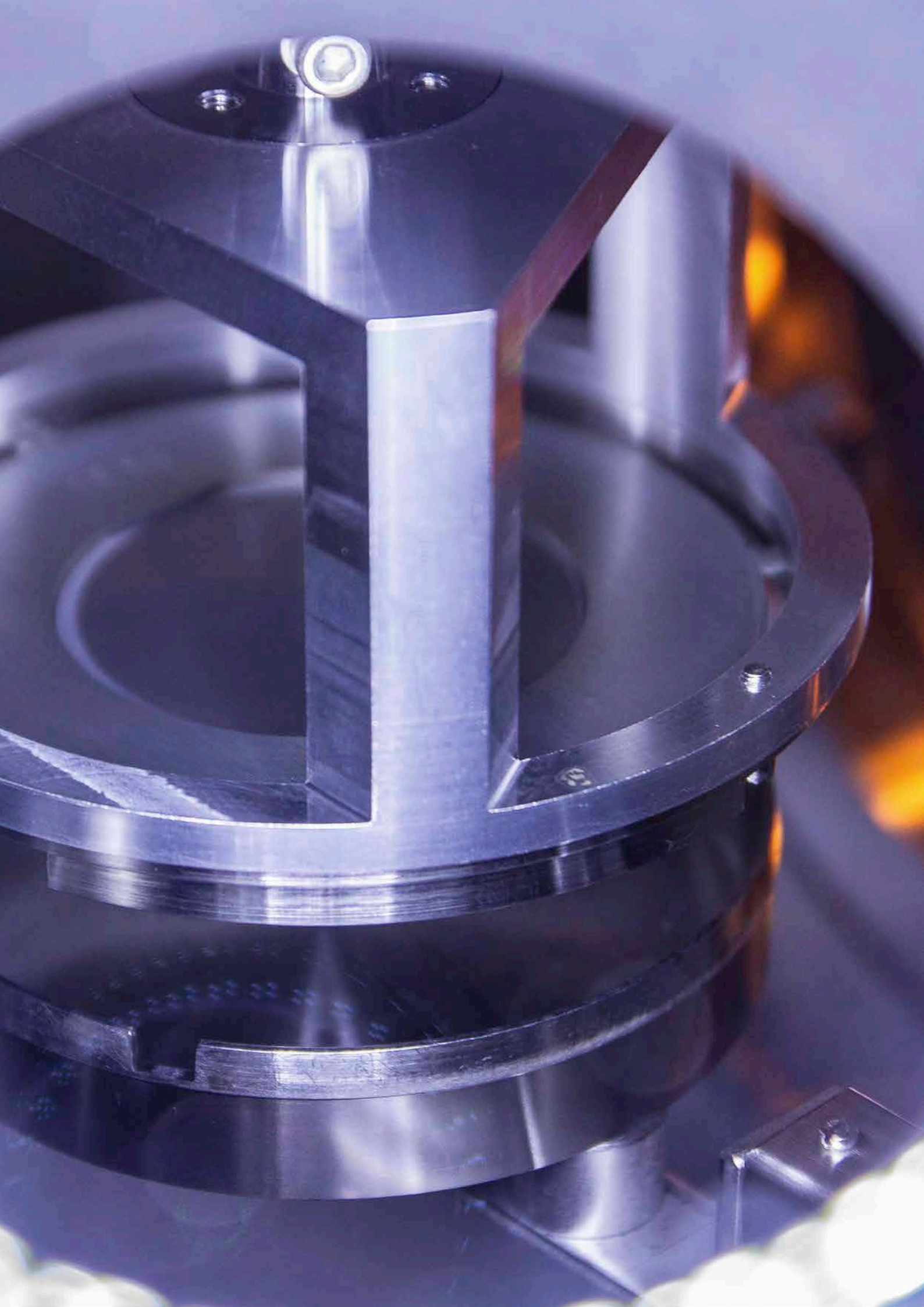
Not surprisingly, the samples have p-type conduction. The linear relationship between the hole concentration p and the excess of Sb in the $\text{Sb}_{2+x}\text{Te}_3$ alloys is shown in Fig. 4(a), emphasized by the linear fit (dashed black line) meant as guide to the eyes. The carrier mobility μ and the thermopower S are shown as a function of the hole concentration in Fig. 4(b).

The mobility decreases following a $\mu \propto p^{-1}$ curve (dotted black line). This is in qualitative accordance with similar measurements

Highlights

of epitaxial $\text{Sb}_2\text{Te}_3/\text{GeTe}$ SLs, in which the intrinsic structural disorder negatively affects the carrier mobility while providing additional carriers [S. Cecchi *et al.*, APL Mater. **5**, 026107 (2017)]. Hence, the present results consistently remark the interplay between structural and electrical properties in layered chalcogenides. As expected, the Seebeck coefficient is lower for Sb-rich samples, having indeed larger carrier concentration. The thermopower as a function of the hole concentration fits nicely a $\mu \propto p^{-2/3}$ curve (dotted blue line), the behavior typical of metals and degenerate semiconductors in the case of constant effective mass.

In summary, we demonstrated the possibility to control very precisely the growth of epitaxial $\text{Sb}_{2+x}\text{Te}_3$ alloys. XRD, XRR, and Raman spectroscopy data are presented. We accessed the structural properties of the material fabricated by MBE by means of dedicated XRD simulations. Notably, we were able to unveil the formation of both Sb_2 and Sb_4 slabs. These results potentially allow us to modulate the bonding character in layered chalcogenide materials, paving the way for the realization of novel strain engineered PCM SL structures. We also studied the thermoelectric properties of the samples, shedding light on the strong link between structural and thermoelectric properties.



Eine geordnete FeGe₂-Struktur stabilisiert durch Festphasenepitaxie

Das ferromagnetische Material Fe₃Si bildet mit Halbleitern wie Si, Ge und GaAs Schottkykontakte. Eine Dreifachstruktur Ferromagnet-Halbleiter-Ferromagnet ist deshalb geeignet für Schottkytransistoren, die eine Spinfunktionalität in integrierten Schaltkreisen realisieren können. Solche Fe₃Si/Ge/Fe₃Si Schichtpakete wurden durch eine Kombination von Molekularstrahlepitaxie (MBE) und Festphasenepitaxie (Ge auf Fe₃Si) hergestellt. Die Festphasenepitaxie gestattet die überwindung prinzipieller Schwierigkeiten beim Wachstum von Halbleitern auf Metallen. Die Ge-Schichten kristallisieren unerwartet in einer wohlorientierten tetragonalen FeGe₂ Struktur mit der Raumgruppe P4mm. Eine solche Struktur existiert nicht im Volumenmaterial, sie ist stabilisiert durch die Festphasenepitaxie. Wir interpretieren das als ein Ordnungsphänomen, welches durch die Minimierung der elastischen Energie der epitaktischen Schicht induziert wird.

Die Strukturen von epitaktischem Ge und Fe₃Si auf GaAs passen gut zu den wohlbekannten Kristallstrukturen der Volumenmaterialien. Wenn jedoch die Fe₃Si-Schicht als Substrat für das epitaktische Wachstum von Ge benutzt wird, erweist sich der Einfluß der Fe₃Si-Struktur auf das Ge-Wachstum als stärker und Ordnungsphänomene treten in Erscheinung. Diese Ordnungsphänomene sind durch das epitaktische Wachstum hervorgerufen und wurden bisher im Volumenmaterial nicht beobachtet. Zuerst wurde die MBE angewendet, um perfekte Ge-Schichten auf ferromagnetischen Fe₃Si zu erzielen. Später haben wir die Festphasenepitaxie von Ge angewendet, um eine hohe Kistallinität und bessere Grenzflächeneigenschaften zu erzielen. Die Interdiffusion von Fe, Si und Ge konnte beim Temperprozeß jedoch nicht vollständig verhindert werden. Darum enthält die Ge-Schicht Anteile von Fe und Si, die zu einer Verschiebung der Röntgenbeugungsmaxima der Ge(Fe,Si)-Epitaxieschicht führen. Des Weiteren kommt es zur Herausbildung einer Übergitterstruktur. Das Ziel unserer Arbeit war es, die Struktur der Ge(Fe,Si)-Schicht im Detail zu untersuchen.

Entsprechend den Ergebnissen der energiedispersiven Röntgenspektroskopie enthält die Ge(Fe,Si)-Schicht Konzentrationen von 60 at. % Ge, 35 at. % Fe und 5 at. % Si. Für ein besseres Verständnis der Struktur nutzten wir den Z-Kontrast im Raster-Transmissions-Elektronen-Mikroskop (STEM). Die Z-Kontrast-Methode nutzt die inkohärente Rutherford-Streuung. Elemente mit höherer Ordnungszahl streuen mit höherer Intensität. Wir wenden die Methode in den zwei Orientierungen [100] und [110] an. Darum können wir die Elemente Ge und Fe klar lokalisieren und die Struktur als FeGe₂ identifizieren (Raumgruppe P4mm). Die experimentellen STEM-Bilder werden mit Simulationsrechnungen verglichen, wobei die bekannte Fe₃Si-Struktur als Referenz dienen kann, und somit die neue FeGe₂-Struktur durch die Ergebnisse bestätigt wird.

Ordered structure of FeGe₂ formed during solid-phase epitaxy

B. Jenichen, M. Hanke, S. Gaucher, A. Trampert, J. Herfort, H. Kirmse¹, B. Haas², E. Willinger², X. Huang², S. C. Erwin³

Ordering phenomena of epitaxial layers have been found in semiconductor mixed crystals as well as in metallic alloys. In general, the ordering has a strong influence on the physical properties of the epitaxial films. The structures of the epitaxial Ge and Fe₃Si films on GaAs substrates correspond well to the known structures of their bulk materials. However, when the Fe₃Si film is used as a substrate for epitaxial growth of Ge, the influence of the Fe₃Si structure on the growing epitaxial Ge film unexpectedly turns out to be stronger and ordering phenomena occur. These ordering phenomena are induced by the epitaxial growth and were not observed in bulk material up to now. First, molecular beam epitaxy was applied to achieve perfect semiconducting (SC) Ge films on top of ferromagnetic (FM) layers. The films were promising but not ideal.

Recently, the method of solid-phase epitaxy (SPE) of Ge was utilized in order to achieve a perfect crystallinity of the film and superior interface quality. However, the diffusion of Fe and Si was not entirely prevented during the annealing process. Therefore, the Ge film contained some amount of Fe and Si, leading to a shift of the X-ray diffraction (XRD) peak of the Ge(Fe,Si) film and to the formation of a superlattice-like structure inside the Ge(Fe,Si) film. The FM Fe₃Si forms Schottky contacts with the SC Ge and GaAs. A triple layer structure FM-SC-FM is therefore suitable for Schottky-barrier tunneling transistors, adding

a spin sensitive functionality to integrated circuits. The aim of the present work is the investigation of the structure of the Ge(Fe,Si) film. [B. Jenichen *et al.*, Phys. Rev. Mat. **2**, 051402(R) (2018)]

Fe₃Si/Ge(Fe,Si)/Fe₃Si thin-film stacks were grown combining MBE for Fe₃Si on GaAs(001) and SPE for Ge on Fe₃Si. A 36 nm thick Fe₃Si film was grown by MBE on the GaAs buffer layer at a growth rate of 16 nm/h and a temperature of 200 °C in a separate growth chamber dedicated to metal growth. In the same chamber the 4 nm thick Ge film was deposited at 150 °C resulting in a smooth interface but with an amorphous structure. For the SPE of the Ge film the sample was heated at 5 K/min up to a temperature of 240 °C and then annealed for 10 min. The 12 nm thick upper Fe₃Si film was then grown by MBE on top of the crystalline Ge under the same conditions as the lower Fe₃Si film.

Let us consider the formation of our Ge(Fe,Si) thin film structure in more detail. During SPE, an initially amorphous material is annealed on top of a crystalline substrate resulting in a lattice-matched crystalline epitaxial film. In a solid solution inside the growing film, at first sight a random distribution of the elements on the different lattice sites can be expected. However, an ordered distribution of the solute atoms can sometimes lead to a minimum of the free energy F of the system. Electron microscopy revealed such an ordering. A high angle an-

¹ Humboldt-Universität zu Berlin, Institut für Physik, Newtonstraße 15, D-12489 Berlin, Germany

² Fritz-Haber-Institut der Max-Planck-Gesellschaft, Faradayweg 4, D-14195 Berlin, Germany

³ Center for Computational Materials Science, Naval Research Lab., Washington, DC 20375, USA

nular dark field (HAADF) STEM micrograph exhibits Z-contrast due to interaction of the electrons with the nuclei of the sample: The intensity diffracted by an atomic column is $I_{\text{HAADF}} \sim Z^{1.7..2}$, thus heavier atoms give brighter image contrast. In Fig. 1, we can recognize the superstructure in the Ge-rich Ge(Fe,Si) film. The image of the [100] oriented sample shows brighter spots forming a square lattice. These spots are caused by Ge columns ($Z=32$). The darker spots, which occur as center of every second square are due to Fe columns ($Z=26$). In the image of the [110] oriented sample, we see rows of brighter spots and can attribute them to Ge columns. Between every second pair of bright rows we recognize darker spots and consider them as contrasts due to Fe columns.

In the Fe_3Si film, we recognize the typical Fe triplets of the image of the [110] oriented

sample and the faint spots of the Si columns between them ($Z=14$). The image of the [100] oriented sample shows a square lattice of relatively bright spots with darker spots in the centers of the squares. The DO_3 structure of Fe_3Si corresponding to this kind of contrast is known and can serve as a reference. On the basis of the Z-contrast of our HAADF micrographs obtained along the two crystal orientations [100] and [110], we are able to propose a structural model for the Ge(Fe,Si) film: It is the FeGe_2 ($\text{P}4\text{mm}$) structure shown on the left side of Fig. 1. Four unit cells are depicted for better correspondence with the Fe_3Si lattice. The structural models of Fe_3Si (below, given as a reference) and FeGe_2 (above, our proposal) are drawn. The experimental micrographs (Exp.) are compared to the structural models and to simulations (Sim.) of HAADF micrographs giving an illustration of our proposal of the FeGe_2 structure. Further on,

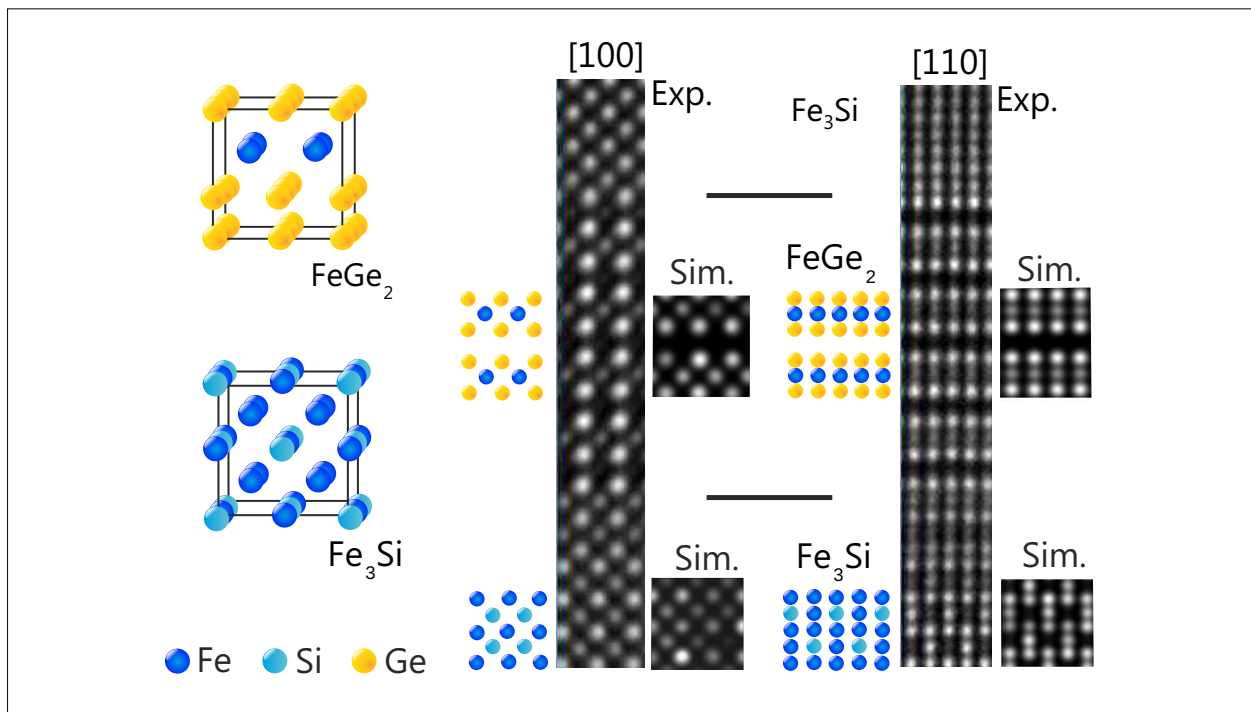


Fig. 1. Comparison of the HAADF experimental cross-section micrographs (larger rectangles, Exp.) with the structural models of FeGe_2 (space group $\text{P}4\text{mm}$) and Fe_3Si shown on the left side as well as the corresponding simulations (small squares, Sim.). The structure of Fe_3Si is well known, whereas the structure of FeGe_2 is obtained from the Z-contrast of the present micrographs, taken along the two projections [100] and [110]. The horizontal lines mark the positions of the $\text{FeGe}_2/\text{Fe}_3\text{Si}$ interfaces. Their lengths correspond to 1 nm.

the well-known structure of the Fe_3Si films is well reproduced, and so we can be sure that we described the FeGe_2 structure in a good approximation.

In Fig. 2 nano-beam diffraction patterns of the thin FeGe_2 film from [100] and [110] oriented samples are given. The beam size was smaller than the film thickness. The patterns were fully indexed using the proposed FeGe_2 structure model and simulated in kinematical approximation. The results of the simulations given below in red color agree well with the experiments further supporting our structural model.

In Fig. 3, the XRD curve (symmetrical $\omega/2\theta$ -scan, i.e. the OOL crystal truncation rod measured at our PHARAO beamline at BESSYII) together with the simulation of the diffraction curve of the $\text{Fe}_3\text{Si}/\text{FeGe}_2/\text{Fe}_3\text{Si}$ film stack in the vicinity of the GaAs

002 peak are shown. Here, the simulated diffraction curve agrees with the main features of the experimental diffraction curve, especially the FeGe_2 001 and 003 maxima are visible, and the FeGe_2 002 peak is shifted with respect to GaAs 002. In addition, reciprocal space maps of asymmetrical crystal truncation rods were analyzed in detail. No plastic relaxation of the layer stack could be detected, i.e., the layers are fully strained.

From the X-ray results, it is clear that the diffusion inside the layer stack has an obvious influence on the formation of the structure of the $\text{Ge}(\text{Fe},\text{Si})$ film. Here, the diffusion during SPE is more important than the diffusion during the subsequent epitaxial growth of Fe_3Si , because the characteristic structure was observed even without the uppermost Fe_3Si film, and the diffusion during Fe_3Si film growth is known to

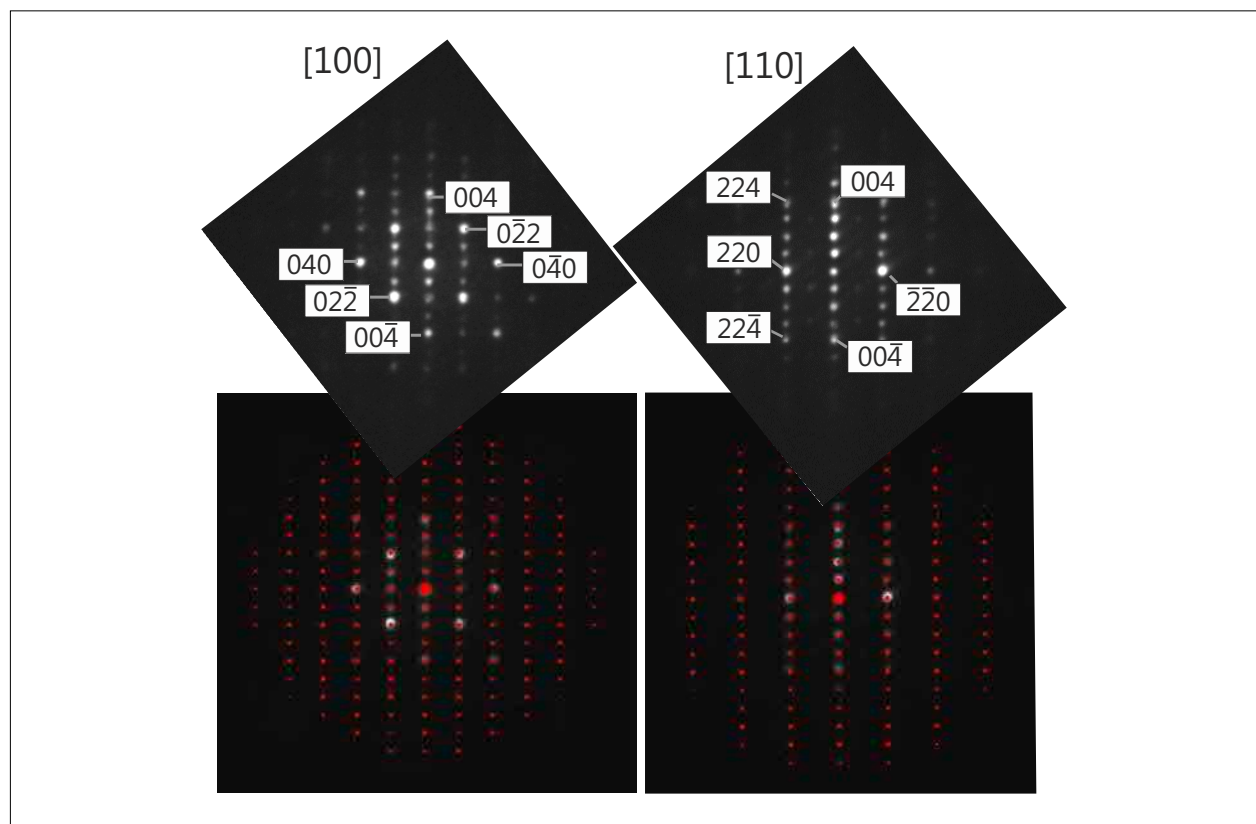


Fig. 2. Nano-beam diffraction patterns of the thin FeGe_2 film from [100] (left) and [110] (right) oriented samples. The comparison of the experimental patterns with the results of the simulations (red) is given below.

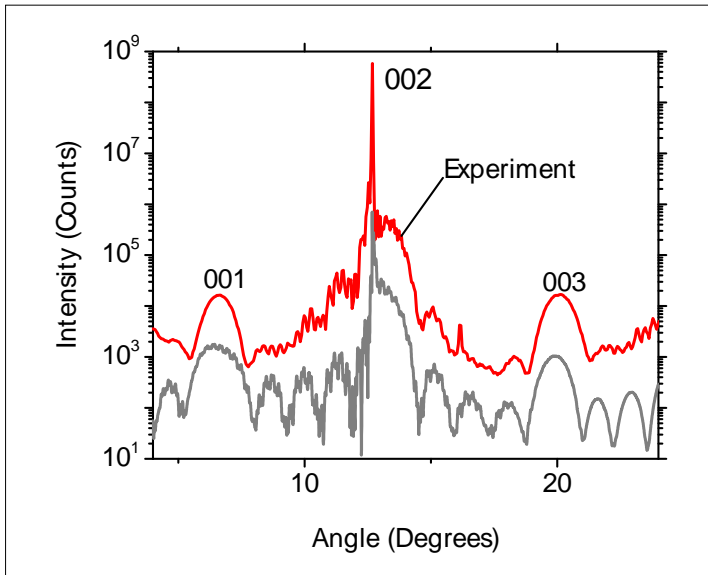


Fig. 3. Comparison of the measured XRD curve and the corresponding simulation (below) near GaAs 002 for the $\text{Fe}_3\text{Si}/\text{FeGe}_2/\text{Fe}_3\text{Si}$ film stack on GaAs 001, obtained using the structure shown in Figure 1.

be low. We obtained the depth dependence of the atomic composition of the different elements by energy dispersive X-ray (EDX) spectroscopy in the scanning TEM (STEM). The Ge(Fe,Si) film consisted of a Ge content of 60 ± 5 at%, an Fe content of 35 ± 5 at% and a Si content of 5 ± 5 at%. Considering in a first approximation the binary phase diagram of Fe–Ge, the phases of FeGe and FeGe_2 could be expected for the given composition range and an annealing temperature of 240°C during the SPE process. According to such a consideration the FeGe_2 should have the tetragonal Al_2Cu structure ($I\bar{4}/m\text{ c }m$). Such a structure was not found in our thin-film stacks.

The distributions of the different elements can be described in the static concentration-wave formalism. [A. G. Khachatryan, Phys. Stat. Sol. B **60**, 9 (1973)] A heterogeneity $\Delta(\vec{r})$ can be written as $\Delta(\vec{r}) = [n(\vec{r}) - n_0]$, where $n(\vec{r})$ is the occupation probability of a lattice site with a certain type of atom, n_0 is the average concentration of that element, and \vec{r} is the site-vector of the lattice in the crystalline

film. The concentration-wave representation of the heterogeneity $\Delta(\vec{r})$ is written as follows: If all the positions of the crystal lattice sites are described by one Bravais lattice, $\Delta(\vec{r})$ can be expanded in a Fourier series, i.e., it can be considered as a superposition of static concentration waves:

$$\Delta(\vec{r}) = \frac{1}{2} \sum_j [Q(\vec{k}_j) \exp(i\vec{k}_j \cdot \vec{r}) + Q^*(\vec{k}_j) \exp(-i\vec{k}_j \cdot \vec{r})], \quad (1)$$

where $Q(\vec{k}_j)$ is the static concentration wave amplitude and can be treated like a long-range order parameter, and \vec{k}_j is the nonzero wave-vector of the static concentration wave defined in the first Brillouin zone of the disordered alloy. The index j denotes the wave vectors in the Brillouin zone. The ordering can result in a reduction ΔF of the free energy. Then, the uniform solid solution becomes unstable with respect to the heterogeneity [Equation (1)] with a certain concentration wave vector $\vec{k} = \vec{k}_0$. In our epitaxial films we clearly observe such an ordering.

In our experiment, the interface between the underlying Fe_3Si film and an amorphous Ge layer is the starting point of the SPE. The lattice mismatch between Ge and Fe_3Si is $\Delta a/a = 1.5 \cdot 10^{-4}$. During the deposition of the Ge and the subsequent annealing, Fe and Si atoms diffuse into the Ge film, leading to a small but finite lattice mismatch. This lattice mismatch can be compensated not only by a tetragonal distortion of a disordered Ge(Fe,Si) film, but in addition by an ordering of a substitutional solid solution which can be described as a concentration wave with the wave vector \vec{k}_0 . From symmetry considerations, it is clear that the wave vector of the static concentration wave \vec{k}_0 should be perpendicular to the $\text{Fe}_3\text{Si}/\text{Ge(Fe,Si)}$ interface, leaving the properties of the film unchanged along the interface. And indeed, the experimental results obtained by XRD and TEM showed the formation of a superlattice only along one direction, the direction perpendicular to the $\text{Fe}_3\text{Si}/\text{Ge(Fe,Si)}$ interface. A possible choice for the length of the vector is $|\vec{k}_0| = 2\pi/c$,

where c is the superstructure period observed. At the same time, we take c as the lattice parameter of the growing Ge(Fe,Si) lattice perpendicular to the interface and a as the lattice parameter parallel to the interface. Such a choice of the lattice leads us to the possibility, that the ordering can be described in the frame of the Ge(Fe,Si) lattice itself with a basis of two types of lattice sites described by fractional lattice coordinates: one type occupied mainly by Ge atoms (or Si atoms) and the other mainly by Fe atoms. In this case, we can write $\vec{k}_0 \cdot \vec{r} = 2\pi z$ where z is the coordinate perpendicular to the $\text{Fe}_3\text{Si}/\text{Ge}(\text{Fe},\text{Si})$ interface. The occupation probability $n(z)$ for a certain type of atom is then

$$n(z) = (1/2) \cdot \eta \cdot \cos(2\pi z / c) + n_0 \quad (2)$$

where η is the order parameter and n_0 is the average concentration.

Our results show that the ordering can be considered as a systematic arrangement of Fe atoms and -vacancies in a CsCl-type FeGe lattice, where both atoms and vacancies are found on the Fe sites, and the number of Fe atoms is reduced by half in order to obtain the stoichiometry of FeGe_2 . A random positioning of the Fe atoms would lead to a cubic lattice. But in our case, we have the boundary condition at the $\text{FeGe}_2/\text{Fe}_3\text{Si}$ interface, where the in-plane lattice parameter of FeGe_2 is fixed to a value of 0.2827 nm. Let us take two CsCl-type unit cells to describe the FeGe_2 lattice as a result of ordering of the Fe atoms and vacancies. Then the diffraction intensity of the fundamental 002 reflection is proportional to $|f_{\text{Fe}} + 2 \cdot f_{\text{Ge}}|^2$ where f_{Fe} and f_{Ge} are the atomic form factors of the Fe-atom and the Ge-atom, respectively. The intensity of the 001 superlattice reflection is

$$I(\vec{k}) \sim |\eta \cdot f_{\text{Fe}} - (1 - \eta) \cdot f_{\text{Fe}}|^2 \quad (3)$$

because all other contributions vanish and only the ordered Fe atoms give a diffraction signal. From the comparison of the inten-

sities of the layer reflections 001 (super-lattice) and 002 (fundamental) we obtain $\eta = (0.805 \pm 0.02)$, i.e., the ordering is nearly complete. The film consists of an almost ideal FeGe_2 lattice. Thanks to the ordered structure of the FeGe_2 film with the extended Fe sheets, we are expecting outstanding properties of the new material. As a first step, using the structural data of the FeGe_2 obtained in the present work, we have calculated by density functional theory the band structure. The Fermi surfaces consist of cylinders along the z -axis, i.e. perpendicular to the Fe sheets. The electrical properties in the plane of the Fe sheets probably will differ considerably from those perpendicular to the sheets. FeGe_2 belongs to a class of quasi-two-dimensional materials.

Single-crystal Ge-rich films were successfully grown by solid phase epitaxy on $\text{Fe}_3\text{Si}(001)$. Surprisingly, the structure of the films was not the expected diamond structure of Ge, but a well oriented and layered tetragonal FeGe_2 ($\text{P}4\text{mm}$) structure. A lattice misfit caused by interdiffusion of Si, Fe, and Ge leads to the formation of a new structure and ordering inside the film. We observe here one of the rare cases, where epitaxy is causing the formation of a distinct crystal structure differing from the equilibrium bulk structure, in particular the strain-induced ordering of the FeGe_2 film with a periodicity along the direction perpendicular to the $\text{FeGe}_2/\text{Fe}_3\text{Si}$ interface.

Radiale (In,Ga)As / GaAs Quantengräben in Zinkblende- verglichen mit Wurtzit-Nanodraht-Segmenten

In den letzten Jahren wurde ein weitgehendes Verständnis des Wachstum von GaAs Nanodrähten entwickelt. Auf dieser Grundlage kann während des Wachstums die Kristallstruktur zwischen dem im Gleichgewicht auftretenden Polytyp Zinkblende (ZB) und dem metastabilen Wurtzit (WZ) gewechselt werden. Dadurch ermöglicht die Nanodraht-Geometrie grundlegende Untersuchungen der optischen und strukturellen Eigenschaften des WZ-Polytyps, aber auch von Strukturen, in denen sich WZ- und ZB-Segmente abwechseln. Auch wenn es sich herausgestellt hat, dass beide Polytypen fast die gleiche Bandlücke aufweisen, kommt es an Grenzflächen zwischen den Polytypen zu einem Versatz in der Bandstruktur. Gleichzeitig sind die Gitterkonstanten der beiden Kristallstrukturen leicht unterschiedlich. Zusätzlich können GaAs-Nanodrähte als Basis für das Wachstum von radialen Heterostrukturen in Form von mehreren Hüllen dienen, die die Kristallstruktur des Kerns annehmen. Ein wichtiges Beispiel hierfür sind (In,Ga)As-Quantengräben als Grundlage für effiziente und abstimmbare Lichtheission im infraroten Spektralbereich. Deshalb stellen solche radialen Nanodraht-Strukturen eine ideale Plattform dar, um den Einfluss der Kristallstruktur auf das Wachstum und die Eigenschaften von (In,Ga)As/GaAs-Quantengräben zu untersuchen.

Um den Unterschied zwischen (In,Ga)As-Quantengräben in der WZ- und ZB-Struktur zu ergründen, verwenden wir in dieser Studie eine einzigartige Kombination von Messmethoden mit hoher Ortsauflösung. Als Proben dienen GaAs-Nanodrähte mit einem (In,Ga)As-Quantengraben als Hülle, die aus längeren Segmenten der beiden Polytypen bestehen. Einerseits untersuchen wir die Emissionseigenschaften mittels Kathodolumineszenz-Spektroskopie (KL) in einem Rasterelektronenmikroskop. Dies zeigt eine systematisch höhere Emissionsenergie im WZ- verglichen mit dem ZB-Quantengraben. Andererseits werden die KL-Messungen an einzelnen Nanodrähten direkt mit der Struktur und Zusammensetzung dieser Nanodrähte korreliert, die hierfür mit Elektronenrückstrahlbeugung und Nano-Röntgenbeugung am Synchrotron bzw. per Tomographie mittels Atomsonde untersucht werden. Während sich die Dicke der Quantengräben nicht ändert, ist der In-Gehalt im WZ-Segment geringer als im ZB-Segment. Dies ist konsistent mit der Änderung in der Emissionsenergie, was durch Rechnungen der Struktur auf Basis der $\mathbf{k}\cdot\mathbf{p}$ -Methodik bestätigt wird. Gleichzeitig zeigen diese Rechnungen aber auch, dass Unterschiede in der Bandstruktur zwischen den beiden Polytypen einen zusätzlichen Einfluss auf die Übergangsenergie haben. Als Konsequenz ist die Kristallstruktur ein wichtiger Parameter bei der Entwicklung von Quantengraben-Emittern auf Basis von Nanodrähten.

(In,Ga)As / GaAs core-shell quantum wells in zincblende versus wurtzite nanowire segments

J. Lähnemann, M. Hill¹, J. Herranz, O. Marquardt², A. Davtyan³, H. Küpers, U. Jahn, U. Pietsch³, L. Lauhon¹, L. Geelhaar

In recent years, the understanding of GaAs nanowire growth has enabled changes of the crystal structure between the equilibrium zincblende (ZB) and the metastable wurtzite (WZ) phase, both by metal-organic vapor phase epitaxy and by molecular beam epitaxy (MBE). Therefore, the NW geometry facilitates studies on the optical and structural properties of the WZ polytype, but also of structures consisting of alternating WZ and ZB segments. Though for GaAs it is now commonly accepted that the band gap of both polytypes is similar, a band offset occurs at the interfaces. Also, the lattice constants vary slightly between the two polytypes. Furthermore, GaAs NWs can serve as a template to radially grow heterostructures in the form of multiple shells around the original core NW, for which the polytype of the core is preserved. A prominent example are (In,Ga)As quantum wells (QWs) used to obtain efficient and tunable light emission in the near-infrared spectral range. Therefore, such core-shell NWs can serve as an ideal platform to investigate the influence of the crystal polytype on the growth and properties of (In,Ga)As/GaAs QWs.

In this study, we employ a unique combination of spatially resolved measurement techniques to elucidate the differences between (In,Ga)As shell QWs around a GaAs NW that contains extended segments of both the ZB and WZ crystal phases. On the one hand, we probe the emission properties of the (In,Ga)As QW by cathodolumi-

nescence (CL) spectroscopy in a scanning electron microscope (SEM). On the other hand, the CL measurements on individual NWs are directly correlated to details of the structure and composition obtained by electron backscatter diffraction (EBSD) in the same SEM, synchrotron-based nanoprobe x-ray diffraction (XRD), as well as atom probe tomography (APT).

The GaAs NWs for this study have been grown by MBE using the Ga-assisted vapor-liquid-solid growth mode. GaAs NWs are grown under As-rich conditions. For relatively low V/III flux ratio, i.e., under sufficient Ga supply, the ZB polytype is formed. When the droplet is consumed at the end of the NW growth by exposure to As without further Ga supply, the crystal structure changes to WZ. Subsequently, such a NW can be radially overgrown with shells to form heterostructures. The inset in Fig. 1(a) illustrates the specific shell sequence used in the current study. For sample A, a GaAs core with a diameter of about 120 nm is followed sequentially by a nominally 10 nm thick (In,Ga)As QW ($\approx 15\%$ In), and a 60 nm thick GaAs outer shell. The resulting NWs have a diameter of about 260 nm. As this diameter is too large to accommodate APT measurements, sample B was grown with reduced thickness of the core (≈ 85 nm) and outer shell (≈ 20 nm), leading to diameters of about 145 nm. An overview of the as-grown NW ensemble A is given by the scanning electron micrograph in Fig. 1(a). Superimposed to this micrograph are two

¹ Northwestern University, Evanston, IL, USA

² Weierstraß-Institut für Angewandte Analysis und Stochastik, Berlin, Germany

³ Naturwissenschaftlich-Technische Fakultät der Universität Siegen, Siegen, Germany

monochromatic CL maps at emission energies of 1.35 and 1.39 eV that both correspond to the QW luminescence and highlight the presence of segments emitting at different energies.

To determine the crystal structure of the NWs, we measured EBSD in a SEM on the upper side facet of single NWs dispersed on a Si substrate as illustrated in Fig. 2(b) for a representative NW. A map of the thus determined polytype distribution is displayed to the left of the corresponding micrograph. Clearly, the base of the NW consists of an about 1 μm long ZB segment, followed by about 400 nm of the WZ polytype. The cap of the NW (≈ 300 nm) exhibits a more complex faceting in the micrograph and a random attribution of the crystal polytype in the EBSD map due to an insufficient quality of the recorded diffraction patterns. From the growth protocol, we can attribute the formation of the WZ phase to the consumption of the Ga droplet during core growth and the cap to axial growth that occurs during the deposition of the radial shells. The thus elucidated polytype struc-

ture along the axis of the NW is sketched in Fig. 1(c). The shell QW (yellow) and outer shell have to adopt the crystal structure of the core NW.

Knowing the crystal structure of the NW, we can now measure the emission properties along the axis of one and the same NW using low-temperature CL spectroscopy. At each dwell point of the electron beam, the luminescence spectrum of the (In,Ga)As QW emission is recorded with a charge-coupled device. In Fig. 1(d), the emission energy is plotted against the axial position and the CL intensity is represented on a logarithmic color scale. The position axis corresponds directly to the position along the NW axis in the micrograph [Fig. 1(b)]. Along the NW, we can clearly distinguish two emission peaks at 1.345 and 1.375 eV, which correspond to the locations of the ZB and WZ segments, respectively. Therefore, the different emission energies already observed in Fig. 1(a) correspond to QWs with different crystal structure. Note that there is a certain interface region between the two segments, from which excited carriers can diffuse to

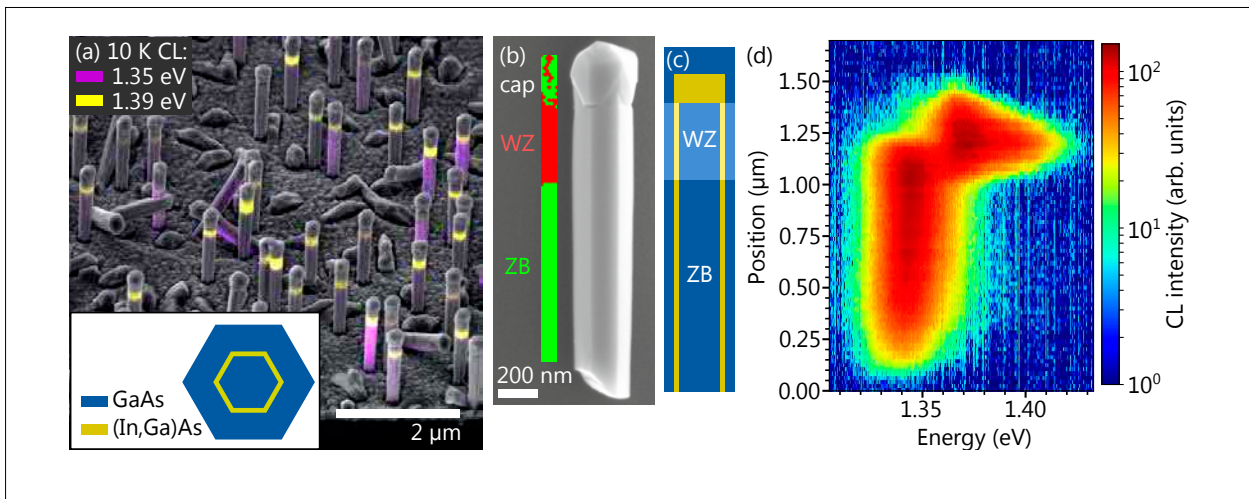


Fig. 1. (a) Scanning electron micrograph of the (In,Ga)As core-shell NW ensemble (sample A) from a birds-eye view perspective. Superimposed are monochromatic CL maps of the low-temperature QW emission at 1.35 and 1.39 eV. The inset shows an in-plane illustration of the core-shell NW geometry. (b) Micrograph of a single dispersed NW together with a map of the crystal phase recorded by EBSD on this NW. (c) Sketch of the NW cross-section along the axis highlighting how the shell QW is grown on the core segments with different crystal structure. (d) CL spectral line scan along the NW axis for the NW shown in (b) acquired at a sample temperature of 10 K. The emission intensity is color-coded on a logarithmic scale.

either the WZ or ZB QW leading to a spatial overlap of the two emission peaks. However, even though the emission energy is higher for the WZ QW, the signal is at least as intense as for the ZB QW. In consequence, there must be a sufficient diffusion barrier at the interface that prevents a notable carrier loss towards the ZB segment. The exact QW emission energies vary by up to 15 meV between individual NWs, while the shift between the ZB and WZ segments is always in the range of 30–40 meV. A much weaker CL signal at around 1.48 eV (not shown), corresponding to the GaAs core, can be observed along both the ZB and WZ segments, which confirms the efficient carrier transfer to the shell QW independent of the crystal polytype. The cap does not show any significant luminescence, indicating strong non-radiative recombination in this part of the NW, which is in line with the reduced crystal quality observed by EBSD.

An independent verification and more in-depth analysis of the crystal structure can be obtained from synchrotron-based nanoprobe XRD measurements that were

carried out at Sector 26 of the Advanced Photon Source at Argonne National Laboratory. Figure 2(a) shows a reciprocal space map of the relevant reflections in this study and their relationship with the NW in real space with (111) growth direction and (110) sidewall facets. Notably, the diffraction on the WZ ($10\bar{1}0$) *m*-planes does not have an equivalent in the ZB polytype, since the ZB (112) reflection is forbidden. Thus, we can use this diffraction geometry to map the position of the WZ segment as shown in Fig. 2(b). The position of the NW can be determined with respect to the x-ray beam by mapping the Ga-K edge x-ray fluorescence (XRF), allowing for a direct alignment of the CL and XRD maps. Again, in the map of the CL peak energy obtained from fits of a Gaussian function to the emission spectra, we see a blueshift of the emission energy from 1.345 to 1.38 eV between the ZB and WZ segments.

It is worth taking a closer look at the diffraction patterns of the $(10\bar{1}0)$ reflection at different positions on the WZ segment, which are shown in Fig. 2(c). These maps

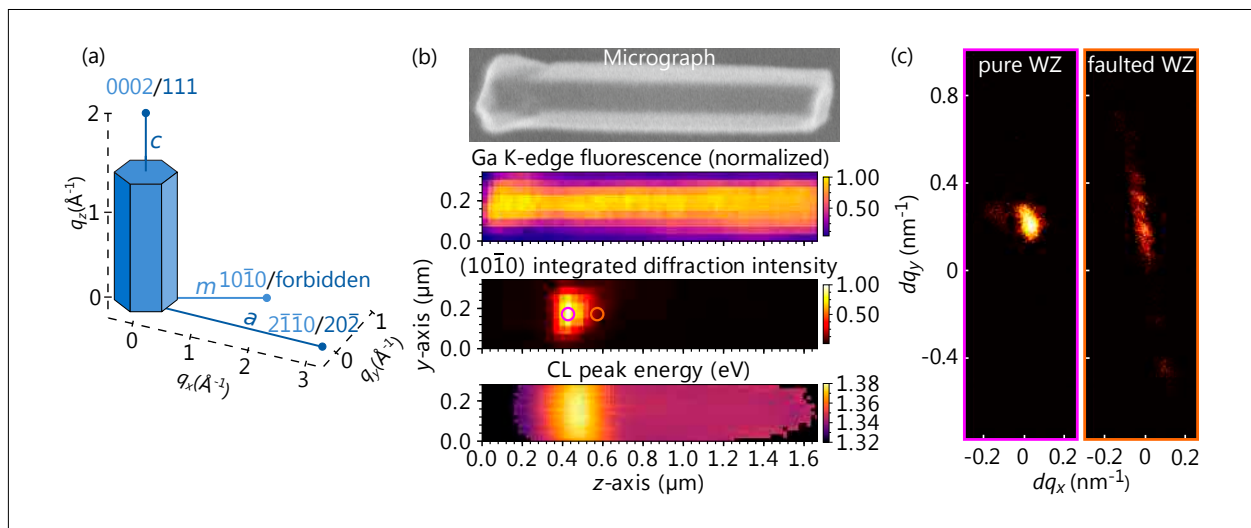


Fig. 2. (a) Sketch of the different diffraction reflections in reciprocal space probed by nanoprobe XRD. The reflections corresponding to the WZ *m*-plane are forbidden for the ZB crystal structure. (b) Two dimensional maps by XRF, XRD and low-temperature CL for the NW from sample A depicted in the scanning electron micrograph at the top. (c) XRD reciprocal space maps recorded at the two positions marked in the diffraction intensity map in (b) plotted using a logarithmic intensity scale.

originate from positions in the center of the segment and close to the ZB interface, as marked in the corresponding diffraction intensity map in Fig. 2(b). The former position corresponds to a single intense diffraction peak. In contrast, for the latter position, additional diffraction at stacking faults (SFs) leads to a spreading of the XRD reflection in reciprocal space. From these measurements, we can infer that a high number of SFs, which act as a diffraction grating, are formed during the transition from the ZB to the WZ phase. At the same time, the central part of the WZ segment appears to be mostly free from SFs. A further analysis of the position of the c-plane and α -plane reflections (not shown) indicates that the α -plane lattice spacing is unchanged between the ZB and WZ segments, while the c-plane lattice spacing is increased by about 1% in the WZ segment. This difference can be attributed to the change in polytype.

Several phenomena have to be considered to understand the emission peak shift between the ZB and WZ segments. In this respect, Fig. 3 shows $\mathbf{k} \cdot \mathbf{p}$ calculations for core-shell QWs in NWs when either the QW thickness or the In content are varied and all other parameters remain unchanged.

A change in In content by 4% could explain the peak shift of 30 meV, but also a change of the QW thickness leads to a notable shift in emission energy. Therefore, it is plausible that the peak shift is a result of growth related changes in the QW composition or thickness when growing on different polytypes. However, these computations neglect the influence from the polytype on the band structure (assuming a ZB structure). Calculations by density functional theory predict a 38 meV higher band gap for the WZ compared to the ZB polytype in (In,Ga)As with an In content of 15% [Bechstedt and Belabbes, *J. Phys: Condens. Matter* **25**, 273201 (2013)], which would be sufficient to explain the shift in emission energy. However, experimental studies suggest a smaller shift of about 10 meV [Vainorius, et al. *Nanoscale* **10**, 1481 (2018); Rota et al., *Nano Lett.* **16**, 5197 (2016)]. To resolve the contributions of these different effects, a more detailed knowledge about the composition and thickness of the QW in the respective NW segments is needed.

A spatially resolved, three-dimensional view on the thickness and composition of the QWs can be obtained from APT measurements. To this end, sample B, with an

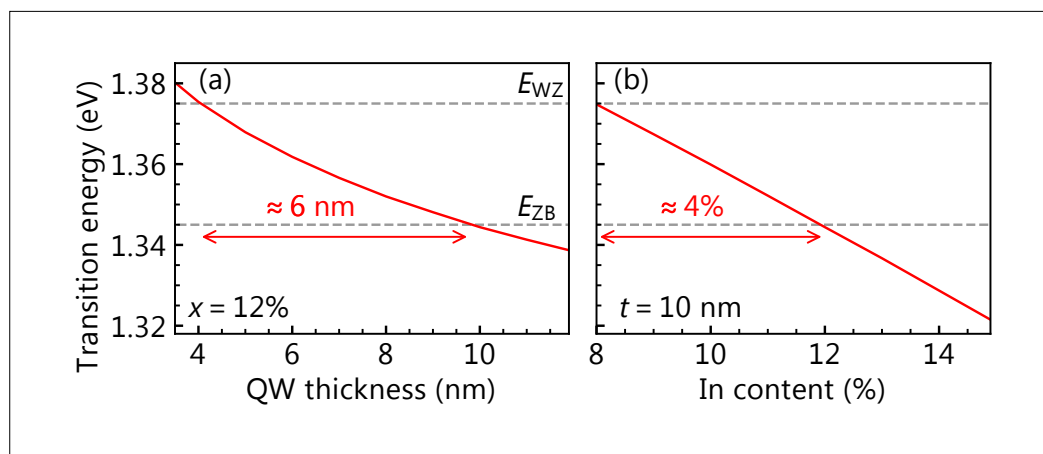


Fig. 3. Transition energies resulting from two-dimensional in-plane $\mathbf{k} \cdot \mathbf{p}$ calculations across the (In,Ga)As core-shell heterostructures for (a) varying QW thickness at constant In content x and (b) varying In content at constant QW thickness t . The arrow in (b) highlights the change in composition necessary to obtain a 30 meV shift in the transition energy associated with the QW emission.

equivalent structure but reduced diameter, is investigated. In APT, laser driven field evaporation is used in conjunction with a mass and position dependent detection scheme to reconstruct a three-dimensional representation of the composition of the specimen. In order to align the limited radial field of view of APT with the QW region, the APT measurements are carried out on a tilted NW, such that mainly one side facet of the NW is probed. Two-dimensional contour plots of the In mole fraction are presented for both the WZ and ZB segments in Fig. 4(a). These in-plane distributions were obtained by integrating over the respective regions marked in Fig. 4(b), which shows different views of the APT data along the NW axis. A two dimensional projection into a plane along the NW axis of the Ga and In atom distributions is complemented by two graphs that highlight the isosurfaces for In

mole fractions of 13% and 8%, respectively. The data in Figs. 4(a)–(b) show a higher In content in the QW on the ZB segment of the NW. The composition amounts to 12% In in the WZ and 15% In in the ZB segments. Line profiles extracted from Fig. 4(a) suggest that the thickness of the (In,Ga)As QW is also reduced by about 10% in the WZ compared to the ZB segment. Finally, APT nicely illustrates how the cap consists of an (In,Ga)As and a GaAs section that correspond to an axial elongation during the respective shell growth steps. Figure 4(c) gives the corresponding CL spectral line scan recorded prior to the APT measurements on the probed NW with the same position axis as in Fig. 4(b). The specific NW exhibits a more pronounced diffusion of carriers excited in the WZ segment to the ZB segment and thus a long tail of the emission at 1.31 eV towards the top of the

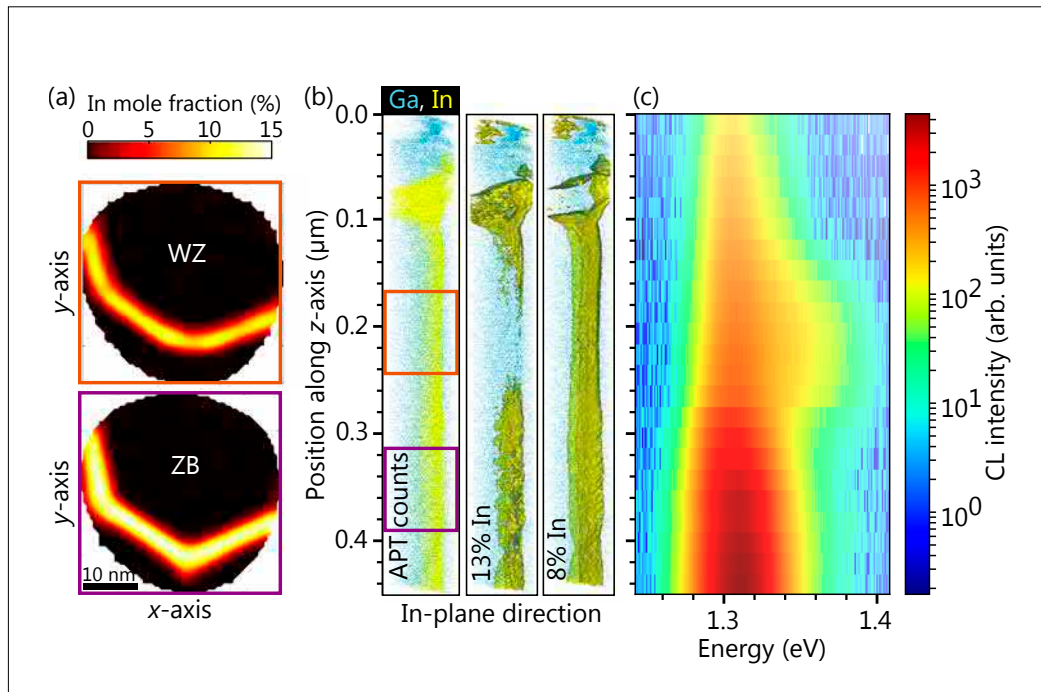


Fig. 4. APT and CL measurements for a NW from sample B. (a) Plan-view cross sections of the In mole fraction extracted from the APT data for the WZ and ZB segments as marked in (b). (b) 2D-representation of the APT measurement on the NW side facet with color-coded composition, where blue and yellow points represent Ga and In atoms, respectively. Additionally, two isosurfaces for mole fractions of 13% In and 8% In are given. (c) CL spectral line scan recorded along the axis of the same NW at a sample temperature of 10 K.

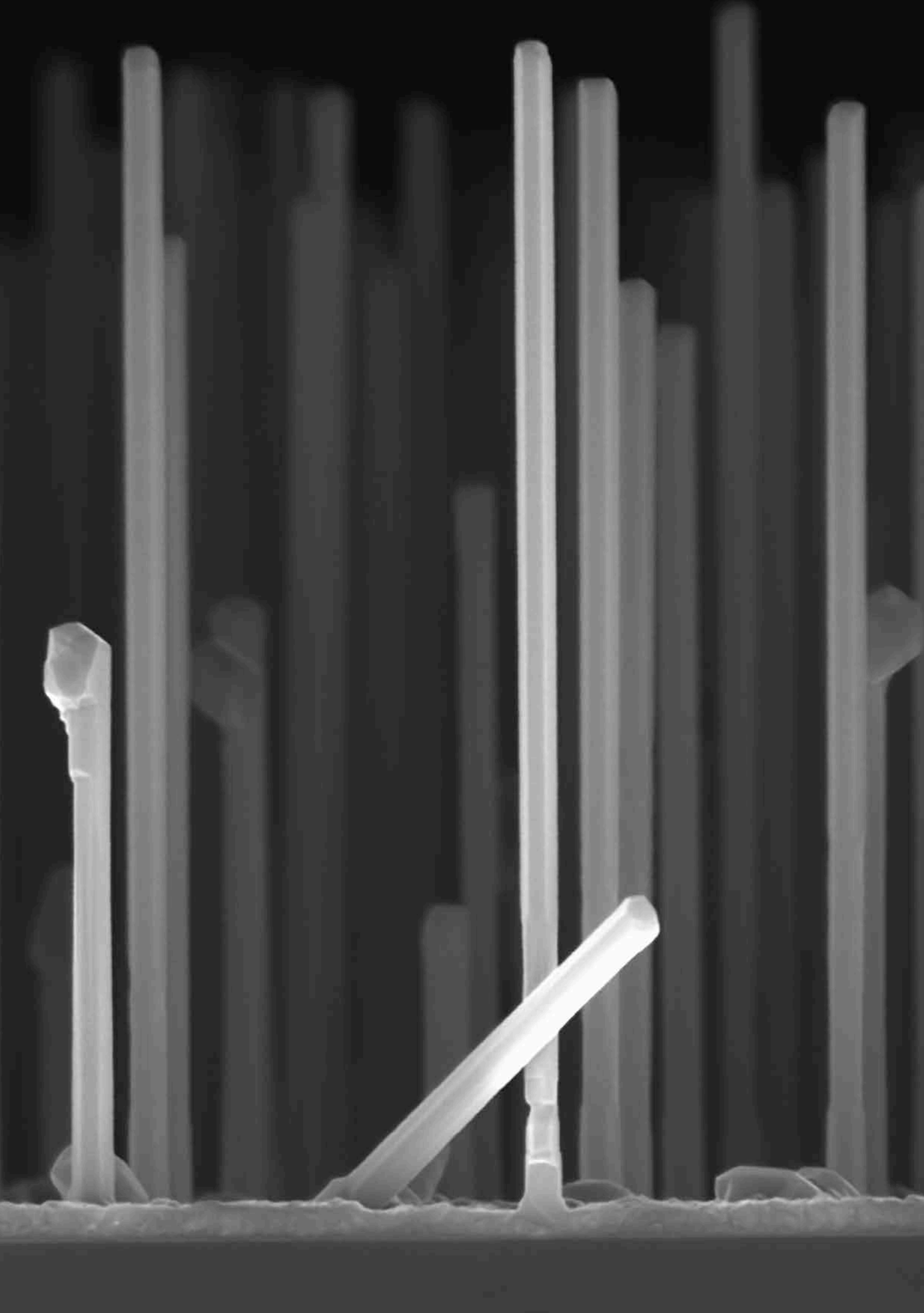
Highlights

NW. Nevertheless, the additional blueshifted component of the WZ QW matches well with the region of reduced In content and confirms the attribution of this segment to the WZ crystal phase.

In summary, the parallel growth of (In,Ga)As QWs on ZB and WZ templates in the form of NW cores together with a specific combination of spatially-correlated measurements on individual NWs, allowed us to investigate the influence of the crystal polytype on the structure and emission properties of such QWs. We emphasize that the correlation of different techniques at the single NW level demonstrated here is essential for such an analysis, as NW-based heterostructures are known to be prone to wire-to-wire fluctuations. For the probed parameters, these fluctuations can be as large as the observed changes within an individual NW. To ensure that the conclusions we draw are representative for the general structure, each of the correlations

was performed on several NWs. On the basis of our comprehensive study, we conclude that a change in the In content between the (In,Ga)As QWs on WZ and ZB GaAs is the main reason for the observed blueshift of the emission energy by 30–40 meV. However, the difference in band gap between the two polytypes can also contribute about 10 meV to the blueshift of the QW emission.

Our study illustrates that the crystal polytype affects In incorporation during the growth of (In,Ga)As/GaAs QWs. This phenomenon is more important for the QW emission energy than differences in band structure between the two polytypes for identical In content. The crystal polytype is therefore an important parameter to be taken into account for the design of NW core-shell QWs. As a perspective, controlled axial changes in polytype in combination with radial ternary QWs offer the opportunity of band gap engineering in three dimensions.



MC sample holder identificatio





Core Research Areas Forschungsschwerpunkte

Nanofabrication

[Nanofabrikation](#) 43

Nanoanalytics

[Nanoanalytik](#) 48

Control of Elementary Excitations by Acoustic Fields

[Die Kontrolle von elektrischen Anregungen in Halbleiter-Nanostrukturen](#) 52

III-V Nanowires for Optoelectronics

[III-V-Nanodrähte und deren Anwendung in der Optoelektronik](#) 55

Intersubband Emitters: GaAs-based Quantum-Cascade Lasers

[Intersubbandemitter: GaAs-basierte Quantenkaskadenlaser](#) 60



Nanofabrication / Nanofabrikation

Dr. Lutz Geelhaar

Dr. Klaus Biermann – Group-III arsenides

Dr. Oliver Bierwagen – Oxides

Dr. Raffaella Calarco – Group-III nitrides, GeTe-Sb₂Te₃ phase-change materials

Dr. Joao Marcelo Lopes – Graphene, hexagonal BN

The subject of this core research area is the fabrication of novel types of nano-structured crystals and the investigation of fundamental growth mechanisms. The perspective of such samples is to enable the investigation of exciting physical phenomena or to offer new tailored functionalities that may inspire innovative devices. In general, we fabricate our samples in the bottom-up approach, i.e. in a process of adding material by growth in contrast to removing material by etching. Thus, for the desirable high level of control over fabrication it is mandatory to understand the underlying growth mechanisms. Moreover, these mechanisms are often highly fascinating by themselves. The standard technique for the fabrication of samples at PDI is molecular beam epitaxy (MBE). Hence, our samples are usually grown as epitaxial thin films on crystalline substrates, and different materials may be stacked on top of each other to form heterostructures of considerable complexity. In addition, we also grow on substrates whose surface has been pre-patterned by lithography to induce lateral variations in growth, and self-organization phenomena can be employed for the deliberate formation of three-dimensional structures like quantum wires instead of two-dimensional planar films. The samples that we aim to fabricate are novel in at least one of the following aspects:

- A material of this chemical composition has not been synthesized before, or at least not in this crystalline quality and/or chemical purity.
- Different materials are monolithically integrated to form an unprecedented hybrid structure.

Das Thema dieses Forschungsschwerpunktes ist die Herstellung neuartiger nanostrukturierter Kristalle und die Untersuchung fundamentaler Wachstumsmechanismen. Solche Proben dienen dazu, spannende physikalische Phänomene zu untersuchen oder aber neue, maßgeschneiderte Funktionalitäten zu ermöglichen, die innovative Anwendungen inspirieren können. Generell werden die Proben in einem sogenannten ‚bottom-up‘-Ansatz (englisch für ‚von unten nach oben‘) hergestellt. Dies bedeutet, dass während des Herstellungsprozesses Material durch Wachstum hinzugefügt wird – im Unterschied zu Verfahren, bei denen aus einer größeren Probe Material durch Ätzprozesse abgetragen wird. Daher ist es für das angestrebte hohe Maß an Kontrolle bei der Probenherstellung unabdingbar, die zugrundeliegenden Wachstumsmechanismen genau zu verstehen – ganz abgesehen davon, dass diese Mechanismen per se faszinierend sind.

Die Standardmethode, die wir am PDI für die Probenherstellung verwenden, ist die Molekularstrahlepitaxie (englisch molecular beam epitaxy, MBE). Infolgedessen werden unsere Proben gewöhnlich als epitaktische dünne Schichten auf kristallinen Substraten gezüchtet. Hierbei können unterschiedliche Materialien als Schichtsystem übereinander gewachsen werden und bilden dann Heterostrukturen von hoher Komplexität. Darüber hinaus wird auf Substraten gewachsen, deren Oberflächen mittels lithographischer Techniken vorstrukturiert sind. Somit können laterale Änderungen im Wachstum induziert werden. Außerdem werden Phänomene der Selbstorganisation ausgenutzt, um die Ausbildung dreidi-

- A known material or combination of materials is structured on the nanoscale in a new way, i.e. the sample is shaped in at least one dimension to a new type of geometry, or a heterostructure of exceptional complexity or precision is created.

Typical examples are extending the range of compositions over which films can be grown in high quality, the use of novel substrates, and the heteroepitaxy of dissimilar materials.

In general, all growth mechanisms are governed by the interplay between thermodynamics and kinetics. At the nanoscale, the role of surface and interface effects is often crucial. In heterostructures, differences between the crystal lattices induce strain which affects crystal growth and is often accommodated by the formation of defects. Hence, the elucidation of growth mechanisms is inextricably linked to the investigation of surface structure, interface formation, and in general the microstructure of the sample. Therefore, the close collaboration with the core research area *Nanoanalytics* is indispensable for the understanding of growth mechanisms and the successful fabrication of nanostructures. Where needed, experiments are complemented by theoretical calculations.

Our research is based on the longstanding expertise of PDI in the MBE of III-As and III-N compound semiconductors, but more and more we study the growth of other materials. One general objective is the monolithic integration of various materials on silicon. In the following, the material systems that are currently under investigation will be presented.

The epitaxial growth of *group-III-arsenide* heterostructures serves as the backbone of various internal and external research projects, due to the unique structural quality of the (Al,Ga)As material system and its very abrupt interfaces even in complex heterostructures—like quantum cascade la-

mensionaler Strukturen – wie zum Beispiel Quantendrähten – anstelle von planaren Schichten zu ermöglichen.

Die Proben, deren Herstellung wir anstreben, sind unter mindestens einem der folgenden Gesichtspunkte neuartig:

- Ein Material dieser chemischen Zusammensetzung wurde zuvor noch nicht synthetisiert – zumindest nicht in dieser kristallinen Qualität oder chemischen Reinheit.
- Unterschiedliche Materialien werden monolithisch integriert, um eine bislang nicht existierende Hybrid-Struktur zu erzeugen.
- Ein bekanntes Material oder eine Materialkombination wird auf der Nanoskala auf neuartige Weise strukturiert – d.h. die Probe wird entlang zumindest einer Raumrichtung zu einer neuartigen Geometrie geformt, oder eine Heterostruktur von außergewöhnlicher Komplexität oder Präzision wird erschaffen.

Typische Beispiele sind die Verwendung neuartiger Substrate, die Erweiterung des Zusammensetzungsbereichs, in dem Schichten in hoher Qualität gezüchtet werden können, und die Heteroepitaxie von sich stark unterscheidenden Materialien.

ters for the THz emission frequency range, which consist of up to some thousands of single thin layers with nominal thicknesses down to one monolayer. A second focus of this activity are microcavity structures for acoustically driven charge and spin transport experiments, for phonon and photon coupling and for exciton-polaritons with and without intra-cavity shallow patterning. Some of these structures are used for spatially resolved photoluminescence measurements to investigate the interaction of polaritons confined to arrayed traps. This year, we have continued our efforts to reach lateral trap dimensions on the order of $0.5\text{ }\mu\text{m}$ as needed for trapping single polaritons. Overgrowth of patterned templates is also employed to fabricate buried in-plane quantum wires as transport channels of acoustically driven single photon sources. One crucial component of such devices are suitable recombination centers coupled to the quantum wires to convert acoustically transported charge carriers into photons. Therefore, we investigated the deposition of $(\text{In},\text{Ga})\text{As}$ quantum dots by droplet epitaxy onto the quantum wires and subsequent overgrowth. Other samples for internal and external partners include heterostructures grown on GaAs substrates of various orientations for experiments like studying the electric amplification of phonons in superlattices, optical generation of THz radiation, random generators working at room temperature, electron scattering and ambipolar diffusion observed by cathodoluminescence, lateral acoustic waveguides for multiplexer devices, and conventional and stacked double quantum well structures for investigating indirect excitons.

In the field of group-*III* nitride epitaxy, our focus is on In-rich $(\text{In},\text{Ga})\text{N}$ layers. This material is important for the development of efficient light emitting and laser diodes in the green spectral range. Yet, the growth of $(\text{In},\text{Ga})\text{N}$ alloys with high In content as required to access the higher wavelength range of the emission spectrum is still challenging. In this context, short period super-

lattices (SPSLs) made of alternating binary InN and GaN layers, have been proposed as an ordered alternative to $(\text{In},\text{Ga})\text{N}$ layers. This year, we have investigated the Mg doping of random alloy $(\text{In},\text{Ga})\text{N}$ and (InN/GaN) superlattices on c-plane GaN templates. In the literature some work on p-type conductivity of InN:Mg and $(\text{In},\text{Ga})\text{N}:\text{Mg}$ layers has been reported, but little is known concerning the effect of Mg on the In incorporation in $(\text{In},\text{Ga})\text{N}:\text{Mg}$ and on $(\text{InN}/\text{GaN}):\text{Mg}$ SPSLs. We have put large effort into the growth of $(\text{In},\text{Ga})\text{N}/\text{GaN}$ SLs doped with Mg employing different sequences of In, Ga, and Mg supply. We have conducted principally two series of experiments. The first one has been devoted to *in-situ* measurements by quadrupole mass spectrometry to investigate the effect of Mg on the In adsorption in vacuum or in presence of N. The second set of experiments has been designed to yield the fabrication of structures to be electrically characterized by van der Pauw and capacitance voltage methods to determine the charge carrier type and density.

The fabrication of *ferromagnet semiconductor hybrid structures* in high crystal perfection is a prerequisite for the investigation of spin transport phenomena relevant for spintronic device concepts. Our focus is on the growth of half-metallic Heusler alloys on GaAs-related structures. The preparation of fully crystalline thin film stacks consisting of a semiconducting channel sandwiched between two ferromagnetic layers constitutes a prerequisite for a new vertical device type. In order to overcome the challenges associated with the growth of a semiconductor on a metal, we have continued to develop solid-phase epitaxy as an approach where an amorphous film of Ge is deposited on Fe_3Si and then crystallized slowly by thermal annealing. Comprehensive structural analysis of $\text{Fe}_3\text{Si}/\text{Ge}(\text{Fe},\text{Si})/\text{Fe}_3\text{Si}$ thin-film stacks grown this way showed that the $\text{Ge}(\text{Fe},\text{Si})$ films crystallize in the well-oriented, layered tetragonal structure FeGe_2 with space

group $P4mm$. This kind of structure does not exist as a bulk material and is stabilized by the solid-phase epitaxy of Ge on Fe_3Si . We interpret this as an ordering phenomenon induced by minimization of the elastic energy of the epitaxial film. Furthermore, we observed independent magnetization switching of the ferromagnetic layers in a $\text{Fe}_3\text{Si}/\text{FeGe}_2/\text{Co}_2\text{FeSi}$ sample, thanks to the different coercive fields of the two metals and to the quality of the interfaces. This result is a step towards the implementation of vertical spin-selective transistor-like devices.

MgO interlayers at the $\text{Co}_2\text{FeSi}/\text{GaAs}$ interface have the potential to prevent the Fe and Co diffusion and to act as spin-filtering barriers. We showed that MgO interlayers efficiently suppress not only the diffusion of Co and Fe atoms into the GaAs layer but also the magnetic interaction of the $\text{Co}_2\text{FeSi}/\text{GaAs}$ interface. Using non-local spin valve and non-local Hanle measurement configurations we determined for an optimized MgO layer thickness, the bias dependence of the spin valve signals. The bias dependence indicates the verification of the half-metallic gap (upper edge) of Co_2FeSi in accordance with first principle calculations. In addition to that, spin generation efficiencies up to 18% reveal the high potential of MgO interlayers at the $\text{Co}_2\text{FeSi}/\text{GaAs}$ interface for further device applications.

Transparent (semi)conducting oxides are widely used in devices. For example, n-type In_2O_3 , Ga_2O_3 , SnO_2 , and NiO traditionally serve as active material in conductometric gas sensors and—highly doped—as transparent contact layers in solar cells, displays, and LEDs. The requirements on material quality for these traditional applications are low, and usually met by polycrystalline, sputtered material. During the last decade, however, transparent semiconducting oxides have been re-discovered as true wide-band-gap semiconductors by virtue of their synthesis to semiconductor standards (single crystalline, highly pure with well-

defined doping). This development enables the investigation of the underlying physics of these materials and their applications. It further opens up the possibility for novel and improved conventional oxide-semiconductor-based devices by rational design. For example, based on its large band gap of $E_g = 4.5$ eV, single crystalline Ga_2O_3 is a promising material for next generation power electronics as well as solar-blind ultra violet sensors. Combined with In_2O_3 ($E_g = 2.7$ eV) and Al_2O_3 ($E_g = 8.8$ eV), band gap engineering and heterostructures with large band offsets are foreseeable. Compared to traditional compound semiconductors, semiconducting oxides are at an early stage of development with many open fundamental questions. Our efforts to answer these questions are embedded in the Leibniz ScienceCampus *GraFOx*, lead by PDI. The main contribution of our core research area in this context is the growth of semiconducting oxides by MBE, a proven tool to synthesize high-quality semiconductor thin films, and to investigate their properties.

After the comprehensive analysis of the Ga_2O_3 growth kinetics and thermodynamics by heteroepitaxy on sapphire substrates in the previous years, we have started this year the homoepitaxy of $\beta\text{-}\text{Ga}_2\text{O}_3$ on (010) oriented substrates aiming at a high material quality for applications. This study resulted in three main findings: 1. We have identified slightly metal-rich growth conditions at high growth temperatures to result in smooth surfaces. 2. We have demonstrated the metal-exchange catalysis discovered by us previously to significantly increase the growth rate also for $\beta\text{-}\text{Ga}_2\text{O}_3(010)$ while maintaining the $\beta\text{-}\text{Ga}_2\text{O}_3$ crystal structure in the grown film and resulting in a smooth surface. 3. Closer inspection of the surface morphology of the films grown under metal-rich conditions or by metal-exchange catalysis revealed the formation of shallow (110) and ($\bar{1}10$) facets on the $\beta\text{-}\text{Ga}_2\text{O}_3(010)$ surface. This finding suggests (110) to be a stable yet unexplored substrate orientation

for the growth of atomically smooth films under metal-rich conditions.

Phase change materials (PCM) are unique compounds employed in non-volatile random access memory thanks to the rapid and reversible transformation between the amorphous and crystalline state that display large differences in electrical and optical properties. Our unique approach in this field is the use of MBE for the fabrication of epitaxial PCM, which makes possible advanced studies on the properties of these materials. The epitaxial growth of GeSbTe alloys is quite demanding as an interplay between composition, phase and ordering occurs. Control over those three parameters is mandatory to obtain material with well defined physical properties. This year we have shown that composition and ordering in the MBE grown GeSbTe are not decoupled: Sb₂Te₃-rich compositions are easier to grow in their stable crystalline phase compared to the GeTe-rich ones. A surprising result, as strongly counterintuitive, is that the GeSbTe alloys are more ordered if grown at lower substrate temperature. High precision in the design of crystalline PCM has been employed also for the growth of Sb-rich Sb₂Te₃ compounds. For low excess of Sb the films display a thermoelectric power factor in the mW m⁻¹ K⁻² range.

Graphene is promising for several applications, and is thus anticipated to play a major role in future technologies. The practical utilization of this material in nanoelectronics will require the development of scalable processes enabling its controlled synthesis on various substrates. For this purpose we have systematically studied MBE large-area synthesis (up to two-inch wafers) of graphene on different metallic and insulating substrates. While on metals state-of-the-art graphene could be realized, achieving the same degree of crystalline perfection for graphene grown on insulators has proven challenging. Hence, we continue to work on the development of growth protocols for graphene epitaxy on insulators, mostly utilizing *hexagonal boron nitride*

(*h-BN*) as a template. H-BN is a two-dimensional dielectric with great technological potential, in particular when combined with graphene to form the so-called van der Waals (vdW) heterostructures. We have demonstrated with plasma-assisted MBE large-area growth of few-layer thick h-BN films which exhibit structural quality comparable to that of state-of-the-art h-BN single crystals. Also, we have realized the fabrication of large-area h-BN/graphene heterostructure films both on Ni templates and based on epitaxial graphene (on SiC). Our results have pointed out a route for a scalable and technologically relevant fabrication of h-BN/graphene heterosystems. Furthermore, we have obtained an in-depth understanding of the defect-mediated vdW epitaxy of h-BN on graphene, and have elucidated how surface modification of epitaxial graphene can be used to tailor nucleation and growth of h-BN. Interestingly, we have observed that this approach also promotes the formation of unconventional BN nanostructures on the graphene surface, whose phase has so far only been predicted to be stable at high pressures.

Parallel to MBE, we operate a furnace in which Si is desorbed from SiC to induce epitaxial graphene formation. This is an established method which enables us to fabricate continuous or nanostructured graphene (single layer to multi-layer thick) on SiC. Recently, we employed this type of samples as templates to perform fundamental growth studies of different materials on graphene such as h-BN (as mentioned above) and GaN nanowires. The high crystalline quality, inertness, and atomic flatness of epitaxial graphene on SiC make it an ideal substrate for the development of growth protocols for vdW epitaxy.

Nanoanalytics / Nanoanalytik

Dr. Achim Trampert

Dr. Stefan Fölsch – Scanning tunneling microscopy and spectroscopy

Dr. Michael Hanke – Synchrotron studies

The ongoing miniaturization in semiconductor technology increases the demand for precise information on the structural and compositional quality of low-dimensional systems and nanomaterials. The mission of this Core Research Area is the development and combination of sophisticated experimental and theoretical tools for materials analysis on the nanometer scale. For this purpose synchrotron X-ray diffraction is carried out to investigate surfaces and interfaces in epitaxial layers and three-dimensional nanostructures during growth. The structural and optical properties of as-grown materials are investigated by various electron microscopy techniques including imaging, diffraction and spectroscopy with high spatial resolution. Low-temperature scanning tunneling microscopy is applied to build and analyze individual nanostructures. The research addresses the following topics:

- Interfaces in low-dimensional hetero-structures and nanosystems
- Order-disorder phenomena and phase transitions in alloys and oxides
- Structure, chemistry and mechanical properties of metastable and nanostructured systems
- Manipulation and spectroscopy of materials at the single-atom scale

A central goal in preparing modern artificial heterostructures and nanomaterials is the control of *interfaces* and the understanding of their building principles. Interfaces have a crucial effect on both, physical properties and device performance, in particular as structure sizes become smaller. Epitaxial hetero-interfaces are generally classified as coherent or semi-coherent, depending on the epitaxial strain state. We are studying

Die stetige Miniaturisierung in der Halbleitertechnologie erhöht den Bedarf an präziser Information über die strukturelle Qualität und chemische Zusammensetzung niedrig-dimensionaler Halbleiterstrukturen und Nanomaterialien. Das Ziel dieser Core Research Area ist die Entwicklung und Kombination ausgereifter experimenteller und theoretischer Untersuchungswerzeuge zur Materialanalyse auf der Nanometerskala. Hier wird Synchrotron Röntgenbeugung für die Untersuchung von Oberflächen und Grenzschichten in epitaktisch gewachsenen Schichtsystemen und dreidimensionalen Nanostrukturen während des Wachstums eingesetzt. Nach der Schichtaufbringung werden die strukturellen und optischen Eigenschaften des gewachsenen Materials mit unterschiedlichen transmissionselektronenmikroskopischen Abbildungstechniken – einschließlich der Elektronenbeugung, der energiedispersiven Röntgenspektroskopie und der Elektronenenergieverlustspektroskopie – mit höchster räumlicher Auflösung untersucht. Darüber hinaus erlaubt die Tieftemperatur-Rastertunnelmikroskopie individuelle Nanostrukturen gezielt herzustellen und strukturell und spektroskopisch zu analysieren.

Die Forschung der Core Research Area Nanoanalytik behandelt folgende Themen:

- Grenzflächen in niedrig-dimensionalen Heterostrukturen und Nano-Systemen
- Ordnungs-Unordnungsphänomene und Phasenübergänge in Legierungen und Oxiden
- Struktur, Chemie und mechanische Eigenschaften von metastabilen und nanostrukturierten Systemen
- Manipulation und Spektroskopie von Materialien auf der Skala von Einzelatomen

the character of epitaxial strain and strain relieving defects as well as the atomic configuration and translation state of coherent interfaces between dissimilar materials. In addition, interfaces in III-V semiconductor heterostructures are quantitatively analyzed with respect to structural roughness and chemical intermixing as defined by compositional profiles.

For some time, we have improved our understanding of interfaces in axial and radial III-V nanowires, two-dimensional layered materials, and, especially, in planar III-V heterostructures and quantum wells. Recently, we have further developed our analysis methods on non-common-atom heterovalent interfaces. The selective combination of closely lattice-matched group II-VI/group III-V semiconductors offers potential benefits due to the wide range of band-gap energies achievable and novel effects at the interface arising from the valence-mismatch. The combination of CdTe and InSb implies the existence of such a heterovalent non-common-atom interface, which must contain mixtures of II-V and/or III-VI bonds. Because of the close atomic numbers of the constituent elements, high-angle annular dark-field and large-angle bright-field scanning transmission electron microscopy (STEM) images, as well as electron energy-loss spectroscopy measurements from the interface region are inherently difficult to interpret. In contrast, we have shown that the use of the 002 dark-field (DF) imaging technique emphasizes the interface location by comparing differences in structure factors between the two materials. Additionally, detailed analysis of the diffracted 002 DF TEM image intensity allows the quantification of the interface width. This interface analysis relies on the comparison of experimental and simulated contrast profiles at the CdTe-on-InSb interface, where a sigmoidal function is assumed for the atomic species. Since the contributions of the III- (II-) and V- (VI-) elements need to be separately considered, the cation and anion intermixing

are independently determined. Our study reveals that the CdTe-on-InSb interface is structurally abrupt to within about 1.5 nm (10-to-90%-criterion).

Interfaces in semiconductor heterostructures are almost never perfectly atomically flat and consequently have a certain degree of three-dimensional (3D) extension. Therefore, the interpretation of two-dimensional projections of those interfaces can be very challenging. We have demonstrated that electron tomography allows an accurate and quantitative determination of the roughness of buried interfaces in III-V multi-layer samples. (Al,Ga)As Bragg reflector structures providing several interfaces with alternating high and low Al content grown on GaAs(001) by MBE are investigated as case study. For the tomography experiment, well-defined needle-shaped specimens are customized fabricated by focused ion-beam (FIB) techniques allowing full 180° rotation for tilt series acquisition. The reconstructed volume is used to create an isosurface for each interface describing its position in 3D space. The isosurfaces are then used to create topographic height maps of the interfaces. These maps enable new approaches to quantitatively characterize the buried interfaces. It is shown that the determination of root mean square (RMS) roughness values for areas larger than 100 nm × 100 nm are feasible. Furthermore, the tomography results reveal anisotropic features of the interface roughness. Additionally, it is found that the RMS roughness systematically varies for the growth on (Al,Ga)As layers with low and high Al content demonstrating the sensitivity of the method.

The physical properties of ferromagnetic Heusler alloys as well as semiconducting oxide layers depend on their *structural order* and phase stability. The stability limitations and phase transformation processes are studied in dependence on internal parameters like chemical composition and strain state as well as external parameters given

by temperature and growth kinetics. The degree of order/disorder and their spatial distribution in thin films are determined quantitatively by X-ray diffraction and electron microscopy.

We have continued our work on Schottky-Barrier-Tunneling-Transistors. The structures of epitaxial Ge and Fe₃Si films on GaAs substrates match well to the known structures of their bulk materials. However, when the Fe₃Si film is used as a substrate for epitaxial growth of Ge, the influence of the Fe₃Si structure on the growing epitaxial Ge film unexpectedly turns out to be stronger and ordering phenomena occur. These ordering phenomena are induced by the epitaxial growth and were not observed in bulk material up to now. We utilized the method of solid-phase epitaxy of Ge in order to achieve a high crystallinity of the film and superior interface quality. However, the interdiffusion of Fe, Si, and Ge was not entirely prevented during the annealing process. Therefore, the Ge film contained some amount of Fe and Si, leading to a shift of the x-ray diffraction peak of the Ge(Fe,Si) film and the formation of a superlattice-like structure inside the film. This superlattice structure is further proven by quantitative STEM analysis combining experimental and simulated images.

Apart from this study, we continued our work on *semiconducting oxides*, a work which is embedded into the Leibniz ScienceCampus GraFOx. Monoclinic β-Ga₂O₃ became one prominent representative of transparent semiconducting oxides (TSO), and although there is a rapidly increasing interest in this material only a few of the fundamental thermal properties are known so far. We have applied synchrotron-based in-situ X-ray diffraction to obtain detailed information on the anisotropic coefficient of thermal expansion α in the temperature window relevant for most growth scenarios between room temperature and 1200 K. The derived temperature dependent functionalities depict a strong anisotropy along

the three main crystallographic directions. Numerically we could describe our experimental findings within the Einstein model for the specific heat of a solid C_v assuming a single phonon mode. These results can be directly translated into an expansion coefficient α since both quantities are connected via the temperature independent Grüneisen parameter $\gamma = \alpha(T) / C_v(T) \neq f(T)$.

In the last years, nanofocus synchrotron radiation has developed into a powerful technique for characterizing *local strain and chemical composition* as well as morphological properties of individual low-dimensional objects. As a direct result of a steadily improved x-ray optics, beam foci as small as 100 nm or below with high photon flux (10^{10} photons/sec) at hard X-ray energies (10–30 keV) are nowadays available at third-generation synchrotron facilities like PETRAIII at DESY in Hamburg or the European Synchrotron Radiation Facility (ESRF) in Grenoble. In a recent study, we have simultaneously combined X-ray ptychographic tomography (XPCT) and X-ray fluorescence (XRF) tomography to study isolated micro-rods with (In,Ga)N/GaN multi quantum wells embedded in a core-shell geometry. A red shift of the emitted light towards the rod apex, as previously observed by spatially resolved cathodoluminescence, could be a result of a thickness and/or an axial concentration gradient within the (In/Ga)N shell. XPCT might distinguish between both options due to its high spatial resolving power of the sample's electron density at sufficient resolution, whereas XRF tomography delivers an even higher elemental contrast, however at the expense of spatial resolution.

The complete three-dimensional knowledge of the *microstructure* is essential for the quality improvement of monolithically integrated optoelectronic components. In this light, electron tomography and complementary TEM methods in conjunction with sophisticated focused ion beam based sample preparation are applied to gain in-

sight into the formation process of morphological surface features, which are a consequence of defect interactions within the heteroepitaxial thin films. Stacks of III-Sb layers were grown on different vicinal Si(001) substrates. This materials system is paradigmatic for the integration of III-V semiconductors on Si. Threading dislocations (TDs) and anti-phase boundaries (APBs) occur as extended defects through the layer stack due to the lattice misfit between the dissimilar materials and due to the growth of polar on nonpolar materials, respectively. The trapping of TDs by APBs leads to the accumulation of line defects. It is shown that a substrate miscut invokes the anisotropic formation of several nanometer high steps at the sample surface where APBs terminate. Eventually, a step bunching model is presented based on the interplay of the substrate miscut and the interaction of TDs and APBs.

We employ *atom manipulation* by low-temperature scanning tunneling microscopy (LTSTM) to investigate the quantum properties of nanostructures on III-V semiconductor surfaces. Understanding and controlling these properties is essential for future device concepts based on quantum effects. State-of-the-art LTSTM is used to create individual nanostructures atom-by-atom and subsequently analyze their electronic structure and elementary excitations by local tunneling spectroscopy. We found that +1 charged adatoms on an InAs surface can be positioned with atomic precision to form perfectly defined quantum dots. Presently, we use this approach to create regular quantum dot assemblies with tunable electronic properties. In addition, we started a new STM research track focused on epitaxial transition metal dichalcogenide (TMD) layers with an emphasis on vertical and lateral heterostructures.

Control of Elementary Excitations by Acoustic Fields / Kontrolle von Halbleiter-Nanostrukturen mittels akustischen Anregungen

Dr. Paulo V. Santos

This core research area explores the dynamic fields of surface acoustic waves (SAWs) for the control of electronic excitations in semiconductor nanostructures. SAWs are elastic vibrations propagating on a solid surface, which resemble seismic waves created during earthquakes. SAWs can be electrically generated on a piezoelectric substrate using interdigital transducers (IDTs)—this standard technique is widely used in signal processing, sensors, and acoustooptical modulation.

In recent years, there has been a growing interest to apply SAW fields to control and manipulate electronic effects in semiconductors. Here, one takes advantage of the fact that these fields are composed of a dynamic strain component and, in piezoelectric semiconductors, of a piezoelectric component. Both components induce a time- and spatially dependent modulation of the materials band structure, which produces moving potentials for the confinement and transport of electronic excitations. Interestingly, the fields produced by high-frequency SAWs (GHz range) have wave lengths on the order of one micrometer, thus being comparable to the dimensions of semiconductor components. The acoustic and acoustoelectric effects can, furthermore, be exploited for novel device functionalities. Quite naturally the studies also include the development of piezoelectric materials compatible with semiconductors as well as efficient processes for the electrical excitation of SAWs in non-piezoelectric materials (such as, e. g. Si).

Diese Core Research Area untersucht die dynamischen Felder, die von akustischen Oberflächenwellen erzeugt werden für die Kontrolle von elektronischen Anregungen in Halbleiter-Nanostrukturen. SAWs sind elastische Schwingungen, die sich auf einer festen Oberfläche ausbreiten. Sie sind ähnlich zu seismischen Wellen, die während Erdbeben entstehen. Diese Wellen können elektrisch auf piezoelektrischen Substraten durch sogenannte Interdigital Transducer (Finger-Wandler) erzeugt werden. Diese Technik ist in der Signal-Verarbeitung, bei Sensoren und akusto-optischen Modulatoren weit verbreitet.

Seit einiger Zeit wächst das Interesse, SAW-Felder für die Kontrolle von elektronischen Effekten in Halbleitern einzusetzen. Hierfür nutzt man die Tatsache, dass die SAW-Felder auf piezoelektrischen Halbleitern aus dynamischen elastischen und piezoelektrischen Komponenten zusammengesetzt sind. Beide Komponenten bewirken eine zeitlich und räumlich abhängige Modulation der Bandstruktur, was wiederum propagierende Potentiale für das Einschließen und den Transport von elektronischen Anregungen erzeugt. Interessanterweise haben hochfrequente SAWs (im GHz-Bereich) Wellenlängen, die vergleichbar mit den Größen von Halbleiterkomponenten sind. Die akustischen und piezoelektrischen Effekte werden darüber hinaus für ihre Eignung für neue Bauelementfunktionalitäten untersucht. Sowohl die Entwicklung von piezoelektrischen Materialien, die mit Halbleitern kompatibel sind, als auch die Entwicklung

The activities carried out in 2018 included (i) investigations of SAW generation and the efficient acoustic transport in GaAs quantum wells (QWs) and epitaxial graphene, (ii) the emission properties of single defect centers in BN and their modulation by SAWs, and (iii) the control of excitonic structures in the form of indirect excitons (IXs) and microcavity polaritons in (Al,Ga)As structures. This report highlights three of these activities. The first (by A. Hernández-Mínguez and co-workers) addresses quantum light emitters on hexagonal boron nitride (h-BN). Here, we report on optically active defect centers contained in nm-thick layers of h-BN grown on Ni substrates by molecular beam epitaxy at the PDI (group of M. Lopes). We investigate the nature of the defects and show that they act as single photon emitters. Their modulation by SAWs is presently under investigation.

In the second report (by M. Yuan and co-workers) we address the selective excitation of single impurity-bound exciton states in a GaAs double QWs (DQWs). These structures are subjected to a transverse electric field to create spatially indirect inter-QW excitons (IXs). We show that this field activates single shallow impurities, which behave as two-level centers emitting single photons. The narrow emission energy distribution (~10 meV) and electric control make them interesting candidates for applications in single-photon sources.

The last contribution (by A. Kuznetsov and co-workers) addresses the modulation of mm-sized intra-cavity traps for microcavity polaritons (MPs) by SAWs. These are required to explore the quantum control of the energy and wave functions of single polariton states. We demonstrate that the trap potential can be dynamically modulated by SAW fields to provide an active control of the trap energy as well as the interaction between neighboring sites in arrays of traps. These results open the way to tunable polariton structures based on lattices of confined polaritons.

von effizienten Prozessen zur elektrischen Anregung von SAW sind Teil dieser Studien.

Die im Jahr 2018 durchgeföhrten Aktivitäten umfassten (i) die Erzeugung von SAWs und des effizienten akustischen Transports in GaAs-Quantentöpfen (QWs) und epitaktischem Graphen, (ii) die Emissions-eigenschaften einzelner Defektzentren in BN und deren Modulation durch SAWs und (iii) die Kontrolle von excitonischen Strukturen in Form indirekter Excitonen (IXs) und Microcavity-Polaritonen in (Al, Ga)As-Strukturen. Dieser Bericht hebt drei dieser Aktivitäten hervor. Die erste (von A. Hernández-Mínguez und Mitarbeitern) befasste sich mit Quantenlichtemittern auf hexagonalem Bornitrid (h-BN). Hier berichten wir über optisch aktive Defektzentren in nm-dicken Schichten aus h-BN, die auf Ni-Substrat durch Molekularstrahlepitaxie hergestellt werden (Gruppe von M. Lopes). Wir untersuchen die Natur der Defekte und zeigen, dass sie als Einzelphotonenemitter wirken. Ihre Modulation durch SAWs wird derzeit untersucht.

In dem zweiten Bericht (von M. Yuan und Mitarbeitern) befassen wir uns mit der selektiven Anregung einzelner defekt-gebundener Exzitonen in GaAs-Doppel-QWs (DQWs). Diese Strukturen werden einem transversalen elektrischen Feld ausgesetzt, um räumlich indirekte Inter-QW-Exzitonen (IXs) zu erzeugen. Wir zeigen, dass dieses Feld einzelne Defekt aktivieren kann, die sich als Zwei-Niveau-Zentren verhalten, die einzelne Photonen emittieren. Aufgrund der engen Emissionsenergieverteilung (~ 10 meV) und der elektrischen Steuerung sind sie interessanten Kandidaten für Anwendungen in Einphotonenquellen.

Der letzte Beitrag (von A. Kuznetsov und Mitarbeitern) befasst sich mit der Modulation von µm-großen Intra-Cavity-Traps für Microcavity-Polaritonen (MPs) durch SAWs. Diese sind erforderlich für die Quantenkontrolle der Energie- und Wellenfunktionen einzelner Polaritonenzustände.

Wir zeigen, dass das Trap-Potential durch SAW-Felder dynamisch moduliert werden kann. Damit erreicht man eine aktive Kontrolle der Trapnergie sowie der Interaktion zwischen benachbarten Traps. Diese Ergebnisse eröffnen den Weg für die Realisierung von durchstimmbaren Polaritonen-Gitterstrukturem für Anwendung in Quantumsimulatoren.

III-V Nanowires for Optoelectronics / III-V-Nanodrähte und deren Anwendung in der Optoelektronik

Dr. Lutz Geelhaar
Dr. Oliver Brandt

Semiconductor nanowires are structures with an extremely high aspect ratio and a diameter typically smaller than 100 nm. In bottom-up approaches, feature sizes down to 10 nm and below can be achieved without any lithography. Complementary top-down approaches offer higher level of control, in particular for the fabrication of regular nanowire arrays. The quasi-one-dimensional shape and the nanometric size of nanowires result in unique properties, often independently of the concrete nanowire material. Their characteristics make nanowires an exciting subject for fundamental studies and offer many conceptual advantages for various applications.

The goal of our research is to inspire and demonstrate new functionalities for optoelectronic applications by employing III-V nanowires. To this end, we investigate fundamental nanowire properties that crucially influence such applications to assess nanowire suitability. We grow both group-III-nitride and group-III-arsenide nanowires by molecular beam epitaxy but pursue also top-down approaches. We analyze nanowire microstructure and optical as well as electronic properties, and we employ technology to guide growth, enable electrical measurements, and process demonstrator devices.

Three different *synthesis* methods represent our platform for both fundamental investigations aimed at elucidating formation mechanisms and the fabrication of nanowire samples for dedicated studies of

Halbleiter-Nanodrähte sind Strukturen mit extrem hohem Aspektverhältnis und Durchmessern von typischerweise weniger als 100 nm. In sogenannten ‚bottom-up‘-Ansätzen (englisch für ‚von unten nach oben‘) werden Nanodrähte hergestellt, indem Material durch Wachstum hinzugefügt wird. Auf diese Weise können Strukturgrößen bis hinunter zu 10 nm ohne lithographische Prozesse erzielt werden. Komplementäre ‚top-down‘-Verfahren („von oben nach unten“), bei denen aus einer größeren Probe Material durch Ätzprozesse abgetragen wird, ermöglichen ein größeres Maß an Kontrolle, insbesondere für die Herstellung von regelmäßigen Nanodraht-Arrays. Die quasi eindimensionale Form und die Größe im Bereich von Nanometern resultieren in einzigartigen Eigenschaften von Nanodrähten, oftmals unabhängig von deren konkretem Material. Ihre Besonderheiten machen Nanodrähte zu einem spannenden Objekt für grundlegende Untersuchungen und bieten zahlreiche konzeptionelle Vorteile für unterschiedliche Anwendungen.

Unser Forschungsziel ist es, durch den Einsatz von III-V-Nanodrähten neue Funktionalitäten für optoelektronische Anwendungen zu inspirieren und zu demonstrieren. Dazu untersuchen wir fundamentale Nanodraht-Eigenschaften, die solche Anwendungen entscheidend beeinflussen, und beurteilen die Eignung von Nanodrähten. Wir züchten Gruppe-III-Arsenid und -Nitrid-Nanodrähte mittels Molekularstrahl-epitaxie aber verfolgen auch ‚top-down‘-Ansätze. Wir analysieren die Mikrostruktur

material properties and applications. First, the best-known bottom-up method resulting in uniaxial growth of nanowires utilizes the vapor-liquid-solid mechanism in which the formation of a solid nanowire from the vapor phase is mediated by a tiny liquid metal droplet. We employ this approach (using Ga as the metal) for the synthesis of group-III-arsenide nanowires on Si(111) substrates. Selective area vapor-liquid-solid growth is readily obtained by patterning these substrates by electron beam lithography and reactive ion etching, leading to ordered nanowire arrays.

Second, an alternative bottom-up approach exists for materials that exhibit the tendency to form nanowires under suitable growth conditions spontaneously, i. e., without any external guidance. GaN is one of these materials, and is prone to the spontaneous formation of nanowires on a wide variety of substrates, including amorphous and crystalline insulators, semiconductors, and metals. We are currently focusing on the growth of group-III nitride nanowires on metallic substrates, and in particular on TiN – both as sputtered film and flexible foil – and graphene. In either case, ensembles of vertical GaN nanowires with excellent structural and optical properties can be obtained.

Spontaneously formed GaN nanowires invariably grow along the $[000\bar{1}]$ direction, i.e., they are N polar. In order to synthesize Ga-polar group-III-nitride nanowires, we utilize as our third synthesis method a top-down process. In particular, we fabricate ordered arrays of nanowires from high-quality group-III-nitride layers and heterostructures by selective area sublimation. This complementary approach allows us to study phenomena depending on, for example, nanowire diameter in a systematic fashion.

In our studies of nanowire *properties*, we pay special attention to phenomena that are a direct consequence of the peculiar wire-like

sowie optischen und elektronischen Eigenschaften von Nanodrähten und nutzen Technologie für die Herstellung regelmäßiger Nanodraht-Arrays, um elektrische Messungen zu ermöglichen und um Demonstrator-Bauelemente zu prozessieren.

shape and nanometric size and are independent of the material the nanowires consist of. For example, the high surface-to-volume ratio of nanowires has several important consequences. In particular, lattice-mis-matched axial heterostructures relax their strain elastically at the free sidewalls, and the formation of dislocations is avoided. For radial heterostructures, a new type of structure only possible due to the nanowire geometry, the strain is shared between core and shell. In both cases, the strain distribution is very complex. Since many semiconductor properties depend sensitively on strain, the dedicated investigation of strain in nanowires is crucial for an understanding of their optoelectronic properties.

Another consequence of sidewall surfaces are radial electric fields induced by surface states. The strength of these fields depends on the doping density in the nanowire and may be large enough to dissociate excitons. Electric fields and doping crucially affect device design and are thus important topics of investigation.

Furthermore, nanowires are not ideal single crystals but exhibit structural defects. Some of these defects, such as twin boundaries, stacking faults, and inversion domain boundaries, act as two-dimensional radiative defects that may dominate luminescence. Others, such as dislocations created by the coalescence of nanowires in close vicinity, act as nonradiative defects. Nonradiative recombination also occurs at the free surface or interfaces and at point defects. Investigations of the microstructure and internal quantum efficiency are thus essential to elucidate the actual potential of group III-V nanowires for optoelectronic applications.

In general, our research relates to *applications* based on either light emission or light absorption, e. g. optical data transmission or energy harvesting. Since the nanowire geometry facilitates the integration of dissimilar materials, substrates with attrac-

tive properties can be employed that were excluded for planar growth. Furthermore, the spectral region of optoelectronic devices can be widened. Also, radial nanowire heterostructures drastically increase the size of the active region, which is associated with stronger light emission and absorption. In addition, light-matter interaction can be tailored by design of nanowire dimensions and their arrangement in arrays.

Currently, we work towards a laser monolithically integrated on Si. Such a laser is of strategic relevance for the application field Si photonics. Our concept will provide the direct coupling of light between arrays of vertical III-V nanowires and planar Si waveguides. This project (MILAS) is funded by the Federal Ministry of Education and Research, and our partner is Technical University of Berlin.

In the nanowire geometry, the chemical composition can be changed in both the axial and the radial direction, leading to corresponding heterostructures and / or doping profiles. Such design concepts still strongly resemble established planar structures. Beyond those strategies, we investigate more advanced structures with the aim to tailor functionality in entirely new directions. For example, we synthesize nanowire heterostructures that are bent in a pre-defined way and employ the resulting complex strain gradients to influence radiative recombination processes. In addition, in many III-V nanowires both the wurtzite and zincblende crystal structure form. We exploit this polytypism to study crystal phase quantum structures of various dimensionalities with inherently atomically sharp interfaces and free from alloy disorder. In combination with compositional heterostructures, we realize complex topologies like quantum rings. Furthermore, we utilize dielectric confinement to modify radiative recombination in ultrathin nanowires.

In the project InterPhase funded by the Federal Ministry of Education and Research, we

study with different partners in Germany charge and energy transfer processes at hybrid organic/inorganic semiconductor interfaces. In particular, group-III nitride nanowires and nanowire heterostructures are coated with organic molecules to demonstrate and analyze two different effects. On the one hand, we aim to passivate the nanowire surface to favor radiative recombination processes in the inorganic semiconductor. On the other hand, our goal is to exploit Förster resonant energy transfer (FRET) to combine efficient charge carrier transport in inorganic semiconductors with highly efficient light emission in organic semiconductors.

This year, we have examined the feasibility of synthesizing pure AlN nanowires. Former attempts of the direct nucleation and growth of AlN nanowire ensembles by molecular beam epitaxy have invariably resulted in highly coalesced structures due to the comparatively low substrate temperature (<900 °C) possible on conventional substrates such as Si. To overcome this limitation, we have developed an approach to deposit stoichiometric δ-TiN films on Al₂O₃ substrates enabling temperatures approaching 1200 °C. As a result of this exceptionally high temperature, we have obtained well-separated AlN nanowires with low coalescence degree and intense exciton transitions at the position characteristic for strain-free AlN. This work opens up the possibility to use AlN nanowires as the base of high-quality AlN/(Al,Ga)N heterostructures emitting in the deep ultraviolet spectral range.

The polytypism occurring in nanowires has been the basis for extensive studies of the metastable wurtzite phase of binary III-V semiconductors, most eminently GaAs. Much less is known, however, about the properties of ternary wurtzite alloys. We have carried out correlated, spatially resolved studies of (In,Ga)As shell quantum wells around GaAs nanowires exhibiting extended segments of both the wurtzite and

zincblende polytype. The comparison of cathodoluminescence with electron back-scatter diffraction and nanoprobe x-ray diffraction measurements on the same single nanowires has revealed that emission from wurtzite (In,Ga)As is blueshifted by tens of meV. Similar correlation experiments involving atom probe tomography and complementary $\mathbf{k}\cdot\mathbf{p}$ calculations have shown that the blueshift results both from reduced In incorporation and the differences in bandstructure between the polytypes. Our results highlight the role of the crystal structure in tuning the emission of (In,Ga)As quantum wells and pave the way to exploiting the possibilities of three-dimensional bandgap engineering in core-shell nanowire heterostructures. At the same time, we have demonstrated an advanced characterization toolkit for the investigation of semiconductor nanostructures.

Nanowires are inherently three-dimensional crystals allowing the fabrication of both axial and radial heterostructures. These structures can be formed by changes of composition or crystal phase. We have found that the simultaneous presence and intersection of inversion domain boundaries and stacking faults in GaN nanowires can lead to the formation of one-dimensional crystal-phase quantum wires or rings with an exciton binding energy as high as 67 meV. Inspired by this finding, we have next demonstrated the controlled fabrication of nearly ideal quantum rings by combining all-binary GaAs/AlAs radial compositional heterostructures with axial crystal-phase quantum structures provided by spontaneously occurring twin boundaries. Doping of the core allows us to accurately tune the radial polarization of the quantum ring exciton and thus enables the observation of the excitonic Aharonov-Bohm effect in rings with a circumference as large as 200 nm. These results demonstrate that GaAs/AlAs core-shell nanowires constitute a platform offering an unprecedented level of control over the design of three-dimensional quantum

structures for the experimental study of excitonic phase coherence phenomena.

The three-dimensional nature of nanowires is also at the heart of another study of ours. By depositing a lattice-mismatched (Al,In)As shell only on one side of GaAs nanowires, we have created highly asymmetric core-shell heterostructures. Strain partitioning between core and shell leads to substantial and controlled bending. This approach can be tailored to make neighboring nanowires touch each other, and nanowires can bent completely over to the substrate. Thus, this

effect could be exploited to fabricate nano-interconnects. Furthermore, the bending results in extreme strain gradients across the nanowire core. As a consequence, the band gap varies, and charge carriers drift to the tensilely strained regions, which we have evidenced by photoluminescence studies. We have exploited this effect to favor carrier recombination in quantum dots grown only on the corresponding nanowire side. In general, engineering of strain gradients opens up new avenues for device design and the study of fundamental phenomena.

Intersubband Emitters: GaAs-based Quantum-Cascade Lasers / Intersubbandemitter: GaAs-basierte Quantenkaskadenlaser

Prof. Dr. Holger T. Grahn

Dr. Lutz Schrottke

The excellent state of semiconductor science and technology allows for the development and application of sophisticated devices such as quantum-cascade lasers (QCLs). These devices rely on the comprehensive understanding and the high-quality growth of complex planar heterostructures. For the terahertz spectral region, which typically ranges from 0.1 to 10 THz bridging the electronics-based microwave region with the optics-based infrared region, GaAs/(Al,Ga)As-based heterostructures are the material of choice. The terahertz region is of great current interest for spectroscopic applications, since rotational states of many molecules, impurity transitions in semiconductors, and fine-structure transitions of atoms as well as ions can result in terahertz absorption or emission. The advantages of terahertz QCLs, covering at present the emission frequency range of about 1 to 5 THz, are their compactness, narrow emission lines, and optical output powers typically between several mW and several tens of mW. Therefore, terahertz QCLs are already used as local oscillators in heterodyne receivers and are promising sources for high-resolution absorption spectroscopy, for instance for the precise determination of the absolute density of atoms and ions in technologically relevant plasma processes. In particular, QCLs for local oscillators at 4.75 THz are currently unrivaled for heterodyne detection of atomic oxygen, which is important in planetary and interstellar science. Meanwhile, the European Space Agency has indicated

Der hervorragende Stand der Halbleiterwissenschaft und -technologie erlaubt die Entwicklung und Anwendung von anspruchsvollen Bauelementen wie Quantenkaskadenlasern (QCLs). Diese Bauelemente erfordern ein umfassendes Verständnis und das Wachstum komplexer planarer Heterostrukturen von hoher Qualität. Für den Terahertz-Spektralbereich, der typischerweise von 0,1 bis 10 THz reicht und den Bereich der elektronisch erzeugten Mikrowellenstrahlung mit dem der optisch erzeugten Infrarotstrahlung verbindet, sind GaAs/(Al,Ga)As-Halbleiterheterostrukturen das bevorzugte Materialsystem. Terahertz-Strahlung ist derzeit von großem Interesse für spektroskopische Untersuchungen, da Rotationszustände vieler Moleküle, Übergänge in Fremdatomen in Halbleitern sowie Feinstrukturübergänge in Atomen und Ionen zu Absorption oder Emission in diesem Spektralbereich führen können. Die Vorteile von QCLs, deren Frequenzbereich sich derzeit von ca. 1 bis 5 THz erstreckt, bestehen in ihrer Kompaktheit, schmalen Emissionslinien und Ausgangsleistungen von typischerweise einigen mW bis zu einigen 10 mW. Diese Laser werden bereits als Lokaloszillatoren in Heterodyn-Empfängern für astronomische Untersuchungen verwendet und sind vielversprechende Quellen für die hochauflösende Terahertz-Spektroskopie, unter anderem für die genaue Bestimmung der absoluten Dichte von Atomen und Ionen in technologisch relevanten Plasmen. Insbesondere sind QCLs als Lokaloszillatoren bei

interest in the exploration of the implementation of terahertz QCLs for space missions based on passive cooling.

In contrast to conventional interband semiconductor lasers, QCLs are so-called intersubband emitters, since the lasing transition takes place within the conduction band rather than across the energy gap. Therefore, they are unipolar lasers, i. e., only one type of carrier, typically electrons, is injected into the laser structure. In order to obtain population inversion between subbands of the conduction band, a rather complex semiconductor heterostructure with typically 6 to 20 layers with thicknesses in the range of a few to about 20 nanometers has to be realized, which is repeated about 100 times forming a semiconductor superlattice with a complex unit cell. The total thickness of the complete structure typically amounts to about 10 µm. The realization of such a structure requires both, a design strategy based on appropriate modeling and a highly accurate growth technique such as molecular beam epitaxy with a very good stability of the growth parameters over up to 20 hours. This growth expertise is one of the core competences of our institute. After growth, the wafers are processed using wet chemical or dry etching to form edge-emitting Fabry-Pérot ridge lasers. For single-mode operation, distributed-feedback lasers using lateral gratings of different order or two-section cavity lasers are realized. Typical dimensions of the laser ridges are widths of 15 to 200 µm and lengths of 0.5 to 7.5 mm.

Our activities in the field of terahertz QCLs cover the design, the growth, the fabrication, and the determination of the operating parameters of these lasers. Since 2014, QCLs developed in our institute have been used as local oscillators in the German REceiver for Astronomy at Terahertz frequencies (GREAT) on board of the Stratospheric Observatory For Infrared Astronomy (SOFIA) for the detection of the fine-structure transition of interstellar neutral atomic

4,75 THz gegenwärtig konkurrenzlos. Inzwischen hat die Europäische Raumfahrtbehörde ihr Interesse an der Erforschung des Einsatzes von Terahertz-QCLs, die für passive Kühlung geeignet sind, in Raumfahrtmissionen bekundet.

Im Gegensatz zu konventionellen Interband-Halbleiterlasern sind QCLs Intersubbandemitter, da der Laserübergang innerhalb des Leitungsbands und nicht über die Energielücke erfolgt. Deshalb sind QCLs unipolare Halbleiterlaser, d. h. nur eine Ladungsträgerart, typischerweise Elektronen, wird in die Laserstruktur injiziert. Um Besetzungsinversion zwischen den Subbändern des Leitungsbandes zu erreichen, wird eine komplexe Heterostruktur mit etwa 100 Perioden, die typischerweise innerhalb einer Periode 6 bis 20 Schichten mit Dicken zwischen etwa 1 und 20 nm enthält und insgesamt etwa 10 µm dick ist, realisiert. Die Entwicklung von Terahertz-QCLs erfordert sowohl das Design auf der Grundlage geeigneter Modellierung der Laser als auch die Herstellung komplexer Heterostrukturen. Dafür wird eine sehr präzise Wachstumsmethode wie die Molekularstrahlepitaxie mit einer guten Stabilität der Wachstumsparameter über bis zu 20 Stunden benötigt. Das Wachstum mittels Molekularstrahlepitaxie ist eine der Kernkompetenzen unseres Instituts. Die Laser werden anschließend mittels nass-chemischer Verfahren oder Trockenätzten als kantenemittierende Fabry-Pérot-Laserstreifen hergestellt. Für den Einzelmodenbetrieb werden Resonatoren mit verteilter Rückkopplung unter Verwendung von lateralen Gittern verschiedener Ordnungen oder Zweisektionslaser verwendet. Typische Abmessungen der Laserstreifen sind Breiten von 15 bis 200 µm und Längen von 0,5 bis 7,5 mm.

Unsere Aktivitäten auf dem Gebiet der Terahertz-QCLs beinhalten das Design, das Wachstum, die Herstellung und die Bestimmung der Betriebsparameter dieser Laser. Seit 2014 werden von uns entwickelte QCLs im German REceiver for Astronomy

oxygen (OI) at 4.7448 THz. Recently, a QCL with improved operating parameters has been implemented in the next generation of astronomical terahertz receivers based on multichannel detection (upGREAT).

QCLs for the terahertz spectral region are usually based on $\text{GaAs}/\text{Al}_x\text{Ga}_{1-x}\text{As}$ heterostructures with $0.1 \leq x \leq 0.25$. Since 2016, we have been able to realize GaAs/AlAs QCLs operating at 4.75 THz, which exhibit an about three times higher wall plug efficiency than $\text{GaAs}/\text{Al}_{0.25}\text{Ga}_{0.75}\text{As}$ QCLs with an almost identical design. Substituting AlAs for the $\text{Al}_{0.25}\text{Ga}_{0.75}\text{As}$ barriers leads to a larger energy separation between the subbands so that the probability for leakage currents through parasitic states and the reabsorption of the laser radiation can be reduced. Based on this alternative materials system, we have realized an improved QCL emitting at 4.75 THz with operating parameters adequate for spaceborne applications, which led to a request to develop QCLs appropriate for passive cooling, i. e., no additional energy source is necessary for cooling the QCL. Furthermore, we have successfully enlarged the frequency range of terahertz QCLs by shifting the upper frequency limit to above 5.6 THz.

The high band offset for GaAs/AlAs heterostructures requires well-controlled barrier thicknesses of a few monolayers, which are on the same order as the real interface widths in III-V systems. Therefore, we have determined the interface profiles of $\text{GaAs}/\text{Al}_{0.25}\text{Ga}_{0.75}\text{As}$ and GaAs/AlAs terahertz QCL structures using transmission electron microscopy (TEM). The experimental composition profiles are directly extracted from the analysis of the diffracted intensity distribution of \mathbf{g}_{002} dark-field TEM images. Due to the interface grading, these actual profiles reveal a significantly lower aluminum content of the barriers than the nominal values. The combination of TEM and simulated composition profiles, which have been obtained using a Fourier-transform-based model and are in remarkably

at Terahertz frequencies (GREAT) während der Beobachtungsflüge des *Stratospheric Observatory For Infrared Astronomy* (SOFIA) für den Nachweis eines Feinstrukturübergangs in interstellarem Sauerstoff bei 4,7448 THz eingesetzt. Vor kurzem wurde ein QCL mit verbesserten Betriebsparametern in der nächsten Generation von astronomischen Terahertz-Empfängern auf der Grundlage von Mehrkanal-Detektion (upGREAT) implementiert.

Terahertz-QCLs beruhen üblicherweise auf $\text{GaAs}/\text{Al}_x\text{Ga}_{1-x}\text{As}$ -Heterostrukturen mit $0.1 \leq x \leq 0.25$. Seit 2016 können wir GaAs/AlAs -Laser für 4,75 THz mit einem mehr als dreifachen Gesamtwirkungsgrad im Vergleich zu $\text{GaAs}/\text{Al}_{0.25}\text{Ga}_{0.75}\text{As}$ -Lasern herstellen. Der Ersatz der $\text{Al}_{0.25}\text{Ga}_{0.75}\text{As}$ -durch AlAs-Barrieren führt zu einem größeren Energieabstand der Subbänder, so dass die Wahrscheinlichkeit von Leckströmen durch parasitäre Zustände reduziert wird. Auf Grundlage dieses alternativen Materialsystems haben wir verbesserte 4,75-THz-Laser, die für weltraumgestützte Beobachtungsmissionen geeignet sein können, realisiert. Deshalb wurden wir aufgefordert, QCLs zu entwickeln, die für passive Kühlung geeignet sind, d.h. ohne zusätzliche Energiequelle für die Kühlung auskommen. Weiterhin haben wir erfolgreich den zur Verfügung stehenden Frequenzbereich von Terahertz-QCLs durch eine Verschiebung der Höchstgrenze auf oberhalb von 5,6 THz vergrößert.

Die große Banddiskontinuität in GaAs/AlAs -Heterostrukturen erfordert das kontrollierte Wachstum von Barrieren mit Dicken von wenigen Monolagen, die von derselben Größenordnung wie die Breiten der Grenzflächenübergänge in III-V-Systemen sind. Deshalb haben wir mittels Transmissionselektronenmikroskopie (TEM) die Grenzflächenprofile in $\text{GaAs}/\text{Al}_{0.25}\text{Ga}_{0.75}\text{As}$ - und GaAs/AlAs -QCL-Strukturen bestimmt. Die experimentellen Zusammensetzungsprofile werden direkt aus der Analyse der Intensitätsverteilung

good agreement with the experimental results, opens a practical path to include realistic interface grading profiles in the design of terahertz QCL structures as well as to study the dependence of the lasing properties on the growth conditions in so far as they may lead to a variation of the interface properties.

For high-resolution terahertz spectroscopy, single-mode operation in conjunction with a sufficient tuning range is necessary. The most straightforward approach is the intrinsic frequency tuning by varying the applied current and/or the heat sink temperature. We have studied the intrinsic frequency tuning of several terahertz QCLs based on our hybrid design. With increasing driving current, most QCLs exhibit either a redshift or a blueshift, while some QCLs show both. The tuning range is about 0.1% of the emission frequency at threshold. In the framework of an oscillator model, we are able to explain the tuning behavior quantitatively or at least qualitatively depending on the complexity of the gain maps. In view of the small tuning range, even a mere qualitative agreement is an important result as it demonstrates both, the applicability and the limits of the oscillator model in this context. The understanding of the intrinsic tuning of terahertz QCLs may be useful for the simultaneous optimization of the output power and tuning range, in particular, for lasers with a hybrid design, which exhibit a sufficiently large degree of freedom.

In some cases of high-resolution terahertz spectroscopy, the available QCLs exhibit a rather small intrinsic tuning range of only about 1 GHz, which in turn allows for a high frequency stability and consequently for a narrow effective linewidth. Therefore, a static tuning of these lasers with a precision of 1 GHz by a controlled change of the resonator length in steps below 0.5 μm is required. We demonstrated that the required accuracy for the definition of the resonator length can be achieved by first cleaving

von g_{002} -Dunkelfeld-TEM-Bildern gewonnen. Durch die abgestuften Grenzflächen weisen die Zusammensetzungprofile einen deutlich geringeren Aluminiumgehalt der Barrieren als nominell vorgegeben auf. Die Kombination von TEM- und simulierten Zusammensetzungprofilen, die mittels eines Fourier-Transform-Modells ermittelt wurden und bemerkenswert gut mit den experimentellen Resultaten übereinstimmen, eröffnet einen praktischen Weg, realistische Grenzflächenprofile in das Design von Terahertz-QCL-Strukturen einzubeziehen und die Abhängigkeit der Lasereigenschaften von den Wachstumsbedingungen zu studieren, insofern sie zu einer Veränderung der Grenzflächeneigenschaften führen.

Für die hochauflösende Terahertz-Spektroskopie müssen die Lasermoden im Einzelmodenbetrieb über die Absorptionslinien abstimmbar sein. Die einfachste Methode besteht in der intrinsischen Abstimmung durch Variation des injizierten Stroms und/oder der Temperatur der Wärmesenke. Wir haben die intrinsische Frequenzabstimmung für eine Reihe von Terahertz-QCLs, die auf unserem Hybriddesign beruhen, untersucht. Mit steigendem Strom zeigen die meisten QCLs entweder eine Rot- oder eine Blauverschiebung, während einige Laser beides aufweisen. Der Abstimmreich beträgt ungefähr 0,1% der Emissionsfrequenz an der Schwelle. Im Rahmen eines Oszillatormodells können wir in Abhängigkeit von der Komplexität der stromabhängigen optischen Verstärkungsspektren das Abstimmverhalten quantitativ oder in einigen Fällen wenigstens qualitativ erklären. Angesichts des kleinen Abstimmreichs ist sogar allein eine qualitative Übereinstimmung ein wichtiges Ergebnis, da sie sowohl die Anwendbarkeit als auch die Grenzen des Oszillatormodells in diesem Kontext aufzeigt. Das Verständnis des intrinsischen Abstimmverhaltens kann für die gleichzeitige Optimierung der Ausgangsleistung und des Abstimmreiches, insbesondere für Laser, die auf Grund des Hybriddesigns hin-

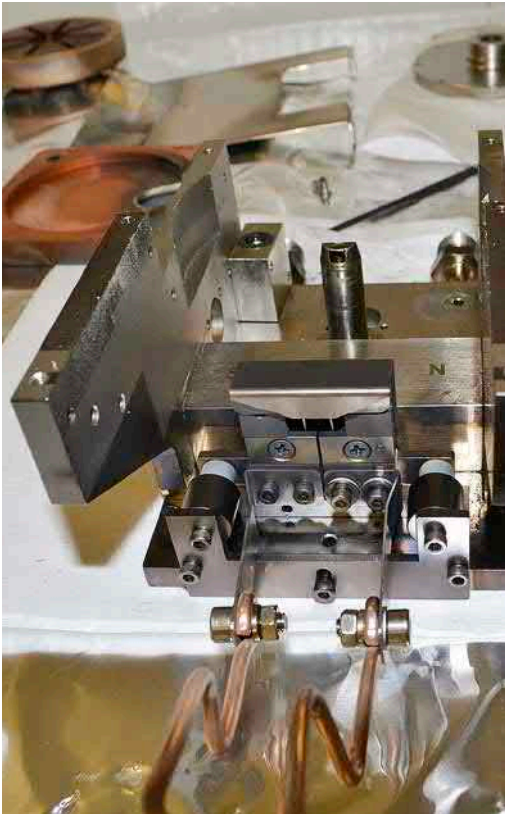
the QCL chip, which defines the resonator length with an accuracy of 10 to 20 µm, and subsequently adjusting the length by mechanical polishing of the front facet aided by a so-called alternating-grain-size technique with an accuracy below 1 µm. Since our approach is compatible with a fully operational QCL, the emission spectrum can be measured prior to polishing in order to determine the required correction of the resonator length. The emission spectrum can also be measured after every polishing run in order to monitor the obtained frequency shift of the modes so that the resonator length can be reduced in reproducible steps of below 0.5 µm and terahertz QCLs for the spectroscopy of a specific absorption line can reliably be fabricated.

Since terahertz QCLs can be conveniently operated in liquid-coolant-free mechanical coolers, new paths have been opened toward various applications. Based on terahertz QCLs and an approach to tuning them by near-infrared optical excitation developed at our institute, the group of Prof. Dr. Heinz-Wilhelm Hübers (Institute for Optical Sensor Systems at the Deutsches Zentrum für Luft und Raumfahrt in Berlin) has demonstrated that spatially well-controlled optical excitation of the terahertz QCLs enables wideband high-resolution spectroscopy with a spectral coverage of as much as 40 GHz for a laser at 3.1 THz, which exceeds the intrinsic frequency tuning range by about one order of magnitude. The method is intrinsically fast, since it relies on the optical excitation of an electron-hole plasma in the substrate of the QCL structure in the vicinity of the facet. In combination with a fast detector, high-resolution molecular spectra covering several tens of GHz are obtained on a millisecond time scale. Finally, the high level of design and growth of terahertz QCLs in our institute is demonstrated by several requests for commercial applications of our QCLs in table-top terahertz systems.

reichend große Freiheitsgrade aufweisen, nützlich sein.

In einigen Fällen der hochauflösenden Terahertz-Spektroskopie weisen die verfügbaren QCLs einen sehr kleinen intrinsischen Abstimmungsbereich von nur ca. 1 GHz auf, der seinerseits jedoch eine große Frequenzstabilität und folglich eine schmale effektive Linienbreite ermöglicht. Deshalb ist eine statische Abstimmung der Laser mit einer Genauigkeit von 1 GHz durch eine kontrollierte Längenänderung des Resonators in Schritten von weniger als 0,5 µm notwendig. Wir haben gezeigt, dass die erforderliche Präzision für die Resonatorlänge erreicht werden kann, wenn nach dem herkömmlichen Spalten des QCL-Bausteins, mit dem die Resonatorlänge auf 10 bis 20 µm genau eingestellt werden kann, eine Feinjustierung der Länge durch mechanisches Polieren der vorderen Facette mittels der sogenannten *Alternating-Grain-Size*-Methode auf weniger als 1 µm genau erfolgt. Um die erforderliche Korrektur der Resonatorlänge zu bestimmen, kann das Emissionsspektrum vor dem Polieren gemessen werden, da unsere Methode mit voll funktionsfähigen QCLs vereinbar ist. Das Emissionsspektrum kann auch nach jedem Polierschritt ermittelt werden, um die erreichte Frequenzänderung der Moden nach jedem Polievorgang zu überwachen, so dass die Resonatorlänge in Schritten von weniger als 0,5 µm reduziert werden kann und Terahertz-QCLs für die Spektroskopie einer spezifischen Absorptionslinie zuverlässig hergestellt werden können.

Da die Terahertz-QCLs problemlos in mechanischen Kühlern ohne kryogene Flüssigkeiten betrieben werden können, eröffnet sich eine Reihe von neuen Anwendungsmöglichkeiten. Basierend auf Terahertz-QCLs und einer Methode zu ihrer Frequenzabstimmung auf der Grundlage der Beleuchtung mit nahinfraroter Strahlung, die in unserem Institut entwickelt wurde, hat die Gruppe von Prof. Dr. Heinz-Wilhelm Hübers (Institut für Opti-



sche Sensorsysteme, Deutsches Zentrum für Luft und Raumfahrt in Berlin) gezeigt, dass die räumlich kontrollierte optische Anregung der Terahertz-QCLs eine breitbandige hochauflösende Spektroskopie mit einer spektralen Abdeckung von 40 GHz für einen Laser bei 3,1 THz ermöglicht, was den intrinsischen Frequenzabstimmungsbereich um etwa eine Größenordnung übertrifft. Diese Methode ist intrinsisch schnell, da sie auf der optischen Anregung eines Elektron-Loch-Plasmas im Substrat der QCL-Struktur in der Nähe einer der Facetten beruht. In Kombination mit einem schnellen Detektor können hochauflösende Molekularspektren über einen Frequenzbereich von einigen 10 GHz innerhalb weniger Millisekunden gemessen werden. Schließlich zeigt sich das hohe Niveau des Designs und des Wachstums von Terahertz-QCLs in unserem Institut durch mehrere Anfragen für kommerzielle Anwendungen unserer Laser in kompakten *Table-Top-Terahertz*-Systemen.





Brief Reports Kurzberichte

Growth as well as structural and spin transport properties of Co ₂ FeSi/MgO/GaAs(001) heterostructures	68
Faceting and growth rate enhancement in (010) β-Ga ₂ O ₃ thin films homoepitaxially grown by plasma-assisted molecular beam epitaxy	71
Phase transformation in BN during van der Waals epitaxy on graphene.....	74
Quantum rings engineered by atom manipulation	77
Thermal expansion of single-crystalline β-Ga ₂ O ₃ from room temperature to 1200 K studied by synchrotron-based high-resolution x-ray diffraction	80
New strategies in the analysis of non-common-atom heterovalent interfaces: CdTe-on-InSb case study.....	83
Electron tomography measurement of III-V semiconductor interface roughness.....	86
Defect interaction as origin of step bunching in epitaxial III-V layers on vicinal Si(001) substrates.....	89
Luminescent centers in a few-layer h-BN film grown by molecular beam epitaxy	92
Tunneling blockade and single-photon emission in GaAs double quantum wells	95
Modulation of confined polariton condensates by high-frequency acoustic waves	98
Quantum rings in III-V semiconductor nanowires.....	101
Nanowires bending over backwards from strain partitioning in asymmetric core-shell heterostructures.....	104
Self-assembled growth of AlN nanowires on sputtered TiN by molecular beam epitaxy	107
Intrinsic frequency tuning of terahertz quantum-cascade lasers.....	110
Determination of the interface parameter in terahertz quantum-cascade laser structures based on transmission electron microscopy	113
Terahertz quantum-cascade lasers for emission at application-specific frequencies	116

Growth as well as structural and spin transport properties of $\text{Co}_2\text{FeSi}/\text{MgO}/\text{GaAs}(001)$ heterostructures

G. Hoffmann, M. Ramsteiner, B. Jenichen, J. Herfort

Epitaxially grown ferromagnet/semiconductor (FM/SC) hybrid structures are promising material systems for the investigation of spin transport in a SC. The spin-polarized contact material Co_2FeSi (CFS) is of particular interest since it belongs to a group of Heusler alloys which is predicted to be halfmetallic. However, the epitaxial growth of CFS on top of a SC suffers from Fe and Co diffusion into the SC, which can lead to a substantial deterioration of spintronic functionalities. In this respect, inserting MgO interlayers at the FM/SC interface is a promising approach, since they act as both diffusion barriers and spin filters, as demonstrated for $\text{Fe}/\text{MgO}/\text{Fe}$ magnetic tunnel junctions.

To probe the effect of MgO interlayers at the CFS/GaAs interface on the spintronic functionalities, a sample series was grown with different MgO interlayer thicknesses ranging from 0 to 10 monolayers (ML) in steps of two ML (1 ML $\text{MgO} \approx 0.21 \text{ nm}$).

The samples were fully grown by molecular beam epitaxy (MBE) on $\text{GaAs}(001)$ substrates without breaking the vacuum between the growth of the different layers, using chambers for the separate growth of III-V-SCs, oxides, and ferromagnetic materials. X-ray reflectivity (XRR) measurements together with XRR simulations and high-resolution transmission electron microscopy (TEM) images [Fig. 1(a)] confirm the successful growth of full CFS/ MgO/GaAs hybrid structures. Furthermore, no precipitates of Fe and Co were found in GaAs using a MgO interlayer thickness of 8 ML. The GaAs layer shown in the TEM image in Fig. 1(a) is single crystalline whereas the MgO layer has a polycrystalline structure, and the CFS layer is strongly textured. The GaAs/MgO interface is very smooth in contrast to the $\text{Co}_2\text{FeSi}/\text{MgO}$ interface. Besides, the TEM analysis for the samples with MgO characterized by this technique (4 and 8 ML) revealed an in-plane rotation of the CFS layer by 45° with respect to the

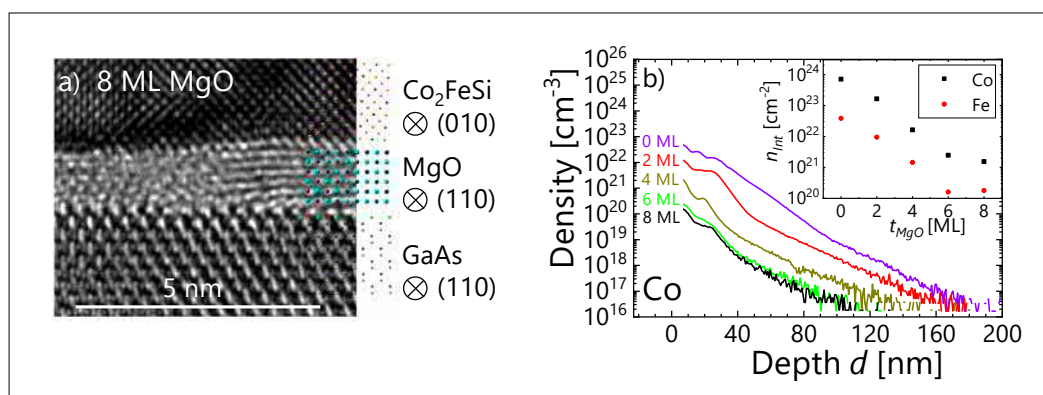


Fig. 1. (a) TEM image of the 8 ML MgO sample and scheme indicating the sequence of the MgO layers, the CFS and GaAs atoms. (b) Co concentration measured by SIMS as a function of the depth below the sample surface for various MgO layer thicknesses. Inset: Integral density n_{int} of Co and Fe atoms as a function of MgO layer thickness t_{MgO} .

GaAs substrate compared to samples without MgO. Such a rotation was found to occur for all samples with MgO interlayers by superconducting quantum interference device (SQUID) magnetometry.

For a quantitative analysis of the influence of MgO on the diffusion of Co and Fe into the GaAs layer, secondary ion mass spectroscopy (SIMS) measurements were carried out. From the depth profiles in Fig. 1(b), we determined the relationship between the integral density of Fe and Co in the GaAs layer and the MgO layer thickness [inset of Fig. 1(b)]. The SIMS measurements show that the amount of Co and Fe atoms diffusing into GaAs decreases exponentially for MgO thicknesses of 0 to 6 ML, hence demonstrating clearly that MgO acts as an effective diffusion barrier.

For the evaluation of electrical and spin transport properties, lateral spin valve (SV) devices were processed and investigated by using three-terminal (3T) and non-local (NL) measurement configurations [see inset in Fig. 2(a)]. The 3T current-voltage (I-V) characteristics of the CFS/MgO/GaAs contacts show non-ohmic, but symmetric behaviour indicating a tunnel barrier. The contact resistances shown in Fig. 2(a)

were calculated for small currents, and in a linear regime. The contact resistances increase exponentially with increasing MgO film thickness, which is a clear sign that the CFS/MgO/GaAs interface is working successfully as a tunnel barrier, which is also a prerequisite for spin injection. However, the calculated effective barrier height of only 0.1 eV indicates that defects in the proximity of the FM/MgO and MgO/GaAs interfaces still play an important role for the charge transport across the interface.

In order to investigate the spin generation and transport, non-local Hanle (NLH) measurements were carried out. The observed oscillations of the NLH curve in Fig. 2(b) reveal the precession of the spins around the z-axis of the magnetic field providing clear evidence for successful spin generation and spin transport in the GaAs channel. Spin diffusion lengths λ and spin lifetimes τ were determined to 5.6 μm and 98 ns, respectively.

Regarding the bias dependence of the spin generation processes, non-local spin valve (NLSV) measurements were carried out, and the NL signal ΔU_{SV} was measured as a function of the bias voltages U_{int} (voltage drop across the CFS/MgO/GaAs contact

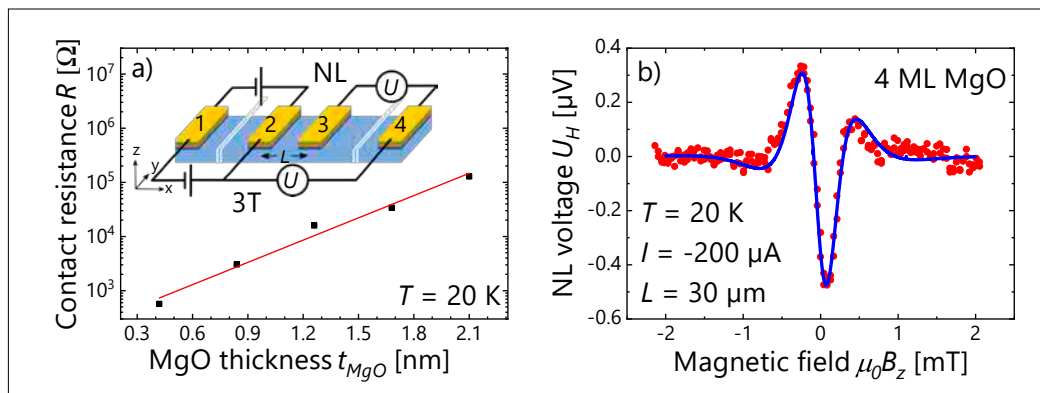


Fig. 2. (a) Contact resistance as a function of MgO film thickness. Inset: sketch of a SV device as well as 3T and NL measurement configuration. (b) NLH signal as a function of an external magnetic field H_z perpendicular to the magnetization M_y of the strips which are separated by a distance of 30 μm , and for an applied current of -200 μA (spin injection) at $T = 20$ K. A linear background signal has been subtracted.

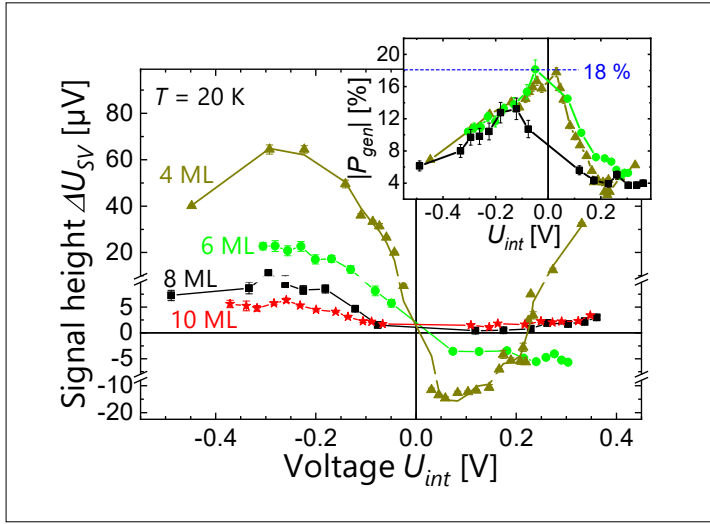


Fig. 3. Signal heights ΔU_{NLSV} determined from NLSV measurements as a function of bias voltage for the 4, 6, 8, and 10 ML MgO samples. Inset: Spin generation efficiency as a function of bias voltage for the 4, 6, and 8 ML MgO sample.

determined by the 3T I - V measurements, see above). Non-abrupt switching of the magnetization from parallel ($\uparrow\uparrow$) to anti-parallel ($\uparrow\downarrow$) configuration for strips 2 and 3 was observed, as expected from SQUID magnetometry. However, all samples from 4 to 10 ML MgO again revealed the successful spin generation and spin-transport in the GaAs channel.

The bias dependent NLSV signals of the samples with 4 and 6 ML MgO shown in Fig. 3 exhibit the expected sign reversal when changing from spin injection (negative bias) to spin extraction (positive bias) conditions. Thereby, the observed positive NLSV signal at negative bias corresponds to majority spin injection. Under spin extraction conditions, the bias dependence of the NLSV signal directly reflects the spin-polarized electronic band structure of CFS. Interestingly, the NLSV signal of the 4 ML sample undergoes a second sign reversal at $U_{int} = +0.2 \text{ V}$ which matches the expectations from first principle calculations of fully ordered (L_2_1) CFS. Deviations of the other samples from this ideal behavior can be explained by electrically active defects which influence the tunneling processes even in MBE grown CFS/MgO/GaAs contacts.

As a last step, the spin generation efficiencies P_{gen} were extracted from the data, and are shown in the inset of Fig. 3. In the low bias regime, the spin generation efficiency reaches a value of 18% for these samples. This value is slightly higher compared to those reported for MBE grown CFS/GaAs structures (16%) without MgO interlayers. Consequently, an improvement of the spin generation seems to be already achievable by the insertion of a MBE grown MgO interlayer, despite the still existing electrically active defects indicated by our results.

Faceting and growth rate enhancement in (010) β -Ga₂O₃ thin films homoepitaxially grown by plasma-assisted molecular beam epitaxy

P. Mazzolini, P. Vogt, R. Schewski¹, C. Wouters¹, M. Albrecht¹, O. Bierwagen

Gallium oxide, in its thermodynamically stable monoclinic crystal structure β -Ga₂O₃, has recently been attracting large interest in the field of power electronic devices due to its wide bandgap ($E_g \approx 4.7$ eV) and the possibility to adjust its electrical properties via extrinsic dopants from semi-insulating to conductive with electron concentrations in excess of $n = 10^{19}$ cm⁻³ [S. J. Pearton *et al.*, Appl. Phys. Rev. **5**, 011301 (2018)]. Nonetheless, the development of gallium oxide is still in its early stage and the full understanding of the physical mechanisms ruling its functional properties is crucial to unveil its full potential. Such an understanding requires a fine control of the material growth. For this reason, we investigated the effect of substrate treatments and deposition parameters on homoepitaxially grown β -Ga₂O₃ thin films synthesized via molecular beam epitaxy (MBE) on β -Ga₂O₃(010) substrates.

The exposure of a Ga₂O₃ surface to a Ga flux at a sufficiently high substrate temperature (while no oxygen is provided) results in the etching of the layer [P. Vogt and O. Bierwagen, Appl. Phys. Lett. **106**, 081910 (2015)]. This is appealing for the fabrication of devices, since a Si contamination is commonly found at the substrate-film interface [E. Ahmadi *et al.*, Appl. Phys. Express **10**, 071101 (2017)]. We thus studied the effect of Ga etching on an (010) surface of β -Ga₂O₃ (substrate temperature $T = 800$ °C, beam equivalent pressure BEP_{Ga} = 4.9×10^{-7} mbar, deposition time $T = 30$ min).

Before the treatment, atomic force microscopy (AFM) evidences a featureless (010) surface with a root mean square roughness as low as rms = 0.19 nm [Fig. 1(a)]. Differently, after the Ga etching the surface exhibits elongated features oriented along

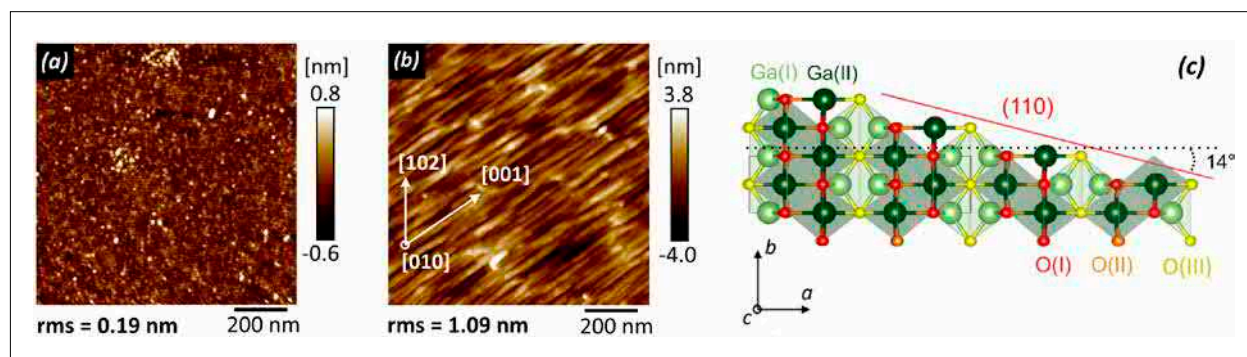


Fig. 1. AFM images of (a) solvent cleaned and (b) Ga-etched Ga₂O₃(010) substrates; (c) β -Ga₂O₃ atomic model.

¹ Leibniz-Institut für Kristallzüchtung, Max-Born-Str. 2, 12489 Berlin, Germany

the [001] direction, which result in an overall roughening [$\text{rms} = 1.09 \text{ nm}$, Fig.1(b)]. In addition, we observed for the Ga-etched Ga_2O_3 surface oblique streaks in the reflection high-energy electron diffraction pattern acquired along the [001] azimuthal direction. This experimental evidence, together with the angle between the oblique streaks and the substrate surface normal of about 14° allows us to relate the appearance of these elongated features to the formation of (110) and ($\bar{1}\bar{1}0$) facets induced by the Ga-etching treatment [Fig.1(c)].

A series of homoepitaxial $\beta\text{-Ga}_2\text{O}_3$ films was also deposited on (010)-oriented substrates. The effect of growth temperature ($T_g = 600 - 900^\circ\text{C}$) and O flows were investigated, while maintaining the Ga flux

($\text{BEP}_{\text{Ga}} = 1.9 \times 10^{-7} \text{ mbar}$) and the deposition time ($t = 30 \text{ min}$) fixed; O flows of 0.33 standard cubic centimeters per minute (sccm), corresponding to metal-rich growth conditions, and 1 sccm, corresponding to oxygen-rich growth conditions, were employed. At a relatively low substrate temperature ($T_g = 600^\circ\text{C}$) we evidence the formation of an irregularly rough surface for metal-rich deposition conditions ($\text{rms} = 1.51 \text{ nm}$, $1 \times 1 \mu\text{m}^2$ image). Similarly, an irregularly rough surface is found when depositing at higher growth temperature ($T_g = 800^\circ\text{C}$), but in oxygen-rich conditions ($\text{rms} = 2.18 \text{ nm}$, $1 \times 1 \mu\text{m}^2$ image). We observe by AFM and transmission electron microscopy (TEM) that for $T_g \geq 700^\circ\text{C}$ the metal-rich deposition conditions result in the formation of (110) and ($\bar{1}\bar{1}0$) facets

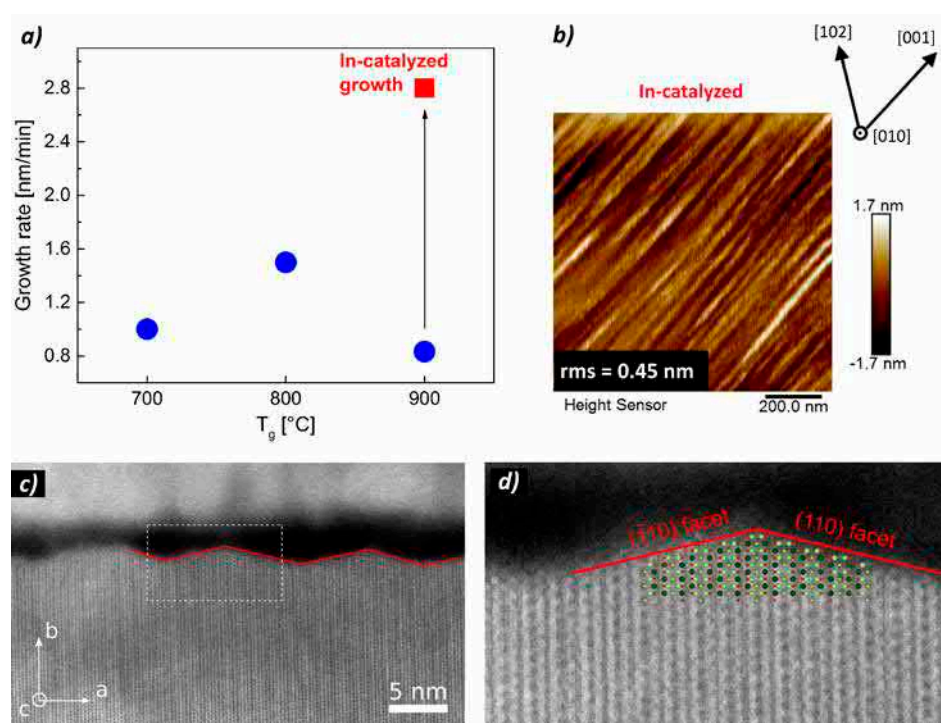


Fig. 2. (a) Growth rate as a function of the growth temperature for the homoepitaxial layers deposited under metal rich conditions with (red square) and without (blue circles) the employment of an additional In flux. (b) AFM image of the layer deposited with In catalysis at $T_g = 900^\circ\text{C}$. (c) High-angle annular dark-field scanning TEM image in the c-projection of the same layer showing the (110) and ($\bar{1}\bar{1}0$) faceting on the growth surface. (d) High-magnification image of the region indicated in (c) with an overlay of the Ga_2O_3 atomic model.

on the (010) surface, as in the case of the Ga-etching treatment. Moreover, we show that the surface roughness of the deposited layers can be decreased by increasing the growth temperature; in particular, for $T_g = 900\text{ }^\circ\text{C}$ it is possible to obtain the lowest surface roughness ($\text{rms} = 0.66\text{ nm}$, $1 \times 1\mu\text{m}^2$ image).

The best scenario for a device-suitable Ga_2O_3 thin film would be a smooth surface obtained at a high growth rate. Unfortunately, while the smoother surfaces for the studied homoepitaxial films are obtained at high T_g ($900\text{ }^\circ\text{C}$), under these conditions the growth rate is limited by the desorption of the volatile Ga_2O suboxide [blue points in Fig.2(a)] [P. Vogt and O. Bierwagen, *Appl. Phys. Lett.* **108**, 072101 (2016)]. Vogt *et al.* recently demonstrated the possibility to drastically increase the growth rate of heteroepitaxially grown Ga_2O_3 thin films on c-oriented sapphire due to metal-exchange-catalysis via the employment of an additional In flux [P. Vogt *et al.*, *Phys. Rev. Lett.* **119**, 196001 (2017)]. Nonetheless, this approach is usually associated with the formation of the orthorhombic phase $\varepsilon\text{-}\text{Ga}_2\text{O}_3$. In this work, we adopted a similar approach, trying to evidence the effect of In-catalysis

on the homoepitaxial growth of $\beta\text{-}\text{Ga}_2\text{O}_3$ thin films. We found that metal-exchange catalysis mediated by an additional In flux ($\text{BEP}_{\text{In}} = 1.3 \times 10^{-7}\text{ mbar}$) strongly increases the growth rate in $\beta\text{-}\text{Ga}_2\text{O}_3$ homoepitaxy at high growth temperatures [$T_g = 900\text{ }^\circ\text{C}$, from 0.83 nm/min to 2.8 nm/min , Fig.2(a)] while maintaining the monoclinic crystal structure, a low surface roughness [$\text{rms} < 0.5\text{ nm}$, Fig.2(b)], and without significant incorporation of In (energy dispersive X-ray analysis). Notably, as previously discussed for Ga-rich deposition and etching treatments, also in the case of the In-catalyzed growth we observe the formation of (110) and ($\bar{1}10$) facets on the (010) surface [Fig.2(c)–(d)].

The results collected in this work suggest that these facets are thermodynamically more stable with respect to the (010) surface under metal-rich conditions, implying the possibility of homoepitaxial growth of unfaceted $\beta\text{-}\text{Ga}_2\text{O}_3$ thin films on (110)-oriented substrates, a crystal orientation which has not yet been studied in literature. Finally, our results demonstrate metal-exchange catalysis as an avenue to overcome the severe growth-rate limitations of $\beta\text{-}\text{Ga}_2\text{O}_3$ films also during homoepitaxy.

Phase transformation in BN during van der Waals epitaxy on graphene

M. Heilmann, A. S. Prikhodko¹, M. Hanke, H. Riechert, N. I. Borgardt¹, J. M. J. Lopes

Boron nitride (BN) and carbon possess many similar allotropes, e.g. the sp^3 -bonded c-BN is analogous to diamond and sp^2 -bonded h-BN is isomorphic to graphene. However, there are also striking differences, e.g. delocalized π electrons can travel through metallic graphene with highest mobilities, while they are localized at the N atoms in h-BN, resulting in its insulating behavior. This makes the combination of h-BN and graphene interesting for transparent and flexible, low-dimensional electronic devices. For a scalable fabrication of the latter an epitaxial approach during which the sp^2 -bonded phases are grown on top of each other appears crucial.

Another fundamental difference between BN and carbon lies in the thermodynamic

stability of their phases, where at ambient conditions c-BN is stable and h-BN is metastable, whereas graphene is stable and diamond is metastable. For BN, the transition temperature from the cubic to the hexagonal phase is around 850 °C. Nonetheless, in a previous study we found that h-BN grew on epitaxial graphene (EG) on SiC(0001) over a large temperature range, from 630 °C to 1000 °C, where h-BN nucleated at point defects and morphological features in EG [M. Heilmann *et al.*, 2D Materials **5**, 025004 (2018)]. We expect that the initial bonding configuration at point defects affects the nucleation of the BN. Therefore, in the present study we attempt to control this configuration by an *in-situ* plasma pretreatment of the substrates, in which EG was exposed to a N_2 plasma source for 30 min at 850 °C before growing BN at the same temperature for 300 or 600 min. We note that Raman measurements indicate no additional defect formation due to the plasma treatment.

After 300 min of growth, atomic force microscopy (AFM) measurements showed the formation of triangular shaped h-BN islands with a thickness of one monolayer (0.35 nm) on N_2 plasma treated EG (N-EG) with a relative orientation of 0° and 30° toward each other [see Fig.1(a)]. This is in strong contrast to the islands forming on untreated EG in the aforementioned study, which were hexagonally shaped and randomly aligned. The N_2 plasma pretreatment also gave rise to the formation of clustered nanoparticles (NPs), which have previously only been observed after the growth of at least one completely coalesced h-BN layer. The NPs were attributed to additional

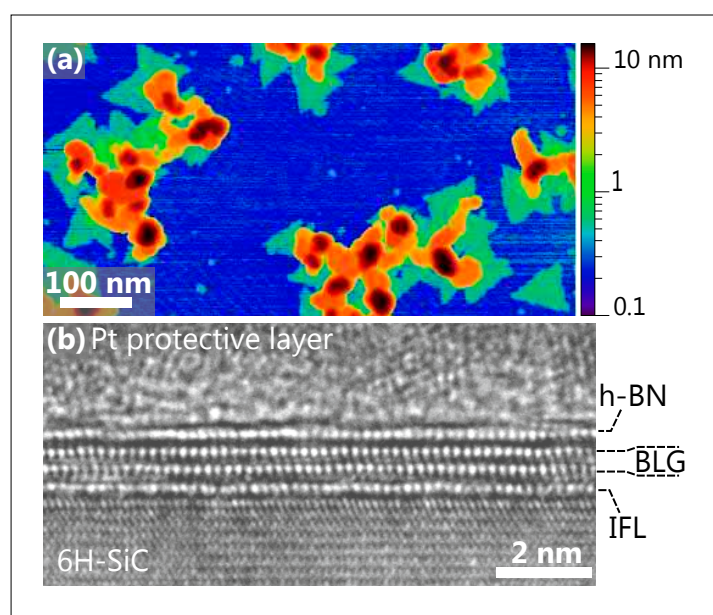


Fig. 1. (a) AFM image of BN grown for 300 min on N-EG. (b) HRTEM image of h-BN grown on N-EG for 600 min, shown along EG[11̄20].

¹ National Research University of Electronic Technology (MIET), Zelenograd, 124498 Moscow, Russia

non-coalesced h-BN layers, growing vertically at defects. Thus, the plasma pretreatment affected both, the lateral and vertical growth of h-BN.

Cross-sectional high-resolution transmission electron microscopy (HRTEM) measurements were performed to characterize the sp^2 -bonded heterostructure as well as the NPs after 600 min of growth. A representative area without a NP on N-EG is shown in Fig.1(b), where the first layer is the graphene-like interface layer (IFL), which is partially sp^3 -bonded to the SiC. The IFL is followed by an AB-stacked bilayer graphene (BLG) with an in-plane atomic spacing of 2.12 Å, while the top most layer shows a spacing of 2.17 Å, as expected for h-BN observed along $\langle 11\bar{2}0 \rangle$ directions.

A cross-section through three NPs is shown in the HRTEM image in Fig.2(a). Fig.2(b) presents the elemental mappings of Pt, N, C, and Si, measured by energy-dispersive X-ray spectroscopy (EDX)-HRTEM from the same NPs as shown in Fig.2(a). Limitations of the detector did not allow the mapping of B. The EDX measurements confirm that

the NPs contain N, whereas Si and C can be detected from the substrate, and the protective layer consists of nanocrystalline Pt embedded in C.

While overall the NPs have no common in-plane orientation toward each other, some of them are well aligned toward the EG and two different lattice spacings of $d_1 = 4.44$ Å and $d_2 = 2.58$ Å are apparent in the HRTEM measurements, as shown exemplarily for two different NPs in the insets of Fig.2(c) and (d), respectively. A multislice algorithm was used to simulate the HRTEM images, where the two different lattice spacings have been found to correspond to two different directions of crystals with a $P4_2/mnm$ space group, exhibiting four-membered rings of two B and two N atoms along the [010] direction [see Fig.2(e)] as well as six-membered rings with three alternating B and N atoms along [100] or [001] directions [see Fig.2(f)]. This so called β -BeO type BN was predicted theoretically as a metastable phase during the pressure induced phase transformation from h-BN to c-BN [L. Hromadová et al., Phys. Rev. B **84**, 224108 (2011)]. It was named after β -BeO

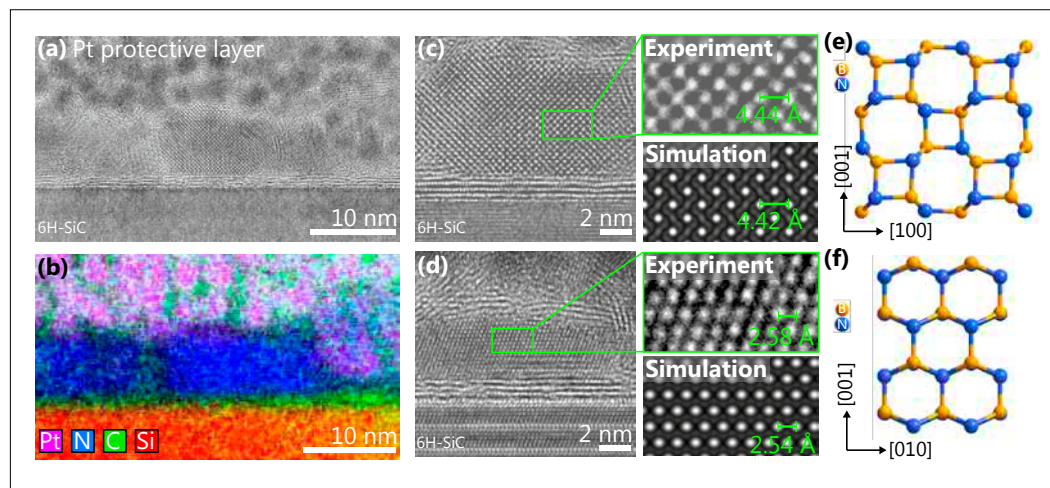


Fig. 2. (a) HRTEM image of NPs on BLG on SiC(0001) shown along EG[11̄20]. (b) Superimposed elemental EDX-HRTEM mappings of Pt, N, C, and Si from the same sample region as shown in (a). (c)–(f), Comparison of two different NPs, aligned to the view along (c) EG[11̄20] and (d) EG[1̄100] in comparison with the simulated HRTEM-images for β -BeO-type BN viewed along either (e) [010] or (f) [100]/[001].

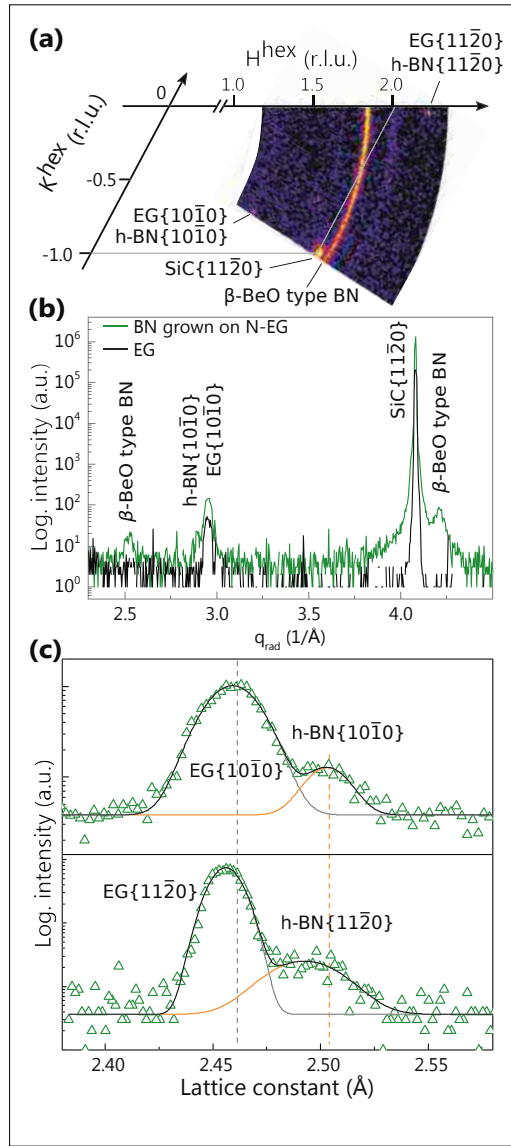


Fig. 3. (a) Reciprocal space map of h-BN on N-EG scaled to SiC. (b) Linescan through the $\text{SiC}\{11\bar{2}0\}$ reflection along the radial direction q_{rad} (green line). For comparison, an equivalent linescan acquired from EG is shown in black. (c) Detailed linescan through the h-BN and $\text{EG}\{10\bar{1}0\}$ and $\{11\bar{2}0\}$ reflections with the x -axis scaled to their lattice parameter.

due to its structural similarity, but it has not been synthesized so far.

The sample was further investigated by synchrotron-based gracing-incidence X-ray diffraction (GID) at the European Synchrotron Radiation Facility in Grenoble. This method allows the evaluation of the in-plane lattice constants and orientations of h-BN, EG and SiC, as shown in the reciprocal space map in Fig. 3(a), with a radial linescan through the $\text{SiC}\{11\bar{2}0\}$ reflection in Fig. 3(b) in comparison to equivalent data acquired for EG. Besides the isolated reflections of h-BN, EG and SiC (showing their single orientation and epitaxial relationship), a ring-like reflection is visible in the map, indicating a random in-plane orientation, which is attributed to the $\beta\text{-BeO}$ type BN NPs. The reflection corresponds to a lattice spacing of 1.492 \AA , which is equal to the in-plane distance between B and N in the four-membered ring, while an additional reflection visible in the linescan corresponds to a lattice spacing of 2.489 \AA , fitting to the distance between B and N across the six-membered rings. Comparing the h-BN and $\text{EG}\{10\bar{1}0\}$ with the $\{11\bar{2}0\}$ reflections reveals an anisotropic strain in the layered heterostructure, which potentially promoted the formation of the $\beta\text{-BeO}$ type BN NPs [see Fig. 3(c)].

In conclusion, the metastable $\beta\text{-BeO}$ type BN has been grown for the first time. Its discovery using a van der Waals epitaxial approach implicates that the growth of BN follows the Ostwald-Volmer rule, according to which at low temperatures the metastable h-BN nucleates first, before phases of higher density form. This mechanism should in principle allow the combination of h-BN with other sp^2 -bonded materials, which are less temperature-stable as compared to EG.

Quantum rings engineered by atom manipulation

V. D. Pham, K. Kanisawa, S. Fölsch

Quantum rings (QRs) enable electron motion along a closed path without loss of phase coherence. They offer the possibility to explore fundamental phenomena in quantum and condensed-matter physics like the Aharonov-Bohm effect and persistent currents. QRs are often fabricated from III-V semiconductor quantum dots transformed to ring-like structures upon post-growth annealing. As an alternative path, we use cryogenic scanning tunneling microscopy (STM) to assemble surface-supported QRs one atom at a time. This approach provides full structural control and allows one to manipulate the QR-confined quantum states, for example, by deliberately introducing point defects.

In our experiment, the InAs(111)A surface is used as a template to generate the QRs by

atom manipulation and probe them by recording the differential tunnel conductance as a measure for the local density of states (DOS). MBE-grown InAs(111)A hosts a low concentration (roughly 0.005 monolayer) of In adatoms weakly bound to the surface. These native adatoms are ionized donors (charge state +1) that can be readily repositioned by the STM tip. Figure 1(a) shows a constant-current topography image of a linear chain composed of thirty In adatoms occupying surface sites along the $\bar{[1}2\bar{1}]$ direction. The adatoms are $\sqrt{3}\alpha'=14.84 \text{ \AA}$ apart from each other, with $\alpha'=8.57 \text{ \AA}$ the lattice constant of the (2×2) In vacancy reconstruction of InAs(111)A. Our previous work revealed that these chains confine surface state electrons due to the electrostatic potential imposed by the +1 charged adatoms. Within a simple tight-binding

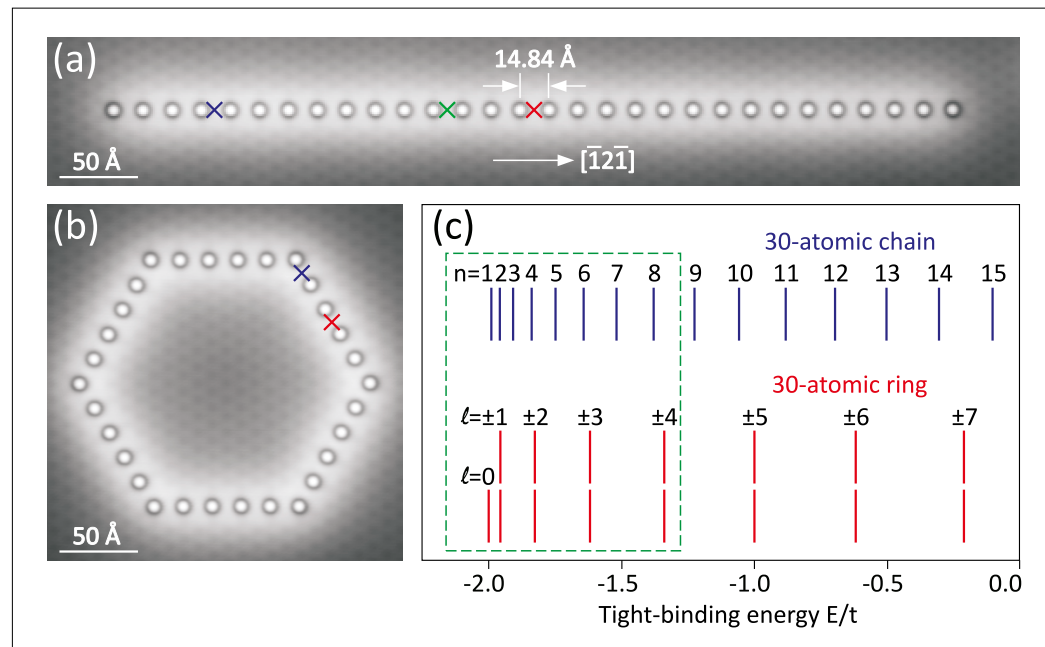


Fig. 1. (a) Constant-current topography image (100 pA, 100 mV) of thirty In adatoms on InAs(111)A assembled into a linear chain oriented along the $\bar{[1}2\bar{1}]$ in-plane direction. (b) Constant-current topography image (100 pA, 100 mV) of thirty In adatoms on InAs(111)A assembled into a hexagon ring. (c) Electronic level scheme of a linear chain made of thirty atoms (blue vertical bars) and a closed ring of thirty atoms (red vertical bars); the x-axis shows the tight-binding energy E/t (t : hopping energy). Levels marked by the green dashed box are the experimentally observed ones shown in Fig. 2.

picture, the confined-state energies are $E = E_0 - 2t \cos(\pi n/[N+1])$ with the hopping energy t , the principal quantum number n ($\{n=1,2,3,\dots\}$), and N the number of atoms. The blue vertical bars in Fig.1(c) show the energies of the fifteen lowest states, each carrying two electrons (E_0 is set zero for simplicity).

The In_{30} chain in Fig. 1(a) can be rearranged to form a hexagon-shaped In_{30} ring as shown in Fig. 1(b). Note that the interatomic spacing of $\sqrt{3}a'$ is maintained. Nevertheless, the corner sites are not equivalent to sites within the linear segments of the

hexagon. Neglecting this inequivalence (the consequence of which will be addressed later), the expected tight-binding energies are $E = E_0 - 2t \cos(\pi l/N)$ with $l \{l=0, \pm 1, \pm 2, \dots\}$ the quantum number of angular momentum $l\hbar$. The red vertical bars in Fig.1(c) indicate the resulting energies and show that the ground state with $l=0$ is non-degenerate (carrying two electrons) whereas higher states with finite angular momentum are doubly-degenerate. Provided that the simple level scheme in Fig.1(c) holds also for the real structures shown in Figs.1(a) and (b), one would expect to observe a reduced number of conductance peaks for the ring as compared to the linear chain.

To verify this expectation, Fig.2 shows tunneling spectra of the linear In_{30} chain in panel (a) and the In_{30} ring in panel (b). Tip positions where spectra were taken are indicated by colored crosses in Figs.1(a) and (b). Starting with panel (a), conductance peaks at eight different energies are observed between -0.3 eV below the Fermi level (at sample bias $V=0$) and 0.1 eV above the Fermi level. The corresponding energy range is marked by the green dashed line in the level scheme in Fig.1(c). Spatial DOS maps recorded at the respective peak energies in Fig.2(a) reveal squared wave functions with n lobes and $(n-1)$ nodes, as expected for particle-in-a-box confinement. Turning to the tunneling spectra of the In_{30} ring [Fig.2(b)], we find that the number of conductance peaks is in fact reduced, analogous to the prediction of the level scheme in Fig.1(c). Within the given energy range we thus observe the ground state with $l=0$ and the doubly-degenerate states with $l=\pm 1, \pm 2, \pm 3$, and ± 4 .

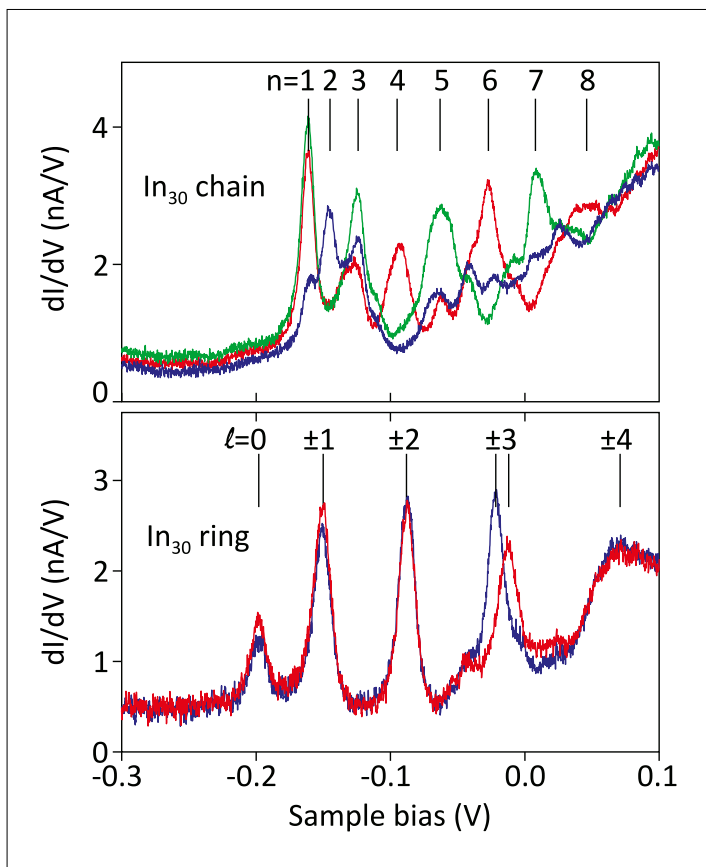


Fig. 2. (a) Tunneling spectra of the linear In_{30} chain reveal conductance peaks corresponding to the chain-confined states with $n=1$ to 8; tip positions where spectra were taken are shown in Fig.1. (b) Tunneling spectra recorded for the In_{30} ring and over the same energy range as in (a). The observed conductance peaks correspond to the ring-confined states with $l=0, \pm 1, \pm 2, \pm 3$, and ± 4 , as also indicated by the green dashed box in Fig.1(c).

Coming back to the role of corner sites, one may argue that their inequivalence to other sites along the ring has an effect primarily on the eigenstate with $l=\pm 3$. This is because the wave functions associated with $l=\pm 3$ have six lobes so that the lobe positions can be in perfect registry either with the corners or the linear segments of the

hexagon. Indeed, for the conductance peak with $l=\pm 3$ the spectra in Fig. 2(b) show an energy splitting on the order of 10 mV when recorded near the corner (blue curve) or at the center of the linear segment (red curve). In contrast, no such splittings are observed for the sharp conductance peaks at smaller and larger angular momentum. We conclude that there is a minor, however, measurable deviation from the idealized picture of a circular quantum ring. Nevertheless, a more sizable effect on the level structure of the ring can be induced on purpose by incorporating point defects in terms of additional adatoms or vacancies, which is the subject of ongoing work.

Our results demonstrate that atom manipulation on III-V semiconductor surfaces is capable of engineering quantum rings with atomic precision. Size and shape of the rings can be controlled, and the level structure can be modified by deliberate incorporation of point defects. The availability of a tunable magnetic field (which, however, is not compatible with our present STM apparatus design) would offer additional fascinating possibilities to manipulate the quantum phase of ring-confined electrons.

Thermal expansion of single-crystalline β -Ga₂O₃ from room temperature to 1200 K studied by synchrotron-based high-resolution x-ray diffraction

Z. Cheng, M. Hanke, Z. Galazka¹, A. Trampert

Ga₂O₃ is a wide-bandgap transparent semiconducting oxide with fascinating optical and electrical properties making it the first choice for various applications, as e.g. deep-UV photodetectors, field effect transistors and high-temperature gas sensors. The rapidly growing interest in this material is evidenced in a 10% increase of publications per year. However, only a few of the basic thermal properties of β -Ga₂O₃ have been addressed in the recent past. An impressive example on how important fundamental properties can be is the paper by Z. Guo *et al.* [Appl. Phys. Lett. **106**, 111909 (2015)] on anisotropic thermal conductivity. Our work addresses another very basic

property of β -Ga₂O₃: its temperature-dependent and anisotropic thermal expansion behavior in the window between room temperature (RT) and 1200 K. Two previous papers provide constant, i.e., temperature-independent values for the coefficient of thermal expansion (CTE). However, there is no comprehensive study available, which tackles this phenomenon in detail. In order to determine the CTEs, lattice plane distances were probed precisely by *in-situ* synchrotron-based high-resolution x-ray diffraction. Our experimental findings are simulated within the Einstein model.

The experiments were carried out at the dedicated PHARAO endstation U125/2-KMC at BESSYII (Helmholtz-Zentrum Berlin). This setup enables a direct *in-situ* access to lattice dynamics, since it combines a fully equipped six-circle diffractometer with a custom-built molecular beam epitaxy (MBE) system allowing to manipulate the wafer temperature from RT and 1200 K. Angular resolution is provided by a 1 mm slit in front of the detector. The Si(111) double-crystal monochromator defines the x-ray energy at 10 keV with a spectral resolution $\Delta E/E$ of about 10^{-4} . We have used $5 \times 5 \times 0.5$ mm³ twin-free wafers of single-crystalline (100)-oriented β -Ga₂O₃ grown by the Czochralski method at Leibniz Institute for Crystal Growth in Berlin.

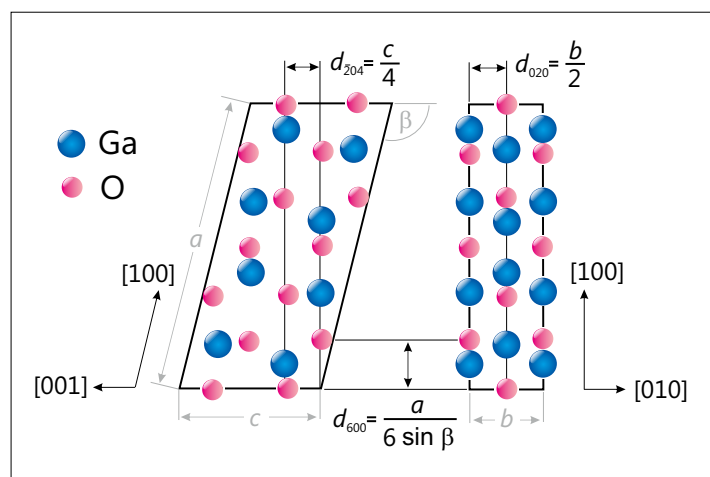


Fig. 1. Crystal structure of β -Ga₂O₃ viewed in [010] (left) and [001] (right) directions. The lattice parameters a , b , and c and their relation to experimentally accessible lattice spacings d for (600), (020), and (204) planes are given. Due to the monoclinic symmetry (i.e., $\beta \neq 90^\circ$) the {h00} planes are not perpendicular to the [100] direction. In the right figure, this direction is depicted as projection onto the paper plane.

A calibration procedure using Si(111) wafer yields a temperature uncertainty of about 10 K above and below the on-site temperature. After the calibration, we have investigated the temperature-dependent diffraction from 298 to 1200 K according to lattice

¹ Leibniz-Institut für Kristallzüchtung, Max-Born-Straße 2, 12489 Berlin

spacings d_{hkl} for $\beta\text{-Ga}_2\text{O}_3$, as sketched in Fig.1. If the angles between the axes are assumed to be constant ($\beta=103.85^\circ$, $\alpha=\gamma=90^\circ$), the respective lattice parameters a , b , and c are given according to $a=6 \cdot d_{600} / \sin \beta$, $b=2 \cdot d_{020}$, $c=4 \cdot d_{204}$.

The blue squares in Fig.2(a)-(c) depict the lattice parameters a , b , and c of bulk $\beta\text{-Ga}_2\text{O}_3$ as a function of wafer temperature T , while the red curves are fits based on the Einstein model. Below each graph, the respective functional dependencies of the various CTEs α_i are plotted as straight lines together with the constant values for powder and bulk. Our findings agree with them in the sense that thermal expansion happens anisotropically with $2\alpha_a \approx \alpha_b \approx \alpha_c$.

According to the definition of CTE by the international organization for standardization (ISO), the coefficient is given by the following equation:

$$\alpha(T) = \frac{1}{a_{RT}} \frac{da(T)}{dT} \quad (1)$$

whereby a_{RT} refers to the lattice parameter at RT (around 298 K), and $\frac{da(T)}{dT}$ is the differential lattice parameter over temperature. By neglecting now the influence of the pho-

non dispersion (i.e., the high-temperature regime), $\alpha(T)$ can be calculated according to the Grüneisen equation $\alpha(T) = \frac{1}{3} \gamma \kappa C_v(T)$. Here, γ and κ are the Grüneisen parameter and the harmonic compressibility, respectively. Within the Einstein model, the specific heat of a solid is coupled to its phonons, all of the same frequency but with different occupation probability at various temperatures. With the Einstein temperature θ_E it yields for the specific heat:

$$C_v(T) \propto \left(\frac{\theta_E}{T} \right)^2 \frac{e^{\theta_E/T}}{(-1 + e^{\theta_E/T})^2}. \quad (2)$$

In a simple model, γ and κ can be considered as constants, independent of temperature T . Therefore $\alpha(T)$ is only proportional to $C_v(T)$, the specific heat per volume. In some cases, e.g. if the CTE is partially negative, a single Einstein term as given in Eq.(2) becomes insufficient and has to be replaced by a summation over m terms:

$$\alpha(T) = \frac{1}{a_{RT}} \sum_{k=1}^m a_k \left(\frac{\theta_k}{T} \right)^2 \frac{e^{\theta_k/T}}{(-1 + e^{\theta_k/T})^2}. \quad (3)$$

Based on that, the lattice parameter can be finally obtained by integration

$$a(T) = a_{RT} + \sum_{k=1}^m a_k \frac{\theta_k}{-1 + e^{\theta_k/T}}. \quad (4)$$

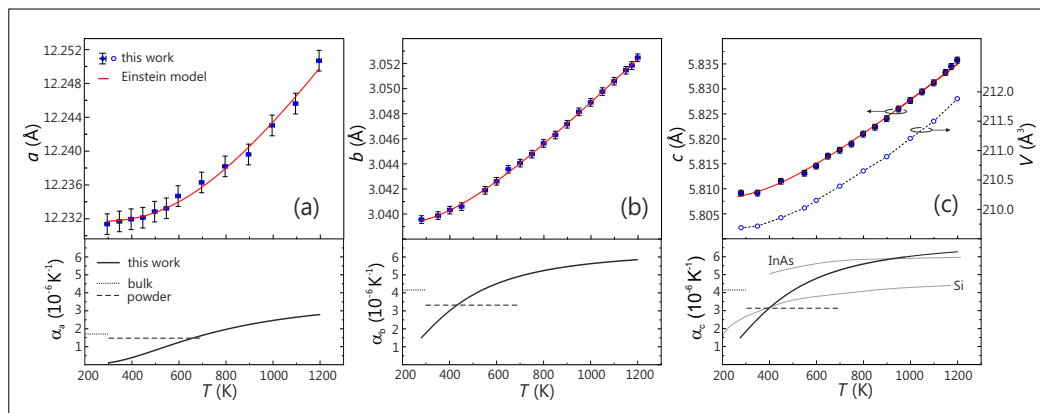


Fig. 2. (a)-(c) Measured lattice parameters a , b , and c and resulting unit cell volume V as function of substrate temperature T . Red curves show numerical fits applying the Einstein model. The CTEs α_i along the three crystallographic directions [100], [010] and [001] of the monoclinic unit cell are the derivatives of the temperature-dependent lattice parameters. They are plotted at the bottom of each figure together with data for $\beta\text{-Ga}_2\text{O}_3$ powder and bulk. For illustrative purposes the isotropic values of α for cubic InAs and Si are also shown in (c).

This equation holds for all three considered directions. It is apparent that in Fig. 2(a)-(c) the simulations based on the Einstein model (the red lines) using a single Einstein term support very well the discrete data points within the entire temperature window.

On the basis of the well fitted simulation, the CTEs can be extracted from the derivative of the thermal expansion. At the bottom of Fig. 2, the CTEs of lattice parameter a , b and c are plotted as a function of temperature. One interesting feature is that in the probed window all functions α_a , α_b , and α_c increase with temperature and gradually even approach their high temperature limit close to 1200 K. This is a general saturation effect indicative for fully occupied phonon modes as also observed in, e.g. InAs and Si [cf. Fig. 2(c)]. As for the amplitude of the CTEs, it is clearly shown that α_b and α_c follow a rather similar dependence, however the value for α_a is approximately only half of values for α_b and α_c . This anisotropic thermal expansion behavior is in correspondence with constant CTEs from 5 to 700 K reported previously by Villora *et al.* [Appl. Phys. Lett. **92**, 202118 (2008)] and Orlandi *et al.* [Appl. Phys. Express **8**, 111101 (2015)]. Finally, we would like to mention that the unit cell volume, based on the measured lattice parameters, depicts a similar functional dependence, Fig. 2(c).

In summary, the lattice parameters a , b , and c of single-crystalline monoclinic β - Ga_2O_3 bulk were precisely probed in the temperature range from 298 to 1200 K. The experimental results for the thermal expansion of β - Ga_2O_3 can be simulated within the Einstein model based on a single Einstein term. Our data provides evidence for an anisotropic behavior within the investigated temperature window.

New strategies in the analysis of non-common-atom heterovalent interfaces: CdTe-on-InSb case study

E. Luna, J. Lu¹, T. Aoki¹, Y.-H. Zhang¹, M. R. McCartney¹, D. J. Smith¹, A. Trampert

The selective combination of closely lattice-matched group II-VI/group III-V semiconductors offers potential benefits due to the wide range of band-gap energies achievable and novel effects at the interface arising from the valence-mismatch. Very little has been done so far to exploit these opportunities, in part due to present challenges in determining the structure and properties of the interface, for instance using scanning transmission electron microscopy (STEM) techniques.

The combination of CdTe (II-VI) and InSb (III-V) implies the existence of a heterovalent non-common-atom (NCA) interface which must contain mixtures of II-V and/or III-VI bonds. Because of the close atomic numbers of the constituent elements, high-angle annular dark-field (HAADF) and large-angle bright-field (LABF) STEM, as well as electron energy-loss spectroscopy measurements from the interface region are inherently difficult to interpret. Hence, details about the interface stoichiometry or the composition profile remains unclear. Investigation of interfacial roughness using different (S)TEM techniques indicate coherent, defect-free CdTe/InSb interfaces, as shown in Fig. 1, which displays several images each probing the interface on different length scales ranging from the hundred-nm scale of conventional dark-field (DF) TEM micrographs to the atomically-resolved aberration-corrected (AC) STEM image, which resolves projections of

individual atomic columns, commonly called "dumbbells".

In order to identify the interface position, quantitative analysis of intensity profiles was carried out on pairs of HAADF and LABF images recorded simultaneously. Both imaging modes provide incoherent, Z-dependent image contrast with no contrast inversions with defocus or sample thickness. Figure 2(a) shows an AC STEM HAADF image across the CdTe/InSb interface and Fig. 2(b) reveals an intensity profile. Clear intensity differences are apparent for the atomic columns within each dumbbell pair, and it is possible to identify the dumbbell polarity with the heavier anion Sb to the left of each pair of atomic columns on the left side of the interface, and the heavier anion Te to the left of each pair on the right side of the interface. Sig-

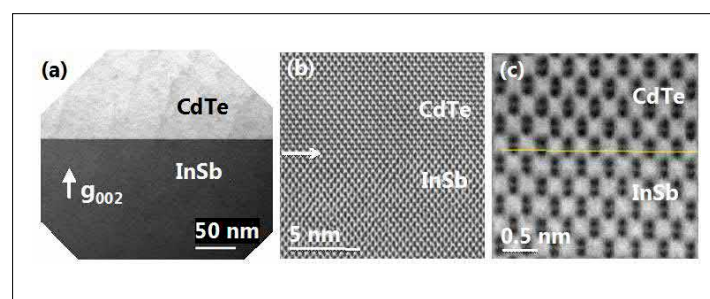


Fig. 1. CdTe/InSb heterostructure recorded in several different TEM imaging modes: (a) \mathbf{g}_{002} DFTEM; (b) high-resolution, phase-contrast TEM; (c) AC STEM LABF image.

¹ Arizona State University, USA

nificantly, the exact interface position cannot be determined unambiguously, because there is no notable difference measurable in the dumbbell spacing across the interface. Furthermore, the intensity variations of the dumbbells do not remarkably change, which can be attributed to chemical intermixing between In and Cd and, on the other hand, between Sb and Te.

In contrast, use of the chemically sensitive \mathbf{g}_{002} DFTEM imaging technique emphasizes the interface location by comparing differences in structure factors between the two materials, as is clearly visible in Fig. 1(a). Furthermore, the composition profile across the interface can be inferred from the analysis of the intensity of the DFTEM micrographs. The diffracted inten-

sity of the 002 reflection under kinematic approximation for compound semiconductors with zincblende (ZB) structure is proportional to the square of the structure factor, which depends on the difference in the atomic scattering factors f of the individual alloy components. Based on \mathbf{g}_{002} DFTEM, a methodology was developed for reliable and systematic quantification of the interface width in *isovalent* NCA interfaces [E. Luna *et al.*, Appl. Phys. Lett. **96**, 021904 (2010)]. An extension of this approach to the *heterovalent* NCA CdTe/InSb interface seems feasible since both, CdTe and InSb compounds, have ZB structure, and \mathbf{g}_{002} DFTEM images still retain their chemical-sensitive character as seen in Fig. 1(a). The basic idea consists of proposing a distribution profile for the different elements. We calculate the corresponding diffracted intensity profile (I_{002}) under kinematic conditions and look for the composition profiles that fit best the experimental data. In order to avoid measuring absolute intensities, the scattered intensity of the layer is normalized to that of a reference layer with the same thickness, $R_{002} = I_{002}/I_{002\text{-ref}}$. The key issue here is the identification of the elemental distribution profile, where it has previously been demonstrated that the smooth variation of element concentration x with position z across the interface follows a sigmoidal law, $x(z) = x_0 / [1 + \exp(-z/L)]$, with the intrinsic interface width L as main fitting parameter, and where x_0 denotes the nominal mole fraction [E. Luna *et al.*, Phys. Rev. Lett. **109**, 126101 (2012)]. The parameter L quantifies the interface width and is proportional to the length W over which the concentration changes from 10%–90% of its plateau value, $W=4.4L$.

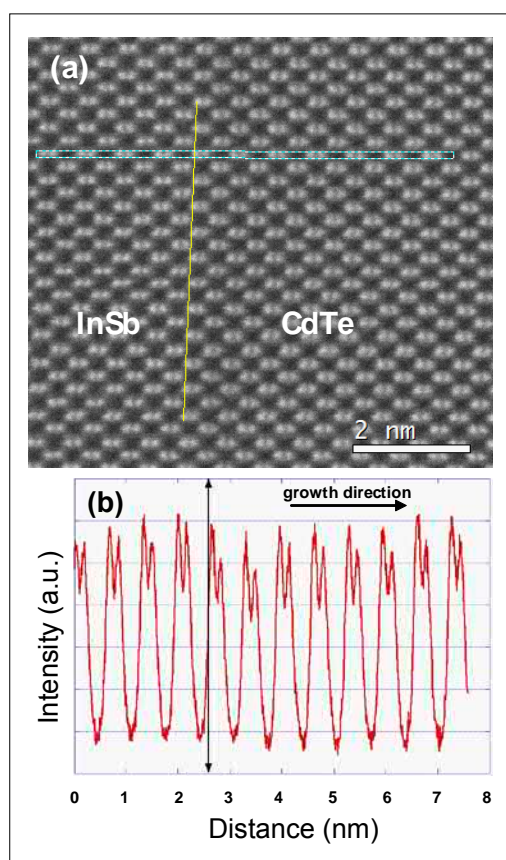


Fig. 2. (a) AC HAADF image. Vertical line indicates approximate interface position; (b) Intensity profile from HAADF image.

In the case of heterovalent NCA interfaces, several assumptions need to be made. The formation of quaternary $\text{In}_{1-x}\text{Sb}_{1-y}\text{Cd}_x\text{Te}_y$ alloys at the interface is postulated. Furthermore, it is assumed that the group-II element Cd would behave like a group-III element and bond with the group-V element Sb (leading to II-V bonds), where-

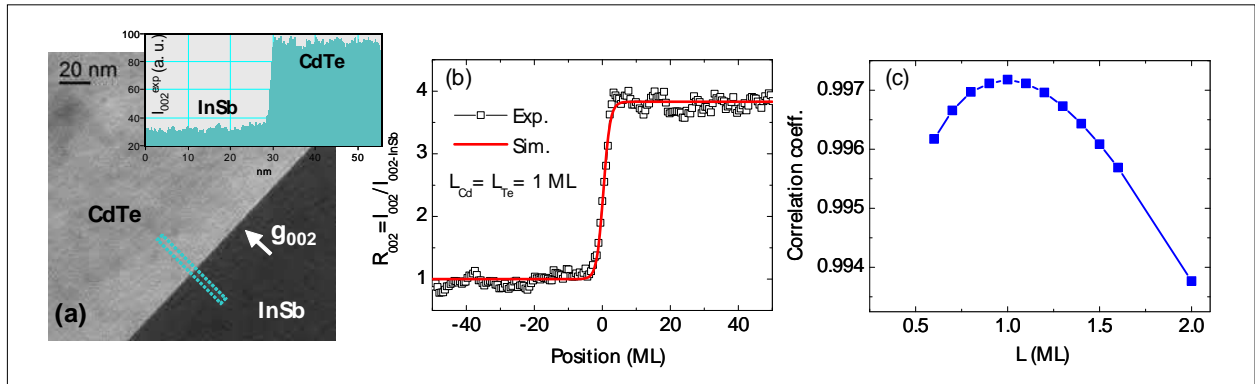


Fig. 3. (a) \mathbf{g}_{002} DFTEM image (inset: intensity line-scan used to evaluate R_{002}); (b) simulated R_{002} as the best fit to experimental data; (c) correlation coefficient as a function of interface width L .

as the group-VI element Te would behave like a group-V element and bond with the group-III element In (giving rise to III-VI bonds). Moreover, mean group-III-II atomic scattering factor $f_{\text{III-II}}$ and mean group-V-VI atomic scattering factor $f_{\text{V-VI}}$, are defined, and it is assumed that the elemental mixing follows a linear dependence so that $f_{\text{III-II}} = xf_{\text{II}} + (1-x)f_{\text{III}}$ and $f_{\text{V-VI}} = yf_{\text{VI}} + (1-y)f_{\text{V}}$. As for the isovalent NCA case, the realistic distributions for Cd and Te based on a sigmoidal function (those for In and Sb are based on $[\text{In}] + [\text{Cd}] = 100\%$ and $[\text{Sb}] + [\text{Te}] = 100\%$) are independently used in the calculation. The simulated diffracted intensity ratio is then calculated and compared with the experimental profile until the best fitting is reached.

Figure 3(a) displays a \mathbf{g}_{002} DFTEM micrograph, together with the intensity linescan used for the analysis. The remarkable good match between R_{002} and $R_{002-\text{exp}}$ corresponding to the best fit is obvious in the profile in Fig. 3(b) for $L_{\text{Cd}} = L_{\text{Te}}$. Further analysis indicates that the method can detect variations in the L parameter as small as 0.1 monolayers (ML). This feature is illustrated in Fig. 3(c) which displays the correlation coefficient between the simulated and experimental curves for a series of profiles where $L_{\text{Cd}} = L_{\text{Te}}$. The plot of the correlation coefficient vs. L clearly shows that the

interface width L can be unambiguously determined since there is a well-defined maximum and that variations in abruptness of the interface profile of only 0.1 ML are distinctly discernable. The intrinsic interface width $L = 1$ ML leading to 1.4 nm is on the same order as the chemical width estimated for the InAs/GaSb isovalent NCA system (1.3 nm) and is considerably smaller than the interfacial intermixing determined for other isovalent common-atom III-V hetero-interfaces, as for instance 2.1 nm for high quality (Al,Ga)As/GaAs interfaces. Meanwhile, the correspondence between the experimental results of (i) $L_{\text{Cd}} = L_{\text{Te}}$ and (ii) no seemingly detectable interface features in the HAADF or LABF images, would seem to suggest a well-balanced mixture of II-V and III-VI bonds at the interface rather than preferential formation of III-VI or II-V interfacial compounds.

Electron tomography measurement of III-V semiconductor interface roughness

L. Nicolai, K. Biermann, A. Trampert

The characterization of heterostructure interfaces plays a key role for the development of advanced semiconductor devices. In contrast to surfaces, where a variety of methods is available for the analysis of the surface topography and chemistry, the possibilities for the characterization of deeply buried interfaces are limited.

Transmission electron microscopy (TEM) is a frequently used tool for microstructural analysis of semiconductor heterostructures and interfaces. Unfortunately, TEM micrographs are projections which affect the interpretation of three-dimensional (3D) structures. A solution for this problem is the application of electron tomography which uses a series of projections from different angles to calculate a 3D reconstruction of the investigated object. This work describes a path to apply electron tomography for

the quantitative characterization of III-V semiconductor interface roughnesses.

The investigated sample is an (Al,Ga)As-based microcavity grown by molecular beam epitaxy providing a variety of interfaces. A tomography needle was prepared out of the volume material by employing a focused-ion beam microscope. The needle was mounted on a full-tilt tomography holder with the needle axis being almost parallel to the interface normal. A bright-field scanning transmission electron microscopy (BF-STEM) image of a part of the needle is shown in Fig.1(a). The first layers of the upper Bragg-reflector showed the highest contrast which consist of alternating $\text{Al}_{0.15}\text{Ga}_{0.85}\text{As}$ and $\text{Al}_{0.75}\text{Ga}_{0.25}\text{As}$ layers including an additional short period superstructure. Therefore, the focus for our interface study was laid upon the upper

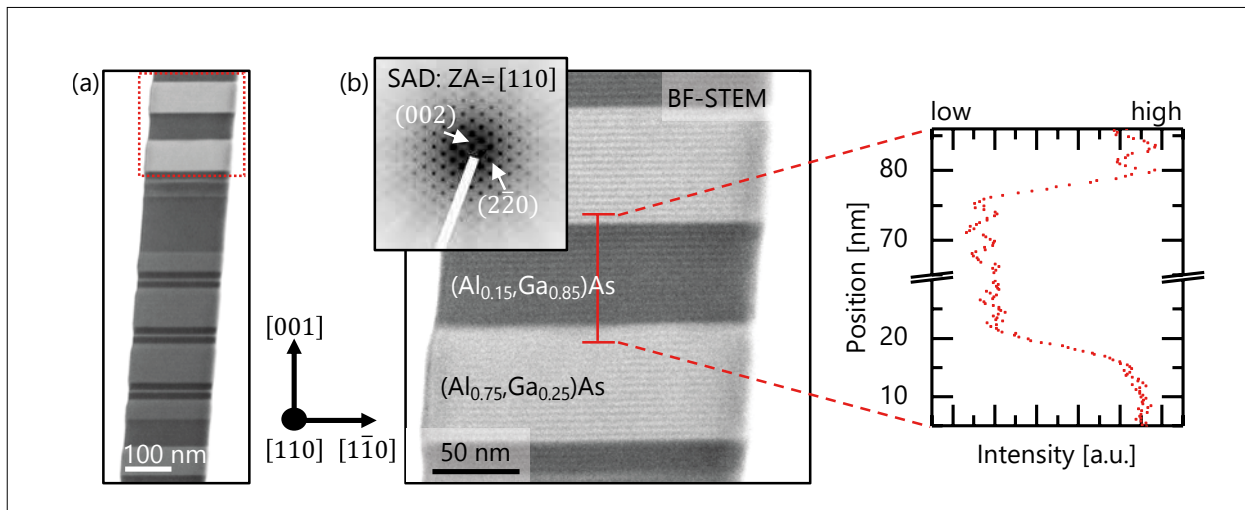


Fig. 1. (a) BF-STEM micrograph of the tomography needle showing the microcavity structure. (b) Higher magnified BF-STEM image of the first layers of the upper (Al,Ga)As Bragg-reflector [red square in (a)] taken along the [110] zone axis (ZA). The inset shows the corresponding selected area diffraction (SAD) pattern. Intensity profile across the interfaces (red line). The profile reveals an interface width of 5.2 nm for the $\text{Al}_{0.75}\text{Ga}_{0.25}\text{As}$ to $\text{Al}_{0.15}\text{Ga}_{0.85}\text{As}$ and 2.3 nm for the inverted interface using the 10%-to-90% criterion for intensity change.

Bragg-reflector structure. A higher magnified BF-STEM micrograph of this structure is shown in Fig.1(b).

Among other aspects, epitaxial semiconductor interfaces are generally described by their chemical width defined by the distance where the composition is changed between 10% and 90% of their plateau value. An intensity line profile across the interfaces is given in Fig.1(b) indicating a width of 5.2 nm for the $\text{Al}_{0.75}\text{Ga}_{0.25}\text{As}$ to the $\text{Al}_{0.15}\text{Ga}_{0.85}\text{As}$ interface in comparison to 2.3 nm for the inversed one. The relatively large width refers to either the presence of an extended chemical intermixing zone or to a topographic roughness of the interface. A simple projection, however, is not able to distinguish between both situations.

Electron tomography was applied to reveal the origin of the difference in the projected interface width. A series of 89 BF-STEM micrographs with 2° tilt-steps between each image was recorded covering a full 180° tilt range for optimal reconstruction conditions. Weighted back-projection and

simultaneous iterative reconstruction technique algorithms were used to obtain the 3D reconstructions. A peculiarity is the application of BF-STEM instead of the typically used high-angle annular dark-field (HAADF) mode. Under the present experimental conditions, the BF-STEM reveals, similar to the HAADF, a chemical sensitive contrast but with a higher detected intensity and therefore with increased signal-to-noise ratio offering the possibility to reduce the scan time and thus potential sample drift and irradiation damage.

Figure 2 presents different visualizations of the reconstructed volume. An overview of the reconstructed volume is displayed in Fig.2(a) reflecting the complex $(\text{Al},\text{Ga})\text{As}$ layer stack. In addition, a cross-sectional slice through the Bragg-reflector structure with an integration thickness of 6 nm is shown in Fig.2(b). This slice gives two essential insights. Firstly, the slice reveals a sharp chemical transition at the interfaces of less than 2 nm width. Secondly, a morphological modulation on the nm-scale is revealed defining a topographic roughness

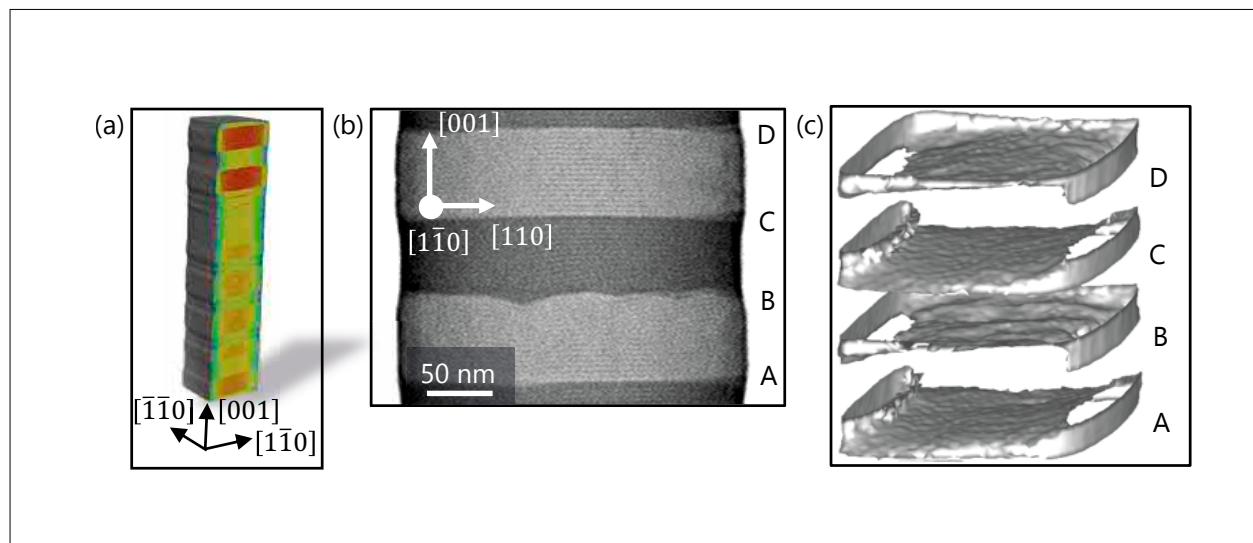


Fig. 2. (a) Visualization of the tomogram showing a cut through the reconstructed volume. (b) Crosssectional slice through the reconstruction with an integration thickness of 6nm showing the alternating $\text{Al}_{0.75}\text{Ga}_{0.25}\text{As}$ and $\text{Al}_{0.15}\text{Ga}_{0.85}\text{As}$ layers. The slice reveals a topographic roughness at the $(\text{Al},\text{Ga})\text{As}$ interfaces. (c) Isosurface representation of the four interfaces marked in (b).

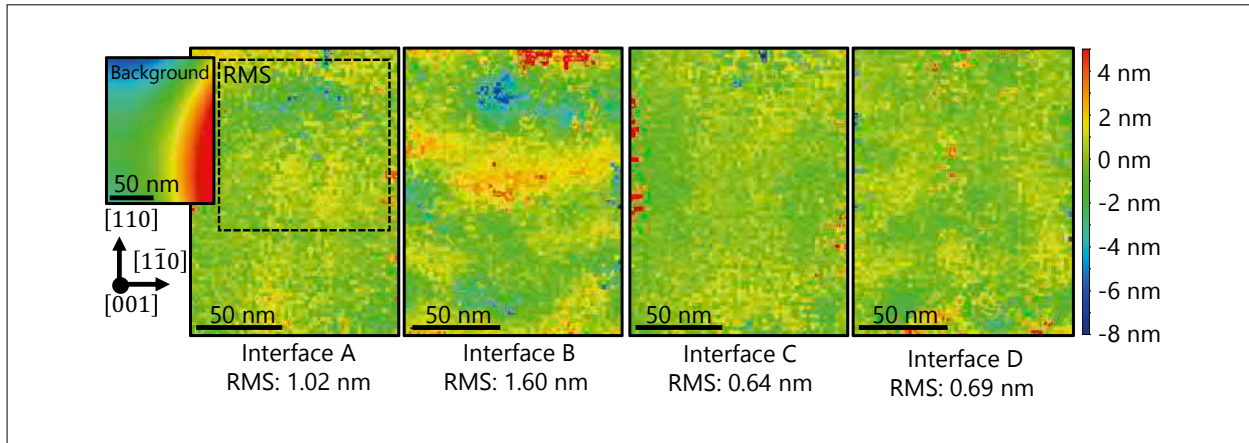


Fig. 3. Topographic maps of the four interfaces shown in Fig. 2(b) and (c). The RMS value for all four surfaces is calculated for a 100 nm x 100 nm area as indicated in map A (black dashed square). The inset of map A shows an exemplary background which was subtracted from the topographic map.

of the interface. Taking the growth direction into account, the interfaces from a Ga-rich to an Al-rich layer are marked as A and C whereas the inversed interfaces are labeled as B and D (cf. Fig.2).

The topographic information has to be extracted to quantitatively describe the interface roughness. For this purpose isosurfaces of the interfaces were calculated. These isosurfaces are presented in Fig.2(c) which already visualize qualitatively different levels of roughness. In a next step, the isosurfaces were exported as meshes. The intersection points of the meshes are described by x-, y- and z-coordinates, respectively. The free software Gwyddion, which is typically used for scanning probe microscopy analysis, was employed to transfer the 3D data set to a topographic map of the interface.

Figure 3 shows color-coded topographic maps of the interfaces marked A,B,C, and D according to the isosurface representation in Fig.2(c). The small inclination of the interfaces to the tilt-axis (cf. Fig.1) leads to a tilt of the isosurfaces. To counteract this problem, a background was subtracted from each topographic map given by a

two-dimensional polynomial of degree 2. An example for a background is shown for interface A as inset in Fig.3.

The root mean square (RMS) value for a 100 nm x 100 nm square (cf. dashed box in Fig. 3) was calculated for each interface. The RMS is defined by:

$$z_{\text{RMS}} = \sqrt{\frac{1}{N} \sum_{n=1}^N (z_n - \bar{z})^2} \quad (1)$$

The RMS value allows a quantitative comparison of the roughnesses of the four interfaces. The Al-rich to Ga-rich interfaces (B and D) have a higher roughness compared to the neighboring Ga-rich to Al-rich interfaces (A and C). The topographic maps of interfaces A and C indicate the presence of surface steps or terraces, whereas interfaces C and D reveal a rather isotropic waviness with characteristic length of several tens of nanometers. The roughness is overall decreasing along the growth direction. The results point to a difference in the migration process of the atoms on either Al-rich or Ga-rich layers and open up new perspectives to correlate buried interface roughnesses with growth processes.

Defect interaction as origin of step bunching in epitaxial III-V layers on vicinal Si(001) substrates

M. Niehle, L. Cerutti¹, J.-B. Rodriguez¹, E. Tournié¹, A. Trampert

The quest for the integration of optoelectronic III-V devices in the economic, mature silicon technology is lasting for decades. Therefore, the permanent demand to understand the formation, behaviour, and interaction of defects in the epitaxial III-V/Si heterostructures remains as prerequisite to control the microstructure prior to device realization. Advanced microscopy methods are indispensable for respective insights.

Here, the interplay of antiphase boundaries (APBs), threading dislocations (TDs) and vicinal Si(001) substrate surfaces is described as origin of the formation of several nanometer high surface steps. The observation of such steps and an asymmetry in the distribution of TDs by scanning/transmission electron microscopy (S/TEM) are demonstrated in the following. The interaction of APBs and TDs has recently been revealed by electron tomography (ET) [M. Niehle et al., Scripta Mater. **132**, 5 (2017)]. Vicinal Si(001) substrates are regarded that exhibit atomic scale steps to implement the small miscut angle between the substrate surface normal and the [001] direction. As a consequence of the tomographic insights and the complementing STEM results, a step bunching mechanism for the formation of interfacial and surface steps is proposed.

The micrographs in Fig. 1 show cross-sectional specimens of III-Sb layer stacks grown on Si(001) substrates. The upper two images in each column are chemically sensitive high-angle annular dark-field (HAADF) images acquired in STEM mode presenting an overview and a magnified part of the layers. The lower one is a high-resolution

TEM image. The columns from the left to the right correspond to specimens grown on nominally on-axis as well as on 3° and on 7° miscut Si(001) substrates. All images are oriented to have the projected [001] direction pointing upwards in order to underline the surface inclination with regard to low indexed crystallographic directions. The interface towards the substrate appears smooth as the atomic scale steps in the miscut samples are not resolved. In contrast, several nanometer high steps are observed at the sample surface as well as at the AlSb and at the (In,Ga)Sb interfaces as demonstrated in Figs. 1(d)-(i). These steps

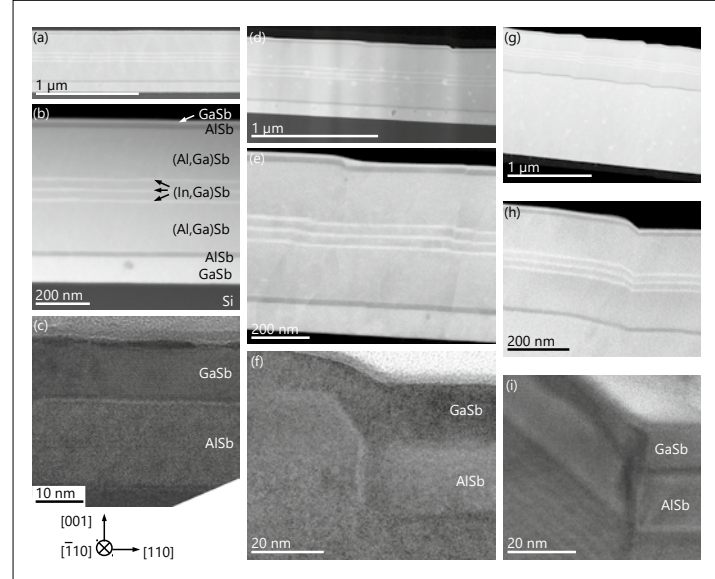


Fig. 1. III-Sb layers grown on Si(001) substrates with different miscut angles are imaged along the $\bar{[1}10]$ direction. The left column of images (a)-(c) represents the case of a nominal Si(001) substrate and the second (d)-(f) and the third one (g)-(i) the cases of 3° and 7° miscut, respectively. The upper two images in the columns are HAADF images. The lower one is a high-resolution TEM image.

¹ Université Montpellier 2 - CNRS, Institut d'Electronique du Sud (IES), Montpellier, France

are absent in antimonide layers on nominal Si(001) as shown in Fig. 1(a)-(c). The lattice resolved HRTEM images present the last epitaxially grown antimonide layers. In case of the miscut samples, the lattice images around a respective step are taken. The {111} facetting as suggested by Fig. 1(f) occurs only coincidentally. Tilted domains are excluded due to the continuous lattice planes. Steps predominantly run along the [110] direction as observations along the perpendicular [110] direction do not reveal respectively pronounced steps.

Figure 2 presents a bright-field STEM image of a cross-sectional specimen prepared from the sample grown on a 7° miscut Si(001) substrate. Lines of dark contrast features are observed threading through the stack of III-Sb layers which are chemically well discernible, too. The red line marks the projection of a (111) lattice plane onto the imaging plane. It is emphasized that the majority of extended dark lines runs parallel to this plane. These lines are attributed to the strain field according to the presence of TDs. The symmetry equivalent (111) planes are sparsely populated by respective features. A further peculiarity are lines that run nearly along the [001] direction and that coincide with the location

of the above described steps. Convergent beam electron diffraction experiments left and right of such features have proved the presence of APBs.

The presented results and the notion of extended defect interaction conveyed by previous ET investigations are illustrated in the schematics of Figs. 3(a) and (b). The observed asymmetry in the dislocation density is explained regarding the misfit relieving character of line defects forming 60°-dislocation segments at the substrate interface. According to the convention for Burgers vectors defined in Fig. 3(a), the dislocations have to obey the following relations in order to compensate the lattice mismatch along the [110] direction in the (001) interface plane as well as along the [001] direction due to the occurrence of substrate surface steps:

$$\frac{a}{2} [101] = \frac{a}{4} [110]_{\text{misfit}} + \frac{a}{2} [001]_{\text{misfit}} + \frac{a}{4} [\bar{1}\bar{1}0]_{\text{screw}}$$

$$\frac{a}{2} [011] = \frac{a}{4} [110]_{\text{misfit}} + \frac{a}{2} [001]_{\text{misfit}} + \frac{a}{4} [\bar{1}10]_{\text{screw}}$$

The other two dislocations on the (111) plane would counteract the misfit relief. Former ET investigations revealed the behaviour of

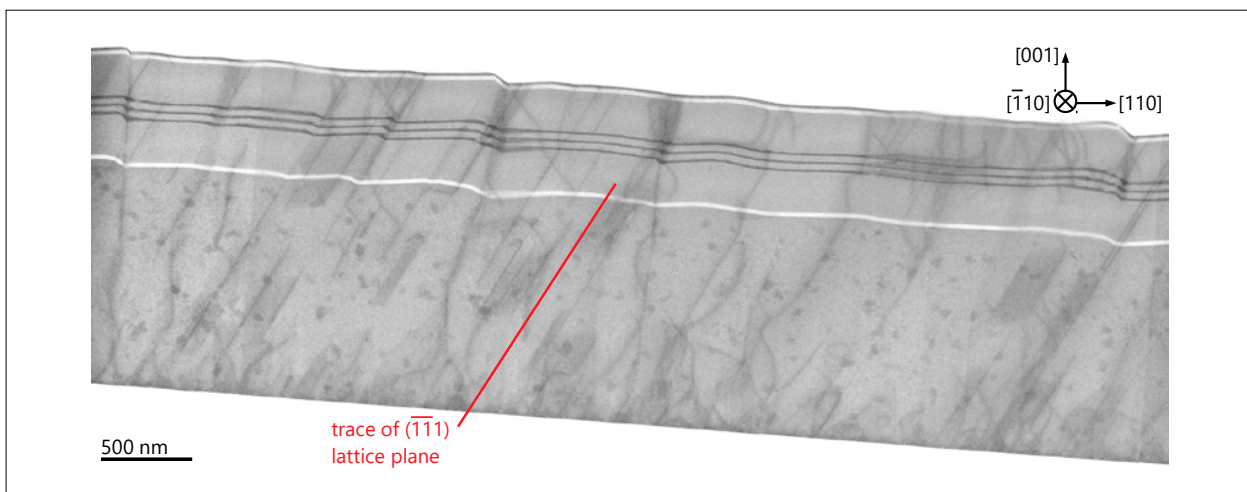


Fig. 2. The bright-field STEM image reveals microstructural defects as dark contrast features beside the material contrast of the antimonide layers in cross-sectional view.

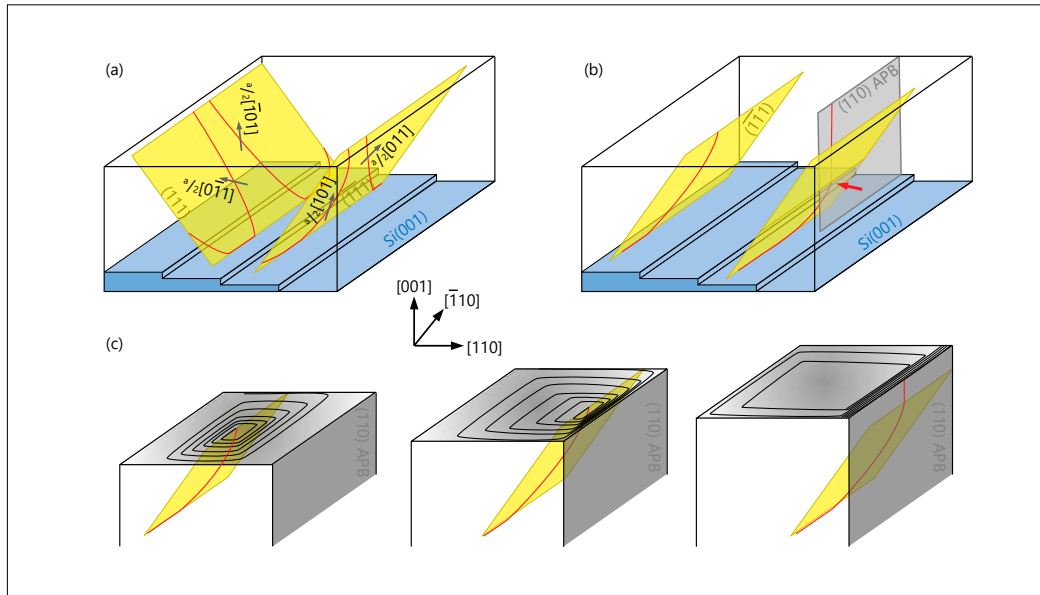


Fig. 3. (a) Perfect dislocations on the (111) and ($\bar{1}\bar{1}1$) glide planes that form 60° misfit dislocations at the interface toward the substrate, are exemplified with relevant Burgers vectors. (b) A dislocation bends away from its common glide plane at the intersection with an APB (red arrow). (c) The idea of step formation is depicted in the suite of schematics.

TDs when meeting an APB. Instead of following the ($\bar{1}\bar{1}1$) glide plane, the dislocation bends into the APB acquiring a direction close to the [001] orientation as depicted in Fig. 3(b).

The interaction of the observed extended defects leads to the proposal of the step bunching mechanism described by Fig. 3(c). A TD with a component of the line direction as well as of the Burgers vector perpendicular to the growth front entails the formation of a surface step as origin for a growth spiral. The TD runs on the ($\bar{1}\bar{1}1$) plane that is inclined to the growth front. Approaching an APB that intersects the surface, the propagation of steps from the spiral is assumed to be hampered because the extension of the APB is energetically less favoured than the single crystalline growth. Consequently, the steps accumulate near

the planar defect. Finally, the TD is trapped and a nanoscale step marks the position of the APB. The accumulation of further TDs in the APB leads to higher steps. Generally, these steps cannot be compensated by dislocations approaching the APB from the other side on (111) planes due to the asymmetry in the TD distribution.

Effectively, the vicinal surface with its steps due to the miscut is followed by the newly formed, several nanometer high steps. It has to be underlined that this accumulation or bunching is a consequence of an interaction of extended defects and not the result of the dynamics of diffusing atoms at the surface during growth as in the common notion of step bunching. Indeed, the effective annihilation of APBs within the buffer layer suppresses the development of the observed steps.

Luminescent centers in a few-layer h-BN film grown by molecular beam epitaxy

A. Hernández-Mínguez, J. Lähnemann, F. Iikawa, S. Nakhaie, J. M. J. Lopes, P. V. Santos

The controlled generation of single photons is a key factor for the development of quantum information technologies. Here, one of the most recent incorporations to the list of potential single-photon sources are luminescent defects in hexagonal boron nitride (h-BN). However, future applications of these quantum light centers will depend on the possibility of growing h-BN over large areas with high structural and morphological quality and of controlling the spatial distribution and luminescent properties of the defects within the h-BN film.

Among the various approaches to synthesize h-BN, molecular beam epitaxy (MBE) is very promising as it allows the formation of h-BN on different substrates with precise control over the growth conditions. In this contribution, we study luminescent centers in a few-layer-thick h-BN film grown on Ni

by MBE [S. Nakhaie *et al.*, *Appl. Phys. Lett.* **106**, 213108 (2015)]. The average thickness of the h-BN film is one nanometer, i.e. about three monolayers. After formation of the h-BN film, we transferred an area of $4 \times 4 \text{ mm}^2$ from the growth template onto a SiO_2/Si wafer and investigated its light emission properties by means of spatially resolved electron beam and laser excitation.

Figure 1(a) displays a scanning electron micrograph of the transferred h-BN film. The image shows triangular islands randomly distributed over the surface of the sample. The islands were observed across all regions of the studied h-BN film, thus indicating that they were homogeneously generated during the MBE growth. The islands are a few layers thicker than their surroundings and are anticipated to form around the h-BN nucleation centers. Figure 1(b) dis-

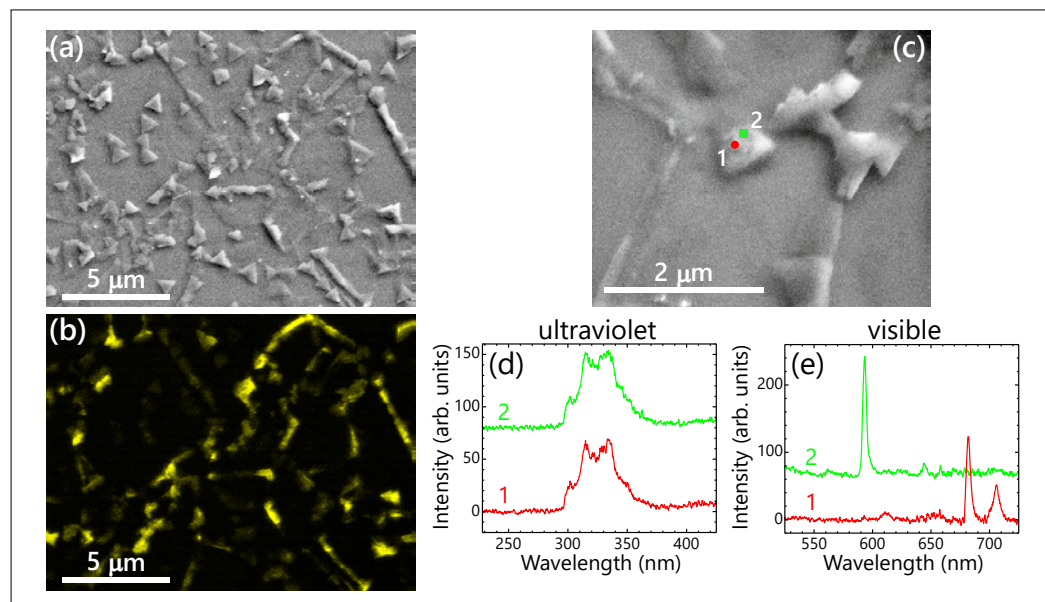


Fig. 1. (a) Scanning electron micrograph of a region of the h-BN film and (b) panchromatic CL map of the same region. (c) Scanning electron micrograph of one of the islands where spatially resolved CL spectra were recorded. (d) Ultraviolet spectra measured at points 1 and 2 marked as a red circle and a green square in (c). (e) Visible spectra for the same points as in (d).

plays a panchromatic cathodoluminescence (CL) map of the same area as in Fig. 1(a). Note that the CL spectrum originates from the islands rather than from the flat areas of the h-BN film.

Spectrally resolved measurements show that the CL spectrum is dominated by centers emitting in the ultraviolet (UV) and in the visible wavelength regions. We have collected two-dimensional CL maps at step sizes of 20 nm for both spectral regions. Figure 1(c) displays a surface electron micrograph of one of the islands studied, while Figs. 1(d) and 1(e) compare the UV and visible CL spectra taken at two different points of the island marked as a red circle and a green square in Fig. 1(c). Both UV spectra are essentially identical, thus indicating that the UV spectrum is fairly homogeneous within the island. A similar spectrum has been reported for single-photon sources in chemically exfoliated h-BN flakes and tentatively attributed to defects consisting of substitutional C atoms, thus suggesting that C impurities could be present in our h-BN film. In contrast to the UV luminescence, the spectra of the light emitted in the visible depend on the position of the electron beam within the island, indicating that they arise from different kinds of defect centers.

To characterize the centers emitting in the visible range in detail, we have studied their luminescence properties using a linearly polarized laser beam (532 nm) for optical excitation. Figure 2 displays the low-temperature (6 K) photoluminescence (PL) spectra of two of these centers (labeled as A and B). The spectrum of center A consists of a sharp zero-phonon line (ZPL) at 572.5 nm together with a broad phonon sideband (PSB) around 625 nm. The spectral characteristics of this center are very similar to those of single-photon emitters that have been tentatively associated with the anti-site complex N_BV_N . In contrast, the PL spectrum of center B consists of a ZPL at 619 nm and much weaker traces of a PSB,

which indicates a weaker coupling to the vibrations of the h-BN lattice. The inset of Fig. 2 displays the photon autocorrelation histogram, $g^{(2)}$, recorded for this center. It shows clear antibunching at zero time delay, thus demonstrating the non-classical nature of the emitted light.

Additional information about the nature of the defects was obtained by analyzing the dependence of their PL intensity on the polarization angle of the exciting laser. Figure 3(a) displays the spectrum of the ZPL of a defect emitting at the same wavelength as center A for two perpendicular polarization directions of the laser. The inset displays the intensity of the ZPL for a full rotation of the laser polarization. The data show two clear maxima and minima and are well fitted by a $\sin^2(\theta)$ function. These results are in agreement with electronic transitions governed by an optical dipole aligned along the symmetry axis of the defect.

Figure 3(b) displays the laser polarization dependence of center B. A close ex-

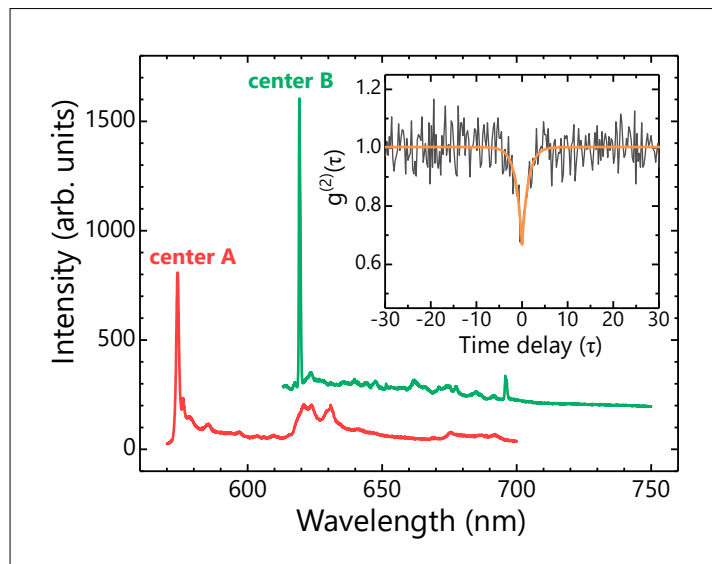


Fig. 2. PL spectra of two centers measured at different points of the h-BN film. The curves are vertically shifted for clarity. The inset displays $g^{(2)}$ of center B. The solid curve is a fit to the data.

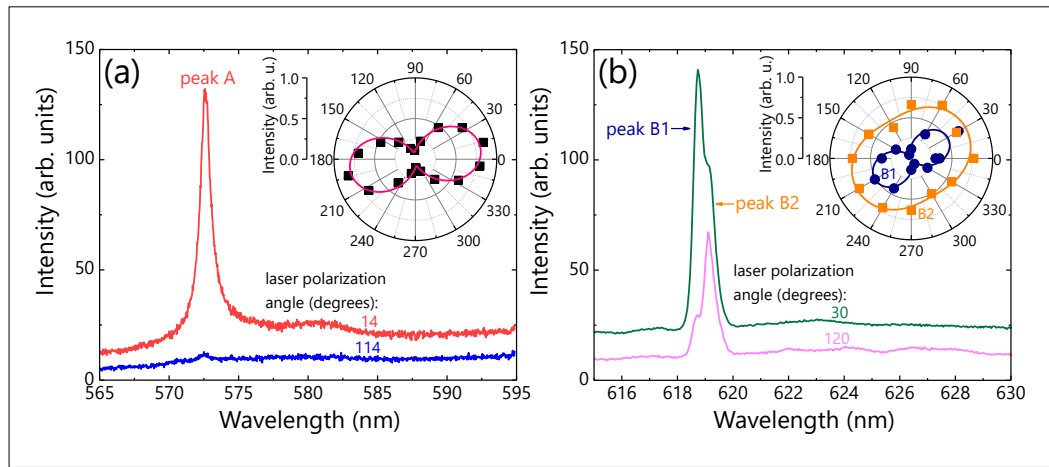


Fig. 3. (a) PL spectrum of a defect emitting at the same wavelength as center A measured for two perpendicular polarization directions of the laser. The inset displays the PL intensity for a full rotation of the laser polarization. (b) Same as panel (a), but for center B. In this case, the ZPL consists of two peaks, B1 and B2. The solid curves in both insets are fits to the data.

amination of the ZPL reveals that it does not consist of one, but of two peaks with a wavelength separation of about 0.4 nm. Interestingly, each peak exhibits a different dependence on the laser polarization angle [cf. inset of Fig. 3(b)]. While the peak denoted as B1 shows a similar dipolar behavior as defect A, the polarization dependence of the peak denoted as B2 is much weaker. These results suggest a different crystallographic nature for this center than for center A. Possible candidates could be defects containing C or O atoms [A. Sajid et al., Phys. Rev. B **97**, 064101 (2018)].

After demonstration of quantum light emission in MBE-grown h-BN films, the next step consists in addressing the on-demand control of the light emission properties. To this end, preliminary measurements in commercially available h-BN flakes deposited on a piezoelectric substrate have demonstrated that surface acoustic waves can modulate the ZPL of such defects. Therefore, future work will focus on incorporating h-BN films grown by MBE into structures suitable for the generation and propagation of surface acoustic waves.

Tunneling blockade and single-photon emission in GaAs double quantum wells

M. Yuan, A. Hernández-Mínguez, K. Biermann, P. V. Santos

The interplay between resonant tunneling and inter-particle interactions in low-dimensional quantum systems gives rise to interesting phenomena in the transport of single particles. While electron blockade has been extensively studied [M. A. Kastner, Rev. Mod. Phys. **64**, 849 (1992)], blockade of excitons has been scarcely reported. Due to natural interface of the excitons with light, transport blockade of excitons can reveal more intricate physics and lead to photonic device functionalities. Here, we report on a blockade phenomenon during the transport of exciton-related species across a thin tunnel barrier between two semiconductor quantum wells (QWs). We further show that in the blockade regime single, impurity-bound exciton states can be selectively excited and act as single-photon emitters.

The GaAs/(Al,Ga)As QW structure shown in Fig. 1(a) is grown by molecular-beam epitaxy. Each QW supports intra-QW neutral excitons (denoted here as direct excitons, DXs) as well as intra-QW charged excitons (trions). A transverse electric field F_z across the double QW (DQW) is generated by a bias voltage V_b applied between a semi-transparent top Ti contact and the n -doped substrate. F_z controls the tunneling probability and enables the creation of spatially indirect, inter-QW excitons (IXs) consisting of electrons and holes resident in different QWs [cf. Fig. 1(b)]. The IX energy is tunable by F_z due to the quantum-confined Stark effect (QCSE). We performed microscopic photoluminescence (PL) studies at 4.2 K excited by a laser with a wavelength of 780 nm.

We observe a blockade of the IX formation in the PL spectra of the DQW recorded at low optical excitation. Figure 2(a) displays

the bias dependence of the PL intensity I_{PL} recorded by exciting a small area of the Ti top contact with a focused laser beam and collecting the emission from the same area. The map shows the spectral lines from DX, IX, and trion. Strikingly, the IX line does not smoothly “branch off” from the DX and trion lines, but only appears for $V_b < 0.25$ V, thus indicating that its formation is blocked within a bias range near the flat band condition. The blockade results in a spectral gap between the trion and the onset of the IX emission, $\delta E_B = 5.7$ meV. Furthermore, the IX appearance at $V_b \sim 0.29$ V is accompanied by a drastic reduction of the trion intensity, which indicates that the IXs result from the dissociation of the trion states. Within the blockade regime with suppressed IX emission, sharp individual emission lines appear, such as the ones labeled as D_1 and D_2 in Fig. 2(a). These lines arise from single excitons bound to localized shallow impurities, which are excited via a resonant process.

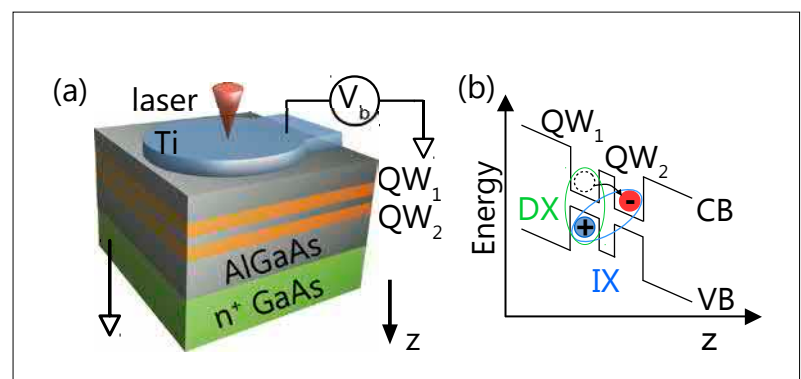


Fig. 1. (a) GaAs/(Al,Ga)As double quantum well (DQW) structure on a doped GaAs (001) substrate. (b) Energy band diagram of the DQW showing the conduction (CB) and valence bands (VB) profiles under an electric field, showing the direct (DX) and indirect exciton (IX) states.

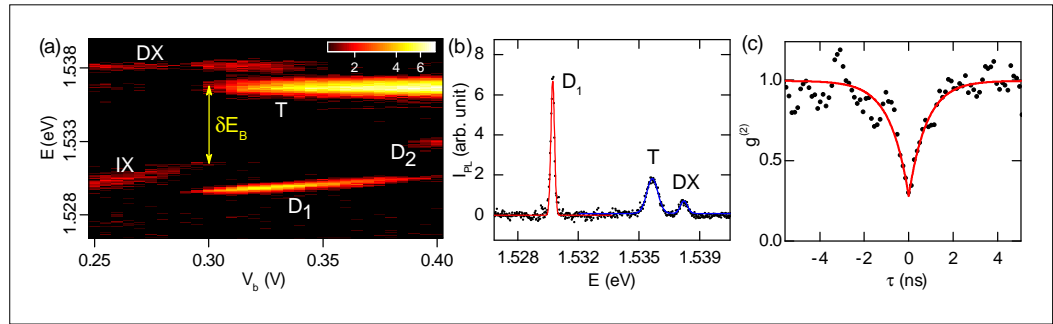


Fig. 2. (a) Photoluminescence (PL) spectral map as a function of V_b (cf. Fig. 1) showing the IX blockade δE_B range as well as impurity-bound exciton lines D_1 and D_2 (T denotes the trion). (b) PL spectrum (background subtracted) at the location of D_1 (symbols). The superimposed lines are Gaussian fits to the indicated resonances. (c) Photon auto-correlation $g^{(2)}$ recorded for D_1 . The background contribution has been corrected. The single-photon nature is confirmed by the observation of $g^{(2)}(0) < 0.5$.

The appearance of bound exciton and IX lines results from the dissociation of the trion, governed by energy conservation. A trion dissociates via the emission of a free carrier in the same QW and the tunneling of the extra electron to form an IX. The free carrier has a higher energy than the trion. IX formation will thus be blocked within an energy range below the trion energy, where the IX energy is not low enough to compensate for the extra energy required for the excitation of a free carrier.

The energy conservation constraint stabilizes trions and opens a gap in the emission spectrum of free IX species. Within the gap, trions can still be resonantly converted into lower energy excitons bound to an impurity, resulting in the activation of the bound excitons. We have studied the properties of these bound exciton states. The shallow impurity centers are typically between 2 to 4 μm apart, thus yielding an areal density $n_d \approx 10^7 \text{ cm}^{-2}$. Figure 2(b) displays the spectral profiles for the D_1 , trion, and DX resonances. The line shape of the bound exciton D_1 is significantly narrower than the ones for free excitons DX and the trion.

Finally, we have investigated the potential of the bound excitons as single-photon emitters. In order to confirm the single-photon

nature of the emission, we measured the second-order auto-correlation function $g^{(2)}(\tau)$ of D_1 using a Hanbury-Brown and Twiss setup. The $g^{(2)}$ histogram in Fig. 2(c) shows the characteristic dip at zero delay $\tau = 0$, signaling photon anti-bunching. The solid line is a fit to delay time dependence of the form $g^{(2)}(\tau) = 1 - (1/N_p) \exp(-|\tau|/\tau_R)$. The fit yields an average number of simultaneously emitted photons at zero delay $N_p < 2$, thus confirming the single-photon nature of the emission. The fitted decay time $\tau_R = 0.8 \text{ ns}$ is comparable with the values measured for self-assembled InAs/GaAs quantum dots [V. Zwiller *et al.*, *Appl. Phys. Lett.* **78**, 4276 (2001)].

In conclusion, we have reported the selective excitation of single excitons bound to shallow impurity centers via resonant tunneling in GaAs DQW structures. The selective excitation of these centers becomes possible because of the blockade of carrier tunneling to form intrinsic exciton states over a range of applied electric fields. Single-photon emitters based on shallow centers benefit from the well-developed semiconductor processing techniques. A major advantage of these centers is the much narrower distribution of emission energies as compared to, for instance, single-photon sources based on self-assembled quantum

dots. In the future, they can also be manipulated by surface acoustic waves to realize remote activation as well as high-frequency operation. Therefore, the shallow centers in GaAs DQWs are promising single-photon emitters with both optical and electrical controls.

Modulation of confined polariton condensates by high-frequency acoustic waves

A. S. Kuznetsov, K. Biermann, P. V. Santos

We investigate the modulation of exciton-polariton states (polaritons) confined in few- μm -sized intra-cavity traps in an (Al,Ga)As microcavity by high-frequency surface acoustic waves (SAWs). Microcavity polaritons are bosonic quasi-particles resulting from the strong coupling between photons and quantum well excitons. The very low effective mass of polaritons (typically on the order of 10^{-5} – 10^{-4} of the free

electron mass) enables their confinement in μm -sized potential traps created by structuring the microcavity.

Beyond fundamental interest, polaritons have been suggested for non-linear optical devices as well as for achieving quantum functionalities in an all-semiconductor platform such as qubits, topological circuits, and quantum simulators. These applications require confinement potentials to control the energy and density of the neutral polariton particles.

Different approaches have been utilized to create single traps with confined polariton states as well as lattices of interacting polariton traps with a well-defined band structure. In most of the cases, these structures are created by patterning the microcavity using a lithographic process to tailor the photonic or excitonic components of polaritons [A. S. Kuznetsov *et al.*, Phys. Rev. B **97**, 195309 (2018)]. These structures are normally static in the sense that they are defined during the fabrication process and cannot be changed afterwards. Dynamic potentials and lattices for polaritons can be generated by exploring non-linear optic effects induced by spatially modulated light beams or by a spatially dependent strain field of MHz SAWs [E. Cerdá-Méndez *et al.*, Phys. Rev. Lett. **105**, 116402 (2010)]. Such tunable potentials enable the control of the interaction between neighboring lattices sites. One important advantage of the acoustic fields over the optical ones is the fact that the potential amplitude can be tuned independently from the polariton density, thus making it possible to form traps down to the single-polariton level.

In the present work, we demonstrate that the static potential for polaritons can be

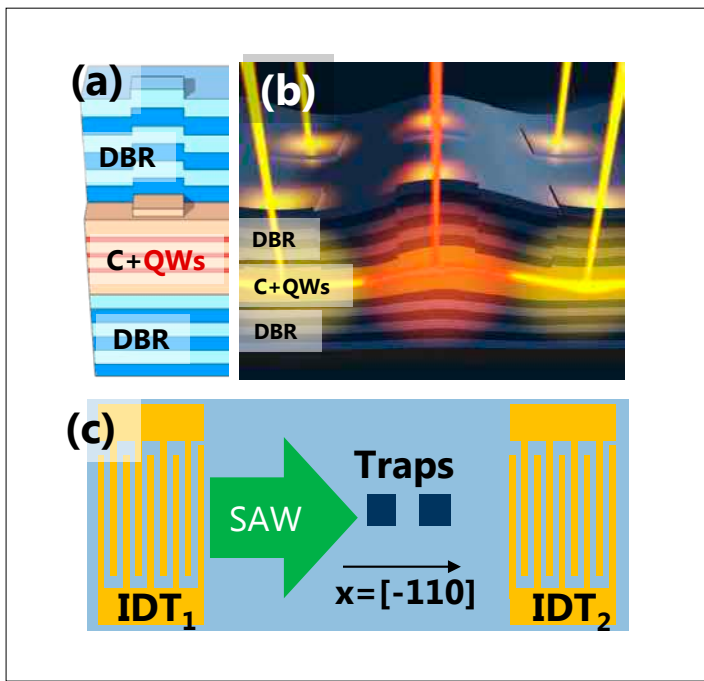


Fig. 1. (a) Schematics of an intra-cavity trap in a patterned polariton (Al,Ga)As microcavity investigated in this work. The cavity active region (C), containing GaAs QWs, was patterned to create mesas of different shapes. (b) A sketch of the microcavity with intra-cavity traps modulated by a SAW. The SAW induces a periodic modulation of the emission energies (colored beams) of the trapped polaritons. The effect is exaggerated. (c) Top-view of the microcavity region showing the SAW resonator defined by two interdigital transducers (IDTs) and polariton traps in between. The SAW with a wavelength of $8 \mu\text{m}$ is generated along the $[\bar{1}10]$ direction by IDT₁ (green arrow) and back-reflected by IDT₂.

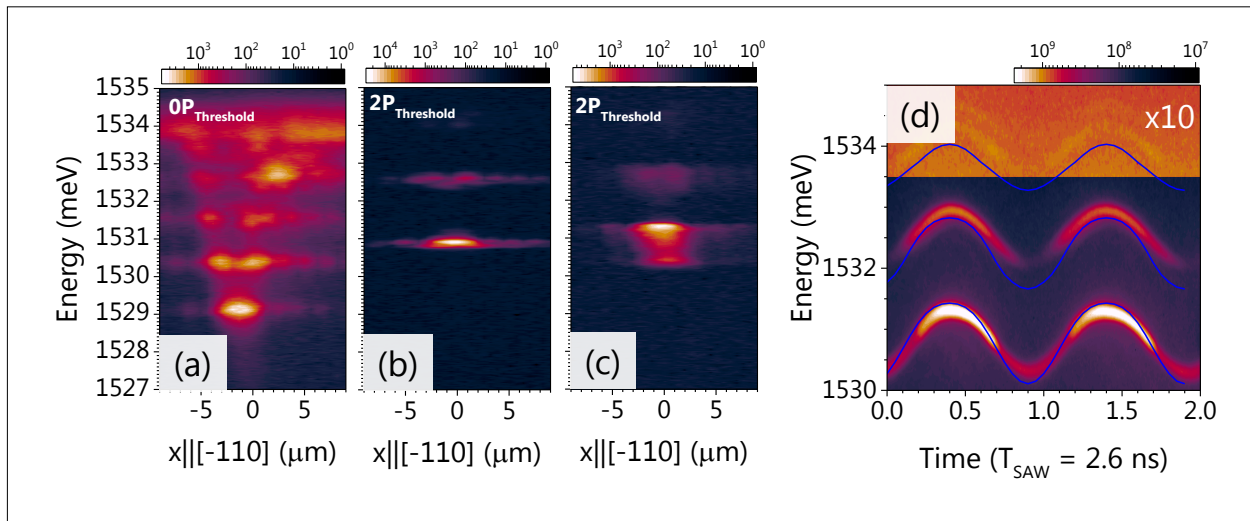


Fig. 2. Time-integrated spatial spectra of the $4 \times 4 \mu\text{m}^2$ trap: (a) below the condensation threshold without SAW, (b) twice the condensation threshold without SAW, and (c) twice the condensation threshold with SAW. (d) Time trace of the trap emission at conditions corresponding to (c).

combined with the dynamic modulation by SAW fields to provide an active control of the energy and, potentially, interactions between confined polariton states. The investigations were carried out using μm -sized intra-cavity traps for polaritons defined by structuring an (Al,Ga)As microcavity in-between two molecular beam epitaxial growth runs. The traps were produced by laterally structuring the thickness of the microcavity spacer in-between the distributed Bragg reflectors (DBR) in order to create a lateral modulation of the photonic resonance energy as shown in Fig. 1(a). The intra-cavity traps have a potential depth of about 5 meV, which is appropriate for polariton confinement.

Figure 1(b) schematically shows (in an exaggerated fashion) the effect of a SAW on a microcavity with mesa traps. The SAW propagation is confined to the surface of the microcavity. The modulation of the quantum wells (QWs) is possible due to the evanescent strain of the SAW, which penetrates the cavity to the depth of approximately one SAW wavelength. The main mechanism of the modulation is the strain-induced change of the bandgap of

the QWs, resulting in the modulation of the QW exciton energy. The modification of the photon energy, due to the strain-induced changes of the spacer thickness and refractive index, is less than 30% of the total modulation. Figure 1(c) shows a schematic top-view of the studied cavity area. A polariton trap is located between two interdigitated transducers (IDTs). The radio frequency signal is supplied only to IDT₁, which generates a SAW in the 381 MHz to 386 MHz frequency range. The opposing IDT₂ acts as a reflector, thus leading to a standing SAW.

Time-integrated spatial photoluminescence (PL) spectra of a $4 \times 4 \mu\text{m}^2$ trap below the condensation threshold (low polariton density) and twice the condensation threshold (high polariton density, which leads to Bose-Einstein-like condensation) without SAW, and twice the threshold with SAW are shown in Figs. 2(a), 2(b), and 2(c), respectively. In the polariton condensation regime at high optical excitation densities, the strain-induced energy shifts are approximately 10 times larger than the resolution-limited spectral linewidth of the condensate [cf. Fig. 2(c)]. Figure 2(d) shows a

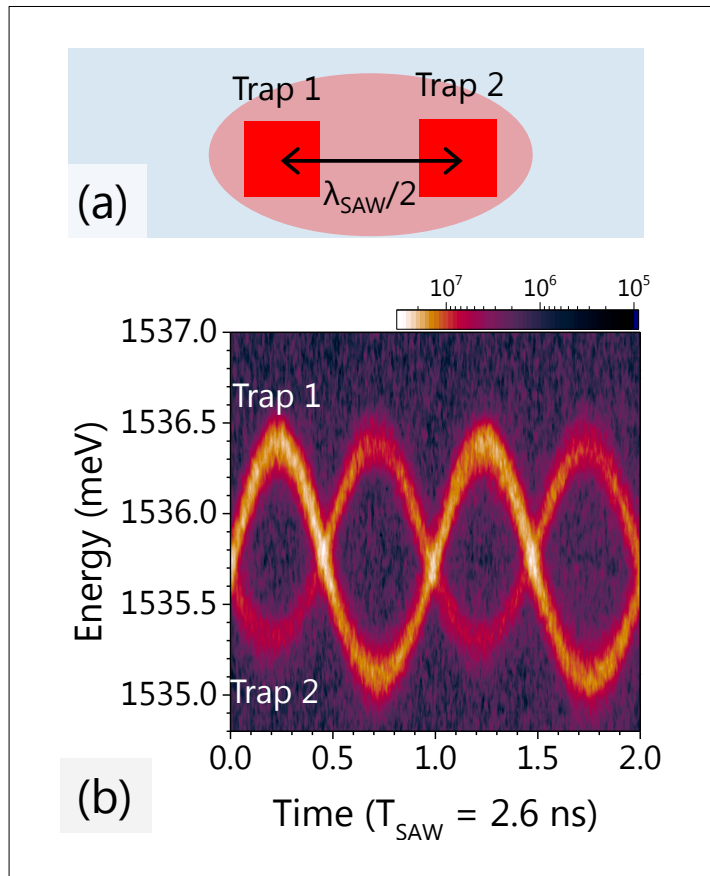


Fig. 3. (a) Two traps (red squares) separated by half of the SAW wavelength. The ellipse represents exciting laser spot. (b) Time traces of the PL of the two neighboring traps corresponding to the geometry as shown in (a).

well-defined in-phase sinusoidal modulation of the energy levels of the trapped condensates at the SAW frequency.

The strain of the standing SAW modulates the static trap as the whole, since the trap size is smaller than the SAW wavelength (8 μm). Note the periodic blinking of the PL intensity in Fig. 2(d). This may result from the piezo-electric character of the SAW along the $\bar{[1}10]$ direction in GaAs. Our model based on the Gross-Pitaevskii equation and the realistic potential shape of the trap (obtained from atomic force microscopy measurements) accurately reproduces the time evolution of the energies of the condensates, represented by solid blue lines in Fig. 2(d).

The spatial dependence of the SAW field can be used to dynamically tune the emission energies of the neighboring traps. In particular, $1.6 \times 1.6 \mu\text{m}^2$ traps separated by half of the acoustic wavelength schematically shown in Fig. 3(a) can be periodically brought in and out of the resonance at the acoustic frequency as displayed in Fig. 3(b). The demonstrated effect may be used to modulate on-site energies and the inter-site coupling of polariton states in arrays of static intra-cavity traps for applications such as lasers as well as topological and simulation devices based on polaritons. These results open the way to polariton devices based on lattices of confined polaritons dynamically tunable by SAWs.

The work was supported by the Deutsche Forschungsgemeinschaft in the framework of the project No. 359162958.

Quantum rings in III-V semiconductor nanowires

P. Corfdir, T. Flissikowski, M. R. Molas¹, R. B. Lewis, G. Gao, A. Trampert, U. Jahn,
M. Ramsteiner, J. K. Zettler, D. van Treeck, C. Sinito, O. Marquardt², H. Li³,
S. Fernández-Garrido, C. Draxl³, M. Potemski¹, V. M. Fomin⁴, L. Geelhaar, H. T. Grahn, O. Brandt

III-V semiconductor nanowires frequently exhibit various planar (two-dimensional) structural defects, such as inversion domain boundaries (IDB*s), twin boundaries (TBs), and different types of basal plane stacking faults (I_1 and I_2 BSFs). All of these defects can be understood as a local alteration of the crystal polytype or phase. The resulting crystal-phase heterostructures offer unique advantages over conventional compositional heterostructures. In particular, their internal interfaces are, by definition, coherent and atomically abrupt, and compositional fluctuations are nonexistent. Due to the resulting absence of scattering, the radiative decay rate of excitons bound to I_1 BSFs [(I_1,X)] has been found to be enhanced by its coherent macroscopic polarization, a phase coherence effect theoretically predicted, but rarely observed experimentally.

In this work, we first show that the simultaneous presence of IDB*s and BSFs in GaN nanowires can lead to the formation of one-dimensional crystal-phase quantum wires or rings with an exciton binding energy as high as 67 meV. Inspired by this finding, we next demonstrate the controlled fabrication of nearly ideal quantum rings by combining all-binary GaAs/AlAs radial compositional heterostructures with axial crystal-phase quantum structures provided by spontaneously occurring TBs. Doping of the core allows us to accurately tune the radial polarization of the quantum ring exciton

and thus enables the observation of the excitonic Aharonov-Bohm effect in rings with a circumference as large as 200 nm.

Figure 1(a) shows photoluminescence (PL) spectra taken on ensembles of GaN nanowires at 10 K. The near-bandedge (NBE) transitions between 3.47 and 3.48 eV arise from donor-bound as well as free excitons. The transitions at 3.449 and 3.455 eV stem from localized and free (IDB^*,X) complexes, respectively, while the bands at 3.41 and 3.32 eV are related to exciton recombination at I_1 and I_2 BSFs, respectively. An additional doublet (labeled Y_4), with low- and high-energy components at 3.3535 and 3.3660 eV, respectively, also develops with increasing substrate temperature. Note that this so far unidentified doublet is particularly intense in nanowire samples with prominent (IDB^*,X) and (I_1,X) bands.

Figure 1(b) shows the temperature (T) dependence of the radiative lifetime τ_r (which varies as $T^{n/2}$ for an n -dimensional exciton) determined by time-resolved PL experiments for the NBE and the (IDB^*,X), (I_1,X), and Y_4 lines. In all cases, τ_r is essentially constant at 5–15 K, reflecting the zero-dimensional character of the emitter as expected for donor-bound exciton transitions in the bulk (NBE) or for donors in the vicinity of the corresponding structural defect. For temperatures higher than 20 K, τ_r increases due to the thermally activated dissoci-

¹ Laboratoire National des Champs Magnétiques Intenses, CNRS-UGA-UPS-INSA-EMFL, 25, Rue des Martyrs, 38042 Grenoble, France

² Weierstraß-Institut für Angewandte Analysis und Stochastik, Leibniz-Institut im Forschungsverbund Berlin e.V., Mohrenstraße 39, 10117 Berlin, Germany

³ Institut für Physik and IRIS Adlershof, Humboldt-Universität zu Berlin, Zum Großen Windkanal 6, 12489 Berlin, Germany

⁴ Institute for Integrative Nanosciences, Leibniz-Institut für Festkörper- und Werkstoffforschung, Helmholtzstraße 20, 01069 Dresden, Germany

ation of the bound exciton. The increase is proportional to $T^{3/2}$ for the NBE as expected for the three-dimensional A excitons (X_A) in nanowires with a diameter of 50 nm and linear for IDB*’s and I_1 BSFs, confirming that these planar defects both act as quantum wells. The increase in τ_r for the Y_4 line, however, follows a $T^{1/2}$ dependence between 10 and 40 K, demonstrating that the excitons giving rise to the Y_4 doublet have a *one-dimensional* character. Indeed, the inset of Fig. 1(b) shows that IDB*’s and I_1 BSFs do coexist in single nanowires, forming one-dimensional quantum rings due to the tubular nature of the IDB*’s.

To estimate the binding energy (E_B) of excitons bound to I_1 BSF/IDB* quantum wires, we measure the diamagnetic shift of the excitonic transitions in a magnetic field for the nanowire ensemble grown at a substrate temperature of 865 °C. Figure 1(c)

shows the blueshift observed for the X_A line and the high-energy component of the Y_4 doublet (corresponding to the free, nonlocalized quantum wire exciton) as a function of the external magnetic field. The inset displays spectra of the high-energy line of the Y_4 doublet for different magnetic fields. Fits of the data with the theoretical expression for the diamagnetic shift yield a value of $E_B = 24.3$ meV for the X_A transition, in reasonable agreement with the exciton binding energy of 26 meV for bulk GaN. For the Y_4 line at 3.366 eV, a much smaller diamagnetic shift is observed, corresponding to a value of $E_B = 67.5$ meV for the I_1 BSF/IDB* quantum wire exciton.

For the intentional fabrication of quantum rings in nanowires, we turn to GaAs-based nanowires as schematically depicted in Fig. 2(a). The all-binary GaAs/AlAs radial quantum well structure is realized by syn-

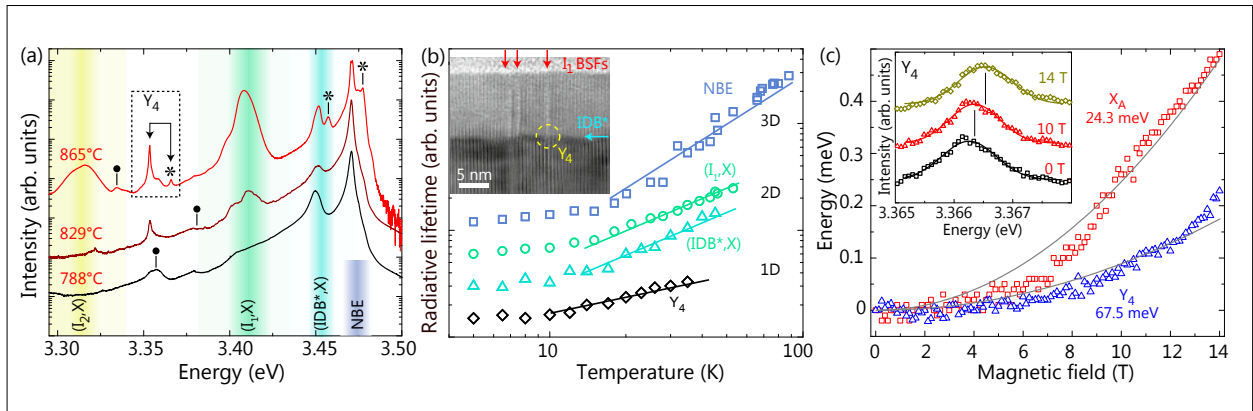


Fig.1. (a) PL spectra taken at 10 K on GaN nanowire ensembles grown at different substrate temperatures. The spectra have been shifted vertically for clarity. The energy ranges for the near band edge (NBE), (IDB^*,X), (I_1,X), and (I_2,X) transitions are highlighted using different colors. The transitions labeled with a • are phonon replicas, while those pointed out with a * arise from free excitons. (b) Temperature dependence of the radiative lifetime of the NBE (squares), (I_1,X) (circles), (IDB^*,X) (triangles), and Y_4 transitions (diamonds). The solid lines show the dependence expected for three-, two-, and one-dimensional excitons. The inset shows a high-resolution transmission electron micrograph of a single nanowire with I_1 BSFs (arrows) intersecting an IDB^* . (c) Diamagnetic shift of the free exciton (squares) and the high-energy component of the Y_4 transition (triangles) at 4 K for the sample grown at a substrate temperature of 865 °C. The lines are the result of fits returning the exciton binding energy as indicated in the figure. Inset: High-energy component of the Y_4 PL doublet at 4 K and at magnetic fields of 0, 10, and 14 T. The spectra have been shifted vertically for clarity. The vertical lines are guides to the eye.

thesizing core-multishell nanowires. Under the specific growth conditions chosen in this work, the GaAs nanowire core forms in the zincblende structure, but undergoes spontaneous rotational twinning during its axial growth as seen in the secondary electron micrograph depicted in Fig. 2(b). Since the twin boundary extends into the shells during radial growth and thus intersects the GaAs shell quantum well, a quantum ring forms at the intersection [Fig. 2(a)]. The plan-view transmission electron micrograph in Fig. 2(c) confirms that the core and shell dimensions of the nanowires are close to the designated values. The *p*-doped core induces a radial electric field polarizing the quantum ring exciton.

Figure 2(d) shows PL spectra that originate from single quantum rings in two different single nanowires. The energy of these states with increasing magnetic field is displayed in Fig. 2(e). The oscillations setting in at a field of 4 T are a clear signature of the excitonic Aharonov-Bohm effect. The different sign of the diamagnetic coefficient γ reflects a different nature of the excitonic complexes responsible for the respective transitions, with trions resulting in a negative and neutral excitons in a positive value. These results demonstrate that GaAs/AlAs core-shell nanowires constitute a platform offering an unprecedented level of control over the design of three-dimensional quantum structures for the experimental study of excitonic phase coherence phenomena.

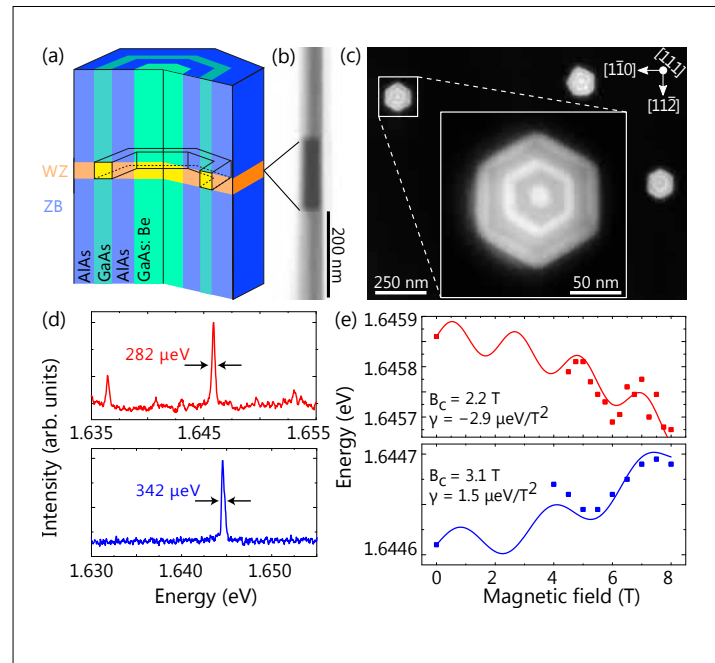


Fig.2. Schematic representation of the GaAs/AlAs core-multishell nanowire under investigation. A wurtzite (WZ) segment created by a TB propagates through the entire diameter of the nanowire (orange and yellow). The quantum ring formed by the intersection of the shell quantum well and the TB is highlighted. (b) Transmission mode secondary electron micrograph of a GaAs nanowire. The contrast variations along the nanowire axis reveal the presence of twin segments. (c) Plan-view high-angle annular dark-field transmission electron micrograph of three GaAs/AlAs core-multishell nanowires. GaAs and AlAs appear bright and dark, respectively. (d) PL spectra recorded from two different nanowires at 4 K and zero magnetic field. The full width at half maximum of the PL lines is about 300 μ eV, suggesting that they originate from excitons in single quantum rings. (e) Dependence of the transition energy on magnetic field for the same quantum rings. The solid lines are fits accounting for Aharonov-Bohm oscillations with period B_C and a diamagnetic shift γ .

Nanowires bending over backwards from strain partitioning in asymmetric core-shell heterostructures

R. B. Lewis, P. Corfdir, H. Küpers, T. Flissikowski, O. Brandt, L. Geelhaar

Strain has always been a double-edged sword for heterostructure design, on the one hand constraining which materials can be combined to form coherent structures, but on the other hand providing a means to modify materials properties by strain engineering. In conventional planar heterostructures, biaxial strain arising from lattice mismatch between the substrate and layers has been employed to improve the performance of optoelectronic and electronic devices. In the nanowire (NW) geometry, elastic relaxation at the free sidewall surfaces widens the range of materials that can be combined without the formation of dislocations. Here, we synthesize highly asymmetric core-shell NW heterostructures to controllably induce NW bending. In turn, this bending leads to extreme strain gradients across the NW core that open up new opportunities for strain engineering.

Our synthesis approach is based on the directional nature of deposition in molecular beam epitaxy, and the result is visualized in Fig. 1(a). First, GaAs NWs were grown in the Ga-assisted mode on pre-patterned Si(111) substrates. Subsequently, the Ga droplets atop the NWs were converted to GaAs by exposure to As. Next, the growth conditions were changed to favor shell formation. The

substrate rotation as well as Al and In fluxes were sequenced in order to deposit an $\text{Al}_{0.5}\text{In}_{0.5}\text{As}$ shell on only one side of the NWs. Strain sharing between the core and the highly asymmetric shell results in bending of the NWs as shown by the scanning electron microscopy (SEM) image in Fig. 1(b). For this particular combination of a 45 nm core diameter and a 20 nm shell thickness, the bending radius is about 1.7 μm . Bending can be predicted fairly well by simple analytical strain calculations. The SEM image illustrates additionally that multiple NWs can also be connected in chains. Thus, bending NWs by more than 90° in controlled directions opens up new ways to engineer connected NW networks. This approach provides great design freedom, as the bending direction is simply determined by the side of the NWs that the incident fluxes impinge on. Fig. 1(c) shows an SEM image of a NW from a different sample with a thinner 30-nm-diameter core bent completely over to contact the substrate (bending radius about 1.1 μm). This striking effect may be exploited to fabricate electrical or possibly optical nano-interconnects.

In order to investigate the photoluminescence (PL) of bent NWs, we focus on a sample for which the surface of 75-nm-di-

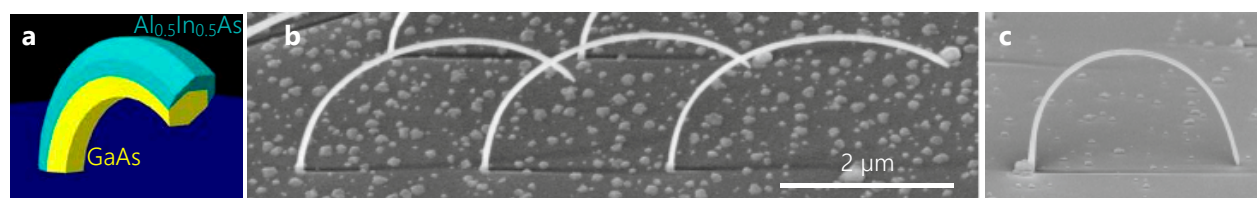


Fig. 1. (a) Schematic representation of the bent NW structure. SEM images of (b) a chain of three NWs with 45 nm diameter core and a 20 nm thick shell (45° viewing angle) and (c) a NW with a thinner 30 nm core, bent completely over and contacting the substrate (20° viewing angle).

ameter GaAs cores was passivated with a symmetric and nearly lattice-matched 10-nm-thick $\text{Al}_{0.3}\text{Ga}_{0.7}\text{As}$ shell before being bent by a 40 nm thick $\text{Al}_{0.5}\text{In}_{0.5}\text{As}$ layer. These NWs exhibit a radius of curvature of about 3.4 μm .

The continuous-wave PL spectrum of these NWs at 10 K is displayed in Fig. 2(a). For comparison, the diagram shows also spectra for a GaAs epilayer, straight GaAs/AlAs/GaAs core-multishell NWs with symmetric shells, and straight GaAs/ $\text{Al}_{0.3}\text{Ga}_{0.7}\text{As}/\text{Al}_{0.5}\text{In}_{0.5}\text{As}$ core-multishell NWs with symmetric $\text{Al}_{0.5}\text{In}_{0.5}\text{As}$ shells with roughly the same volume as for the bent NWs. The spectrum for the epilayer is dominated by a donor-bound exciton transition at 1.514 eV, as expected for strain-free GaAs. Although the GaAs/AlAs/GaAs core-multishell NWs are also strain-free, the PL signal from the GaAs core is redshifted. Such a redshift arises from the presence of stacking defects that localize carriers along the NW axis at low temperatures. The spectrum for the straight GaAs/ $\text{Al}_{0.3}\text{Ga}_{0.7}\text{As}/\text{Al}_{0.5}\text{In}_{0.5}\text{As}$ core-multishell NWs is redshifted even further. This is consistent with the fact that the $\text{Al}_{0.5}\text{In}_{0.5}\text{As}$ shell induces tensile strain in the GaAs core. Moreover, the GaAs PL signal for the bent NWs is clearly redshifted compared to that of the straight GaAs/ $\text{Al}_{0.3}\text{Ga}_{0.7}\text{As}/\text{Al}_{0.5}\text{In}_{0.5}\text{As}$ core-multishell NWs, despite the fact that both samples contain similar amounts of $\text{Al}_{0.5}\text{In}_{0.5}\text{As}$.

Strain calculations (not shown) demonstrate that the strain parallel to the NW axis varies across the core of the bent NWs linearly from -0.011 to 0.020 between the inner and outer sides of the GaAs core, respectively. In addition, the average core strain is actually lower in the bent NWs than in the straight ones. One may expect the detection of light from carriers recombining at the core regions under compression, i. e., light at energies higher than those observed for the GaAs/AlAs/GaAs NWs. The absence of such a signal suggests that in bent NWs photogenerated

charge carriers drift from compressively to tensilely strained regions of the core. In the time-resolved PL measurements presented in Fig. 2(b), we indeed observe for time delays below 50 ps a broad emission band containing energies below and above the emission band obtained for the straight strain-free GaAs/AlAs/GaAs NWs. With increasing time delay, the PL signal signifi-

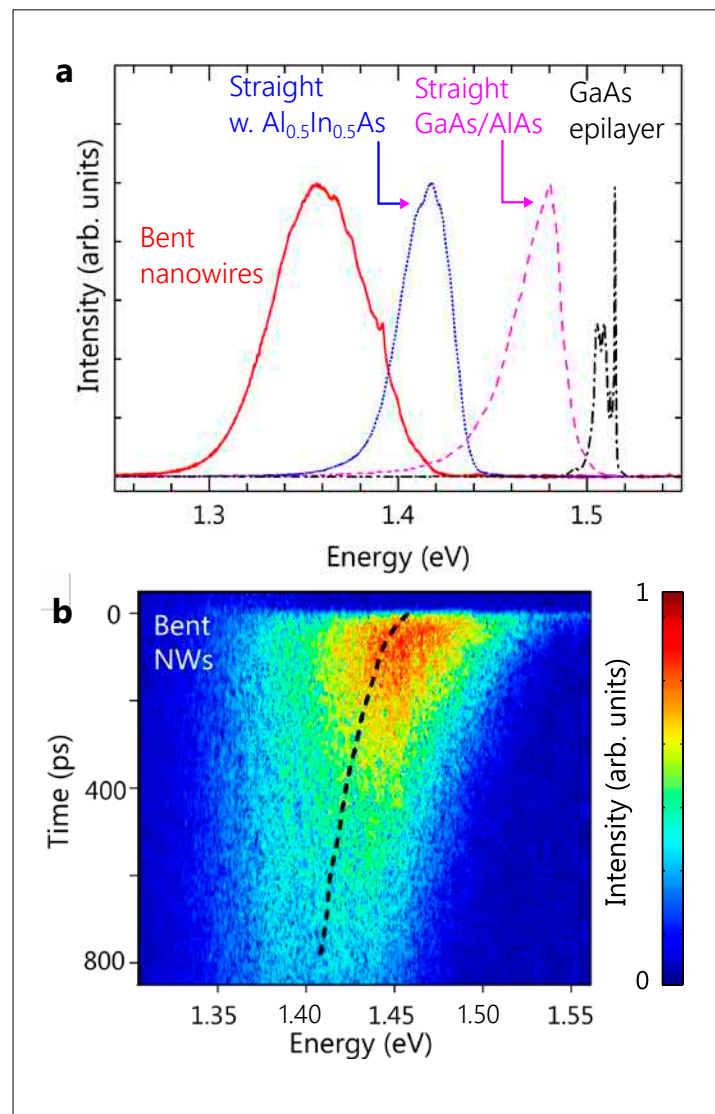


Fig. 2. (a) Normalized PL spectra at 10 K from a GaAs epilayer (dashed-dotted line), an ensemble of GaAs/AlAs/GaAs NWs (dashed line), and ensembles of straight and bent GaAs/ $\text{Al}_{0.3}\text{Ga}_{0.7}\text{As}/\text{Al}_{0.5}\text{In}_{0.5}\text{As}$ NWs (dotted line and solid line, respectively). (b) Streak camera image taken on the bent NWs at 10 K. The evolution of the PL peak energy extracted from Gaussian fits is shown as a dashed line.

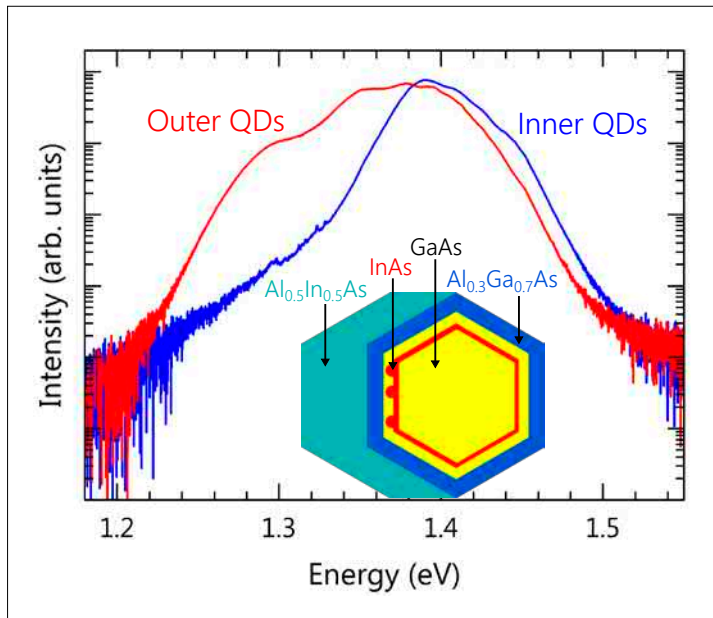


Fig. 3. PL spectra at 10 K from bent NWs with InAs QDs incorporated on the tensilely strained outer side of a GaAs NW core as sketched in the inset (red line) as well as from bent NWs with InAs QDs located on the compressively strained inner side of the GaAs core (blue line).

cantly redshifts and narrows. In particular, the redshift is much larger than for straight $\text{GaAs}/\text{Al}_{0.3}\text{Ga}_{0.7}\text{As}/\text{Al}_{0.5}\text{In}_{0.5}\text{As}$ NWs (not shown), which confirms the drift of charge carriers towards the outer side of the bent NWs.

Next, we exploit the carrier drift resulting from the strain gradient in bent NWs for light emission with a novel heterostructure, which includes an active region at the outer side of the NW core. The inset in Fig. 3 shows a schematic of a NW cross section, in which InAs quantum dots (QDs) have been placed on the same side of the GaAs core as a 40-nm-thick $\text{Al}_{0.5}\text{In}_{0.5}\text{As}$ bending layer. Fig. 3 displays the continuous-wave PL spectrum recorded for this sample at 10 K. For comparison, a PL spectrum from bent NWs with the InAs QDs present on the compressively strained inner side of the GaAs core is also shown. Based on past studies, we attribute the main PL peak for each sample to the InAs wetting layer. We see that the dominant peak from NWs with outer QDs is redshifted compared to NWs with inner QDs. More importantly, NWs with outer QDs exhibit a prominent low-energy shoulder at about 80 meV below the main peak, indicating that the emission intensity in this range is more than an order of magnitude higher than that for the sample with inner QDs. The PL spectra acquired at lower excitation power exhibit sharp transitions in this energy range (not shown), which confirms that the shoulder arises from enhanced light emission from the InAs QDs. These findings demonstrate that the strain gradients in bent NWs can significantly increase the carrier capture of QDs placed in a region of tensile strain.

In conclusion, we have realized highly controlled, intrinsic bending of NWs giving rise to extreme strain gradients by depositing asymmetric lattice-mismatched shells. This new design freedom resulting from the three-dimensional nature of NWs opens up many possibilities for exploitation in devices.

Self-assembled growth of AlN nanowires on sputtered TiN by molecular beam epitaxy

T. Auzelle, M. Azadmand¹, J. Lähnemann, G. Gao, M. Ramsteiner, A. Trampert, O. Brandt, S. Sanguinetti¹, L. Geelhaar

Within the family of nitride semiconductors, AlN stands out owing to its ultra-wide band gap ($> 6\text{eV}$), allowing the realization of deep UV emitters with wavelengths in a range between 210 and 360 nm. High-quality AlN films and AlN-based devices can be fabricated on bulk AlN substrates, which have become available in the last few years, but are still prohibitively expensive. An economically attractive alternative is the synthesis of AlN in the shape of nanowires (NWs). As for the case of GaN NWs, the high surface-to-volume ratio of these nanostructures provides an efficient channel for strain relaxation, which allows their growth on a variety of lattice-mismatched substrates, including metal foils, while preserving a high structural perfection. Former attempts of the direct nucleation and growth of AlN NW ensembles by molecular beam epitaxy (MBE) were carried out at substrate temperatures below 1000 °C and have invariably ended up in columnar films. In fact, higher temperatures are difficult to reach for conventional substrates such as Si. In this work, we develop TiN substrates to explore exceptionally high substrate temperatures for AlN by MBE ($> 1000\text{ }^{\circ}\text{C}$). In this way, we pioneer the self-assembled growth of ensembles of well-separated AlN NWs.

TiN films with a thickness of 850 nm are reactively sputtered on Al_2O_3 substrates using a magnetron sputtering setup. The substrate is then transferred in ultra-high vacuum into the MBE chamber and is exposed to active N coming from a radio-fre-

quency plasma source for about 30 min at 930–1180 °C. The substrate temperature is measured by a pyrometer, taking into account the emissivity of TiN and absorption in the viewport. The presence of TiN(111) is confirmed by reflection high-energy electron diffraction (RHEED). Next, AlN growth itself is initiated by opening the Al shutter at 1180 °C. The growth proceeds in N-rich conditions (III/V ratio of 0.1) as typically also chosen for the self-assembly of GaN NW ensembles. The first AlN-related diffraction spots become visible by RHEED after 20 min, evidencing the existence of a long incubation time. The growth is carried out for another 250 min.

Ex-situ scanning electron microscopy (SEM) imaging of the sample as shown in Figs. 1(a) and (b) confirms the formation of well-defined AlN NWs with an average diameter of 55 nm. A statistical analysis of the contour of the NW top facets suggests a coalescence degree of only 30%. This value is low even when compared to typical GaN NW ensembles grown on Si. The NWs are 850 nm long which corresponds to an average vertical growth rate, once the incubation time is over, of 3.4 nm/min. An analysis of the involved atomic fluxes shows that the Al atoms directly impinging on the NW top facets can only account for a fraction of this value, namely, up to 2.0 nm/min. Al adatoms impinging on the NW sidewalls thus significantly contribute to the NW elongation by diffusing toward the top facets where they are eventually incorporated. This diffusion-induced growth is also ob-

¹ L-NESS and Dipartimento di Scienza dei Materiali, Università di Milano-Bicocca, Milano, Italy

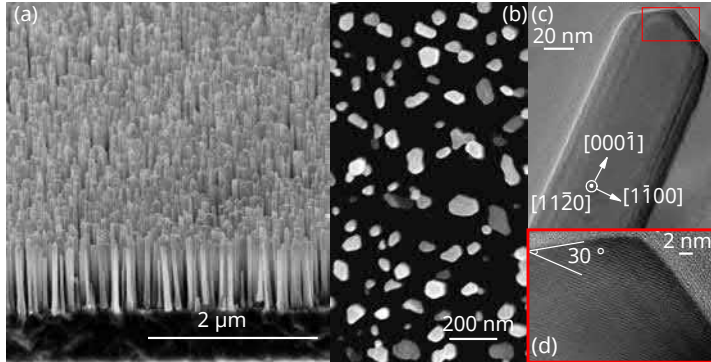


Fig. 1. Bird's eye and (b) top-view SEM images of the AlN NWs grown on sputtered TiN. (c) Cross-sectional bright-field and (d) high-resolution TEM images of a dispersed AlN NW.

served in the MBE of GaN NWs and is enabled here for AlN by the exceptionally high substrate temperature.

Transmission electron microscopy of dispersed AlN NWs reveals that they are free of extended defects away from the AlN/TiN interface [Figs. 1 (c) and (d)]. The NWs are also seen to exhibit well defined top and sidewall facets. The side facets are deduced to be formed by $\{11\bar{2}0\}$ planes by correlating x-ray pole figures and SEM imaging. According to density-functional theory calculations, these planes have a higher surface energy compared to the $\{1\bar{1}00\}$ ones

[V. Jindal *et al.*, *J. Appl. Phys.* **105**, 084902 (2009)], suggesting that kinetic effects play a decisive role for the growth of these NWs. The top facets are systematically found to be formed by semi-polar planes with an inclination angle of $30 \pm 1^\circ$ relative to the $(000\bar{1})$ plane. These facets can correspond either to $\{11\bar{2}5\}$ or $\{1\bar{1}0\bar{3}\}$ planes.

The key factor that enables the growth of these NWs is the TiN substrate. Spectroscopic ellipsometry (SE) is used to confirm that the sputtered film consists of stoichiometric TiN as shown in Figs. 2 (a) and (b). The pseudodielectric function observed reflects the metallic nature of TiN. Indeed, electrical measurements yield a resistivity of $0.3\text{ m}\Omega\text{cm}$ at room temperature. The TiN film is not affected by the high-temperature growth as testified by Raman scattering and x-ray diffractometry performed after the AlN growth [Figs. 2 (c) and (d)]. No x-ray reflection of TiN_xO_y alloys is observed, demonstrating that TiN does not react with the Al_2O_3 substrate. The spectral position of the AlN E_2 phonon mode in the Raman spectrum of Fig. 2 (c) and the angular position of the AlN 0002 Bragg reflection displayed in Fig. 2 (d) confirm that the AlN NWs are free of strain within the experimental accuracy of 10^{-3} .

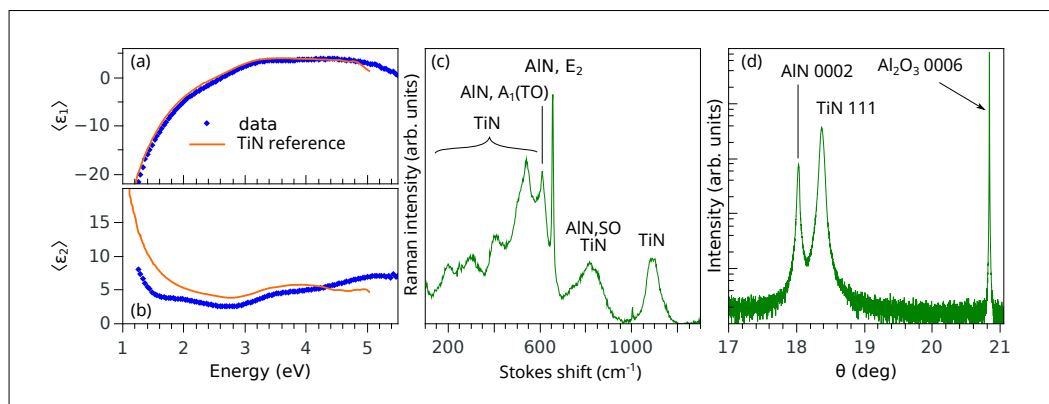


Fig. 2. (a) Real and (b) imaginary part of the pseudodielectric function of sputtered TiN measured by SE. The TiN reference is from Langereis *et al.*, *J. Appl. Phys.* **100**, 023534 (2010). (c) Raman spectrum and (d) symmetric $\omega-2\Theta$ x-ray diffraction scan of the ensemble of AlN NWs on sputtered TiN.

Figure 3 presents the cathodoluminescence (CL) spectra of the NW ensemble and of bulk AlN used as a reference (courtesy of M. Bickermann, Leibniz Institute for Crystal Growth). The AlN NWs exhibit an intense emission line at 6.01 eV arising from the radiative decay of donor-bound $[(D^0, X_A)]$ and free excitons (X_A) as well as the commonly observed emission from deep levels at 3.9 eV (see inset). The emission energy of the (D^0, X_A) transition coincides with that of the AlN bulk crystal, confirming that the NWs are strain free. Moreover, the comparatively intense band-edge emission of the NWs opens up perspectives for optoelectronic applications.

To sum up, an exceptionally high growth temperature of 1180 °C has been found to be crucial for the formation of ensembles of well-separated AlN NWs. The high temperature results in a long incubation time (associated with a low NW number density) and enables Al adatom diffusion. Reaching such high temperatures is enabled by employing sputtered TiN on Al_2O_3 as the substrate. This work opens up the possibility to use AlN NW ensembles as quasi-substrates for the growth of high-quality AlN/(Al,Ga)N heterostructures emitting in the deep UV range.

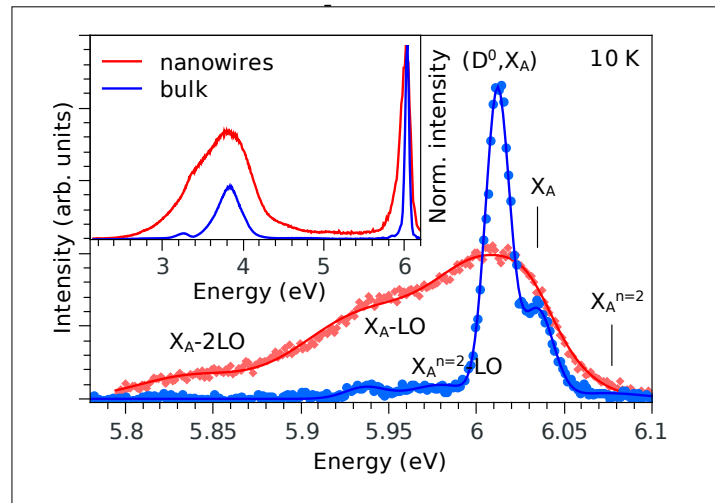


Fig. 3. CL spectrum of the ensemble of AlN NWs on sputtered TiN compared with that of bulk AlN. The symbols are the experimental data, and the lines are lineshape fits taking into account the (D^0, X_A) and X_A transitions and the first two longitudinal optical phonon (LO) replica of the latter. The inset shows the data over an extended energy range.

Intrinsic frequency tuning of terahertz quantum-cascade lasers

L. Schrottke, X. Lü, B. Röben, K. Biermann, H. T. Grahn

The development of quantum-cascade lasers (QCLs) for the terahertz (THz) spectral region has given rise to numerous spectroscopic applications during the last decade, for which the fine tuning of the emission frequency of the QCL is of great importance. The most straightforward tun-

ing mechanism, although for a rather small tuning range, is the intrinsic tuning by adjusting the heat sink temperature and/or the driving current. The temperature and current tuning mechanisms have already been applied to several spectroscopic approaches. One example is the local oscillator in the German Receiver for Astronomy at Terahertz Frequencies, which has allowed for various observations based on the 63 μm emission line of oxygen from several astronomical objects.

The mode tuning is simulated by calculating the refractive index n for different applied electrical field strengths F obtained from an oscillator model for the complex-valued dielectric function $\varepsilon(\nu) = \varepsilon_1(\nu) + i\varepsilon_2(\nu)$, with ν indicating the frequency of the electromagnetic radiation

$$\varepsilon(\nu) = \varepsilon_B - \frac{2e^2}{\varepsilon_0} N_{av} \sum_{i,j}^{(E_i > E_j)} \frac{E_{ij}(\rho_{ii} - \rho_{jj})|D_{ij}|^2}{E_{ij}^2 - h^2\nu^2 - i\Gamma_{ij}h\nu}, \quad (1)$$

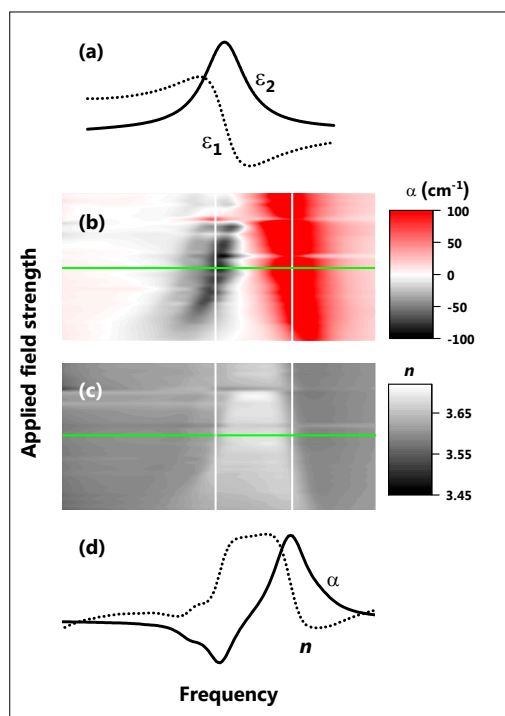


Fig. 1. (a) Schematic representation of $\varepsilon_2(\nu)$ (solid line) and $\varepsilon_1(\nu)$ (dotted line) of a single oscillator (intersubband transition) for the case of absorption. Simulation results for (b) the absorption coefficient α and (c) the refractive index n as a function of ν and F for an exemplary QCL structure. The vertical lines indicate frequencies close to the gain and absorption maxima, for which the refractive index slightly continuously decreases with increasing F as shown in (c). The horizontal lines mark the field strengths for which the absorption coefficient α and the refractive index n are shown as a function of ν in (d).

where N_{av} denotes the average volume density of carriers, $E_{ij} = E_i - E_j$ the transition energy between states i and j , ρ_{ii} (ρ_{jj}) the population of states i (j), $\Gamma_{ij} = \Gamma_i + \Gamma_j + 2\Gamma_0$ the width of the transition, and D_{ij} the respective dipole matrix element. The level broadening $\Gamma_i + \Gamma_0$ is determined by the lifetime broadening Γ_i and an additional parameter Γ_0 in order to account for inhomogeneous broadening due to interface roughness. The background dielectric function of the material is given by $\varepsilon_B = 13$, while e denotes the elementary charge and ε_0 the vacuum permittivity. This procedure has been included into our Fourier-transform-based hybrid model, which allows us to solve the Schrödinger-Poisson equations self-consistently.

Figure 1(a) shows schematically $\varepsilon_1(\nu)$ and $\varepsilon_2(\nu)$ for a single oscillator. Close to the absorption maximum, ε_1 exhibits a large change, which leads to a change of the refractive index if the absorption (or gain) maximum is shifted. Figures 1(b) and 1(c) show the absorption/gain and refractive index maps, respectively, for an exemplary QCL with a strong gain peak, which is blueshifted with increasing F , and a strong absorption peak, which is redshifted. Close to both, the gain and the absorption maximum, the refractive index decreases with increasing F , for instance along the vertical lines in Fig. 1(c) leading to a blueshift of a possible lasing mode.

The challenge consists in a projection of the gain map, which displays the calculated gain values as a function of ν and F , onto the observed mode map, which consists of a compilation of all identified laser modes

of the respective multi-mode THz QCL as a function of ν and the measured applied voltage U . The projection allows us to correct the voltage scale so that a reliable relation between U and F for the comparison of the observed behavior with the results of our simulations can be established. This procedure is very reliable for laser structures exhibiting a clear shift of the gain maximum with increasing voltage/field strength.

Figure 2(a) shows the calculated gain map of a QCL structure, which exhibits basically a single gain maximum shifting to higher frequencies for larger field strengths within the operating range. The measured mode map can be projected onto the calculated gain map reasonably well and exhibits a blueshift of the center of the multi-mode spectrum obtained for pulsed operation. This projection allows us to compare the

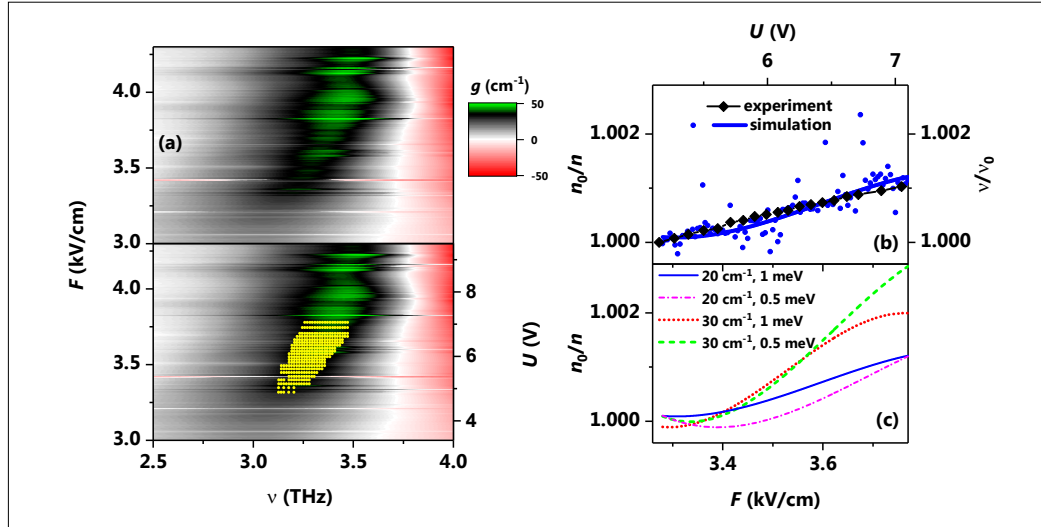


Fig. 2. (a) Gain map as a function of ν and F calculated without taking into account stimulated emission (upper panel). We used $\Gamma_0 = 1 \text{ meV}$. The lower panel shows the same gain map superimposed by the positions of all identified lasing modes as a function of ν and U regardless of their intensities (dots). (b) Experimental values for the normalized frequency ν/ν_0 of the lasing mode at 3.27 THz as a function of U compared to values for the reciprocal normalized refractive index n_0 , which have been calculated by taking into account stimulated emission for a resonator loss $\alpha_r = 20 \text{ cm}^{-1}$ and $\Gamma_0 = 1 \text{ meV}$ as a function of F . The thick solid line depicts a polynomial fit to the data as a guide to the eye. We use the identical projection of U onto F as shown in (a). (c) Normalized refractive index n_0 for two values of α_r and of Γ_0 as a function of F as indicated. Here, we show only the polynomial fits of the calculated results for clarity.

simulated values for n_0/n between 3.26 and 3.77 kV/cm with the observed values for ν/ν_0 between 5.1 and 7.1 V as shown in Fig. 2(b) making use of $\nu/\nu_0 \approx n_0/n$ with ν_0 and n_0 denoting the frequency and refractive index, respectively, at threshold.

For the analysis, we focus on modes which are present over most part of the operating range. All other modes show a similar tuning behavior. Here, the n_0/n characteristics have been calculated for a single lasing mode at 3.27 THz including stimulated emission. We have used two values for both, Γ_0 and the effective resonator losses α_r , which take into account the mode confinement factor. The curve for $\Gamma_0 = 1$ meV and $\alpha_r = 20$ cm $^{-1}$, which are reasonable model parameters, agrees well with the experimentally obtained curve. In order to demonstrate how sensitively the tuning behavior depends on the gain spectra, we show in Fig. 2(c) also the corresponding curve for $\Gamma_0 = 0.5$ meV. Similarly, the influence of the resonator properties is demonstrated by the clear difference between the two curves for $\alpha_r = 20$ cm $^{-1}$ and the two curves for $\alpha_r = 30$ cm $^{-1}$.

We have investigated four different THz QCLs in pulsed operation. One of them exhibits a redshift for increasing voltage. In some cases, even both types of frequency shift can be observed for the same QCL. The tuning range is in all cases about 0.1% of the mode frequency at threshold. In the frame-

work of the oscillator model, we are able to explain the tuning behavior quantitatively, semi-quantitatively, or at least qualitatively, depending on the complexity of the gain maps. In view of the small tuning range, even a mere qualitative agreement is an important result as it demonstrates both, the applicability and the limits of the oscillator model in this context. For two QCLs, we have also investigated single-mode lasers, for which also lateral distributed-feedback gratings have been employed, in continuous-wave operation [L. Schrottke et al., J. Appl. Phys. **123**, 213102 (2018)]. Single-mode lasers fabricated from the same wafers as corresponding multi-mode lasers exhibit the same tuning direction, but with a larger frequency shift as compared to the multi-mode lasers under pulsed operation.

For a comprehensive understanding of the tuning behavior of individual modes, also nonlinear effects such as hole burning, the interaction of modes in multi-mode lasers, and, in case of distributed-feedback lasers, the influence of the grating on the Fabry-Pérot modes have to be taken into account. For continuous-wave operation, also thermal effects may play a role. The understanding and modeling of the intrinsic tuning of THz QCLs may be useful for the simultaneous optimization of output power and tuning range, in particular for lasers with a hybrid design, which exhibit a sufficiently large degree of freedom.

Determination of the interface parameter in terahertz quantum-cascade laser structures based on transmission electron microscopy

X. Lü, E. Luna, L. Schrottke, K. Biermann, H. T. Grahn

Quantum-cascade lasers (QCLs) are promising light sources that cover a wide range of mid-infrared and terahertz (THz) frequencies. Recently, we have realized THz QCLs based on GaAs/AlAs heterostructures exhibiting higher wall plug efficiencies and lower threshold current densities in comparison to GaAs/Al_{0.25}Ga_{0.75}As THz QCLs with similar emission frequencies. However, in order to maintain a sufficiently strong resonant tunneling necessary for achieving population inversion, the thicknesses of the energetically higher AlAs barriers are significantly smaller than those of the typically employed, corresponding Al_{0.25}Ga_{0.75}As barriers and are on the order of several monolayers (MLs). Since the interface grading due to intermixing leads to interface widths on the same order, the actual composition of the AlAs barriers may not reach a purely binary nature. Therefore, a comprehensive understanding of the composition profile of the (nominally) binary AlAs barriers is of great importance. Furthermore, QCLs are semiconductor superlattices with a complex unit cell and are typically composed of the order of one thousand layers. Therefore, the profile at the heterointerface is expected to play an important role for the optical and transport properties of the QCLs.

The interface grading can be taken into account for the simulation of semiconductor heterostructures and the design of QCLs in a straightforward way using our Fourier-transform-based model [X. Lü *et al.*, Appl. Phys. Lett. **104**, 232106 (2014) and L. Schrottke *et al.*, J. Appl. Phys. **117**, 154309 (2015)]. This model allows for both, an efficient simulation of the impact of the in-

terface profiles on the lasing properties of QCLs and a direct comparison of the potential profile of the entire heterostructure with experimentally determined composition profiles. The interfaces of heterostructures and superlattices can be investigated by transmission electron microscopy (TEM). A method to reliably quantify the chemical interfaces in III-V semiconductor quantum wells and superlattices has been developed based on chemically sensitive \mathbf{g}_{002} dark-field (DF) TEM imaging. The detailed analysis of the experimental element distribution profiles reveals that the interface is well described by a sigmoidal function [E. Luna *et al.*, Phys. Rev. Lett. **109**, 126101 (2012)]. The thickness of the thinnest barriers in the THz QCL structures is only a few MLs, which is on the same order as the interface parameter.

For GaAs/(Al,Ga)As, the sigmoidal function, which describes the interface composition profiles can be very well approximated by an error function, which is beneficial for the incorporation of the interface grading into the Fourier-transform-based model. The Fourier components of the potential including graded interfaces (\tilde{V}_{mj}) are given by

$$\tilde{V}_{mj} = \frac{\Phi_{jm}}{L_z} \int_0^{L_z} e^{-2\pi i \frac{m}{L_z} z} V(z) e^{2\pi i \frac{j}{L_z} z} dz, \quad (1)$$

with

$$\Phi_{jm} = e^{-16\pi \frac{(j-m)^2 L_z^2}{L_z^2}}, \quad (2)$$

where i denotes the imaginary unit, $j(m)$ the index of the Fourier component, L , the interface parameter, and L_z the length of the simulation cell. In order to obtain the

realistic potential $V_{\text{grad}}(z)$ including graded interfaces in real space, we carry out the transformation

$$V_{\text{grad}}(z) = \sum_{m-j} \tilde{V}_{mj} e^{2\pi i \frac{m-j}{L_z} z}. \quad (3)$$

While \tilde{V}_{mj} is applied to the simulations of the transport properties, $V_{\text{grad}}(z)$ is used for the presentation of the (real-space) composition profiles. For the actual shape of the interface grading, a linear dependence of the potential $V_{\text{grad}}(z)$ on the Al composition is a very good approximation. We obtain the simulated composition profile from the conduction band profile including interface grading, which we can directly compare with the experimentally determined composition profiles.

We investigated two QCL structures, one with very thin AlAs barriers down to 1 ML and one with thicker $\text{Al}_{0.25}\text{Ga}_{0.75}\text{As}$ barriers. Figure 1(a) shows a cross-sectional chemically sensitive \mathbf{g}_{002} DFTEM image of the GaAs/AlAs QCL structure, while the intensity linescan obtained from the area marked in Fig.1(a) is displayed in Fig.1(b). The intensities of the thinnest AlAs barriers are significantly reduced, and the two peaks cor-

responding to the thinnest barriers (about 1 ML) overlap. It is found that the intensity ratio $R_{002}(x) = I_{002}(\text{Al}_x\text{Ga}_{1-x}\text{As})/I_{002}(\text{GaAs})$ relates to the Al composition x via $R_{002}(x) = (1 + 2.94 \cdot x)^2$. Figure 2 shows the experimental Al content profile across one period (circles). The Al content of all AlAs barriers in the QCL structure is below 55 % instead of the nominal 100 %. For the simulations, the only adjustable parameter is the length of a single period d_p^{exp} of the structure. We rescaled the nominal thickness of a single period d_p to the value determined by DFTEM. By assuming $L_i = 1.6$ MLs as deduced from experiments on GaAs/(Al,Ga)As heterostructure [E. Luna et al., Phys. Rev. Lett. **109**, 126101 (2012)] and using $d_p^{\text{exp}} = 1.096d_p$, we can very well reproduce the experimental Al composition profiles by the simulations, the result of which is shown in Fig.2 by the solid lines. In Fig.2 at a position of about 72 nm, we obtain for a 2 ML AlAs barrier in the QCL structure an Al content of only about 30 % in the center of the layer using the interface parameter $L_i = 1.6$ MLs. For the barrier with 1 ML thickness, the experimental Al content is only 15.6 %. In the case of very thin AlAs layers (< 2 MLs), the actual interface width of 7 MLs, which corresponds to a change in the Al content from 10 % to 90 %, is already considerably larger than the layer thickness. Therefore, interface grading should be carefully taken into account in the simulations for the design of this type of THz QCLs. For the GaAs/ $\text{Al}_{0.25}\text{Ga}_{0.75}\text{As}$ QCL structure, we can also reproduce the composition profile very well, but the difference between the nominal and the actual Al content for the thinnest barriers is much smaller.

Finally, the overlap of the two thinnest barriers in the Al content profile can be well reproduced by the simulations. The inset of Fig.2 shows two 1 ML barriers at the positions around 6.9 and 9.0 nm, which are well resolved in both, the experimental and the simulated profiles. Since the interface parameter is experimentally determined for the complete GaAs-based THz QCL struc-

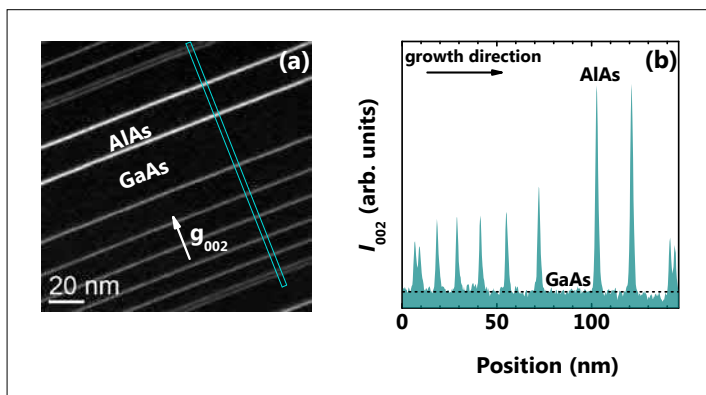


Fig. 1. Chemically sensitive \mathbf{g}_{002} DFTEM image of a single period of a QCL structure with AlAs barriers. (b) Intensity linescan from the area marked in (a) that includes a single period of the QCL structure.

tures, the actual composition profile including a possible overlap of thin adjacent barriers can be used for the design and optimization of QCLs. Furthermore, the experimentally determined interface parameter may be correlated to the growth conditions and may contribute to an improvement of the structural parameters.

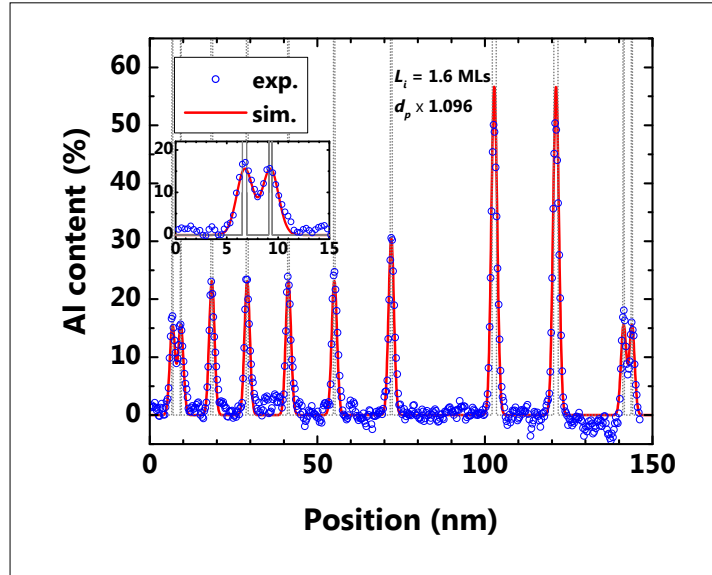


Fig. 2. The Al composition (circles) experimentally determined using the intensity profile shown in Fig. 1(b) and the Fourier-transform-based simulated composition profile assuming abrupt (dotted line) and graded interfaces with $L_i = 1.6$ MLs (solid line). The inset magnifies the first two barriers on the left around 6.9 and 9.0 nm.

Terahertz quantum-cascade lasers for emission at application-specific frequencies

B. Röben, X. Lü, K. Biermann, A. Trampert, L. Schrottke, H. T. Grahn

Terahertz (THz) quantum-cascade lasers (QCLs) are currently unchallenged for high-resolution spectroscopy of narrow absorption lines in the range between 2 and 6 THz with high sensitivity. For each application, a particular QCL needs to be fabricated that emits at the frequency of the investigated absorption line. However, establishing a reliable procedure to fabricate QCLs with a sufficient accuracy of the emission frequency is very challenging.

A prerequisite to obtain emission at a specific frequency is an adequately designed heterostructure that provides optical gain in the desired frequency range. This already quite challenging task can be solved efficiently by means of our Fourier-transform based hybrid model for the simulation of the gain spectra. However, the exact emission frequency is actually determined by the resonator length. The most important type

is the Fabry-Pérot resonator. It is formed by cleaved facets, which act as mirrors in the longitudinal direction of the QCL chip. Figure 1 shows the calculated frequency difference $\Delta\nu$ between a reference resonator of length L and a resonator only slightly shorter by $\Delta L = 1 \mu\text{m}$. Depending on the length L of the reference resonator and on the emission frequency, the frequency difference $\Delta\nu$ ranges between 0.8 and 4 GHz, which is comparable to the intrinsic tuning range amounting to typically less than 6 GHz. Therefore, emission at a specific target frequency can only be accomplished if the resonator length is controlled with a precision of at least $1 \mu\text{m}$, since otherwise the frequency range accessible via tuning would not include the target frequency. Hence, a precise control of the resonator length is crucial for matching the target frequency.

A Fabry-Pérot resonator of a QCL based on a single-plasmon waveguide is usually defined by cleavage. While manual cleaving is only possible with a precision of $100 \mu\text{m}$ at best, most commercial cleaving accessories or machines achieve a higher precision of 3 to $10 \mu\text{m}$, which is still insufficient. Therefore, our approach is to precisely adjust the resonator length in a post-process *after* cleavage. We realize this post-processing step by means of mechanical polishing the front facet. An important advantage of this procedure is that it can be applied to fully operational QCLs.

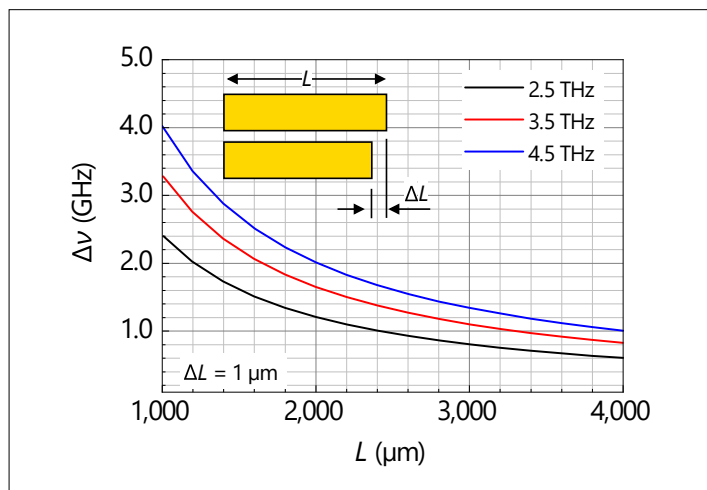


Fig. 1. Frequency difference $\Delta\nu$ between a reference Fabry-Pérot resonator of length L and a resonator with a length reduced by $\Delta L = 1 \mu\text{m}$. The reference and the slightly shorter resonator are shown schematically in the inset.

Figure 2(a) shows the emission modes measured before polishing (polishing run $N = 0$) and after each of the six polishing runs $N = 1–6$ that were performed. In the measurements after polishing runs $N = 1–6$, we observe a red shift of the mode as the cur-

rent density is increased, which is due to current-induced tuning. For $N = 0$, we only consider the current density of 300 A cm^{-2} , since at the other current densities we observe a hopping to another resonator mode at a 20 GHz larger frequency, which would add unnecessary complexity to the discussion. The comparison between the different polishing runs in Fig. 2(a) clearly shows that we obtain a blue shift of the modes due to the reduction of the resonator length by the polishing process. The polishing was stopped after $N = 6$, since we achieved emission at the target frequency. Figure 2(b) shows the incremental frequency shift $\Delta\nu$ between polishing run N and the previous polishing run $N - 1$. For the optimized polishing runs $N = 4–6$, we observe frequency shifts of about 1 GHz per polishing run. Figure 2(c) shows the incremental length reduction ΔL corresponding to the average values of $\Delta\nu$ as displayed in Fig. 2(b) using the correspondence between $\Delta\nu$ and L from Fig. 1. We obtain values of well below 1 μm for the optimized polishing runs $N = 4–6$.

These results clearly demonstrate that the polishing technique is well-suited to precisely control the emission frequency of a QCL. Hence, the polishing technique will form the basis for a reliable and well-controlled procedure to obtain emission at application-specific frequencies.

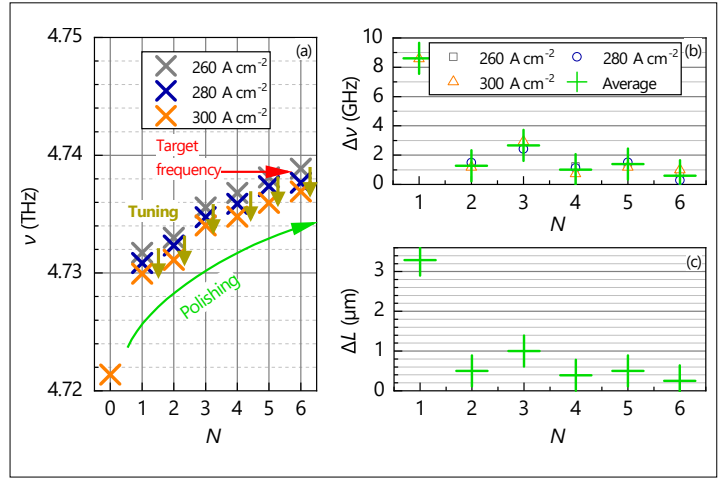


Fig. 2. (a) Frequency of the Fabry-Pérot modes before the polishing (referred to as polishing run $N = 0$) and after the polishing runs $N = 1–6$ for injection currents of 260 , 280 , and 300 A cm^{-2} . Note that for $N = 0$ we neglect the modes at 260 and 280 A cm^{-2} because of mode hopping to a higher frequency. (b) Incremental frequency shift between polishing runs N and $N - 1$ extracted from (a). (c) Incremental reduction of the resonator length due to polishing derived from the average values of the frequency shift in (b) using the correspondence between $\Delta\nu$ and L from Fig. 1.

GATES® POWERGLIDE

TYPE: GATESELEKTOR
CONVENTIONAL
THERMOCELL: SEPAROMOTOR
REV.



Departments Abteilungen

Department of Epitaxy Abteilung für Epitaxie	120
Department of Semiconductor Spectroscopy Abteilung für Halbleiterspektroskopie	125
Department of Microstructure Abteilung für Mikrostruktur	132
Department of Technology and Transfer Abteilung für Technologie und Transfer	138

Department of Epitaxy

Abteilung für Epitaxie

Head of Department: Dr. Lutz Geelhaar, geelhaar@pdi-berlin.de



The overall competence of this research department is the growth of crystalline thin films and nanostructures with extremely well-defined properties by epitaxy. Epitaxy is a process in which one crystal, the adsorbate, is grown on another crystal, the substrate, in such a way that there is a unique relation between the orientations of the two crystal lattices. Typically, the adsorbate is at most a few micrometers thick. Compared to the growth of bulk crystals, epitaxy offers several advantages: First, epitaxy allows the synthesis of materials that are only metastable and cannot be grown as bulk crystals at all. Thus, materials can be grown with specific and tailored properties that could not be obtained in any other way. Second, during epitaxy the composition of the growing crystal can be changed very abruptly—on the atomic scale—so that heterostructures consisting of different materials can be fabricated. In such heterostructures quantum phenomena can be observed, and by tailoring the heterostructures quantum phenomena can be manipulated and new functionalities can be achieved. Therefore, epitaxy is a means to realize nanostructured materials as well as artificial low-dimensional semiconductor systems and to tune their mechanical, optical, electronic, and magnetic properties.

The research activities in the epitaxy department are directed at two complementary tasks. On the one hand, our experimental contribution to the overall research of the institute is the fabrication of custom-designed nanostructured samples. On the other hand, the underlying growth mechanisms themselves are investigated, both for their own scientific sake and in order to optimize properties that are investigated in the core research areas. Our comprehensive expertise is based on the long tradition for

Die Kernkompetenz dieser Abteilung ist die Züchtung kristalliner Schichten und Nanostrukturen mit äußerst präzise definierten Eigenschaften mittels Epitaxie. Mit Epitaxie bezeichnet man den Prozess, in dem ein Kristall – das Adsorbat – auf einem anderen Kristall – dem Substrat – mit einer eindeutigen Beziehung zwischen den Kristallorientierungen gezüchtet wird. Dabei ist das Adsorbat typischerweise nicht dicker als einige Mikrometer. Epitaxie weist einige Vorteile im Vergleich zu der Züchtung von Volumenkristallen auf. So lassen sich mittels Epitaxie auch Materialien herstellen, die nur metastabil und als Volumenkristall gar nicht zu züchten sind. Auf diese Weise können besondere Materialien mit spezifischen, maßgeschneiderten Eigenschaften hergestellt werden. Der zweite wichtige Vorteil der Epitaxie liegt in der Möglichkeit, während des epitaktischen Wachstums die Zusammensetzung des Kristalls sehr abrupt – auf atomarer Skala – zu ändern, so dass sogenannte Heterostrukturen erzeugt werden können, die aus unterschiedlichen Materialien bestehen. In solchen Heterostrukturen können Quantenphänomene beobachtet und durch definiertes Einstellen der Strukturparameter manipuliert werden. Dies ermöglicht die Realisierung und Untersuchung neuer Funktionalitäten, die für Anwendungen interessant sein können. Epitaxie ist somit ein Werkzeug, mit dem nanostrukturierte Materialien wie auch künstliche niedrigdimensionale Halbleiterstrukturen mit einstellbaren mechanischen, optischen, elektronischen und magnetischen Eigenschaften hergestellt werden können.

Die Forschungsaktivitäten in der Epitaxie-Abteilung konzentrieren sich auf zwei komplementäre Linien. Auf der einen Seite werden für ein breites Spektrum an wei-

the fabrication of two-dimensional heterostructures comprising III-V semiconductors, but in addition we work on more and more other materials. Furthermore, research on the vertical growth of III-V nanowires has become a major activity of this research department.

The technique for crystal growth that we employ at PDI is molecular beam epitaxy (MBE). In MBE, growth takes place under extremely pure conditions in ultra-high vacuum. Crystal growth is fed by beams of neutral atoms or molecules that are typically obtained by evaporating source material in effusion cells. Due to the low pressure, these atoms or molecules do not scatter or interact with each other before they reach the substrate. In order to modify the kinetics of crystal growth, the substrate temperature is adjusted. In general, MBE offers a very high level of control over the growth conditions, and growth can be monitored *in situ* by several characterization techniques.

Arguably the most mature class of compound semiconductors is formed by the group-III arsenides GaAs, AlAs, InAs, and their alloys. Very complex heterostructures can be realized in this material system with impressive precision and reproducibility. Such samples are fabricated for investigation in the core research areas *Intersubband Emitters: GaAs-based Quantum-Cascade Lasers and Control of Elementary Excitations by Acoustic Fields*.

The performance and functionality of future semiconductor devices will be enhanced by making use of three-dimensional nanostructures. Our efforts in this direction concentrate on the creation of such structures directly by growth, i.e. in a bottom-up approach with the help of self-organization mechanisms. In particular, we grow both group-III arsenides and nitrides not only as planar layers but also in the form of nanowires. Nanowires are structures with an extremely high aspect ratio and a diameter of the order of 100 nm. Their formation, prop-

terführenden Forschungsaktivitäten am Institut maßgeschneiderte nanostrukturierte Proben hergestellt. Auf der anderen Seite werden die Wachstumsmechanismen selbst untersucht – aus wissenschaftlichem Interesse an den zugrundeliegenden Prozessen und um die Materialeigenschaften, die in den Forschungsschwerpunkten untersucht werden, zu optimieren. Unsere umfassende Expertise basiert auf einer langen Tradition der Herstellung zweidimensionaler Heterostrukturen, die aus III-V-Halbleitern bestehen. Mittlerweile arbeiten wir aber auch intensiv an weiteren Materialsystemen. Zudem hat sich das senkrechte Wachstum von III-V-Nanodrähten zu einer Kernaktivität der Abteilung entwickelt.

Am PDI setzen wir als Methode für Kristallzüchtung die Molekularstrahlepitaxie (MBE für englisch molecular beam epitaxy) ein. Bei diesem Verfahren findet das Wachstum unter äußerst reinen Bedingungen im Ultrahochvakuum statt. Das Kristallwachstum wird durch Atom- oder Molekülstrahlen versorgt, die typischerweise durch das Verdampfen von Quellmaterial in Effusionszellen erzeugt werden. Aufgrund des niedrigen Drucks in der Wachstumskammer streuen die Atome bzw. Moleküle nicht und erfahren auch keine Wechselwirkung untereinander, bis sie auf das Substrat treffen. Um die Kinetik des Kristallwachstums zu modifizieren, wird die Substrattemperatur geregelt. Generell bietet MBE ein sehr hohes Maß an Kontrolle über Wachstumsbedingungen, und das Wachstum kann *in situ* mittels mehrerer Charakterisierungstechniken überwacht werden.

Die wohl am weitesten entwickelte Klasse von Verbindungshalbleitern wird von den Gruppe-III-Arseniden GaAs, AlAs, InAs und deren Legierungen gebildet. In diesem Materialsystem lassen sich sehr komplexe Heterostrukturen mit beeindruckender Präzision und Reproduzierbarkeit herstellen. Solche Proben werden für weitere Untersuchungen in den Forschungsschwerpunkten *Intersubband-Emitter: GaAs-basierte Quan-*

erties, and applications are the subject of the core research area *III-V Nanowires for Optoelectronics*.

Research activities with the focus on the synthesis of materials are carried out in the core research area *Nanofabrication*. At present, the epitaxy of group-III arsenides, group-III nitrides, ferromagnetic Heusler alloys like Co_2FeSi in hybrid structures with group-III arsenide heterostructures and MgO , transparent semiconducting oxides (Ga_2O_3 , In_2O_3 , and NiO), phase-change alloys in the material system Ge-Sb-Te, graphene (the two-dimensional allotrope of carbon), and hexagonal BN is investigated. This research takes place in close collaboration with the core research area *Nanoanalytics* in which the emphasis of the research is on materials properties.

In practice, the key features of MBE described before can only be achieved by combining a considerable number of different technical components, and hence MBE systems are fairly complex. The core component of such systems is a chamber made from stainless steel in which ultra-high vacuum is maintained and the actual crystal growth takes place. In order to preserve ultra-purity and avoid cross-contamination, each material system requires its own, dedicated MBE chamber. For the two main material systems of PDI, group-III arsenides and group-III nitrides, we can pursue the multitude of research projects only by operating more than one MBE chamber each. In total, there are at present eleven MBE systems in use. For the fabrication of hybrid structures comprising different materials, growth on the same sample has to take place subsequently in more than one MBE chamber. In order to avoid contamination of the interface between two materials, such samples have to be transported from one MBE chamber to the other under ultra-high vacuum conditions. Thus, some of our MBE chambers are connected as cluster systems. As an alternative, mobile ultra-high vacuum shuttle chambers are

tenkaskadenlaser und Kontrolle von Elementaranregungen durch akustische Felder hergestellt.

Die Leistung und Funktionalität zukünftiger Halbleiter-Bauelemente wird durch die Verwendung von dreidimensionalen Nanostrukturen verbessert werden. Unsere Bemühungen in diesem Zusammenhang konzentrieren sich auf die Ausbildung solcher Strukturen direkt während des Wachstums, d.h. durch Ausnutzung von Selbstorganisationsphänomenen. Insbesondere züchten wir sowohl Gruppe-III-Arsenide als auch -Nitride nicht mehr nur als planare Schichten, sondern auch als Nanodrähte. Nanodrähte sind Strukturen, die ein äußerst hohes Aspektverhältnis und einen Durchmesser in der Größenordnung von 100 nm aufweisen. Die Bildung, die Eigenschaften und die Anwendungen von Nanodrähten sind Untersuchungsgegenstand des Forschungsschwerpunkts *III-V-Nanodrähte für Optoelektronik*.

Die Synthese von Materialien steht hingen im Fokus des Forschungsschwerpunkts *Nanofabrikation*. Gegenwärtig werden hier die Epitaxie von Gruppe-III-Arseniden und -Nitriden, ferromagnetischen Heusler-Legierungen wie Co_2FeSi in Hybridstrukturen mit Gruppe-III-Arsenid-Heterostrukturen und MgO , transparenten halbleitenden Oxiden (Ga_2O_3 , In_2O_3 und NiO), Phasenwechsel-Materialien des Systems Ge-Sb-Te, Graphen (das zweidimensionale Allotrop von Kohlenstoff) und hexagonalem BN untersucht. Diese Forschung wird in enger Zusammenarbeit mit dem Forschungsschwerpunkt *Nanoanalytik* durchgeführt.

In der Praxis lassen sich die beschriebenen Schlüsselmerkmale von MBE nur erreichen, wenn eine beträchtliche Anzahl unterschiedlicher technischer Komponenten kombiniert wird. Daher sind MBE-Anlagen recht komplex. Die Kernkomponente eines solchen Systems ist eine Kammer, die aus Edelstahl gefertigt wird. Hier findet das eigentliche Kristallwachstum statt. Um die

also employed to transfer samples between MBE systems.

As a distinctive experimental feature, PDI owns three special MBE chambers that allow the in-situ, real-time analysis of growth processes by x-ray diffraction. To this end, these chambers can be connected to our own beamline at the synchrotron BESSY II (Helmholtz-Zentrum Berlin für Materialien und Energie). The successful operation of such a setup critically depends on the continuous stationary operation of the MBE system at the synchrotron, since a high quality of the epitaxial layers and interfaces is imperative for a reliable quantitative analysis. Consequently, at least one of these special MBE chambers is always located at the synchrotron. Currently, a system equipped for the study of semiconducting oxides is installed there.

This year, we have improved our research infrastructure in several ways. We have installed around MBE chambers active magnetic field cancelling systems that compensate magnetic noise stemming in particular from the nearby subway. These systems have led to a drastic improvement of reflection high-energy electron diffraction measurements. Also, we have revisited our laboratory safety measures and have implemented different changes. Specifically, the laboratory air is now continuously monitored for poisonous arsine gas. Furthermore, the MBE system for semiconducting oxides has been substantially modified with the objective to enable sample growth at higher substrate temperature. To this end, we have equipped the system with a new substrate manipulator, which in turn has necessitated an exchange of the sample transfer system.

extreme Reinheit zu erhalten und wechselseitige Verunreinigungen zu vermeiden, braucht jedes Materialsystem seine eigene, dedizierte Wachstumskammer. Für die zwei zentralen Materialsysteme des PDI, Gruppe-III-Arsenide und -Nitride, lässt sich die Vielfalt der Forschungsprojekte nur durchführen, wenn jeweils mehr als eine Kammer zur Verfügung steht. Insgesamt sind am Institut zurzeit elf MBE-Anlagen in Betrieb. Wenn hybride Strukturen aus unterschiedlichen Materialien hergestellt werden sollen, muss das Wachstum an derselben Probe nach einander in mehr als einer MBE-Kammer stattfinden. Um eine Verunreinigung der Grenzfläche zwischen zwei Materialien zu vermeiden, müssen diese Proben zwischen MBE-Kammern unter Ultrahochvakuumbedingungen transportiert werden. Deshalb sind einige unserer MBE-Anlagen als Cluster-Systeme konzipiert. Alternativ verwenden wir kleine mobile Ultrahochvakuumkammern, um den Probentransfer zwischen MBE-Kammern zu gewährleisten.

Als experimentelle Besonderheit stehen dem PDI drei spezielle MBE-Anlagen zur Verfügung, die In-situ-Studien der Wachstumsprozesse mittels Röntgenbeugung in Echtzeit ermöglichen. Hierfür können die Kammern mit unserem eigenen Strahlrohr am Synchrotron BESSY II (Helmholtz-Zentrum Berlin für Materialien und Energie) verbunden werden. Der erfolgreiche Betrieb eines derartigen Aufbaus hängt wesentlich vom kontinuierlichen, stationären Einsatz der MBE-Anlage am Synchrotron ab. Infolgedessen befindet sich mindestens eine dieser speziellen MBE-Anlagen stets am Synchrotron. Zurzeit wird dort eine MBE-Anlage betrieben, die für die Analyse halbleitender Oxide eingerichtet ist.

Dieses Jahr verbesserten wir unsere Forschungsinfrastruktur in verschiedenen Aspekten. Wir installierten um MBE-Kammern aktive Magnetfeldkompensationssysteme, die magnetische Störungen insbesondere durch die nahe gelegene U-Bahn abschirmen. Diese Systeme führen zu

einer erheblichen Verbesserung von Messungen mittels Beugung hochenergetischer Elektronen in Reflexion. Zusätzlich überprüften wir die Sicherheitsmaßnahmen im Labor und setzten einige Änderungen um. So wird jetzt zum Beispiel die Raumluft kontinuierlich auf giftiges Arsingas überwacht. Außerdem wurde die MBE-Anlage für halbleitende Oxide deutlich verändert, um Probenwachstum bei höheren Substrattemperaturen zu ermöglichen. Dazu rüsteten wir die Anlage mit einem neuen Substratmanipulator aus, was wiederum einen Austausch das Probentransfersystems erforderte.

Department of Semiconductor Spectroscopy

Abteilung für Halbleiterspektroskopie

Head of Department: Prof. Dr. Holger T. Grahn, htgrahn@pdi-berlin.de

The overall competence of this research department lies in the physics and applications of semiconductor hetero- and nanostructures, in particular with regard to their electronic and optical properties. The research topics include the investigation of elementary excitations in solids controlled by surface acoustic waves, the optical properties of III-V nanowires and heterostructures, terahertz quantum-cascade lasers, spin generation and transport in ferromagnet-semiconductor hybrid structures, quantum transport in semiconductor-based nanoscale systems, and topological insulators. Dedicated spectroscopic and magneto-transport techniques are used to determine the electronic, optical, and transport characteristics of these semiconductor hetero- and nanostructures.

Elementary excitations in solids such as photons, electrons, and spins are investigated and controlled by surface acoustic waves. These elementary excitations can be manipulated at gigahertz frequencies opening new perspectives for applications in optoelectronic devices. The optical properties of III-V nanowires and heterostructures are investigated by spatially and time-resolved photoluminescence spectroscopy as well as by cathodoluminescence spectroscopy in a scanning electron microscope. Of particular importance is the correlation between structural defects and optical properties in III-V nanowires. Quantum-cascade lasers for the terahertz spectral region are designed, their optical as well as transport properties are simulated, complete lasers are realized, and their lasing properties are investigated. These lasers are compact sources, can be operated in single mode, exhibit typical optical output powers between several mW and several tens of mW, and function at temperatures, which do not re-

Die übergreifende Kompetenz dieser Forschungsabteilung liegt in der Physik und den Anwendungen von Hetero- und Nanostrukturen aus Halbleitern, insbesondere bezüglich ihrer elektronischen und optischen Eigenschaften. Die Forschungsthemen umfassen Elementaranregungen in Festkörpern kontrolliert durch akustische Oberflächenwellen, die optischen Eigenschaften von III-V-Nanodrähten und -Heterostrukturen, Terahertz-Quantenkaskadenlaser, Spinerzeugung und -transport in Ferromagnet-Halbleiter-Hybridstrukturen, Quantentransport in nanoskaligen Halbleiter-Systemen und topologische Isolatoren. Dediizierte spektroskopische und Magnetotransport-Methoden werden zur Bestimmung der elektronischen, optischen und Transport-Charakteristika von diesen Hetero- und Nanostrukturen aus Halbleitern verwendet.

Elementaranregungen in Festkörpern wie Photonen, Elektronen und Spins werden spektroskopisch untersucht und durch akustische Oberflächenwellen kontrolliert. Die Möglichkeit, diese Elementaranregungen bei Gigahertz-Frequenzen zu manipulieren, eröffnet neue Perspektiven für Anwendungen in optoelektronischen Bauelementen. Die optischen Eigenschaften von III-V-Nanodrähten und -Heterostrukturen werden mit räumlich und zeitlich aufgelöster Photolumineszenz-Spektroskopie sowie Kathodolumineszenz-Spektroskopie in einem Rasterelektronenmikroskop untersucht. Von besonderer Bedeutung ist die Korrelation von strukturellen Defekten mit den optischen Eigenschaften von III-V-Nanodrähten. Quantenkaskadenlaser werden für den Terahertz-Spektralbereich entwickelt. Deren optische und Transport-Eigenschaften werden berechnet sowie gemessen und es werden vollständige Bauelemente



quire cooling with liquid helium. The generation and the transport of spins are studied using ferromagnet-semiconductor hybrid structures by looking at their magneto-optical and magneto-transport properties. In order to achieve spin control, all-electrical spin injection and detection are investigated using lateral and vertical spin valve devices. The electronic and spin properties of semiconductor-based nanoscale systems such as nanowires and quantum dots defined laterally in heterostructures are studied by quantum transport experiments with the aim of developing new strategies for information processing. Finally, the electronic transport properties of topological insulators, in which charges are only transported on the surface and not in the bulk, are examined by studying the weak antilocalization effect due to spin orbit coupling and the electron-electron interaction.

The facilities for optical spectroscopy include Raman spectroscopy to study the vibrational modes in semiconductor films, heterostructures, and nanowires as well as in topological insulators and graphene. Continuous-wave photoluminescence and photoluminescence excitation spectroscopy from the ultraviolet (244 nm) to the near-infrared spectral region (1.7 μm) are used to investigate III-V films, heterostructures, and nanowires. The spectroscopic techniques for the near-infrared to ultraviolet spectral regions such as Raman and photoluminescence spectroscopy can also be used with a spatial resolution down to about 0.5 μm and in magnetic fields up to 8 T. Furthermore, using cathodoluminescence spectroscopy and imaging in a scanning electron microscope, the spatial resolution can be enhanced into the range of ten nanometers. In addition, element identification is achieved by energy- and wavelength-dispersive x-ray spectroscopy, and the crystallographic orientation as well as the strain state can be determined using electron backscatter diffraction. Time-resolved photoluminescence spectroscopy on a pico- to microsecond time

realisiert. Diese Quantenkaskadenlaser sind kompakte Quellen, erlauben Einzelmodenbetrieb, besitzen typische optische Ausgangsleistungen zwischen einigen mW und einigen zehn mW, und funktionieren bei Temperaturen, die keine Kühlung mit flüssigem Helium erfordern. Die Erzeugung und der Transport von Spins werden in Ferromagnet-Halbleiter-Hybridstrukturen untersucht, indem ihre magneto-optischen und Magnetotransport-Eigenschaften gemessen werden. Ein Ziel ist es, Kontrolle über Spins in einem Halbleiter zu erhalten. Hierfür werden die rein elektrische Spininjektion und -detektion mit lateralen und vertikalen Spinventil-Bauelementen untersucht. Die elektronischen und Spin-Eigenschaften von nanoskaligen Halbleiter-Systemen wie beispielsweise Nanodrähte und Quantenpunkte, die lateral in Heterostrukturen definiert sind, werden mittels Quantentransportexperimenten für die Entwicklung neuer Strategien in der Informationsverarbeitung untersucht. Schließlich werden die elektronischen Transporteigenschaften von topologischen Isolatoren studiert, in denen Ladungsträger nur an der Oberfläche und nicht im Volumen transportiert werden.

Im Bereich der spektroskopischen Messmethoden steht uns die Ramanspektroskopie für Untersuchungen der Schwingungsmoden in Halbleiterschichten, Heterostrukturen, Nanodrähten, topologischen Isolatoren und Graphen zur Verfügung. Darüber hinaus werden Halbleiterschichten, Heterostrukturen und Nanodrähte mittels Photolumineszenz- und Photolumineszenzanregungs-Spektroskopie vom ultravioletten (244 nm) bis zum nahen infraroten (1,7 μm) Spektralbereich untersucht. Diese Methoden können mit einer räumlichen Auflösung von bis zu 0,5 μm und in Magnetfeldern von bis zu 8 T eingesetzt werden. Kathodolumineszenz-Spektroskopie in Kombination mit den Abbildungsmöglichkeiten eines Rasterelektronenmikroskops erreicht eine Ortsauflösung bis in den Bereich von zehn Nanometern. Hinzu kommt die Mög-

scale from the ultraviolet (240 nm) to the near-infrared spectral region (1.3 μm) and pump-and-probe spectroscopy with a sub-picosecond time resolution are employed to investigate the carrier and polarization dynamics in III-V films, heterostructures, and nanowires. Fourier-transform spectroscopy is used in the far-infrared spectral region to record the lasing parameters of terahertz quantum-cascade lasers and in the mid-infrared region to study vibrational modes. The magneto-transport experiments on ferromagnet-semiconductor hybrid devices, semiconductor-based nanoscale systems, and topological insulators can be performed in magnetic fields up to 16 T and at temperatures down to 20 mK.

In 2018, the selective excitation of single excitons bound to shallow impurity centers via resonant tunneling in GaAs double quantum well structures has been demonstrated. These bound excitons behave as two-level systems emitting single photons so that this system is an interesting candidate for applications in single-photon sources. Luminescent centers contained in a few-layer-thick hexagonal boron nitride film grown on Ni by molecular beam epitaxy exhibit sharp lines in photo- and cathodoluminescence spectra in both, the ultraviolet and the visible range. The characterized luminescent defects may have potential applications as quantum light sources. The confinement of microcavity polaritons in traps with an effective potential width down to 1 μm has been realized by patterning the active region of a (Al,Ga)As microcavity between two molecular beam epitaxy growth runs. The structuring method is suitable for the fabrication of arrays of neighboring traps, supporting hybridization between adjacent lattice sites.

In conventional semiconductor quantum-wire heterostructures, interface roughness leads to exciton localization and to a radiative decay rate much smaller than that expected for structures with flat interfaces. The electronic and optical properties of the

lichkeit, chemische Elemente durch energie- und wellenlängendispersive Röntgenspektroskopie zu identifizieren. Mittels der Elektronenrückstreuung erhalten wir Informationen über die kristallographische Orientierung sowie Verspannungen im Material. Zeitaufgelöste Photolumineszenz-Spektroskopie auf einer Zeitskala von Piko- bis Mikrosekunden vom ultravioletten (240 nm) bis zum nahen infraroten (1,3 μm) Spektralbereich und Anrege-Abtast-Spektroskopie mit einer Zeitauflösung unterhalb einer Pikosekunde werden eingesetzt, um die Ladungsträger- und Polarisationsdynamik in III-V-Schichten, -Heterostrukturen und -Nanodrähten zu untersuchen. Mittels Fouriertransform-Spektroskopie werden im ferninfraroten Spektralbereich die Emissionseigenschaften von Terahertz-Quantenkaskadenlasern und im mittleren infraroten Spektralbereich Schwingungsmoden untersucht. Die Magnetotransport-Experimente an Ferromagnet-Halbleiter-Hybrid-Bauelementen, nanoskaligen Halbleiter-Systemen und topologischen Isolatoren können in Magnetfeldern bis zu 16 T und Temperaturen bis herunter zu 20 mK durchgeführt werden.

Im Jahr 2018 wurde die selektive Anregung von Einzelexzitonen, die an flachen Störstellen gebunden sind, durch resonantes Tunneln in einer GaAs-Doppelquantenfilmstruktur nachgewiesen. Diese gebundenen Exzitonen verhalten sich wie ein Zwei-Niveau-System, das Einzelphotonen emittiert, so dass dieses System ein interessanter Kandidat für Anwendungen in Einzelphotonenquellen ist. Lumineszierende Zentren, die in einem wenige Lagen dicken, hexagonalen Bornitridfilm enthalten sind, der mit Molekularstrahlepitaxie auf Ni gewachsen wurde, weisen scharfe Linien in Photo- und Kathodolumineszenzspektren, sowohl im ultravioletten als auch sichtbaren Spektralbereich, auf. Die untersuchten lumineszierenden Defekte könnten möglicherweise als Quantenlichtquellen eine Anwendung finden. Der Einschluss von Mikrokavitätspolaritonen in Haftstellen mit

one-dimensional extended defects that form at the intersection between stacking faults and inversion domain boundaries in GaN nanowires have been investigated. These defects act as crystal-phase quantum wires, a novel one-dimensional quantum system with atomically flat interfaces. As a result of their unprecedented interface quality, these crystal-phase quantum wires constitute a model system for the study of one-dimensional excitons. Nanowires can also be considered to be an ideal platform for studies of the Aharonov-Bohm effect of neutral and charged excitons, as they facilitate the controlled fabrication of nearly ideal quantum rings by combining all-binary radial heterostructures with axial crystal-phase quantum structures. The all-binary GaAs/AlAs radial quantum well structures were realized by synthesizing core-multishell nanowires. Due to the atomically flat interfaces and the absence of alloy disorder, excitonic phase coherence is preserved even in rings with circumferences as large as 200 nm.

During the formation of GaN nanowires in molecular beam epitaxy, the temporal variation of the optical reflectance of the substrate using transverse electric and transverse magnetic polarized light has been analyzed. The time dependence of the reflectance signal has been simulated using an effective-medium approach that takes into account the spatial fluctuations in the length and density of the nanowire ensemble within the area probed by the laser beam. This study demonstrates that optical reflectometry is a powerful technique to detect the onset of nanowire nucleation, assess the deposition rate, and estimate the fluctuations in the nanowire length and covered area fraction at the micrometer scale. III-V nanowires have been comprehensively studied because of their suitability for optoelectronic quantum technology applications. However, their small dimensions and the spatial separation of carriers from the wire surface render electrical contacting difficult. By systematically studying ohmic

einer effektiven Potenzialbreite bis hinunter zu 1 µm wurde durch Strukturierung des aktiven Bereichs einer (Al,Ga)As-Mikrokavität zwischen zwei Wachstumsdurchläufen mit Molekularstrahlepitaxie realisiert. Diese Strukturierungsmethode ist für die Herstellung von Feldern von benachbarten Haftstellen geeignet, die die Hybridisierung angrenzender Gitterplätze fördert.

In konventionellen Halbleiter-Quantendraht-Heterostrukturen führt die Grenzflächenrauigkeit zu Exzitonlokalisierung und zu einer strahlenden Zerfallsrate, die wesentlich kleiner ist als für Strukturen mit atomar abrupten Grenzflächen erwartet wird. Die elektronischen und optischen Eigenschaften von eindimensional ausgedehnten Defekten, die sich an dem Schnittpunkt zwischen Stapelfehlern und Inversionsdomänengrenzen in GaN-Nanodrähten ausbilden, wurden untersucht. Diese Defekte verhalten sich wie Kristallphasen-Quantendrähte, ein neuartiges eindimensionales Quantensystem mit atomar abrupten Grenzflächen. Als Resultat ihrer beispiellosen Grenzflächenqualität stellen diese Kristallphasen-Quantendrähte ein Modellsystem für die Untersuchung eindimensionaler Exzitonen dar. Nanodrähte können auch als ideale Basis für Untersuchungen des Aharonov-Bohm-Effekts von neutralen und geladenen Exzitonen angesehen werden, da diese die kontrollierte Herstellung von nahezu idealen Quantenringen durch die Verbindung von rein binären radialen Heterostrukturen mit axialen Kristallphasen-Quantenstrukturen ermöglichen. Die rein binären radialen GaAs/AlAs-Quantenfilmstrukturen wurden durch die Synthese von Nanodrähten mit einem Kern und einer Vielfachumhüllung realisiert. Auf Grund der atomar abrupten Grenzflächen und dem Fehlen von Legierungsunordnung bleibt die exzitonische Phasenkohärenz sogar in Ringen mit einem Umfang von bis zu 200 nm erhalten.

Während der Entstehung von GaN-Nanodrähten in der Molekularstrahlepitaxie

contact formation by diffusion to n -doped GaAs nanowires, a set of optimal annealing parameters has been provided for Pd/Ge/Au ohmic contacts. A phenomenological model has been developed to describe the contact resistance as a function of the diffusion parameters. The results indicate that the contact resistance can be predicted with various barrier shapes, but further insights into structural properties would require a full microscopic understanding of the complex diffusion processes.

The intrinsic frequency tuning of several terahertz quantum-cascade lasers based on our hybrid design has been studied. With increasing driving current, most quantum-cascade lasers exhibit either a redshift or a blueshift of the emission frequency, while some quantum-cascade lasers show both. In the framework of an oscillator model, the tuning behavior can be explained quantitatively or at least qualitatively depending on the complexity of the current-dependent gain spectra of the terahertz quantum-cascade lasers. In view of the small tuning range, even a mere qualitative agreement is an important result as it demonstrates both, the applicability and the limits of the oscillator model in this context. Composition profiles across the interfaces of $\text{GaAs}/\text{Al}_{0.25}\text{Ga}_{0.75}\text{As}$ and GaAs/AlAs terahertz quantum-cascade laser structures have been determined using transmission electron microscopy (TEM). The experimental composition profiles are directly extracted from the analysis of the diffracted intensity distribution of \mathbf{g}_{002} dark-field TEM images. Simulated composition profiles, which have been obtained using a Fourier-transform-based model, are in remarkably good agreement with the experimental results so that the determined interface parameter can be used for designing terahertz quantum-cascade lasers. However, the actual profiles reveal a significantly lower aluminum content of the $\text{Al}_{0.25}\text{Ga}_{0.75}\text{As}$ and AlAs barriers than the nominal values due to the interface grading.

wurde die zeitliche Änderung des optischen Reflexionsgrades des Substrats mittels transvers-elektrisch und transvers-magnetisch polarisierten Lichtes analysiert. Die Zeitabhängigkeit des Reflexionssignals wurde mittels der Methode des effektiven Mediums, das die räumlichen Fluktuationen in der Länge und Dichte des Quantendrahtensembles innerhalb der mit dem Laserstrahl untersuchten Fläche berücksichtigt, simuliert. Die Untersuchung zeigt, dass optische Reflektometrie ein leistungsfähiges Verfahren ist, um den Beginn der Nanodraht-Keimbildung zu detektieren, die Abscheiderate zu bestimmen und die Fluktuationen in der Nanodrahtlänge und dem bedeckten Flächenanteil auf der Mikrometerskala abzuschätzen. III-V-Nanodrähte sind eingehend auf Grund ihrer Eignung für optoelektronische Quantentechnologieanwendungen untersucht worden. Allerdings erschweren deren kleine Abmessungen und die räumliche Trennung der Ladungsträger von der Drahtoberfläche die elektrische Kontaktierung. Durch eine systematische Untersuchung der Bildung von ohmschen Kontakten durch Diffusion in n -dotierte GaAs-Nanodrähte konnte ein Satz von optimalen Temperparametern für Pd/Ga/Au-Kontakte zur Verfügung gestellt werden. Ein phänomenologisches Modell zur Beschreibung des Kontaktwiderstandes als Funktion der Diffusionsparameter wurde entwickelt. Die Resultate zeigen, dass der Kontaktwiderstand für verschiedene Barriereförderungen vorhergesagt werden kann, aber weitere Erkenntnisse bezüglich der strukturellen Eigenschaften würden ein vollständiges mikroskopisches Verständnis der komplexen Diffusionsprozesse erfordern.

Die intrinsische Frequenzabstimmung für eine Reihe von Terahertz-Quantenkaskadenlasern, die auf unserem Hybriddesign basieren, wurde untersucht. Mit zunehmendem Betriebsstrom zeigen die meisten Quantenkaskadenlaser entweder eine Rot- oder eine Blauverschiebung der Emissionsfrequenz, während einige Quanten-

In an attempt to form nanosheets on epitaxially-grown ferromagnetic layers of Fe, Fe_3Si , and Co_2FeSi , Bi_2Te_3 has been deposited by hot-wall epitaxy. While Bi_2Te_3 reacts strongly with pure Fe, producing FeTe_2 , the reaction is suppressed for the silicides Fe_3Si and Co_2FeSi . By finding the material combinations for which the overlayer-substrate reaction is circumvented, a way to epitaxially create topological-insulator-ferromagnet multiple layer structures is opened. When Bi_2S_3 films are deposited on III-V compound semiconductors and transition metals using hot-wall epitaxy, the replacement of a constituent in the overgrown layers with the materials provided by the substrates has been investigated. The substitution caused by the S atoms is stronger than that by the Se and Te atoms in the deposition of Bi_2Se_3 and Bi_2Te_3 films. Mere exposure to Bi_2Se_3 vapor of In-containing compounds (InP and InAs) and Ga-containing compounds (GaAs and GaSb) at epitaxial growth temperatures results in a capping of their surfaces by In_2S_3 and GaS, respectively. Finally, the sulfides synthesized on the surfaces of Cu, Ag, Ni, Mo, and W have been examined. The sulfides produced on Cu and Ag undergo material alterations when they are irradiated by a laser.

kaskadenlaser beides aufweisen. Im Rahmen eines Oszillatormodells können wir in Abhängigkeit von der Komplexität der stromabhängigen optischen Verstärkungsspektren das Abstimmverhalten quantitativ oder zumindest qualitativ erklären. Angesichts des kleinen Abstimmbereichs ist sogar allein eine qualitative Übereinstimmung ein wichtiges Ergebnis, da sie sowohl die Anwendbarkeit als auch die Grenzen des Oszillatormodells in diesem Kontext aufzeigt. Zusammensetzungsprofile über die Grenzflächen von $\text{GaAs}/\text{Al}_{0.25}\text{Ga}_{0.75}\text{As}$ - und GaAs/AlAs -Terahertz-Quantenkaskadenlaserstrukturen wurden mittels der Transmissionselektronenmikroskopie (TEM) bestimmt. Die experimentellen Zusammensetzungsprofile werden direkt aus der Analyse der gebeugten Intensitätsverteilung von \mathbf{g}_{002} -Dunkelfeld-TEM-Bildern gewonnen. Simulierte Zusammensetzungsprofile, die mittels eines Fourier-Transform-Modells ermittelt wurden, stimmen bemerkenswert gut mit den experimentellen Resultaten überein, so dass die bestimmten Grenzflächenparameter für das Design von Terahertz-Quantenkaskadenlasern genutzt werden können. Die tatsächlichen Profile weisen jedoch auf Grund der Grenzflächenabstufung einen deutlich geringeren Al-Gehalt in den $\text{Al}_{0.25}\text{Ga}_{0.75}\text{As}$ - und AlAs-Barriären als die nominellen Werte auf.

In einem Versuch, Nanofilme auf epitaktisch gewachsenen ferromagnetischen Schichten von Fe, Fe_3Si und Co_2FeSi zu realisieren, wurde Bi_2Te_3 mittels *hot-wall epitaxy* abgeschieden. Während Bi_2Te_3 stark mit reinem Fe reagiert und dabei FeTe_2 gebildet wird, ist die Reaktion für die Silicide Fe_3Si und Co_2FeSi unterdrückt. Durch Identifikation der Materialkombinationen, die die Reaktion von Deckschicht mit Substrat umgehen, eröffnet sich eine Möglichkeit, Vielfachschichten aus einem topologischen Isolator und einem Ferromagneten epitaktisch zu erzeugen. Während der Abscheidung von Bi_2S_3 -Filmen auf III-V-Verbindungshalbleitern und Übergangsmetallen mittels *hot-wall epitaxy* wurde der Austausch eines der

Bestandteile in der überwachsenen Schicht mit den Materialien, die durch das Substrat zur Verfügung gestellt werden, untersucht. Hier ist die Substitution, die durch die S-Atome verursacht wird, stärker als die durch die Se- und Te-Atome bei der Abscheidung von Bi_2Se_3 - und Bi_2Te_3 -Filmen. Allein die Exposition von In-enthaltenden Verbindungen (InP und InAs) bzw. Ga-enthaltenden Verbindungen (GaAs und GaSb) zu Bi_2S_3 -Dampf bei epitaktischen Wachstumstemperaturen resultiert in einer Abdeckung ihrer Oberflächen durch In_2S_3 bzw. GaS. Schließlich wurden Sulfide, die auf den Oberflächen von Cu, Ag, Ni, Mo und W synthetisiert wurden, untersucht. Die Sulfide, die auf Cu und Ag hergestellt wurden, erfahren Materialveränderungen, wenn diese mit einem Laser bestrahlt werden.

Department of Microstructure

Abteilung für Mikrostruktur

Head of Department: Dr. Achim Trampert, trampert@pdi-berlin.de



The major research goal of the department Microstructure is to understand material properties on the basis of detailed knowledge of their microstructure (structure-property-relation). Here the term "microstructure" in the broadest sense includes all kinds of defects, i.e. all deviations from the regular structure, and their geometry and physical configuration – regardless of length scales. The probe volume detecting these features must therefore range from the macroscopic scale to the single atom level. Consequently, advanced X-ray and electron diffraction techniques, transmission electron microscopy imaging and spectroscopy as well as scanning tunneling microscopy and spectroscopy are applied with high spatial resolution and high sensitivity to analyze quantitatively the structural, chemical and electronic properties of the wide range of material systems grown at PDI or by external collaborators. Examples are low-dimensional semiconductor heterostructures, ferromagnet-semiconductor hybrid systems, and metastable materials and novel material combinations. Experimental results on hetero-phase interfaces and phase stability, epitaxial strain relaxation processes and the formation of extended and complex defects, and artificial nanostructures are compared with computer simulations and supported by theoretical modeling. Finite Element calculations can virtually cover any non-trivial geometry and chemical composition profile of low-dimensional structures and may thereby provide a highly realistic view of elastic strain relaxation and piezoelectric polarization fields within heteroepitaxial systems.

Transmission electron microscopy (TEM) is one of the key tools for direct imaging of the local atomic structure of materials. An important supplement are the high-angle

Das Ziel der Abteilung Mikrostruktur liegt darin, Materialeigenschaften auf der Basis einer detaillierten Kenntnis ihrer Mikrostruktur zu verstehen (Struktur-Eigenschaftsbeziehung). Hierbei werden als „Mikrostruktur“ alle Arten von Defekten in Kristallen, also alle Abweichungen von der regelmäßigen Struktur, deren Geometrie und physikalischen Konfiguration unabhängig von der Längenskala verstanden. Das Volumen, innerhalb dessen die Struktur detektiert wird, muss infolgedessen den gesamten Bereich von makroskopischer Dimension über die Nanometerskala bis zur Ebene einzelner Atome abdecken. Dementsprechend werden Röntgen- und Elektronenbeugungstechniken, abbildende und spektroskopische Transmissionselektronenmikroskopie sowie Rastertunnelmikroskopie jeweils mit hoher räumlicher Auflösung und Empfindlichkeit eingesetzt, um die strukturellen, elektronischen und chemischen Eigenschaften einer großen Vielfalt von Materialsystemen, die am PDI oder von externen Kooperationspartnern hergestellt werden, quantitativ zu untersuchen. Beispiele für untersuchte Materialien sind niedrig-dimensionale Halbleiterheterostrukturen, Ferromagnet-Halbleiter Hybridstrukturen sowie metastabile Materialien und neuartige Materialkombinationen. Experimentelle Ergebnisse zu Phasengrenzflächen und zur Phasenstabilität, zu Relaxationsmechanismen der Gitterfehlanpassung und zur Entstehung ausgedehnter und komplexer Defekte, sowie zu künstlichen Nanostrukturen werden mit Computersimulationen verglichen und die Interpretationen durch theoretische Modelle untermauert. Aufgrund ihrer universellen Möglichkeiten bei der Simulation sehr realitätsnaher Modelle mit nicht-trivialer Geometrie und chemischer Komposition kommt der Methode der Finiten Ele-

annular dark-field and annular bright-field detectors in a scanning (S)TEM, which are used for chemical sensitive contrast imaging with atomic resolution. Electron energy-loss spectroscopy and energy dispersive x-ray spectroscopy complete the analytical performance of our microscopes in the field of chemical bonding and composition, and allow two-dimensional mappings.

As one of our strengths high-resolution and analytical TEM is used to quantitatively determine the structural roughness of semiconductor heterostructure interfaces and their chemical intermixing. In particular, we are able to analyze the composition profiles of planar interfaces up to the atomic level. Moreover, there is an attempt to correlate the interface property with the physical functionality of the heterostructure. Examples are here the investigations of ultra-thin (Al,Ga)As/GaAs interface profiles in quantum cascade laser structures or of Ga(Sb,Bi)/GaSb quantum wells in infrared laser diodes, and the interface study of monolithically integrated III-Sb on Si. On the other hand, the atomic configurations – atom position and type – at coherent interfaces between dissimilar materials or in nanosized clusters are analyzed on the basis of (S)TEM in combination with image contrast simulations. Further examples comprise the interface character in three-dimensional core/shell or axial heterojunction nanowires and epitaxial interfaces in van der Waals heterostructures such as graphene on SiC or sapphire substrates.

In parallel to our scientific research on specific materials issues, we continually refine and develop our experimental methods per se. In the recent years, we have implemented electron tomography, a technique for obtaining three-dimensional object reconstructions of complex structures and nanoscale materials. Essential condition for this purpose is the tomography sample preparation using the focused ion beam technique. In 2018, investigations

menten hierbei eine Schlüsselrolle zu. Als numerisches Pendant zu rein analytischen Ansätzen liefert diese quantitativ, räumlich aufgelöst Deformations- und Spannungstensoren in realen Objekten sowie, für heteroepitaktische Systeme mit fehlender Inversionssymmetrie ein dreidimensionales Bild der piezoelektrischen Polarisation.

Die Transmissionselektronenmikroskopie (TEM) ist eines der zentralen Werkzeuge, um die lokale atomare Struktur von Materialien abzubilden. Eine wesentliche Erweiterung im Raster-TEM-Betrieb sind der Weitwinkel-Dunkelfeld- sowie der ringförmige Hellfeld-Detektor, die eine chemisch sensible Abbildung mit atomarer Auflösung ermöglichen. Dazu vervollständigen die Elektronenenergieverlustspektroskopie und die energiedispersive Röntgenspektroskopie die analytische Leistungsfähigkeit unserer Mikroskope im Bereich der Messung chemischer Bindungen und Zusammensetzungen, und ermöglichen zweidimensionale Kartierungen.

Eine unserer besonderen Stärken liegt im Einsatz von hochauflösender und analytischer TEM, um die strukturelle Grenzflächenrauhigkeit und Durchmischung von Halbleiterübergängen zu bestimmen. Insbesondere das chemische Zusammensetzungsprofil über planare Grenzflächen kann bis auf die atomare Ebene quantitativ ermittelt und modelliert werden. Darüber hinaus wird versucht, die strukturelle Grenzflächeneigenschaft direkt mit der physikalischen Funktionalität der Heterostruktur zu korrelieren. Als Beispiele dienen die Untersuchungen der Profile von ultradünnen (Al,Ga)As/GaAs Grenzflächen in Quantenkaskadenlasern oder von Ga(Sb,Bi)/GaSb Quantentöpfen in Infrarotlaserdioden, und die Grenzflächenuntersuchung von monolithisch integrierten III-Sb Schichten auf Si. Andererseits wird die atomare Konfiguration – das heißt, die Art und Position der Atome – an kohärenten Grenzflächen zwischen stark unterschiedlichen Materialien oder in nanoskopischen

on the three-dimensional morphology of (In,Ga)N/GaN nanowires with a pencil-like apex were carried out to unambiguously identify the "dot-in-a-wire" configuration. Further tomography results on the origin of threading dislocations in planar compound semiconductor heterostructures and their interaction with planar defects evidence the enormous potential of the method. The final goal is to study not only the structure and morphology but also its related physical and chemical properties.

The tomography activities are part of our newly established "Application Laboratory Electron Tomography". The Application Laboratory is financially supported by the European Regional Development Fund (ERDF) and by the Senate of Berlin. Very recently, the construction of a specially designed laboratory is finished within which our new cutting-edge aberration corrected Cs-STEM microscope is currently installed. This Cs-STEM will drastically increase the performance of the tomography method. Objective of the Application Laboratory is the methodical development and extensions to promote materials research, to collaborate with external partners and to utilize the tomography method to industrial applications.

A further methodical development affects our in-situ electron microscopy of dynamic processes. Heating experiments in the microscope serve to analyze defect formation and propagation, structural phase transitions and solid-state reactions with high spatial resolution. The direct observation of atoms in real-time and their correlated motion open the opportunity for basic understanding of materials properties and functionalities. Phase stability and anisotropic sublimation dynamics at high temperature of the cubic Ge-Sb-Te alloy have been made visible with atomic resolution. It is further shown that the anisotropic process leads to the formation of stable {111} facets via kink nucleation on steps as predicted by the prominent terrace-step-kink model.

schen Clustern mit Hilfe von (Raster-) TEM in Kombination mit Bild-Kontrastsimulationen analysiert. Weitere Beispiele umfassen die Natur von Grenzflächen in Nanosäulen mit lateraler oder axialer Heterostruktur, oder in van-der-Waals-gebundenen Schichtsystemen wie Graphen auf SiC oder Saphir.

Parallel zu unserer Forschung zu spezifischen Materialeigenschaften, bei der ein breites Spektrum mikroskopischer Techniken als Werkzeug verwendet wird, verbessern und entwickeln wir kontinuierlich die experimentellen Methoden selbst. So haben wir die Technik der Elektronentomographie eingeführt – eine Technik, mit der man dreidimensionale (3D) Rekonstruktionen komplexer nanoskaliger Strukturen und Materialien erhalten kann. Eine wesentliche Voraussetzung dazu ist die Herstellung spezieller Tomographieproben unter Nutzung fokussierter Ionenstrahlen. In 2018 wurden Untersuchungen zur 3D Morphologie von (In,Ga)N/GaN Nanosäulen mit stiftähnlicher Spitze durchgeführt, um die „Dot-in-a-wire“ Konfiguration eindeutig zu bestimmen. Weitere Tomographieergebnisse zum Ursprung von Durchstoßversetzungen in Halbleiterschichtstrukturen und ihre Wechselwirkung mit 2D Defekten belegen das enorme Potential der Methode für die Materialentwicklung. Ziel ist hierbei, nicht nur die Struktur und Morphologie, sondern auch die physikalischen und chemischen Eigenschaften zu studieren und miteinander zu korrelieren.

Die Tomographiearbeiten sind Bestandteil des neu gegründeten „Applikationslabor Elektronentomographie“. Das Applikationslabor wird vom Berliner Senat sowie aus Mitteln des Europäischen Fonds für regionale Entwicklungen (EFRE) gefördert. In diesem Jahr ist ein speziell entwickeltes Labor fertig gestellt worden, in das das durch Fördermittel neu angekaufte und topmoderne aberrationskorrigierten Rastertrans-missionselektronenmikroskops (Cs-STEM) installiert wird. Das Cs-STEM wird die Leistungsfähigkeit der

The physical properties of ultimately small structures at solid-vacuum interfaces are explored by low-temperature scanning tunneling microscopy (LTSTM) carried out in ultrahigh vacuum and at liquid-helium temperature. Our microscopes feature a highly stable "Besocke-Beetle" type scanner design allowing us (i) to manipulate single atoms and molecules adsorbed on a surface, and (ii) to probe the local density of electronic states as well as elementary excitations of individual nanostructures by scanning tunneling spectroscopy. In this way, the correlation between structure and properties of semiconductor-based nanostructures can be analyzed at the atomic scale. Starting at a base temperature of 5 K, the sample temperature can be varied in-situ up to ~100 K, enabling to study, e. g., surface diffusion at the single-atom level, as well as the competition between thermally excited and current-induced dynamics of engineered nanostructures and molecular switches linked to the semiconductor surface. One of our microscopes offers the capability to detect current-induced light emitted from the tunnel junction to combine optical spectroscopy with the spatial resolution of STM.

X-ray diffraction as a non-destructive probe can penetrate fairly thick layers and therefore allows to study beside surfaces, buried interfaces and structures inside the volume of the crystal. As a diffraction technique, it combines sub-Ångstrom resolution with a large interaction volume that provides statistically reliable structural properties. Results are analyzed quantitatively on the basis of modeling and simulation of diffraction data and complemented by electron microscopy measurements. In this way, we were just recently able to discover a novel superlattice-like structure in ultra-thin epitaxial FeGe₂ layers, which has been formed during solid phase epitaxy of Ge on Fe₃Si/GaAs(100) substrate.

Moreover, in the x-ray laboratory of our institute the basic parameters of many

Elektronentomographie deutlich verbessern. Aufgabe dieses Applikationslabors ist es, die Methode und ihre Weiterentwicklungen in der Materialforschung und Materialentwicklung voranzutreiben, mit externen Partnern zu kooperieren und die Elektronentomographie für industrielle Anwendungen nutzbar zu machen.

Eine weitere methodische Entwicklung betrifft unsere in-situ Elektronenmikroskopie dynamischer Prozesse. Temperaturabhängige Experimente im Mikroskop nutzen wir dazu, Defektbildung und -propagationen, strukturelle Phasenübergänge und Festkörperreaktionen an Grenzflächen mit hoher räumlicher Auflösung zu studieren. Durch die direkte Beobachtung von Atomen und deren korrelierte Bewegung in Echtzeit eröffnet sich die Möglichkeit, ein grundlegendes Verständnis von Materialverhalten und -eigenschaften zu gewinnen. Phasenstabilität und anisotrope Sublimation in kubischen Ge-Sb-Te Verbindungen sind so mit atomarer Auflösung sichtbar gemacht worden. Es konnte gezeigt werden, dass der anisotrope Prozess über die Nukleation von Kinken an atomaren Stufen zur Bildung stabiler {111} Facetten führt – in Übereinstimmung zum bekannten Terassen-Stufen-Kinken-Modell.

Die physikalischen Eigenschaften von kleinsten Strukturen an der Grenzfläche zwischen Festkörper und Vakuum werden mit Tieftemperatur-Rastertunnelmikroskopie untersucht. Diese Experimente finden im Ultrahochvakuum und bei Temperaturen von flüssigem Helium statt. Unsere Mikroskope sind mit einem äußerst stabilen „Besocke-Beetle“-Scanner Typ ausgestattet, der es uns ermöglicht, einzelne Atome und Moleküle, die auf einer Oberfläche adsorbiert sind, abzubilden und zu manipulieren. Ortsaufgelöste Tunnelspektroskopie-Experimente erlauben uns, die lokale elektronische Zustandsdichte auszumessen und Elementaranregungen zu untersuchen, die durch inelastische Streuung der Tunnellektronen selbst induziert werden.

grown structures are quickly obtained in order to give immediate feedback for further growth experiments.

The *in-situ* x-ray diffraction to investigate epitaxial layers during molecular beam epitaxy (MBE) has been established in our PHARAO facility at the synchrotron BESSY II (Helmholtz-Zentrum Berlin, HZB). Performed *in-situ*, under real growth conditions, and in real-time, our research improves the understanding of fundamental growth processes during MBE. Our work focuses on the study of epitaxial growth modes, structural analysis of interfaces and layer stacks, phase transitions, and phenomena associated with the combination of very dissimilar materials. The successful operation of such a setup critically depends on the continuous stationary operation of the MBE system at the synchrotron, since a high quality of the epitaxial layers is imperative for a reliable quantitative analysis. That is why this activity is organized in joint work with the Epitaxy department.

Addressing particular questions, relying on very high source brilliance, we are regularly applying for and performing complementary x-ray diffraction measurements at dedicated third-generation synchrotron sources like PETRAIII in Hamburg and ESRF in Grenoble. Of particular interests are newly approaching techniques like diffraction with highly focused x-rays in order to study individual low-dimensional structures. Thereby, we overcome the ensemble average inherent to x-ray techniques applying millimeter-sized x-ray spots. On the other hand, investigations of ultrathin 2D van der Waals layers, in particular if consisting of week scatterers, as B, N, and C-atoms, require extremely brilliant sources and have this been performed at the external sources as well.

Die Kombination, einerseits Halbleiter-Nanostrukturen aus einzelnen Atomen aufbauen zu können, und andererseits ihre Eigenschaften lokal zu charakterisieren, ermöglicht es uns, Korrelationen zwischen Struktur und Eigenschaften auf atomarer Skala zu studieren. Der hier experimentell erreichbare Temperaturbereich zwischen 5 K und 100 K lässt uns zum Beispiel Oberflächendiffusionsprozesse mit atomarer Auflösung studieren und ermöglicht es, die Wechselwirkung zwischen thermisch angeregter und strominduzierter Dynamik von künstlichen Nanostrukturen und molekularen Schaltern auf Halbleiteroberflächen zu untersuchen. Eines unserer Mikroskope bietet die Möglichkeit, strominduziertes Licht, das im Tunnelkontakt erzeugt wird, zu detektieren, um so optische Spektroskopie mit ortsaufgelöster Rastertunnelmikroskopie zu verbinden.

Röntgenbeugung ist eine zerstörungsfreie Methode zur Strukturaufklärung mit relativ großer Eindringtiefe. Sie ermöglicht somit neben dem Studium von Oberflächen auch Untersuchungen von Grenzflächen und Strukturen innerhalb des kristallinen Materials. Als Beugungstechnik verbindet sie Sub-Ångström Auflösung mit einem großen Wechselwirkungsvolumen, wodurch Material-eigenschaften mit statistischer Zuverlässigkeit bestimmt werden können. Ergebnisse werden mittels Modellierung und Simulation der Beugungsdaten quantitativ ausgewertet und durch elektronen-mikroskopische Messungen komplettiert. Auf diese Weise ist es uns gelungen, eine neuartige Überstruktur in ultradünnen FeGe_2 Lagen zu entdecken, die sich während der Festphasenepitaxie von Ge auf $\text{Fe}_3\text{Si}/\text{GaAs}$ Substraten bildet. In unserem Röntgenlabor können die wesentlichen strukturellen Parameter sehr schnell bestimmt werden, um so unmittelbare Rückkopplung für die Wachstumsexperimente zu geben.

In-situ Röntgenbeugung wurde an unserem PHARAO Experiment am Synchrotron BESSY II (Helmholtz Zentrum Berlin, HZB)

etabliert, um epitaktische Schichten bereits während des Wachstums mittels Molekularstrahlepitaxie zu untersuchen. Da diese Experimente in-situ, bei realen Wachstumsbedingungen und in Echtzeit durchgeführt werden können, vertiefen wir hiermit unser Verständnis der fundamentalen Wachstumsprozesse. Unsere Untersuchungen konzentrieren wir hierbei auf epitaktische Wachstumsformen, die strukturelle Analyse von Grenzflächen und Schichtstrukturen, auf Phasenübergänge und Phänomene, die bei der Kombination von stark unterschiedlichen Materialien auftreten. Der erfolgreiche Betrieb eines solch komplexen experimentellen Aufbaus hängt wesentlich vom durchgängigen, stationären Betrieb des Epitaxie-Systems am Synchrotron ab, da die hohe strukturelle Qualität der Schichten Grundvoraussetzung für die quantitative Analyse ist. Die Aktivität wird gemeinsam mit der Abteilung Epitaxie betrieben.

Zur Adressierung von Fragestellungen, die den Einsatz höchstbrillianter Quellen erfordert, beantragen und nutzen wir regelmäßig den Zugang zu Synchrotronquellen der 3. Generation wie beispielsweise PETRAIII in Hamburg und ESRF in Grenoble. Insbesondere für die Untersuchung einzelner Nanostrukturen ist der Einsatz hochfokussierter Röntgenstrahlung interessant. Dabei ergänzen wir die bisher typische Ensemblemittelung durch Anwendung extrem kleiner Röntgenspots. Untersuchung von ultradünnen, 2D van der Waals Schichten, die zudem oft aus leichten und daher weniger stark streuenden Elementen wie B, N und C bestehen, sind extrem brillante Quellen erforderlich, so dass die entsprechende Experimente dazu ebenfalls an externen Quellen durchgeführt werden.

Department of Technology and Transfer

Abteilung für Technologie und Transfer

Head of Department: Dr. Carsten Hucho, hucho@pdi-berlin.de



Research activities at PDI rely on a support infrastructure that ranges from services such as building equipment, appliances, utilities management and the machine shop over cleanroom operation and semiconductor technology to administration of human resources, and finances to transfer of know-how and intellectual property. This wide range of activities is arranged in four sections, which will be described in more detail below: I Utilities Management, II Semiconductor Technology, III Administration, IV Knowledge Transfer.

I Utilities Management

PDI is tenant in a building administered by Humboldt-Universität (HU). While the central services are provided by HU, the special infrastructural needs of a materials science institute are coordinated within this department. This comprises the supply with technical gases (especially liquid Helium for temperature-dependent experiments and liquid Nitrogen as a coolant for MBE-systems), electricity, the data- and communication-infrastructure, the operation of clean-rooms and chemistry labs and air-conditioning as well as cooling systems of the research laboratories.

II Semiconductor Technology

Most materials that are grown in the epitaxy department need further processing for subsequent scientific investigations. Our technologists provide structuring on sub-micrometer scales and processes like metallization and contacting, cutting of wafers, prepatternning, cleaning and electrical characterization of processed structures. The semiconductor technology group operates clean rooms with facilities for the whole process of photolithography

Die Forschungsaktivitäten des PDI werden durch eine Infrastruktur unterstützt, die von Haustechnik über Wartung, die feinmechanische Werkstatt und den Betrieb von Reinräumen bis zur Personalverwaltung, Einkauf und Finanzen und den Transfer von Wissen und Intellectual Property reicht. Dieses breite Spektrum an Aktivitäten kann in vier Bereiche zusammengefasst werden: I Haustechnik, II Halbleiter-Technologie, III Verwaltung, IV Wissenstransfer.

I Haustechnik

Das PDI ist Nutzer eines Gebäudes, das von der Humboldt-Universität verwaltet wird. Während zentrale Dienste (Strom, Heizung, Wasser) durch die HU sichergestellt werden, werden die spezielleren Infrastrukturbedürfnisse eines materialwissenschaftlichen Instituts innerhalb der Abteilung Technologie und Transfer koordiniert. Dies umfasst neben der Versorgung mit Spezialgasen (wie Helium für temperaturabhängige Experimente und flüssigem Stickstoff für MBE-Systeme), Strom, die Daten- und Kommunikations-Infrastruktur, den Betrieb der Reinräume und Chemielabore und Klima und Gerätekühlung für die Labore.

II Halbleiter-Technologie

Die meisten Materialien, die in der Abteilung Epitaxie gewachsen werden, benötigen eine weitere Prozessierung für anschließende wissenschaftliche Untersuchungen – zum Beispiel Vereinzeln von Wafers, Strukturierungen, Metallisierung und das Überwachsen mit Schichten außerhalb der MBE, elektrische und strukturelle Charakterisierungen, etc. Unsere Technologie ermöglicht laterale Strukturierun-

(mask-design, mask-writing, exposing and developing) which is employed to prepare the samples for subsequent selective metallization or overgrowth (with, e.g., piezoelectric material), wet and dry etching, sputtering and thermal evaporation. The rather limited resolution of photolithography is offset by its high flexibility and extended by electron-beam lithography. Photolithography can be used for rapid prototyping as well as for small series.

The wet chemical etching and the dry etching capabilities are optimized for the materials prepared within the epitaxy department and are constantly developed further.

III Administration

The administration of PDI relies on the backbone of the central administration of Forschungsverbund Berlin e.V. (FVB). All legally binding processes like salaries, work-contracts, purchase-orders, the administration of travel, etc. are administered at FVB. At the institute a small number of specially trained administrative staff provide an interface between research and administration, supervised by the scientific administrative coordinator. The person responsible for human resources supports with all necessary paperwork related to the job and assists to make the unavoidable bureaucracy when arriving from a different country bearable. Purchasing and finances is taken care of in a way that shields scientists from the intricacies of accounting and the administration of third-party-funded projects is supported by a specially trained person.

This interfacing-approach is set up to free scientist from administrative burden as much as possible while at the same time translating their needs for the professional administration at FVB and reconciling the sometimes complex administrative needs with the reality of rapidly developing research activities, involving strategic changes, unforeseeable developments, and inter-

gen auf der sub-Mikrometer-Skala mittels konventioneller optischer Lithographie und Elektronenstrahllithographie und stellt Verfahren für die Metallisierung, Kontaktierung, das Vereinzen, Reinigen und einfache elektrische Charakterisierungen zur Verfügung. Die Halbleiter Technologie verfügt über einen Reinraum mit einer Prozessstrecke für Photo- und Elektronenstrahllithographie (vom Maskenentwurf und -schreiben über Belichtung und Entwicklung bis zum Ätzen und Beschichten). Hierbei stehen nasschemische Ätzverfahren und Trockenätzverfahren sowie Sputteranlagen und Anlagen für das thermische Verdampfen von Metallen zur Verfügung. Die Ätzverfahren werden auf die Materialien angepasst, die in der Abteilung Epitaxie hergestellt werden und werden ständig weiterentwickelt.

III Verwaltung

Die Verwaltung des PDI baut auf die zentrale Verwaltung des Forschungsverbund Berlin e.V. (FVB) auf, dem gemeinsamen Träger von acht Instituten. Alle rechtlich bindenden Prozesse wie die Zahlbarmachung von Gehältern, Arbeitsverträge, Beschaffungsaufträge, die Abrechnung von Dienstreisen etc. werden zentral im FVB durchgeführt. Am Institut werden alle Personalvorgänge vorbereitet und die Mitarbeiterinnen und Mitarbeiter sowie Gäste werden bei allen Fragen zu Verträgen und Aufenthalt persönlich unterstützt. Einkauf und Finanzen werden von einer Mitarbeiterin am PDI betreut, die Drittmittelprojekte liegen in der Hand einer weiteren Mitarbeiterin. Diese Schnittstellenaktivitäten werden von einem wissenschaftlich-administrativen Koordinator am Institut organisiert, um die Übersetzung zwischen wissenschaftlichen und Wissenschaft-unterstützenden Aktivitäten zu optimieren.

IV Wissenstransfer

Wissenschaft zum Wohl der Gesellschaft zu betreiben, ist ein Kernpunkt des Selbst-

national staff with varying bureaucratic necessities but also the need for practical, personal support.

IV Knowledge Transfer

The simplistic approach to ask for proof of practicability or usability of research results—especially from institutes doing 'hard' science—is recently being substituted by a deeper understanding of the necessities of transferring knowledge into society. Rather than proving short-term applicability of our research results, our understanding of transfer ranges from informing the public about nanotechnology and materials science at large (involving public relations, developing concepts for science-communication and -visualization), providing expertise to industry, education and politics, to tracing, securing and making available

verständnisses der Einrichtungen der Leibniz-Gemeinschaft. Dies bedeutet, dass Leibniz-Einrichtungen die Verwendbarkeit ihrer Forschungsergebnisse fördern. Das PDI, dessen Forschung auf fundamentale Fragen der Materialwissenschaften zielt, die künftige Anwendungen beeinflussen, inspirieren oder gar erst ermöglichen, sieht eine wichtige Aufgabe darin, dieses Wissen zum gesellschaftlichen Nutzen zur Verfügung zu stellen.

In der Abteilung Technologie und Transfer werden Kompetenzen und Ressourcen für den Technologietransfer (im Technologietransferbüro durch die Transferbeauftragte) ebenso bereitgestellt wie für den Transfer des Wissens in die Gesellschaft

In der Leibniz-Gemeinschaft wird Transfer disziplinübergreifend verstanden. Die



intellectual property—be it in the frame of open source arrangements, licensing or marketing of patents.

The engagement of our technology transfer manager has in recent years lead to a considerable professionalization of the transfer activities. Besides the development of transfer-concepts and the definition of internal processes, the idea of technology transfer of PDI is being discussed within Leibniz-Gemeinschaft and in an increasing network of technology transfer professionals. The Head of the Technology and Transfer department is speaker of the workgroup Knowledge transfer of Leibniz-Gemeinschaft and member of the group initiated by the president defining the guidelines for knowledge-transfer.

Disziplinspezifika werden schließlich bei der Umsetzung durch die maßgeschneiderten Transferwerkzeuge sichtbar. Das PDI stellt seit November 2014 mit dem Leiter der Abteilung Technologie und Transfer den Sprecher des Arbeitskreises Wissenstransfer der Leibniz-Gemeinschaft – der als Mitglied der Präsidiumsgruppe auch das Leibniz Leitbild für Wissenstransfer mitformulierte







Facts & Figures

Zahlen und Fakten

Publications	144
Ph.D. Theses	153
Master Theses	153
Students Working on their Master Thesis	154
Conferences and workshops organized by the Institute	154
Seminar of Visitors	154
Budget Summary	157
Summary of External Funding	158
Visiting Scientists	160
Staff	162
Supporting Staff	164

Facts & Figures

Zahlen und Fakten

Publications

R. Addou, C. M. Smyth, J.-Y. Noh, Y.-C. Lin, Y. Pan, S. M. Eichfeld, S. Fölsch, J. A. Robinson, K. Cho, R. M. Feenstra, and R. M. Wallace,
One dimensional metallic edges in atomically thin WSe₂ induced by air exposure,
2D Mater. **5**, 025017, 10 pages (2018).
DOI : 10.1088/2053-1583/aab0cd

A. Al-Hassan, A. Davtyan, H. Küpers, R. B. Lewis, D. Bahrami, F. Bertram, G. Bussone, C. Richter, L. Geelhaar, and U. Pietsch,
Complete structural and strain analysis of single GaAs/(In,Ga)As/GaAs core-shell-shell nanowires by means of in-plane and out-of-plane x-ray nano-diffraction,
J. Appl. Cryst. **51**, 1387–1395 (2018).
DOI: 10.1107/S1600576718011287

A. Al Hassan, R. B. Lewis, H. Küpers, W.-H. Lin, D. Bahrami, T. Krause, D. Salomon, A. Tahraoui, M. Hanke, L. Geelhaar, and U. Pietsch,
Determination of indium content of GaAs/(In,Ga)As/(GaAs) core-shell(-shell) nanowires by x-ray diffraction and nano x-ray fluorescence,
Phys. Rev. Materials **2**, 014604, 10 pages (2018).
DOI: 10.1103/PhysRevMaterials.2.014604

K. Berlin and A. Trampert,
Phase stability and anisotropic sublimation of cubic Ge-Sb-Te alloy observed by in situ transmission electron microscopy,
J. Phys. Chem. C **122**, 2968–2974 (2018).
DOI: 10.1021/acs.jpcc.7b09855

T. Berthold, S. Katzer, J. Rombach, S. Krischok, O. Bierwagen, and M. Himmerlich,
Towards understanding the cross-sensitivity of In₂O₃ based ozone Sensors: Effects of O₃, O₂, and H₂O adsorption at In₂O₃(111) surfaces,
Phys. Status Solidi B **255**, 1700324, 8 pages (2018).
DOI: 10.1002/pssb.201700324

O. Bierwagen and Z. Galazka,
The inherent transport anisotropy of rutile tin dioxide (SnO₂) determined by van der Pauw measurements and its consequences for applications,
Appl. Phys. Lett. **112**, 092105, 5 pages (2018).
DOI: 10.1063/1.5018983

J. E. Boschker, X. Lü, V. Bragaglia, R. N. Wang, H. T. Grahn, and R. Calarco,
Electrical and optical properties of epitaxial binary and ternary GeTe-Sb₂Te₃ alloys,
Sci. Rep. **8**, 5889, 8 pages (2018).
DOI: 10.1038/s41598-018-23221-9

V. Bragaglia, F. Arciprete, A. M. Mio, and R. Calarco,
Designing epitaxial GeSbTe alloys by tuning the phase, the composition, and the vacancy ordering,
J. Appl. Phys. **123**, 215304, 6 pages (2018).
DOI: 10.1063/1.5024047

D. Braun, M. Schmidbauer, M. Hanke, and J. Schwarzkopf,

Hierarchy and scaling behavior of multi-rank domain patterns in ferroelectric $K_{0.9}Na_{0.1}NbO_3$ strained films,
Nanotechnol. **29**, 015701, 8 pages (2018).

DOI: 10.1088/1361-6528/aa98a4

M. Budde, C. Tschammer, P. Franz, J. Feldl, M. Ramsteiner, R. Goldhahn, M. Feneberg, N. Barsan,
A. Oprea, and O. Bierwagen,

Structural, optical, and electrical properties of unintentionally doped NiO layers grown on MgO by
plasma-assisted molecular beam epitaxy,

J. Appl. Phys. **123**, 195301, 10 pages (2018).

DOI: 10.1063/1.5026738

S. Cecchi, D. Dragoni, D. Kriegner, E. Tisbi, E. Zallo, F. Arciprete, V. Holý, M. Bernasconi, and R. Calarco,
Interplay between structural and thermoelectric properties in epitaxial $Sb_{2+x}Te_3$ alloys,

Adv. Funct. Mater. **29**, 1805184, 10 pages (2019).

DOI: 10.1002/adfm.201805184

E. A. Cerda-Méndez, D. N. Krizhanovskii, M. S. Skolnick, and P. V. Santos,

Quantum fluids of light in acoustic lattices,

J. Phys. D: Appl. Phys. **51**, 033001, 25 pages (2018).

DOI: 10.1088/1361-6463/aa9ec7

Z. Z. Cheng, M. Hanke, Z. Galazka, and A. Trampert,

Growth mode evolution during (100)-oriented β - Ga_2O_3 homoepitaxy,

Nanotechnol. **29**, 395705, 6 pages (2018).

DOI: 10.1088/1361-6528/aad21b

Z. Z. Cheng, M. Hanke, Z. Galazka, and A. Trampert,

Thermal expansion of single-crystalline β - Ga_2O_3 from RT to 1200 K studied by synchrotron-based high
resolution x-ray diffraction,

Appl. Phys. Lett. **113**, 182102, 4 pages (2018).

DOI: 10.1063/1.5054265

C. Chèze, F. Feix, J. Lähnemann, T. Flissikowski, M. Kryško, P. Wolny, H. Turski, C. Skierbiszewski, and
O. Brandt,

Luminescent N-polar (In,Ga)N/GaN quantum wells achieved by plasma-assisted molecular beam epitaxy
at temperatures exceeding 700 °C,

Appl. Phys. Lett. **112**, 022102, 5 pages (2018).

DOI: 10.1063/1.5009184

P. Corfdir, G. Calabrese, A. Laha, T. Auzelle, L. Geelhaar, O. Brandt, and S. Fernández-Garrido,

Monitoring the formation of GaN nanowires in molecular beam epitaxy by polarization-resolved optical
reflectometry,

CrystEngComm **20**, 3202–3206 (2018).

DOI: 10.1039/C8CE00431E

P. Corfdir, H. Li, O. Marquardt, G. H. Gao, M. R. Molas, J. K. Zettler, D. van Treeck, T. Flissikowski,

M. Potemski, C. Draxl, A. Trampert, S. Fernández-Garrido, H. T. Grahn, and O. Brandt,

Crystal-phase quantum wires: One-dimensional heterostructures with atomically flat interfaces,
Nano Lett. **18**, 247–254 (2018).

DOI: 10.1021/acs.nanolett.7b03997

Facts & Figures – Publications

E. Courtade, B. Han, S. Nakhaie, C. Robert, X. Marie, R. Renucci, T. Taniguchi, K. Watanabe, L. Geelhaar, J. M. J. Lopes, and B. Urbaszek,

Spectrally narrow exciton luminescence from monolayer MoS₂ and MoSe₂ exfoliated onto epitaxially grown hexagonal BN,

Appl. Phys. Lett. **113**, 032106, 4 pages (2018).

DOI: 10.1063/1.5033554

A. Davtyan, V. Favre-Nicolin, R. B. Lewis, H. Küpers, L. Geelhaar, D. Kriegner, D. Bahrami, A. Al-Hassan, G. Chahine, O. Loffeld, and U. Pietsch,

Coherent X-ray diffraction imaging meets ptychography to study core-shell-shell nanowires, MRS Adv., **3**, 2317–2322 (2018).

DOI: 10.1557/adv.2018.466

T. Ernst, C. Chèze, and R. Calarco,

InN and GaN/InN monolayers grown on ZnO (0001̄) and ZnO (0001),

J. Appl. Phys. **124**, 115305, 7 pages (2018).

DOI: 10.1063/1.5041880

M. Feneberg, C. Lidig, M. E. White, M. Y. Tsai, J. S. Speck, O. Bierwagen, Z. Galazka, and R. Goldhahn, Anisotropic optical properties of highly doped rutile SnO₂: Valence band contributions to the Burstein-Moss shift,

APL Mater. **7**, 022508, 7 pages (2019).

DOI: 10.1063/1.5054351

S. Fernández-Garrido, M. Ramsteiner, L. A. Galves, C. Sinito, P. Corfdir, Z. de Souza Schiaber,

J. M. J. Lopes, L. Geelhaar, and O. Brandt,

Plasma-assisted molecular beam epitaxy of GaN nanowires on epitaxial single-layer graphene,

Proc. SPIE **10532**, Gallium Nitride Materials and Devices XIII, 105321U, 11 pages (2018).

DOI: 10.1117/12.2288233

S. Gaucher, B. Jenichen, and J. Herfort,

Ferromagnet/semiconductor/ferromagnet hybrid trilayers grown using solid-phase epitaxy,

Semicond. Sci. Technol. **33**, 104005, 5 pages (2018).

DOI: 10.1088/1361-6641/aaddf0

A. Ghalgaoui, K. Reimann, M. Woerner, T. Elsaesser, C. Flytzanis, and K. Biermann,

Resonant second-order nonlinear terahertz response of gallium arsenide,

Phys. Rev. Lett. **121**, 266602, 6 pages (2018).

DOI: 10.1103/PhysRevLett.121.266602

C. Gradl, R. Winkler, M. Kempf, J. Holler, D. Schuh, D. Bougeard, A. Hernández-Mínguez, K. Biermann, P. V. Santos, C. Schüller, and T. Korn,

Asymmetric g tensor in low-symmetry two-dimensional hole systems,

Phys. Rev. X **8**, 021068, 17 pages (2018).

DOI: 10.1103/PhysRevX.8.021068

Z. W. Guo, T. Liu, Q. T. Wang, and G. H. Gao,

Construction of cost-effective bimetallic nanoparticles on titanium carbides as a superb catalyst for promoting hydrolysis of ammonia borane,

RSC Adv. **8**, 843–847 (2018).

DOI: 10.1039/c7ra10568a

M. Heilmann, M. Bashouti, H. Riechert, and J. M. J. Lopes,
 Defect mediated van der Waals epitaxy of hexagonal boron nitride on graphene,
2D Mater. **5**, 025004, 11 pages (2018).
 DOI: 10.1088/2053-1583/aaa4cb

L. von Helden, M. Schmidbauer, S. J. Liang, M. Hanke, R. Wördensweber, and J. Schwarzkopf,
 Ferroelectric monoclinic phases in strained $K_{0.70}Na_{0.30}NbO_3$ thin films promoting selective surface acoustic
 wave propagation,
Nanotechnol. **29**, 415704, 7 pages (2018).
 DOI: 10.1088/1361-6528/aad485

A. Hernández-Mínguez, J. Lähnemann, S. Nakhaie, J. M. J. Lopes, and P. V. Santos,
 Luminescent defects in a few-layer h-BN film grown by molecular beam epitaxy,
Phys. Rev. Applied **10**, 044031, 8 pages (2018).
 DOI: 10.1103/PhysRevApplied.10.044031

A. Hernández-Mínguez, Y.-T. Liou, and P. V. Santos,
 Interaction of surface acoustic waves with electronic excitations in graphene,
J. Phys. D: Appl. Phys. **51**, 383001, 17 pages (2018).
 DOI: 10.1088/1361-6463/aad593

V. Hortelano, H. Weidlich, M. P. Semtsiv, W. T. Masselink, M. Ramsteiner, U. Jahn, K. Biermann, and
 Y. Takagaki,
 Nanostructuring of conduction channels in (In,Ga)As-InP heterostructures: Overcoming carrier generation
 caused by Ar ion milling,
Appl. Phys. Lett. **112**, 151602, 4 pages (2018).
 DOI: 10.1063/1.5022967

L. Hüttenhofer, D. Xydias, R. B. Lewis, S. Rauwerdink, A. Tahraoui, H. Küpers, L. Geelhaar, O. Marquardt,
 and S. Ludwig,
 Optimization of ohmic contacts to *n*-Type GaAs Nanowires,
Phys. Rev. Applied **10**, 034024, 11 pages (2018).
 DOI: 10.1103/PhysRevApplied.10.034024

F. Ishikawa, K. Higashi, S. Fuyuno, M. Morifuji, M. Kondow, and A. Trampert,
 Annealing induced atomic rearrangements on (Ga,In) (N,As) probed by hard X-ray photoelectron
 spectroscopy and X-ray absorption fine structure,
Sci. Rep. **8**, 5962, 13 pages (2018).
 DOI: 10.1038/s41598-018-23941-y

B. Jenichen, M. Hanke, S. Gaucher, A. Trampert, J. Herfort, H. Kirmse, B. Haas, E. Willinger, X. Huang, and
 S. C. Erwin,
 Ordered structure of $FeGe_2$ formed during solid-phase epitaxy,
Phys. Rev. Materials **2**, 051402(R), 6 pages (2018).
 DOI: 10.1103/PhysRevMaterials.2.051402

J. Kalt, M. Sternik, I. Sergueev, J. Herfort, B. Jenichen, H.-C. Wille, O. Sikora, P. Piekarz, K. Parlinski,
 T. Baumbach, and S. Stankov,
 Lattice dynamics of epitaxial strain-free interfaces,
Phys. Rev. B **98**, 121409(R), 6 pages (2018).
 DOI: 10.1103/PhysRevB.98.121409

Facts & Figures – Publications

V. M. Kaganer, K. K. Sabelfeld, and O. Brandt,
Piezoelectric field, exciton lifetime, and cathodoluminescence intensity at threading dislocations in
GaN{0001},
Appl. Phys. Lett. **112**, 122101, 5 pages (2018).
DOI: 10.1063/1.5022170

J. Kellner, G. Bihlmayer, M. Liebmann, S. Otto, C. Pauly, J. E. Boschker, V. Bragaglia, S. Cecchi, R. N. Wang,
V. L. Deringer, P. Küppers, P. Bhaskar, E. Golias, J. Sánchez-Barriga, R. Dronskowski, T. Fauster, O. Rader,
R. Calarco, and M. Morgenstern,
Mapping the band structure of GeSbTe phase change alloys around the Fermi level,
Commun. Phys. **1**, 5, 11 pages (2018).
DOI: 10.1038/s42005-018-0005-8

P. Klenovský, P. Steindl, J. Aberl, E. Zallo, R. Trotta, A. Rastelli, and T. Fromherz,
Effect of second-order piezoelectricity on the excitonic structure of stress-tuned In(Ga)As/GaAs quantum
dots,
Phys. Rev. B **97**, 245314, 6 pages (2018).
DOI: 10.1103/PhysRevB.97.245314

H. Küpers, R. B. Lewis, A. Tahraoui, M. Matalla, O. Krüger, F. Bastiman, H. Riechert, and L. Geelhaar,
Diameter evolution of selective area grown Ga-assisted GaAs nanowires,
Nano Res. **11**, 2885–2893 (2018).
DOI: 10.1007/s12274-018-1984-1

A. S. Kuznetsov, P. L. J. Helgers, K. Biermann, and P. V. Santos,
Quantum confinement of exciton-polaritons in a structured (Al,Ga)As microcavity,
Phys. Rev. B **97**, 195309, 10 pages (2018).
DOI: 10.1103/PhysRevB.97.195309

J. Lähnemann, D. A. Browne, A. Ajay, M. Jeannin, A. Vasanelli, J.-L. Thomassin, E. Bellet-Amalric, and
E. Monroy,
Near- and mid-infrared intersubband absorption in top-down GaN/AlN nano- and micropillars,
Nanotechnol. **30**, 054002, 8 pages (2019).
DOI: 10.1088/1361-6528/aaef72

S. Lazić, E. Chernysheva, A. Hernández-Mínguez, P. V. Santos, and H. P. van der Meulen,
Acoustically regulated optical emission dynamics from quantum dot-like emission centers in GaN/InGaN
nanowire heterostructures,
J. Phys. D: Appl. Phys. **51**, 104001, 10 pages (2018).
DOI: 10.1088/1361-6463/aaa8d5

S. Lazić, E. Chernysheva, A. Hernández-Mínguez, P. V. Santos, and H. P. van der Meulen,
Surface acoustic wave modulation of single photon emission from GaN/InGaN nanowire quantum dots,
J. Phys.: Conf. Ser. **1092**, 012075, 4 pages (2018).
DOI: 10.1088/1742-6596/1092/1/012075

R. B. Lewis, P. Corfdir, H. Küpers, T. Flissikowski, O. Brandt, and L. Geelhaar,
Nanowires bending over backward from strain partitioning in asymmetric core-shell heterostructures,
Nano Lett. **18**, 2343–2350 (2018).
DOI: 10.1021/acs.nanolett.7b05221

Y.-C. Lin, B. Jariwala, B. M. Bersch, K. Xu, Y. F. Nie, B. M. Wang, S. M. Eichfeld, X. T. Zhang, T. H. Choudhury, Y. Pan, R. Addou, C. M. Smyth, J. Li, K. H. Zhang, M. A. Haque, S. Fölsch, R. M. Feenstra, R. M. Wallace, K. Cho, S. K. Fullerton-Shirey, J. M. Redwing, and J. A. Robinson,
Realizing large-scale, electronic-grade two-dimensional semiconductors,
ACS Nano **12**, 965–975 (2018).
DOI: 10.1021/acsnano.7b07059

T. Liu, Q. T. Wang, J. Z. Yuan, X. Zhao, and G. H. Gao,
Highly dispersed bimetallic nanoparticles supported on titanium carbides for remarkable hydrogen release from hydrous hydrazine,
ChemCatChem **10**, 2200–2204 (2018).
DOI: 10.1002/cctc.201701633

J. M. J. Lopes and D. Vignaud,
Molecular beam epitaxy of graphene and hexagonal boron nitride,
in: *Molecular Beam Epitaxy - From Research to Mass Production*, 2nd edition, edited by M. Henini (Elsevier, 2018), pp. 487–513.
DOI: 10.1016/B978-0-12-812136-8.00023-2

X. Lü, E. Luna, L. Schrottke, K. Biermann, and H. T. Grahn,
Determination of the interface grading parameter for terahertz quantum-cascade laser structures based on transmission electron microscopy,
Appl. Phys. Lett. **113**, 172101, 5 pages (2018).
DOI: 10.1063/1.5042326

E. Luna, O. Delorme, L. Cerutti, E. Tournié, J. B. Rodriguez, and A. Trampert,
Transmission electron microscopy of Ga(Sb, Bi)/GaSb quantum wells with varying Bi content and quantum well thickness,
Semicond. Sci. Technol. **33**, 094006, 8 pages (2018).
DOI: 10.1088/1361-6641/aad5c4

E. Luna, O. Delorme, L. Cerutti, E. Tournié, J. B. Rodriguez, and A. Trampert,
Microstructure and interface analysis of emerging Ga(Sb,Bi) epilayers and Ga(Sb,Bi)/GaSb quantum wells for optoelectronic applications,
Appl. Phys. Lett. **112**, 151905, 5 pages (2018).
DOI: 10.1063/1.5024199

L. Lymerakis, T. Schulz, C. Freysoldt, M. Anikeeva, Z. Chen, X. Zheng, B. Shen, C. Chèze, M. Siekacz, X. Q. Wang, M. Albrecht, and J. Neugebauer,
Elastically frustrated rehybridization: Origin of chemical order and compositional limits in InGaN quantum wells,
Phys. Rev. Materials **2**, 011601(R), 6 pages (2018).
DOI: 10.1103/PhysRevMaterials.2.011601

P. Mazzolini, P. Vogt, R. Schewski, C. Wouters, M. Albrecht, and O. Bierwagen,
Faceting and metal-exchange catalysis in (010) β -Ga₂O₃ thin films homoepitaxially grown by plasma-assisted molecular beam epitaxy,
APL Mater. **7**, 022511 (2019).
DOI: 10.1063/1.5054386

Facts & Figures – Publications

J. Momand, J. E. Boschker, R. Wang, R. Calarco, and B. J. Kooi,
Tailoring the epitaxy of Sb_2Te_3 and GeTe thin films using surface passivation,
CrystEngComm **20**, 340–347 (2018).
DOI: 10.1039/C7CE01825H

E. Mompo, M. Ruiz-Garcia, M. Carretero, H. T. Grahn, Y. H. Zhang, and L. L. Bonilla,
Coherence resonance and stochastic resonance in an excitable semiconductor superlattice,
Phys. Rev. Lett. **121**, 086805, 6 pages (2018).
DOI: 10.1103/PhysRevLett.121.086805

Y. Pan, S. Fölsch, Y. F. Nie, D. Waters, Y.-C. Lin, B. Jariwala, K. H. Zhang, K. Cho, J. A. Robinson, and
R. M. Feenstra,
Quantum-confined electronic states arising from the Moire pattern of MoS_2 -WSe₂ heterobilayers,
Nano Lett. **18**, 1849–1855 (2018).
DOI: 10.1021/acs.nanolett.7b05125

C. Rinaldi, S. Varotto, M. Asa, J. Ślawińska, J. Fujii, G. Vinai, S. Cecchi, D. Di Sante, R. Calarco, I. Vobornik,
G. Panaccione, S. Picozzi, and R. Bertacco,
Ferroelectric control of the spin texture in GeTe,
Nano Lett. **18**, 2751–2758 (2018).
DOI: 10.1021/acs.nanolett.7b04829

G. K. Rolim, S. A. Corrêa, L. A. Galves, J. M. J. Lopes, G. V. Soares, and C. Radtke,
Chemical and morphological modifications of single layer graphene submitted to annealing in water
vapor,
Appl. Surf. Sci. **427**, 825–829 (2018).
DOI: 10.1016/j.apsusc.2017.09.055

L. Schrottke, X. Lü, B. Röben, K. Biermann, M. Wienold, H. Richter, H.-W. Hübers, and H. T. Grahn,
Intrinsic frequency tuning of terahertz quantum-cascade lasers,
J. Appl. Phys. **123**, 213102, 8 pages (2018).
DOI: 10.1063/1.5024480

M. P. Semtsiv, S. S. Kurlov, D. Alcer, Y. Matsuoka, J.-F. Kischkat, O. Bierwagen, and W. T. Masselink,
Reduced interface roughness scattering in InGaAs/InAlAs quantum cascade lasers grown on (411)A InP
substrates,
Appl. Phys. Lett. **113**, 121110, 4 pages (2018).
DOI: 10.1063/1.5049090

A. Senichev, P. Corfdir, O. Brandt, M. Ramsteiner, S. Breuer, J. Schilling, L. Geelhaar, and P. Werner,
Electronic properties of wurtzite GaAs: A correlated structural, optical, and theoretical analysis of the
same polytypic GaAs nanowire,
Nano Res. **11**, 4708–4721 (2018).
DOI: 10.1007/s12274-018-2053-5

Z. Z. Shao, Z. Z. Yin, H. L. Song, W. Liu, X. J. Li, J. B. Zhu, K. Biermann, L. L. Bonilla, H. T. Grahn, and
Y. H. Zhang,
Fast detection of a weak signal by a stochastic resonance induced by a coherence resonance in an
excitable $GeTe/Al_{0.45}Ga_{0.55}As$ superlattice,
Phys. Rev. Lett. **121**, 086806, 5 pages (2018).
DOI: 10.1103/PhysRevLett.121.086806

G. V. Soares, S. Nakhaie, M. Heilmann, H. Riechert, and J. M. J. Lopes,
 Growth of boron-doped few-layer graphene by molecular beam epitaxy,
Appl. Phys. Lett. **112**, 163103, 5 pages (2018).
 DOI: 10.1063/1.5019352

Y. Takagaki, J. Herfort, M. Ramsteiner, U. Jahn, and B. Jenichen,
 Overgrowth of Bi_2Te_3 nanoislands on Fe-based epitaxial ferromagnetic layers,
CrystEngComm **20**, 4173–4178 (2018).
 DOI: 10.1039/c8ce00882e

Y. Takagaki, B. Jenichen, and A. Trampert,
 Manifestation of axiotaxy induced by the (10.4) plane in high-temperature-grown bismuth telluride films
 on InP(111),
CrystEngComm **20**, 983–989 (2018).
 DOI: 10.1039/c7ce02021j

Y. Takagaki, M. Ramsteiner, U. Jahn, and B. Jenichen,
 Constituent substitution in hot wall deposition of Bi_2S_3 films by reaction with substrates,
J. Solid State Chem. **270**, 219–225 (2019).
 DOI: 10.1016/j.jssc.2018.11.013

Z. Trabelsi, M. Yahyaoui, S. Ben Radhia, K. Boujdaria, E. Zallo, O. G. Schmidt, P. Atkinson, M. Chamarro,
 and C. Testelin,
 Neutral, charged excitons and biexcitons in strain-free and asymmetric GaAs quantum dots fabricated by
 local droplet etching,
J. Lumin. **197**, 47–55 (2018).
 DOI: 10.1016/j.jlumin.2018.01.012

D. van Treeck, G. Calabrese, J. J. W. Goertz, V. M. Kaganer, O. Brandt, S. Fernández-Garrido, and
 L. Geelhaar,
 Self-assembled formation of long, thin, and uncoalesced GaN nanowires on crystalline TiN films,
Nano Res. **11**, 565–576 (2018).
 DOI: 10.1007/s12274-017-1717-x

P. Vogt and O. Bierwagen,
 Quantitative subcompound-mediated reaction model for the molecular beam epitaxy of III-VI and IV-VI
 thin films: Applied to Ga_2O_3 , In_2O_3 , and SnO_2 ,
Phys. Rev. Materials **2**, 120401(R), 5 pages (2018).
 DOI: 10.1103/PhysRevMaterials.2.120401

R. N. Wang, F. R. L. Lange, S. Cecchi, M. Hanke, M. Wuttig, and R. Calarco,
 2D or not 2D: Strain tuning in weakly coupled heterostructures,
Adv. Funct. Mater. **28**, 1705901, 7 pages (2018).
 DOI: 10.1002/adfm.201705901

M. Wienold, T. Alam, L. Schrottke, H. T. Grahn, and H. W. Hübers,
 Doppler-free spectroscopy with a terahertz quantum-cascade laser,
Opt. Express **26**, 6692–6699 (2018).
 DOI: 10.1364/OE.26.006692

Facts & Figures – Publications

P. Wolny, M. Anikeeva, M. Sawicka, T. Schulz, T. Markurt, M. Albrecht, M. Siekacz, and C. Skierbiszewski,
Dependence of indium content in monolayer-thick InGaN quantum wells on growth temperature in
 $\text{In}_x\text{Ga}_{1-x}\text{N}/\text{In}_{0.02}\text{Ga}_{0.98}\text{N}$ superlattices,
J. Appl. Phys. **124**, 065701, 9 pages (2018).
DOI: 10.1063/1.5032287

M. Yuan, A. Hernández-Mínguez, K. Biermann, and P. V. Santos,
Tunneling blockade and single-photon emission in GaAs double quantum wells,
Phys. Rev. B **98**, 155311, 7 pages (2018).
DOI: 10.1103/PhysRevB.98.155311

E. Zallo, S. Cecchi, J. E. Boschker, A. M. Mio, F. Arciprete, S. Privitera, and R. Calarco,
Author correction: Modulation of van der Waals and classical epitaxy induced by strain at the Si step
edges in GeSbTe alloys,
Sci. Rep. **8**, 5015, 2 pages (2018).
DOI: 10.1038/s41598-018-23156-1

J. Y. Zhang, W. W. Li, R. L. Z. Hoye, J. L. MacManus-Driscoll, M. Budde, O. Bierwagen, L. Wang, Y. Du,
M. J. Wahila, L. F. J. Piper, T.-L. Lee, H. J. Edwards, V. R. Dhanak, and K. H. L. Zhang,
Electronic and transport properties of Li-doped NiO epitaxial thin films,
J. Mater. Chem. C **6**, 2275–2282 (2018).
DOI: 10.1039/C7TC05331B

Correction: Electronic and transport properties of Li-doped NiO epitaxial thin films,
J. Mater. Chem. C **6**, 4326–4326 (2018).
DOI: 10.1039/C8TC90056F

Y. H. Zhang, Y. Aviad, and H. T. Grahn,
Chaotic current self-oscillations in doped, weakly coupled semiconductor superlattices for true random
number generation,
in: *Coupled Mathematical Models for Physical and Biological Nanoscale Systems and Their Applications*,
edited by L. Bonilla, E. Kaxiras, and R. Melnik, Springer Proceedings in Mathematics & Statistics **232**,
35–50 (2018).
DOI: 10.1007/978-3-319-76599-0_2

Y. Y. Zhang, Z. Y. Sun, A. M. Sanchez, M. Ramsteiner, M. Aagesen, J. Wu, D. Y. Kim, P. Jurczak, S. G. Huo,
L. J. Lauhon, and H. Y. Liu,
Doping of self-catalyzed nanowires under the influence of droplets,
Nano Lett. **18**, 81–87 (2018).
DOI: 10.1021/acs.nanolett.7b03366

Ph. D. Theses

Feix, Felix

"Recombination dynamics in (In,Ga)N/GaN heterostructures: Influence of localization and crystal polarity"
 Humboldt-Universität zu Berlin, April 2018

Nakhaie, Siamak

"Growth of graphene/hexagonal boron nitride heterostructures using molecular beam epitaxy"
 Humboldt-Universität zu Berlin, April 2018

Berlin, Katja

"In-situ transmission electron microscopy on high-temperature phase transitions of Ge-Sb-Te alloys"
 Humboldt-Universität zu Berlin, May 2018

Buller, Jakov

"Structure and dynamics of microcavity exciton-polaritons in acoustic square lattices"
 Humboldt-Universität zu Berlin, July 2018

Küpers, Hanno

"Growth and properties of GaAs/(In,Ga)As core-shell nanowire arrays on Si"
 Humboldt-Universität zu Berlin, July 2018

Röben, Benjamin

"Terahertz quantum-cascade lasers for spectroscopic applications"
 Technische Universität Berlin, July 2018

Aranha Galves, Lauren

"Fabrication and characterization of graphene nanoribbons epitaxially grown on SiC(0001)"
 Humboldt-Universität zu Berlin, October 2018

Master Theses

Hoffmann, Georg

"Structural and spin transport studies of Co₂FeSi/MgO/GaAs heterostructures"
 Humboldt-Universität zu Berlin, March 2018

Oliva, Miriam

"Axial Ga(As,Bi) insertions in GaAs nanowires grown by molecular beam epitaxy"
 Technische Universität Berlin, March 2018

Lapsanska, Ivana

"Plasma-induced conductivity in MBE-grown thin films of gallium oxide"
 University of Strathclyde, Glasgow, August 2018

Paillet, Colin

"Growth of vertical graphene/hexagonal boron nitride heterostructures by molecular beam epitaxy"
 Polytech Grenoble, Grenoble Alpes University, France, September 2018

Di Biagio, Francesco

"Crystallization and Epitaxy Studies of Ge-rich (GeTe)_m(Sb₂Te₃)_n alloys"
 Università degli Studi di Roma "Tor Vergata", October 2018

Correa Sampaio, Ian

"Electron optics in a parabolic cavity with two quantum point contacts"
 Freie Universität Berlin, October 2018

Students Working on their Master Thesis

Pianetti, Andrea
Università degli Studi di Roma "Tor Vergata", Italy

Sabelfeld, Alexander
Technische Universität Berlin

Stramma, Alexander
Rheinisch-Westfälische Technische Hochschule Aachen

Winkler, Daniel
Technische Universität Berlin

Conferences and Workshops organized by the Institute

PDI Topical Workshop on Cathodoluminescence of Semiconductor Nanostructures

April 16-17, 2018
Jonas Lähnemann, Paul-Drude-Institut für Festkörperforschung
Workshop held at Magnus-Haus

Leibniz-Workshop on Knowledge-Transfer, "Impact"

May 03, 2018
Carsten Hucho, Paul-Drude-Institut für Festkörperforschung
Johannes Graupner, Leibniz-Institut für Gewässerökologie und Binnenfischerei
Workshop held at Senckenberg Biodiversität und Klima Forschungszentrum, Frankfurt/Main

Leibniz-Workshop on Knowledge-Transfer, "Innovation"

November 14, 2018
Carsten Hucho, Paul-Drude-Institut für Festkörperforschung
Johannes Graupner, Leibniz-Institut für Gewässerökologie und Binnenfischerei
Workshop held at Paul-Drude-Institut für Festkörperforschung, Berlin

WIAS-PDI Open Access Day 2018

Co-organized with Weierstrass Institut in Berlin
November 22, 2018
Jonas Lähnemann, Paul-Drude-Institut für Festkörperforschung
Mercedes Reischel, Paul-Drude-Institut für Festkörperforschung
Ilka Kleinod, Weierstrass Institut in Berlin
Workshop held at Weierstrass Institut in Berlin

Seminars of Visitors

11.01.2018
Mikhail Kiselev, The Abdus Salam International Centre for Theoretical Physics (ICTP), Trieste
Coupled pendulums – a classical simulator for quantum two-level systems

02.02.2018
Nicolas Grandjean, EPFL (Ecole polytechnique fédérale de Lausanne)
Efficiency of InGaN/GaN quantum wells: impact of alloy disorder

26.03.2018

Werner Dietsche, Max-Planck-Institut for Solid-State Research, Stuttgart and Laboratory for Solid-State Physics, ETH Zürich
The BCS condensate in Quantum-Hall Bilayers

06.04.2018

Carsten Ronning, Institut für Festkörperphysik, Universität Jena
Semiconductor nanowire photonics

19.04.2018

Robert Lovrincic, Institut für Hochfrequenztechnik, TU Braunschweig
Metal halide perovskites: vibrational and electronic properties

01.06.2018

Katharina Franke, Fachbereich Physik, Freie Universität Berlin
From single magnetic adatoms on superconductors to coupled spin chains

01.06.2018

Kohei Hamaya, Department of Systems Innovation, Graduate School of Engineering Science, Osaka University, Japan
Electrical spin injection in Ge using Heusler/Ge heterointerfaces

08.06.2018

Cornelius Niedsch, IFW Dresden
Why are quantum materials essential for thermoelectric energy conversion?

11.06.2018

Debdeep Jena, Cornell University
The new nitrides: X-piezo, superconductor, and semiconductor hybrid heterostructures and devices

18.06.2018

Ullrich Pietsch, Universität Siegen
Structure to property relations of single semiconductor nanowires

29.06.2018

Martien den Hertog, Institut Néel, Grenoble, France
Characterization of semiconducting nanowires by transmission electron microscopy

18.07.2018

Kimberly Dick Thelander, Solid State Physics, Lund University
Design of advanced one-dimensional nanowire materials

23.07.2018

Manfred Helm, Institut für Ionenstrahlphysik und Materialforschung, Helmholtz-Zentrum Dresden-Rossendorf
THz spectroscopy of solids with a free-electron laser

26.07.2018

Emanuele Polian, TU-Berlin
Near-field light-matter interaction in tip-enhanced Raman spectroscopy

30.07.2018

Stefano Sanguinetti, L-NESS Laboratory, Università degli Studi di Milano-Bicocca, Milan, Italy
Metal droplets in MBE growth of compound semiconductors: from bulk to nanostructures

Facts & Figures – Seminars of Visitors

20.08.2018

Mario Bomers, University of Montpellier

III-V semiconductor plasmonics for enhanced microfluidic molecular sensing

21.08.2018

Antonio Crespo Poveda, University of Valencia

Optical waveguide devices modulated by surface acoustic waves

03.09.2018

Katja Höflich, Helmholtz Zentrum Berlin

Focused ion and electron beam processing

07.09.2018

Heiner Linke, Lund University

Overview of NanoLund

Lars Samuelson, Lund University

Dislocation-free GaN platelets for LEDs and power Electronics

Anders Mikkelsen, Lund University

MAX IV and opportunities for nanoscience

10.09.2018

Paul C. McIntyre, Stanford University, USA

Group-IV Semiconductor Nanowire Structure, Luminescence and Carrier Dynamics

21.09.2018

Amalia Patane, Professor of Physics, School of Physics and Astronomy, The University of Nottingham

From epitaxy to science and processing technologies of novel van der Waals crystals

24.09.2018

Dr. Hubert Krenner, Institut für Physik, University of Augsburg, Germany

Acoustic Control of Light and Matter on a Chip

04.10.2018

Junwoo Son, Department of Materials Science and Engineering, POSTECH, Korea

Physics and applications of hydrogen-induced reversible phase transition in correlated oxides

01.11.2018

Sergei Novikov, University of Nottingham, UK

High temperature MBE of graphene and boron nitride

05.11.2018

Emil J. W. List-Kratochvil, Institut für Physik, Institut für Chemie & IRIS Adlershof,

Humboldt-Universität zu Berlin

Active control of electro/optical interface properties in hybrid inorganic/organic and devices systems using self-assembled monolayer molecules

Budget Summary

Fiscal year	2017 (actual amount) k€	2018 (actual amount) k€
Revenues		
Allocations	9,633.4	9,747.0
Earnings	11.1	18.0
Sum	9,644.5	9,765.0
Expenditures		
Staff	5,757.7	5,640.3
Administrative expenses	2,954.1	3,275.2
Equipment investment funds	932.7	849.5
Sum	9,644.5	9,765.0
External funding through projects		
Granted funds	3,201.4	5,063.0
Spent funds	2,858.9	1,387.5

Facts & Figures – Summary of External Funding

Summary of External Funding

Agency	Period	Title	Projektleiter
BMBF	01.12.2015–31.05.2019	Design principles in organic electronics: Heterogeneities in the volume and at phase boundaries – Charge and energy transfer processes at hybrid organic/inorganic semiconductor interfaces(LETOIG)	Dr. Oliver Brandt
BMBF	15.04.2018–15.04.2020	Monolithically integrated laser made from III-V nanowires for silicon photonics (MILAS)	Dr. Lutz Geelhaar
BMBF	01.06.2018–31.05.2021	InterPOL - Verbundprojekt: Polariton lattices: a solid-state platform for quantum simulations of correlated and topological states – Teilvorhaben: Development of polariton lattices with correlated and topological states for quantum simulation	Dr. Paulo Ventura Santos
DAAD	01.01.2018–31.12.2019	Study of the incorporation of Bi in GaSb for development of high performance lasers	Dr. Esperanza Luna
DAAD	01.01.2018–31.12.2019	Assessment of non-polar m-plane AlGaN surfaces, interfaces and heterostructures	Dr. Jonas Lähnemann
EFRE	01.08.2016–31.07.2020	Application laboratory electron tomography	Dr. Achim Trampert
DFG	01.10.2015–31.03.2018	Interactions in non-equilibrium mesoscopic structures	Dr. Stefan Ludwig
DFG	01.07.2016–30.06.2020	Manipulation of single electrons and single excitons by surface acoustic waves	Dr. Paulo V. Santos
DFG	01.12.2015–30.11.2018	Quantum Hall based Aharonov-Bohm spectroscopy: electron-electron interaction in non-linear magnetotransport	Dr. Stefan Ludwig
DFG	01.05.2017–30.04.2020	Nonequilibrium phenomena and interactions in ultrapure III-V nanowires	Dr. Stefan Ludwig
DFG	01.09.2017–31.08.2019	Manipulation and spectroscopy of quantum structures on semiconductor surfaces by cryogenic scanning tunneling microscopy	Dr. Stefan Fölsch
DFG	01.03.2018–28.02.2021	Coherent acousto-optical interactions in structured polariton microcavities	Dr. Alexander Kuznetsov
DFG	01.03.2018–28.02.2021	Coherent acousto-optical interactions in structured polariton microcavities	Dr. Paulo Ventura Santos
EU	01.01.2015–31.12.2018	SPRInG – short period superlattices for rational (In,Ga)N	Dr. Raffaella Calarco
EU	01.06.2015–31.05.2019	SAWtrain – dynamic electromechanical control of semiconductor nanostructures by acoustic fields	Dr. Paulo V. Santos

Agency	Period	Title	Projektleiter
WGL (SAW)	01.07.2015– 30.06.2019	Epitaxial phase change superlattices designed for the investigation of non-thermal switching	Dr. Raffaella Calarco
WGL (SAW)	01.04.2018– 31.03.2021	Barium stannate based heterostructures for electronic applications (BaSTet)	Dr. Oliver Bierwagen
WGL (SAW)	01.06.2018– 31.05.2021	Terahertz detection of atoms in plasma processes (TERAPLAS)	Dr. Holger T. Grahn
WGL (SAS)	01.07.2016– 30.06.2020	Growth and fundamentals of oxides for electronic applications (GraFOx)	Dr. Oliver Bierwagen

Facts & Figures – Visiting Scientists

Visiting Scientists

Name	Institute	Period	Topic	Country
G. Copetti	Universidade Federal do Rio Grande do Sul, Porto Allegre	03.08.2018– 28.02.2019	Halogenation as a route to modification of graphene's properties	Brazil
Dr. J. M. C. da Silva Filho	Universidade Estadual de Campinas, Campinas-SP	26.08.2018– 04.09.2018	Dielectric oxides on epitaxial graphene	Brazil
D. H. de Oliveira Machado	Universidade Estadual Paulista Júlio de Mesquita Filho, São Paulo	15.05.2018– 14.05.2019	Piezoelectric excitation of GHz vibrations in GaAs-based structures	Brazil
Prof. Dr. F. Iikawa	Instituto de Física "Gleb Wataghin", Universidade Estadual de Campinas, Campinas-SP	07.05.2018– 07.07.2018	Optomechanical effects in defect centers in crystals driven by surface acoustic waves	Brazil
T. Orestes Feijó	Universidade Federal do Rio Grande do Sul, Porto Allegre	17.09.2018– 30.09.2019	Growth of van der Waals heterostructures by MBE for nanoelectronics	Brazil
A. Hubley	University of Calgary, Calgary	01.08.2018– 31.10.2018	Electrical and optical analysis of LEDs based on single group-III-As nanowires	Canada
O. Delorme	Université de Montpellier-IES, Montpellier	21.08.2018– 01.09.2018	Transmission electron microscopy investigation of emerging GaSbBi alloys for the development of high performance mid-infrared lasers	France
M. Rio Calvo	Université de Montpellier-IES, Montpellier	25.11.2018– 09.12.2018	Transmission electron microscopy of novel laser structures	France
Dr. A. Caballero Lorenzo	Institut Kurz GmbH, Köln	01.06.2018– 31.05.2019	Curved-channel magneto-rectification using (In,Ga)As/InP heterostructures	Germany
Dr. S. Hietzschold	Institute for High-Frequency Technology, c/o InnovationLab, Heidelberg	29.01.2018– 02.02.2018	Hybrid organic/inorganic heterostructures	Germany
Prof. Dr. U. Pietsch	Department of Physics, Universität Siegen, Siegen	14.05.2018– 30.09.2018	Synchrotron-based x-ray diffraction of nanostructures	Germany
D. Ruhstorfer	Walter-Schottky-Institut, TU München, Garching	20.08.2018– 24.08.2018	Dotierte GaAs Nanodrähte	Germany

Name	Institute	Period	Topic	Country
Dr. P. Vogt	Helmholz-Zentrum Berlin, Berlin	13.08.2018– 31.12.2018	Investigation of the MBE growth kinetics of group III-oxides	Germany
S. Saadat Niavol	University of Mazandaran, Babolsar	19.03.2018– 31.08.2018	Growth and characterization of heterostructures combining semiconducting oxides and graphene for gas sensing applications	Iran
M. Azadmand	Università degli studi di Milano - Bicocca, Milano	01.04.2018– 30.09.2018	Growth of group-III nitride nanowires on sputtered TiN	Italy
Dr. S. Zanotto	CNR NANO Laboratorio NEST, Pisa	04.11.2018– 17.11.2018	GHz optomechanical effects in semiconductor metasurfaces	Italy
Prof. Dr. B. Ma	Chiba University, Chiba	11.06.2018– 10.09.2018	Raman scattering and infrared spectroscopy on semiconductor nanostructures	Japan
T. Wataru	Tohoku University, Sendai	06.09.2018– 02.12.2018	Transport spectroscopy of InAs and GaAs/AlGaAs nanowires	Japan
Dr. Z. Yin	Suzhou Institute of Nano-Tech and Nano-Bionics, Chinese Academy of Sciences , Jiangsu Province	15.08.2018– 30.08.2018	Chaotic self-oscillations in semiconductor superlattices: materials and devices	P. R. China
Dr. Y. Zhao	Suzhou Institute of Nano-Tech and Nano-Bionics, Chinese Academy of Sciences , Jiangsu Province	01.12.2018– 30.11.2019	Molecular beam epitaxy of (Al,Ga)N nanowires on graphene	P. R. China
A. Reszka	Institute of Physics, Polish Academy of Sciences, Warsaw	27.08.2018– 31.08.2018	Scanning electron microscopy related techniques	Poland
Prof. Dr. K. Sabelfeld	Institute of Computational Mathematics and Mathematical Geophysics Russian Academy of Sciences, Novosibirsk	25.04.2018– 02.05.2018	Study of cathodoluminescence at threading dislocations in GaN	Russian Federation
R. Fandan	Universidad Politécnica de Madrid	10.10.2018– 16.11.2018	Raman spectroscopy of graphene on piezoelectric substrates coupled to surface acoustic waves	Spain

Facts & Figures – Visiting Scientists – Staff

Name	Institute	Period	Topic	Country
Dr. S. Lazic	Universidad Autónoma de Madrid	01.10.2018– 31.12.2018	Production and controllable manipulation of quantum entangled photons using surface acoustic waves in semiconductor nanostructures	Spain
I. Lapsanska	University of Strathclyde, Glasgow	21.05.2018– 20.08.2018	Analysis of the functional properties of doped Ga_2O_3 thin films	United Kingdom
Dr. S. C. Erwin	Center for Computational Materials Science, Naval Research Laboratory, Washington, D.C.	21.04.2018– 28.04.2018	DFT theory of phase stability and surface/interface structure	USA
D. Hanggi	University of Alabama, Tuscaloosa, AL	17.05.2018– 02.08.2018	Electrical and structural characterization of indium oxide for applications in gas-sensors	USA
Prof. Dr. M. Msall	Bowdoin College , Brunswick, ME	26.07.2017– 31.07.2018	Multi-frequency Interdigital Transducers, Spatial Scanning of Surface Acoustic Waves and the Control of Quantum Electronic States	USA

Staff

(December 31, 2018)

Scientific staff: including Ph. D. students (D) and externally funded personnel (P)

Auzelle, Thomas (P)	Charge and energy transfer at hybrid organic/inorganic semiconductor interfaces
Ayuso Pérez, Irene (D, P)	Quantum transport in nanowires
Biermann, Klaus	Molecular beam epitaxy of GaAs-based advanced heterostructures
Bierwagen, Oliver	Molecular beam epitaxy of oxides
Brandt, Oliver	Group-III nitrides and semiconductor nanowires
Budde, Melanie (D, P)	Molecular beam epitaxy and doping of p-type semiconducting oxides
Calarco, Raffaella	Molecular beam epitaxy of group-III nitrides and phase-change materials
Cecchi, Stefano (P)	Growth and optical pump-x-ray as well as THz probe measurements of chalcogenide superlattices
Cheng, Zongzhe (D)	In-situ x-ray diffraction on group-III sesquioxides
Chèze, Caroline (P)	Molecular beam epitaxy of nitride-based short-period superlattices
Crespo Poveda, Antonio (P)	Polariton lattices as a solid-state platform for quantum simulations of correlated and topological states

Czubak, Dietmar (D)	Spin transport in ferromagnet-semiconductor hybrid structures with two-dimensional transport channels
Drube, Hardy (D)	Electron tomography of interfaces and thin films
Feldl, Johannes (D, P)	Optical spectroscopy of semiconducting oxides, in particular perovskites and sesquioxides
Flissikowski, Timur	Ultrafast dynamics of semiconductor structures
Fölsch, Stefan	Low-temperature scanning tunneling microscopy and spectroscopy
Freudenfeld, Jaan (D)	Interacting electronic nanostructures
Gao, Guanhui	Transmission electron microscopy of nanowire heterostructures
Gaucher, Samuel (D)	Molecular beam epitaxy of Ge-containing multiple ferromagnet/semiconductor hybrid structures
Geelhaar, Lutz	Molecular beam epitaxy and semiconductor nanowires
Grahn, Holger	Optical and electrical properties of semiconductor nanostructures
Hanke, Michael	Synchrotron x-ray diffraction
Heilmann, Martin	Molecular beam epitaxy of graphene/h-BN van der Waals heterostructures
Helgers, Paul (D, P)	Acoustically modulated gigahertz single-photon sources using coupled quantum wires and dots in microcavities
Hellemann, Jan (D)	Electron-phonon interaction in nanostructures
Herfort, Jens	Ferromagnet-semiconductor heterostructures
Hernández Mínguez, Alberto	Manipulation of optical and electronic properties of low-dimensional structures using surface acoustic waves
Herranz Zamorano, Jesús (P)	Devices based on group-III arsenide nanowires
Hoffmann, Georg (D, P)	Growth and doping of BaSnO ₃ and LaInO ₃
Hucho, Carsten	Technology and transfer
Jenichen, Bernd	X-ray diffraction and electron microscopy
Jordão Lopes, João Marcelo	Graphene and h-BN epitaxy
Kaganer, Vladimir	Theories of molecular-beam-epitaxial growth and x-ray scattering
Kuşdemir, Erdi (D, P)	Influence of Mg on the growth of (In,Ga)N/GaN short period superlattices
Kuznetsov, Alexander (P)	Microcavity exciton-polaritons in artificial potential landscapes
Lähnemann, Jonas	Spatially resolved optical spectroscopy and structural and chemical analysis of nanostructures
Liou, Yi-Ting (D, P)	Acousto-electric modulation of epitaxial graphene
Lü, Xiang	Terahertz quantum-cascade lasers
Ludwig, Stefan	Quantum transport in nanoelectronic systems

Facts & Figures – Staff

Luna Garcia de la Infanta, Esperanza	Transmission electron microscopy of heterointerfaces
Mazzolini, Piero	Growth kinetics and doping of $(\text{Ga},\text{Al})_2\text{O}_3$
Nicolai, Lars (D, P)	Spectroscopic electron tomography and microscopy of nanomaterials
Niehle, Michael (P)	Electron tomography of semiconductor heterostructures
Oliva, Miriam (D)	Growth of axial GaAs/Ga(As,Bi) nanowire heterostructures
Papadogianni, Alexandra (D)	$(\text{In}_{1-x}\text{Ga}_x)_2\text{O}_3$ based gas sensors
Pham, Van Dong (P)	Atom manipulation on III-V semiconductors by low-temperature scanning tunneling microscopy
Ramsteiner, Manfred	Electronic, vibrational, and magnetic properties of semiconductors
Riechert, Henning	Director
Röben, Benjamin (P)	Terahertz quantum-cascade-lasers for spectroscopic applications
Santos, Paulo	Acoustic, optic, and magnetic properties of nanostructures
Schrottke, Lutz	Quantum-cascade lasers and optical properties of heterostructures
Tahraoui, Abbes	Comprehensive semiconductor technology
Takagaki, Yukihiko	Electric properties of nanometer-scale materials
Terker, Markus (D)	In-situ transmission electron microscopy on semiconductor interfaces and defect structures
Trampert, Achim	Microstructure and electron microscopy
van Treeck, David (D)	Molecular beam epitaxy of axial and radial group-III nitride nanowire heterostructures
Yin, Yefei (D, P)	Quantum Hall effect and quantum transport
Yuan, Mingyun (P)	Manipulation of single excitons by surface acoustic waves
Zallo, Eugenio (P)	Growth and optical pump-optical probe measurements of chalcogenide superlattices

Supporting Staff

Anders, Walid	Technology
Arnhold, Kerstin	Finances/Purchasing
Baumann, René	Workshop
Behnke, Steffen	Technician
Bluhm, Anne-Kathrin	Technician
Ehrensack, Kerstin	Technician
Ferber, Thomas	Workshop

Galwadu Arachchige, Vidushi (P)	Student Assistant
Hablizel, Kai (P)	European and National Grant Management
Hartung, Andreas	Human Resources and Travel Management
Heinitz, Sebastian	Electrician
Herrmann, Claudia	Technician
Holldack, Anja	Personal Assistant to Prof. Riechert/Third Party Funding
Hörlicke, Michael	Technician
Krauß, Sabine	Technician and Chairwoman Works Council
Litschauer, Maximilian (P)	Student Assistant
Matzeck, Margarita (P)	Technician
Meister, Sebastian	Technology
Morgenroth, Katrin (P)	Technician
Pakulat, Bernd	Head of IT and Data Protection Officer
Pfeiffer, Astrid	Technician
Pfeiffer, Jörg	Head of Workshop
Rauwerdink, Sander	Technology
Reischel, Mercedes	Transfer Management
Riedel, Angela	Technician
Schönherr, Hans-Peter	Technician
Seidel, Werner	Technology
Sieg, Michael	Workshop
Steffen, Doreen	Technician
Stemmler, Carsten	Technician
Suchilina, Ekaterina	Office Assistant
Venohr, Thomas	Workshop
Wirsig, Arno	Technology
Wirt, Andreas	IT



Contact Kontakt



DIRECTORATE

Prof. Dr. Henning Riechert

Director
phone: +49 30 20377-365
fax: +49 30 20377-201
riechert@pdi-berlin.de

Anja Holldack

Office
phone: +49 30 20377-352
holldack@pdi-berlin.de

Dr. Carsten Hucho

Scientific-Administrative Coordinator
phone: +49 30 20377-234
hucho@pdi-berlin.de

Ekaterina Suchilina

Office
phone: +49 30 20377-481
suchilina@pdi-berlin.de

PUBLIC RELATIONS

Dr. Carsten Hucho

phone: +49 30 20377-234
fax: +49 30 20377-515
hucho@pdi-berlin.de

GENDER EQUALITY OFFICER

Dr. Raffaella Calarco

phone: +49 30 20377-351
fax: +49 30 20377-515
raffaella.calarco@pdi-berlin.de

TRANSFER

Dr. Carsten Hucho

phone: +49 30 20377-234
fax: +49 30 20377-515
hucho@pdi-berlin.de

Mercedes Reischel

Technology Transfer Manager
phone: +49 30 20377-289
fax: +49 30 20377-515
reischel@pdi-berlin.de

ADMINISTRATION

Andreas Hartung

Human Resources
phone: +49 30 20377-475
hartung@pdi-berlin.de

Kerstin Arnhold

Purchasing/Finances
phone: +49 30 20377-358
fax: +49 30 20377-425
arnhold@pdi-berlin.de

CHAIR OF WORK COUNCIL

Sabine Krauß

phone: +49 30 20377-258
sabine.krauss@pdi-berlin.de

SPEAKER OF SCIENTISTS

Dr. Oliver Bierwagen

phone: +49 30 20377-491
bierwagen@pdi-berlin.de

DEPARTMENTS

Dr. Lutz Geelhaar

Head of Department Epitaxy
phone: +49 30 20377-359
fax: +49 30 20377-201
geelhaar@pdi-berlin.de

Dr. Achim Trampert

Head of Department Microstructure
phone: +49 30 20377-280
fax: +49 30 20377-201
trampert@pdi-berlin.de

Prof. Dr. Holger T. Grahn

Head of Department Semiconductor Spectroscopy
phone: +49 30 20377-318
fax: +49 30 20377-301
htgrahn@pdi-berlin.de

Dr. Carsten Hucho

Head of Department Technology and Transfer
phone: +49 30 20377-234
fax: +49 30 20377-515
hucho@pdi-berlin.de



Imprint Impressum



Imprint

Impressum

Paul-Drude-Institut für Festkörperelektronik,
Leibniz-Institut im Forschungsverbund Berlin e.V.

Hausvogteiplatz 5-7
10117 Berlin
Germany

Tel. +49 30 20377-481
Fax +49 30 20377-515
info@pdi-berlin.de

PUBLISHED BY / HERAUSGEGEBEN VOM
Paul-Drude-Institut für Festkörperelektronik, 2019

EDITORIAL / REDAKTION
Dr. Carsten Huchó

DESIGN / GESTALTUNG
unicom-berlin.de

PHOTOS / FOTOS
Kornelius Glaser (S.1, cover), Irene Krawczyk (S.2,15,16), Mercedes Reischel (S.8),
Sander Rauwerdink (S.10,12,13,14,25,42,66,67,118,119,140,141,173),
Sadie Weis (S.40,41), Anja Holldack (S.142,143,166,167),
Jonas Lähnemann (S.170,171)

www.pdi-berlin.de

Power (% vs. Time)





Scientists and administrative staff experience phases of extreme stress at their workplace. The final stage of a dissertation, preparations for large conferences, or development of proposals for scholarship programs, leave little or no time for life outside the office or the lab. The employees' enormous personal engagement arises from their strong identification with the research they are involved in. While such identification can be very positive, leading to profound satisfaction with one's professional activity, it can also result in pressure and tensions in the family environment.

We at PDI place great importance on promoting work-life balance and support our employees in this respect through individual solutions. Our measures are continuously developed within an external audit process. On December 10, 2018 PDI was re-certified by berufundfamilie gGmbH for its engagement in pursuing a family-friendly human resources policy.

Alle Wissenschaftlerinnen und Wissenschaftler und die Wissenschaft unterstützenden Mitarbeiterinnen und Mitarbeiter kennen Phasen extremer zeitlicher Belastungen bei ihrer Arbeit. Während der Endphase einer Doktorarbeit, im Umfeld großer Tagungen oder in der Antragsphase für ein Stipendienprogramm ist oft kaum noch Platz für ein Leben außerhalb des Büros und Labors. Das enorme persönliche Engagement der Mitarbeiterinnen und Mitarbeiter speist sich aus der starken Identifikation mit der Forschung. Im positiven Fall bedeutet diese Identifikation große Zufriedenheit mit der beruflichen Tätigkeit – sie kann aber auch zu Belastungen und Einschränkungen im familiären Umfeld führen.

Wir legen am PDI großen Wert auf die Vereinbarkeit von Beruf und Familie und unterstützen unsere Mitarbeiterinnen und Mitarbeiter hierbei durch individuelle Maßnahmen. Im Rahmen eines externen Auditierungsprozesses werden unsere Maßnahmen weiterentwickelt. Das PDI wurde am 10. Dezember 2018 erneut für sein Engagement für eine familienbewusste Personalpolitik durch die berufundfamilie gGmbH zertifiziert.



Paul-Drude-Institut für Festkörperelektronik,
Leibniz-Institut im Forschungsverbund Berlin e.V.

Hausvogteiplatz 5-7
10117 Berlin
Germany

www.pdi-berlin.de

